TECHNISCHE UNIVERSITÄT MÜNCHEN

Munich School of Engineering

Morphology Formation and Manipulation in Printed Organic Solar Cells

Stephan Hubert Pröller

Vollständiger Abdruck der von der Munich School of Engineering der Technischen Universität München zur Erlangung des akademischen Grades eines

Doktors der Naturwissenschaften (Dr. rer. nat.)

genehmigten Dissertation.

Vorsitzender:	Prof. Dr. Karsten Reuter
Prüfer der Dissertation:	1. Prof. Dr. Eva M. Herzig
	2. apl. Prof. Dr. Peter Müller-Buschbaum

Die Dissertation wurde am 26.10.2017 bei der Technischen Universität München eingereicht und durch die Munich School of Engineering am 02.02.2018 angenommen.

Abstract

The present work investigates the formation kinetics and possible manipulations of the morphology of printed organic solar cells. For this purpose, an up-scalable printing device is designed and constructed. The slot die coater is built in a modular way to easily adapt it to different measurement techniques and control parameters. The printer is inserted into a synchrotron beamline and the structure formation of printed organic films is followed *in situ* with grazing incidence small and wide angle X-ray scattering. A model of the structure formation is extracted, serving as basis of the establishment of a process to tailor the structure via electrophoresis-assisted printing. The application of an electric field during film deposition yields an optimized inner film structure. For further control of the morphological evolution, a chamber is developed, which enables the variation of the chemical atmosphere surrounding the sample. The comparison of the structure formation of films printed in a dry versus a solvent-enriched atmosphere via grazing incidence X-ray scattering illuminates the positive effect of subsequent solvent annealing. This work contributes to the understanding of the structure formation in printed organic solar cells and provides pathways to tailor their morphology.

Zusammenfassung

Diese Arbeit befasst sich mit der Strukturbildung in gedruckten organische Solarzellen und Möglichkeiten, diese Strukturbildung zu beeinflussen. Dafür wurde ein hochskalierbarer Druckeraufbau konstruiert und gebaut. Um Anpassungen an verschiedene Messmethoden sowie Kontrollparameter einfach durchzuführen, ist der Schlitzdüsendrucker in modularer Bauweise entworfen. Der Drucker wird in eine Synchrotron-Endstation eingebaut, um die Strukturbildung in gedruckten organischen Filmen *in situ* mit Röntgenklein- und -weitwinkelstreuung unter streifendem Einfall zu verfolgen. Ein daraus entstandenes Modell der Strukturbildung dient als Basis, um einen Prozess zu etablieren, der die Struktur mittels eines elektrophorese-unterstützten Druckprozesses beeinflusst. Das während des Druckens angelegte elektrische Feld führt zu einer optimierten inneren Struktur. Zur weiteren Kontrolle der Morphologiebildung dient die Entwicklung einer Kammer, die es erlaubt, die chemische Atmosphäre um die Probe zu variieren. Der Vergleich der Strukturentwicklung zwischen Filmen, die entweder in einer trockenen oder einer mit Lösemittel angereicherten Atmosphäre gedruckt werden, zeigt den positiven Effekt des Lösemitteltemperns. Diese Arbeit liefert einen Beitrag zum Verständnis der Strukturbildung in gedruckten organischen Solarzellen und bietet mögliche Ansätze, deren Morphologie zu beeinflussen.

Contents

List of abbreviations

AFM ..... atomic force microscopy

ALS ..... Advanced Light Source

BHJ ..... bulk-heterojunction

CB ..... conduction band

CBZ ..... chlorobenzene

CCD ..... charge coupled device

DCBZ ..... dichlorobenzene

DI water ..... deionized water

DWBA ..... distorted wave Born approximation

EG ..... ethylene glycol

FF ..... fill factor

FTIR ..... Fourier transformed infrared spectroscopy

FTO ..... fluorine doped tin oxide, SnO_2:F

FWHM ..... full width at half maximum

GID ..... grazing incidence diffraction

GISAXS ..... grazing incidence small angle X-ray scattering

GIWAXS ..... grazing incidence wide angle X-ray scattering

GIXS ..... grazing incidence X-ray scattering

HOMO ..... highest occupied molecular orbital

I/V ..... current-voltage characteristics

IPA ..... isopropyl alcohol, C_3H_8O

ITO ..... indium doped tin oxide

LBNL ..... Lawrence Berkeley National Laboratory

LCAO ..... Linear combination of atomic orbitals

LED ..... light emitting diode

LMA ..... local monodisperse approximation

LUMO ..... lowest unoccupied molecular orbital

MIS-CELIV ..... metal-insulator-semiconductor - charge extraction by linearly increasing voltage

MPP ..... maximum power point

NIR ..... near infrared

NREL ..... National Renewable Energy Laboratory

OE ..... organic electronic

OLED ..... organic light emitting diode

OPV ..... organic photovoltaic

OSC ..... organic solar cell

P3HT ..... poly(3-hexyl-thiophene), $(C_{10}H_{14}S)_n$

PA ..... polyacetylene

$PC_{70}BM$ ..... [6,6]-phenyl-C_{71}butyric acid methyl ester

PCBM ..... [6,6]-phenyl-C_{61}butyric acid methyl ester

PEDOT:PSS ..... poly(3,4-ethylenedioxythiophene):poly(styrenesulfonate)

PEEK ..... poly(ether ether ketone)

PL ..... photoluminescence

PTFE ..... poly(tetrafluoroethylene)

PV ..... photovoltaic

PVDF ..... poly(vinylidene fluoride)

rpm ..... revolutions per minute

SDD ..... sample-detector distance

SEM ..... scanning electron microscopy

SLD ..... scattering length density

TCO ..... transparent conductive oxide

TEM ..... transmission electron microscopy

UV/Vis ..... UV/Vis spectroscopy

VB ..... valence band

Vis-NIR ..... visible-near infrared

WLI ..... white light interferometry

XRD ..... X-ray diffraction

XRR ..... X-ray reflectivity

1 Introduction

Solar power - and in particular photovoltaics (PVs) - is one of the pillars of renewable energy supply. An enormous increase in global PV capacity has led to 303 GW installed capacity by the end of the year 2016. [1] This is an increase of 75 GW compared to 2015, and 297 GW additional capacity since 2006 - an increase by a factor of 50. [1] This trend emphasizes the rising demand for PV devices. Studies show the area potential of buildings in Germany of 2344 km^2 split into 1760 km^2 of roof area and 584 km^2 of facades to be equipped with PV. [2, 3] A recent study of the National Renewable Energy Laboratory (NREL) estimates the potential in US housings to 8130 km^2. [4, 5] However, 60-80% of the surface can not be equipped with heavy glass or conventional photovoltaic technology but needs a light weight PV solution. [5] To fill this gap new technologies are needed.

The discovery of electrical conductivity of polyacetylene via oxidative doping in the 1970s was awarded with the Nobel prize in chemistry in 2000 for Alan J. Heeger, Alan G. MacDiarmid and Hideki Shirakawa. [6, 7] This triggered the interest on organic semiconductors and led to extensive research on organic photovoltaics (OPVs). Their light weight offers the possibility to supply the demand in niche markets. Next to the light weight, OPV exhibits a number of further advantages, amongst them the high mechanical flexibility, the optical tunability and the good performance under low light conditions and low angle of incidence. [5, 8–11] Moreover, a cost-efficient processing of organic solar cells (OSCs) is possible by evaporation or printing techniques. [12–14] The production of OPVs in roll-to-roll coating processes enables the fabrication of large scale devices. [15, 16] This potentially allows for a number of applications including integration into buildings, wearables and portable devices as well as mobility and the Internet of Things (IoT). [5] For device commercialization, five core technologies have to be addressed by both, academic and industrial research. These include device efficiency and stability, flexible transparent electrodes, module design and printing technologies. [17]

The conversion of sun light into electrical energy in photovoltaic devices can be divided into the main processes of light absorption and excitation of charge carriers, their separation into free charge carrier and following transportation to the respective electrodes. In inorganic solar cells, these processes happen within the same material, as the weak Coulombic binding of the excited charge carriers and the built-in pn-junction are

sufficient to split the charge carriers at room temperature and transport them to the respective materials. In OSCs, at least two materials are needed to generate and provide the free charge carriers. A promising approach for OSCs is the combination of semiconducting polymers with methano fullerenes. [18–20] One of the most intensely studied material systems - and therefore applied as a benchmark - is the combination of the polymer poly(3-hexyl-thiophene) (P3HT) with the fullerene derivative [6,6]-phenyl-C_{61}butyric acid methyl ester (PCBM). [21–23] In OSCs, the light is absorbed in the strongly absorbing polymer, which excites an electron and creates a bound electron-hole pair, an exciton. The short lifetime of the exciton allows it to diffuse within a limited radius of only a few nanometers, before it recombines again to the ground state. [24] In order to be split into its respective charge carriers, this exciton needs to reach a polymer/fullerene interface within its lifetime. Therefore, one of the most efficient morphologies is an interpenetrating network of the polymer and the fullerene with length scales of a few nanometers. This is commonly achieved by so-called bulk-heterojunction (BHJ) solar cells. [25–29] Once the exciton reaches such an interface, it can be split into free charge carriers, the electron and the hole. Consequently, the active layer morphology on the nanoscale is of utmost importance in order to produce free charge carriers, a prerequisite to obtain current from the OSC. However, after successfully splitting an exciton, the electrons and holes are found in polymer and fullerene domains, respectively. In order to extract the charge carriers, transportation to the respective electrodes must be ensured. For this a percolation path for the charge carriers as well as a sufficient charge carrier mobility in the material are needed. While the percolation paths are a morphological matter in the order of several nanometers, the charge carrier mobility is influenced by the packing and orientation of polymer crystals in the Ångstrom to nanometer regime. [30] Therefore, the morphology on different length scales is essential for efficiently working solar cells. Understanding and manipulating the structure formation in organic solar cells is hence highly desirable as a key to improve the device performance.

A lot of research investigated the relationship between the morphology and the functionality of OSCs. Common techniques to investigate the inner film structure are optical absorption spectroscopy, reflectometry and scattering using optical or X-ray radiation, scanning and transmission electron microscopy, optical and atomic force microscopy, to name a few. [31–36] Often, the materials are characterized on static samples after the production. While this yields information about the structure-function relation, it does not provide insights into the kinetics taking place during the structure formation. Due to the evolving experimental techniques and computational power, investigations of the involved kinetics have recently become possible. With *in situ* studies, the morphological evolution is investigated for example for spin coated or solution cast samples. [37–40] The

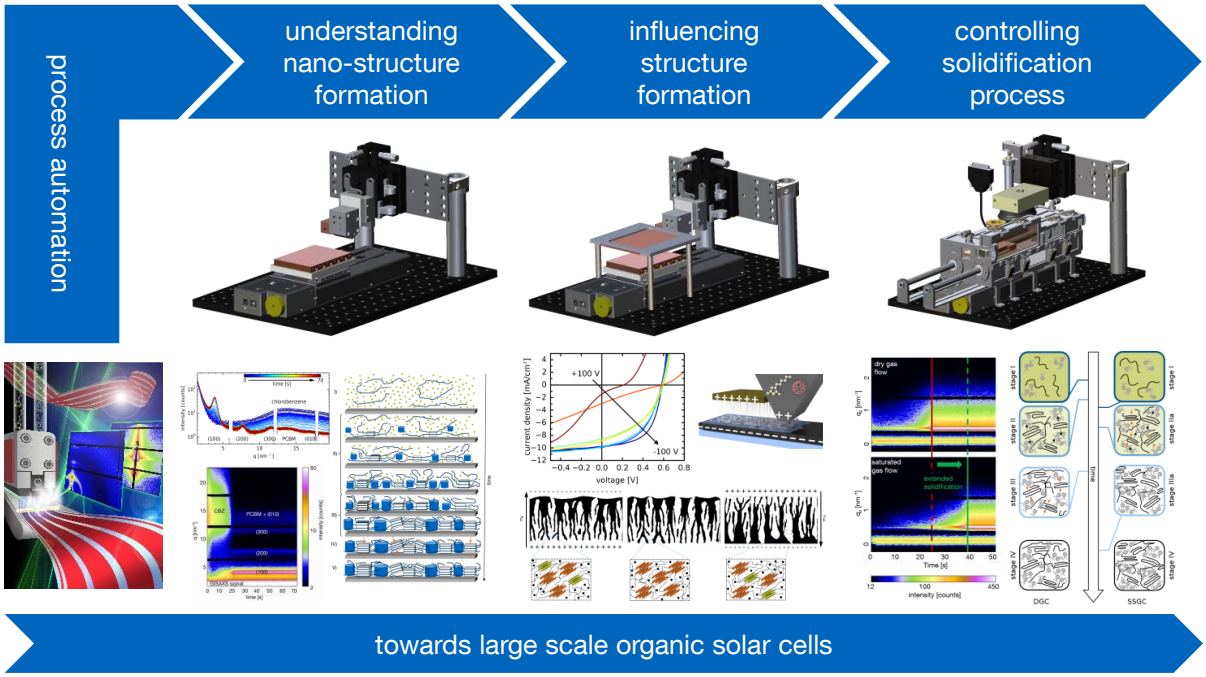

Figure 1.1: Overview of the topics covered within the scope of this thesis. The overall goal is to gain knowledge necessary for the production of large scale organic solar cells. Therefore, the work is split into four work packages. For all physical investigations, the prerequisite is to automatize the process of printing solar cells. As basis, a printer for lab applications is designed, set up and adapted to the different purposes of the individual research topics. First, the processes during the nano-structure formation are investigated in order to contribute to understand the basic morphology formation on the nano-scale. Based on this work, the assembly of the active layer is actively influenced on the nanometer scale during coating via the application of an external electric field and the assistance of electrophoretic forces. The development of an atmospheric gas control chamber finally allows to control the solidification process of the printed film by varying the solvent content in the surrounding atmosphere.

deposition techniques mostly applied to date are well established on a laboratory scale yielding high performing OSCs. Up-scaling to large area devices is not easily possible, especially with spin coated devices. However, the structure formation dynamics might differ depending on the applied deposition methods and are thus not simply transferable to printing techniques. In order to bridge the gap from lab to fab applications, further research on the processes involved in printed OSCs is necessary, especially in terms of structure evolution dynamics and possibilities to influence the morphology formation.

The presented thesis contributes to the understanding of the relationship between structure and function in up-scalable printing techniques, which is an important factor towards large scale OSCs. The focus lies on the kinetics involved in the structure formation and

possible manipulations during the morphological evolution. Figure 1.1 gives an overview of the aspects addressed within this thesis. The principal aim of the work presented in this thesis is to acquire knowledge, that is necessary when moving towards large-scale OSCs. The basis of the work is the development and construction of a printing setup for organic thin films to automatize the sample processing. It additionally requires the possibility to perform *in situ* studies on the structure formation in the printed organic films. This experimental setup should be designed in a modular way in order to expand it with additional parameter control building blocks and adapt it to the required measurement techniques. The printer should be capable to picture the printing process of OSCs at a laboratory scale. With the basic printer setup, an understanding of the structure formation should be gained by performing *in situ* X-ray scattering studies on the printed organic thin films. The knowledge about the structure formation in printed films is used to actively influence its morphology while processing. This aims to provide an easy and versatile approach to optimize the device performance. The printer setup is therefore equipped with electrodes for the application of an electric field during thin film deposition. Moreover, the design of an atmospheric chamber for the printer setup allows to control the atmosphere surrounding the printed film. With a varying solvent atmosphere, the solidification process should be controlled and the influence is investigated with *in situ* X-ray scattering.

The thesis first introduces the physical background in chapter 2. This background is intended to give a brief overview to follow the processes and techniques used within the scope of this work. The applied characterization methods are presented in chapter 3 and the sample preparation in chapter 4. The design and versatility of the printer setup is described in chapter 5. The results of the morphology evolution in printed layers are compared to the known processes in spin coated or solution cast films. The investigations are presented in chapter 6. Chapter 7 presents the possibility arising from the electrophoretic assisted printing by depositing the organic film in the presence of an electric field. The control of the solidification process by varying atmospheres is presented in chapter 8. The thesis closes with a conclusion of the findings and an outlook in chapter 9.

2 Theoretical aspects

This chapter considers the most basic theoretical background in the frame of the topics covered in this thesis. First, the basics of polymer physics are introduced in section 2.1. Special focus is put on the conductivity of polymers and their crystallization and phase separation behavior. The presented topics are prerequisites for the functioning of organic solar cells and thus explained to introduce the working principles of organic solar cells presented in section 2.2. In this section all involved principles from light absorption to charge carrier generation to the final charge extraction are covered. Subsequently, the background of printing methods with a focus on slot-die coating is given in section 2.3. X-ray scattering is utilized as the main characterization method in this thesis. Hence, section 2.4 addresses the concepts involved in investigating the inner film structure using X-ray scattering.

As this chapter only provides a very brief overview over the fundamentals of polymers, organic semiconductors, liquid film coating and scattering, the reader is referred to literature for further details, from which the following overview is mainly extracted. [41–52]

2.1 Polymer fundamentals

Polymers are macromolecules which consist of a sequence of monomers (*poly* greek for 'many'). A monomer is therefore the smallest unit of a polymer, typically an atom or a small molecule. Monomers covalently bind to other monomers to form the polymer. The number of monomers in a polymer is defined as degree of polymerization n. The definition of a polymer generally depends on the chain length. The end of chains might interact differently with the surroundings compared to the chain itself. Different to polymers, oligomers have a lower degree of polymerization and are thus shorter. As the ratio of end to middle part of the chain differs for oligomers and polymers, the properties between both typically differ, too. The terms used to describe polymers are defined by the International Union of Pure and Applied Chemistry (IUPAC). [53] To graphically illustrate a polymer, different notations are used as exemplary depicted in figure 2.1 as example for polystyrene or short PS. The chemical formula of PS is $(C_8H_8)_n$, where n is the average number of monomer units per polymer (degree of polymerization). The simplest way to depict a

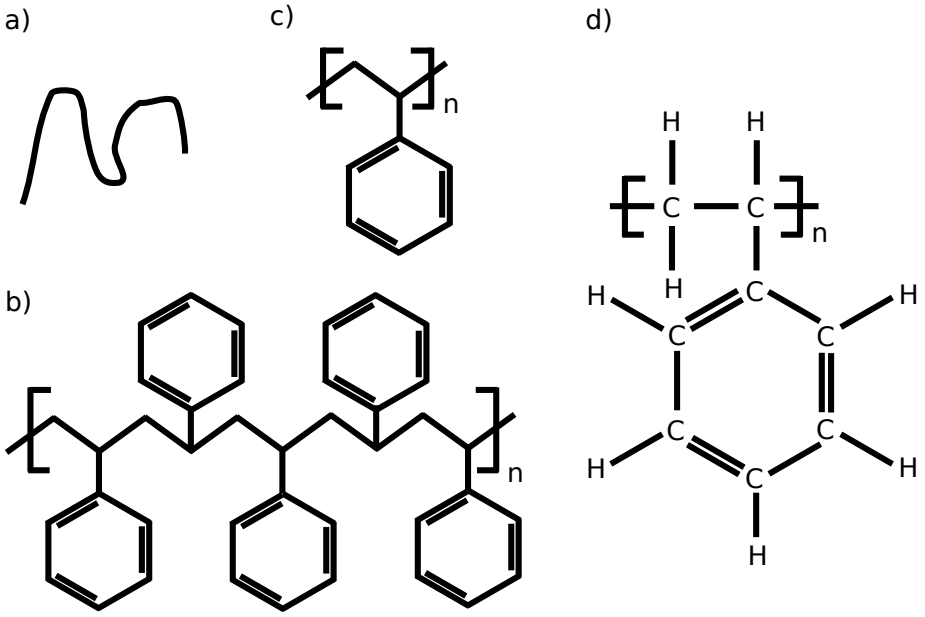

Figure 2.1: Different representations of polymers: (a) Most simple representation by a line indicating the backbone of the polymer. (b) The skeletal formula for several monomers or (c) the abbreviated skeletal formula for one monomer and the degree of polymerization n. (d) The complete Lewis structure formula for one monomer. The examples are given for polystyrene.

polymer is to simply draw the backbone chain as a curled line (figure 2.1a). A common way to show the chemical formula is to show the skeletal formula for several monomers (figure 2.1b). One line represents a single bond, two lines a double bond. The skeletal formula is also used in an abbreviated representation as depicted in figure 2.1c. There, only one monomer is depicted and brackets indicate the repeating unit with the degree of polymerization n. The long hydrocarbon chain is usually denoted as polymer backbone and the phenyl side group - in the case of PS -is periodically attached. The complete components are shown in figure 2.1d in the Lewis representation, in which all the atoms are explicitly labeled. In this thesis, the polymers are usually represented by either of figure 2.1a-c.

Polymers are synthesized by covalently binding the monomer molecules together, called polymerization. This is an statistical process and thus never leads to one single degree of polymerization but a statistical collective. Therefore, all definitions for polymers are based on statistics. The first central moment of the statistical distribution of molar masses is the number average molar mass M_n:

$$M_n = \frac{\sum\limits_i n_i M_i}{\sum\limits_i n_i} \tag{2.1}$$

where n_i is the number of moles of each polymer species, and M_i is the molar mass of that species i. The total mass of the macromolecules of the i-th species is $w_i = n_i \cdot M_i$. With that the weight average molar mass M_w is defined as

$$M_w = \frac{\sum\limits_i w_i M_i}{\sum\limits_i w_i}. \tag{2.2}$$

An important characteristic of polymers is the width of the distribution of molar masses, i.e. the distribution of the degree of polymerization. It is called polydispersity index PDI:

$$PDI = \frac{M_w}{M_n} = U + 1 \tag{2.3}$$

with U, the inconsistency coefficient as a measure of the distribution width. A monodisperse polymer, which would mean the same degree of polymerization of all components, has PDI = 1 and U = 0. The PDI for synthetic polymers is larger than 1. For scientific purposes a PDI close to 1 is desirable as the properties of the polymers are better defined. This is for example obtained by a chain-growth polymerization, in which monomers are attached to already existing polymer fragments.

The shape of a polymer chain is described by its conformation. It is generated by the rotation of polymers or chain segments around single bonds. The shape of the polymer depends on the surrounding environment like the solvent. In a good solvent, meaning that the optimization of Gibb's free energy favors the mixing of polymer and solvent, the chains are rather stretched resulting in an open chain conformation. Gaussian coils or tightly coiled conformations are obtained by mixing the polymer with a bad solvent, meaning the optimization of Gibb's free energy favors two phases.

Depending on the conformation of the polymers, different characteristic length scales are of interest. The contour length describes the length of a completely stretched polymer chain, which is rarely used to describe a polymer as it is not observed in reality. To account for the coiled structure, a more reasonable length scale is the end-to-end distance R_e between the first and last monomer of a polymer chain, which on the other hand does not provide information on the polymer's volume. A commonly used length scale is the radius of gyration R_g, describing the polymer chain with a Gaussian coil conformation:

$$R_g^2 = \frac{1}{M} \sum_i m_i \mid \vec{r_i} - \vec{r_c} \mid^2 . \tag{2.4}$$

It describes the average distance of the monomers to the center of mass $\vec{r_c}$, with the complete single polymer mass M, and m_i and $\vec{r_i}$ the mass and the position vector of the i-th component. Hence, the chain is described as a sphere with radius R_g around the center of mass.

2.1.1 Conductive polymers

The strength of polymers in terms of mechanical properties at light weight with their electrically insulating properties has lead to a wide field of applications. Shirakawa, MacDiarmid and Heeger, however, discovered in 1997 the possibility to dope polymers to make them electrically conductive. [6] This discovery was awarded with the Nobel prize in chemistry in 2000 and since then, the research on conducting polymers has increased significantly. For conducting charges, the polymer needs to have delocalized π-electrons to overlap and form a large orbital in which the electrons can freely move. These π-π-bonds lead to bonding π- and anti-bonding π*-bands. In inorganic semiconductor physics, the former one is known as valence band (VB) and the latter one as conduction band (CB). In polymer physics, however, they are known as highest occupied molecular orbital (HOMO) and lowest unoccupied molecular orbital (LUMO). Polymers with alternating carbon-carbon single and double bonds are referred to as conjugated polymers. They typically show semiconducting behavior. The first polymer, for which electrical conductivity was observed was polyacetylene (PA). [6] Due to its chemical simplicity - it only consists of a carbon chain with conjugated double bonds - it serves as model system for conductivity in polymers.

Electrical conductivity requires the possibility to transport electrical charges. Therefore, an introduction to band structures and an overview on charge carriers possibly appearing in polymers is given in the following section. Thereafter, the doping mechanism and the transport of charge carriers is described.

Band structure

The linear combination of atomic orbitals (LCAO) explains the superposition of atomic orbitals and therefore helps to calculate the molecular orbitals. In this framework, the molecular orbitals can overlap with each other. As the orbitals can be described as waves, they can overlap constructively and destructively to form a bonding or an anti-bonding orbital, respectively. A conjugated π-system consists of sp^2 hybridized carbon atoms. The LCAO predicts the forming of binding (π, filled) and anti-binding (π*, empty) orbitals, that are delocalized (figure 2.2). Between the highest occupied molecular orbital (HOMO) and lowest unoccupied molecular orbital (LUMO) is typically an energy gap. For additional coupled monomers (also for molecules in an organic molecular crystal) the HOMO and LUMO of each molecule interact with each other. A further splitting of the molecular orbitals is the result, which transfers to band-like structure for a large number of monomers.

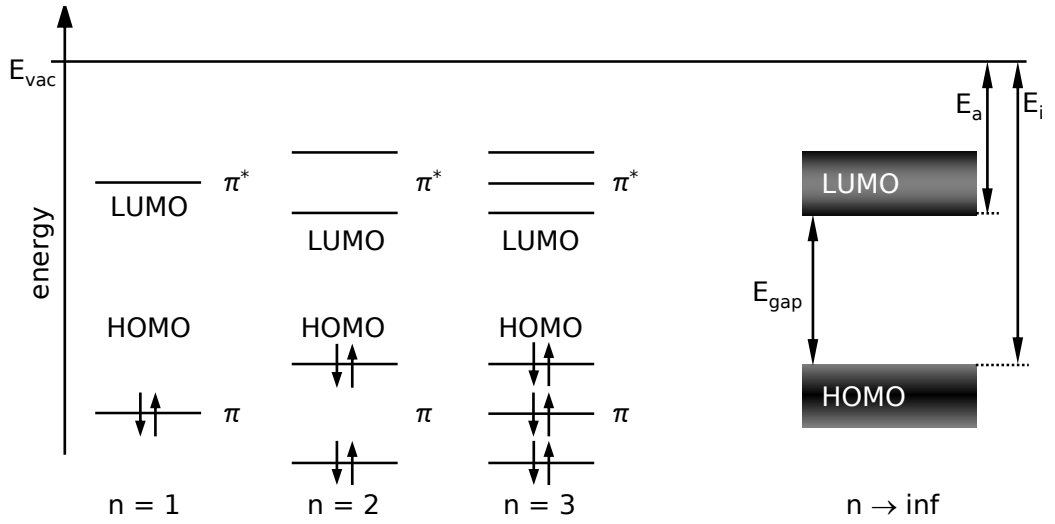

Figure 2.2: Band structure obtained from the linear combination of atomic orbitals (LCAO) for different numbers of coupled monomers n. For a higher number of coupled monomers, the HOMO and LUMO levels split and broaden to a band like structure. The HOMO is also known as ionization energy E_i and the LUMO as electron affinity E_a with respect to the vacuum energy E_{vac}. The difference between HOMO and LUMO is the gap energy E_{gap}.

An explanation for the occurrence of a band structure for polymers having a backbone with conjugated double bonds is given by Peierl's instability theorem. Figure 2.3 schematically depicts its principle. The theorem assumes a one dimensional chain with atoms having a periodic distance a, leading to a half-filled band up to the Fermi level E_F (figure 2.3a). Such a system behaves metallic. In case of a conjugated double bond, a periodic superstructure of dimers with a periodicity of $2a$ occurs. Thus, delocalized π-electron systems are explained by Peierl's instability that way, that the backbone appears as dimerized periodic structure with $2a$-periodicity instead of the undisturbed chain (figure 2.3b). This disturbance causes the formation of a band gap and hence a reduction of the total energy. The Fermi level remains unchanged and is found in the energy gap, which results in an insulating behavior. This transition is called metal-insulator-transition and is generally known as Peierl's instability. For polymers, the structure, degree of polymerization or the later introduced doping can influence the width of the band gap. For many semiconducting polymers, the band gap is in a range of 1.5 eV to 3 eV, for the widely used polymer poly(3-hexyl-thiophene) (P3HT) the band gap is around 2.0 eV. [54–56]

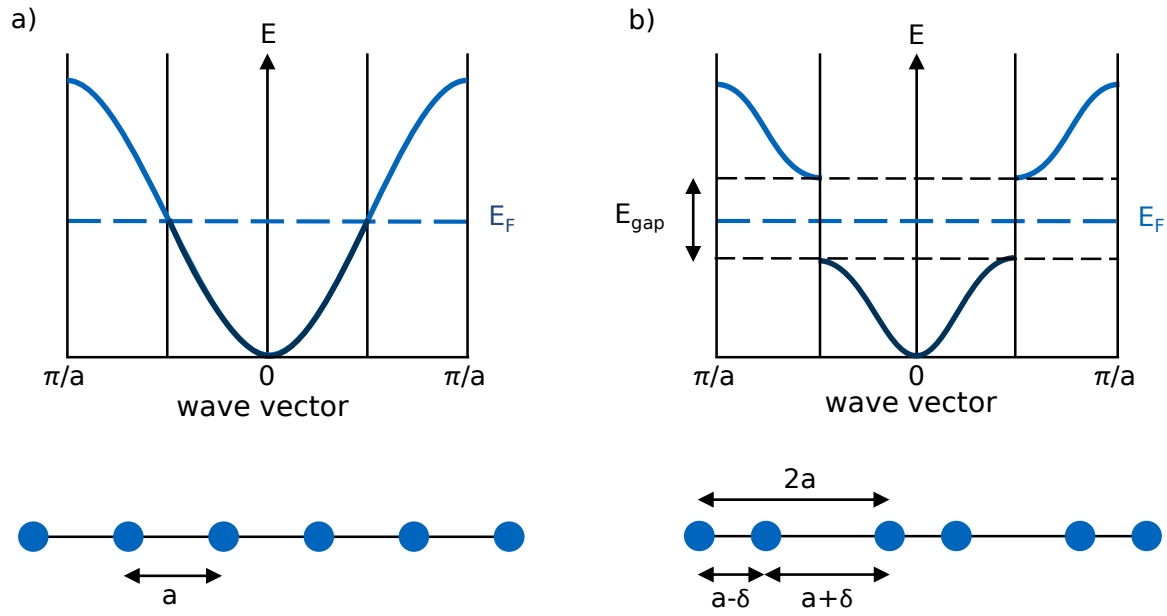

Figure 2.3: Schematic representation of the polymer band structure explained with Peierl's instability theorem. (a) The band structure of a one-dimensional metal with a period a. The energy band is filled up to the Fermi Energy E_F. (b) After dimerization and the formation of a superstructure an energy gap E_{gap} is formed. Below the energy representation, the respective one dimensional chains with periodicity a and $2a$ are depicted.

Charge carriers

In inorganic systems charges are carried either via electrons or holes. However, in polymers, charge carriers are quasi-particles, which combine charges and lattice distortions. In inorganic lattices, the atoms are locally strongly bound and can only move slightly around this position. In contrast to that, the chain in polymeric systems can change its conformation and move quite freely leading to stronger polarization effects. Solitons, polarons and bipolarons exist as quasi-particles in polymeric systems with an energetically degenerated ground state. Solitons are not observed in systems without degenerated ground state. Figure 2.4 gives an overview over the energetic state of the different quasi-particles and a schematic representation for the model system polyacetylene (PA). The quasi-particles are not located at fixed positions, but rather distributed over several atoms due to the structural relaxation of the chain. In case of PA the soliton is extended over 14 carbon atoms with an effective mass of six electrons. [57] PA has two degenerated ground states leading to the presence of neutral solitons S^0. Charged Solitons S^+ and S^- are created via doping or excitation via light, yielding photoconductivity. In contrast to electrons or holes, charged solitons do not exhibit a spin, while neutral solitons have

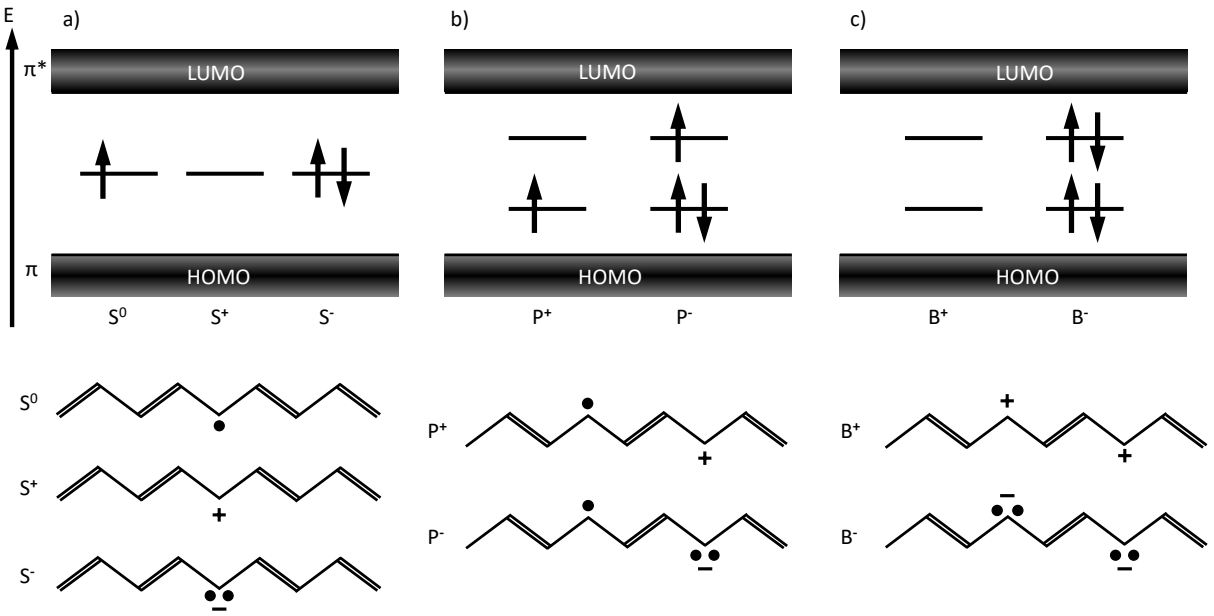

Figure 2.4: Schematic of the energetic state of the three different quasi-particles as charge carriers with a representation for the example of polyacetylene. The black dots represent electrons that are not part of the π-bonds and the + and − signs the net charge. (a) Solitons are depicted in neutral state S^0, positively S^+ and negatively S^- charged. (b) Polarons are found with a positive P^+ and negative P^- net charge. (c) Bipolarons exhibit two positive B^+ or two negative B^- charges.

spin 1/2. Polarons exhibit a spin 1/2 and are charged, while bipolarons are spin-less and charged. Despite the Coulomb repulsion of the net charges with same sign in bipolarons, they are stable due to the polarization of the lattice. The combination of quasi-particles can lead to annihilation or the formation of new ones. The combination of two S^0 leads to annihilation, while combining S^0 with S^+ or S^- leads to P^+ or P^-. Similarly, combining P^+ with P^- leads to annihilation, while the combination of the polarons of same sign forms bipolarons with the respective net charge.

Doping

Amongst others, the doping via reduction or oxidation of a polymer chain is the most common way to achieve high conductivity. PA for example can be doped via the addition of iodine. [58] Figure 2.5 schematically depicts the doping process of PA with iodine. If the iodine molecule approaches the PA chain without the presence of a neutral soliton, it oxidizes the PA, leaving behind a positively charged polaron. If, however, it approaches the PA where there is a neutral soliton, it oxidizes the PA leading to a positively charged

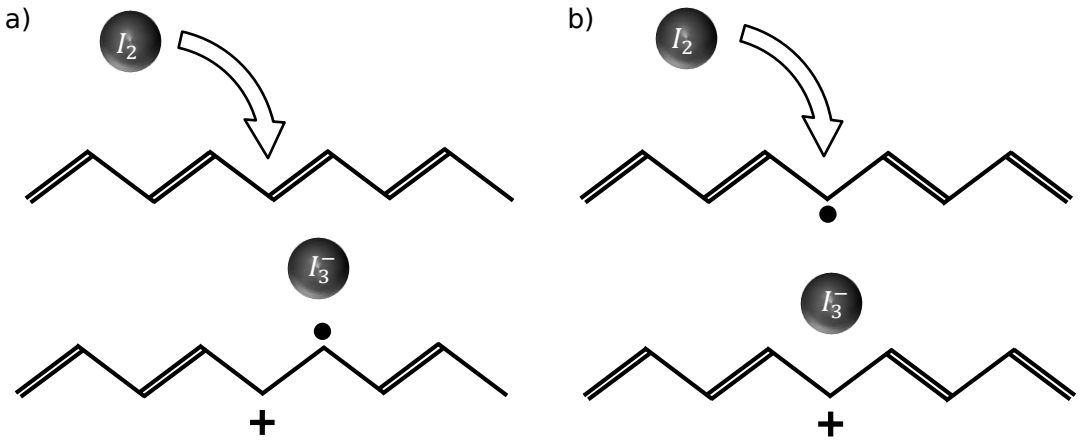

Figure 2.5: Doping of polyacetylene (PA) with iodine. (a) In the case there is no neutral soliton, the approach of the iodine molecule leads to the formation of a positively charged polaron. (b) An iodine approaches the PA with neutral soliton leading to the formation of a positively charged soliton. For both cases, the iodine gets reduced, while the chain in return is oxidized.

soliton. In both cases the iodine molecule gets reduced. Due to Coulombic attraction, the counter ion I_3^- is bound to the charged quasi-particles and thus acts as a stabilizing agent.

Charge transport

The transport of charges in organic semiconductors is generally characterized by

- low mobility,
- strong polaronic effects and
- hopping transport.

Within the polymer system, the charge transport along a chain is described as an efficient band-like transport within the delocalized π-bands with the Su-Schrieffer-Heeger (SSH) theory. However, polymers are of finite size and in order to macroscopically transport charges, an interchain transport has to be considered, that occurs via hopping processes. The hopping mechanism in disordered semiconducting polymers is best described by a model with Gaussian disorder of the energetic states. [59, 60] The charges are located at energetic states that are smeared out with a Gaussian shape to account for spacial and energetic disorder in the system. Charges can hop to a neighboring stage via a tunneling process, which requires the energies of the neighboring states to overlap. Figure 2.6 schematically depicts the hopping transport occurring in disordered systems. A charge is moving in time and space along an external electric field. The conductivity is thereby

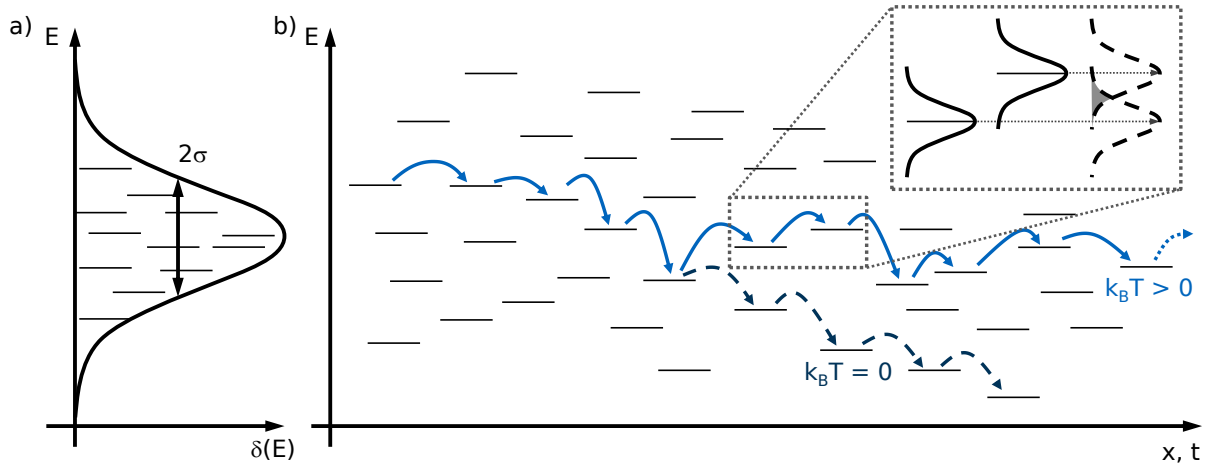

Figure 2.6: Illustration of the charge transport via hopping mechanism. (a) Total density of states (DOS) with Gaussian disorder and width 2σ. The possible states for the charge carriers are depicted with lines. (b) The hopping transport in case of an external electric field. In the case of low temperatures, the relaxation ends at a trapped state, while thermal activation allows for hopping towards energetically higher states. The inset shows the case for higher temperatures, for which the Gaussian distribution of the single states smears out and overlaps slightly allowing for the occupation of energetically higher states.

thermally activated. Energetically higher states can be occupied if additional energy k_BT is provided. In case of low or no thermal energy, the charge carrier relaxes to lower energetic states until it gets finally trapped. Hence, the conductivity increases with temperature. This effect is highly beneficial for applications like photovoltaics, for which the operation temperature is well above room temperature and even further increases at high solar irradiance. In general, the mobility of charge carriers in organic semiconductors is much lower compared to inorganic semiconductors. A higher mobility in polymeric systems is reached in crystalline regions of the polymer matrix.

2.1.2 Polymer crystallization and phase separation

The arrangement of the polymer chains within a thin film highly influences the charge carrier mobility. For that purpose, a high order in crystalline domains is beneficial. [30,61] In polymer:molecule blends, the involved materials might undergo a phase separation. The separation of different domains is of utmost importance for applications in organic solar cells, since material interfaces are important to separate the strongly bound excitons, which exhibit only a short diffusion length. In conclusion, a special emphasis needs to be

put on the inner morphology of the polymer blends. Hence, the polymer crystallization as well as the phase separation on a mesoscale is described in the following section.

Polymer crystallization

In general, polymers are entangled. If they crystallize, they do not form complete crystals, but a mixture of crystalline and amorphous domains. This is called a semicrystalline state. A high activation barrier resulting from the need of disentanglement of the coiled polymer chains hinders a complete crystallization. The degree of crystallinity Φ_c of polymers is defined in terms of the volume fractions of crystalline V_c and amorphous V_a material:

$$\Phi_c = \frac{V_c}{V_a + V_c} \tag{2.5}$$

The amorphous part contains chain ends, entangled chains, impurities and other defects. Polymer crystals often have a layered structure (crystalline lamellae) and can extend laterally over several micrometers. Macroscopically the layered structure arranges in spherulites. For organic solar cells, however, the size of spherulites would be too large and is thus avoided and therefore not discussed in the following. Each polymer possesses characteristic temperatures. The glass transition temperature T_g for example describes the temperature at which the polymer switches from a solid, glassy state to a more soft, rubber-like state when heated. This is understood as a melting of degrees of freedom in a polymer, allowing for a rearrangement of the polymer chains above T_g. In polymers that can crystallize, further characteristic temperatures are the melting temperature T_m and the crystallization temperature T_c. In general, T_c is found between T_g and T_m. A widely used model to describe the crystallization process in polymers is the multistage model proposed by Strobl (figure 2.7). [41, 62]

Nucleation The crystallization of a polymer starts with the formation of nuclei. Domains with an enhanced inner order form and disappear again to form nuclei from which crystal growth starts. The nucleation rate τ_{nuc}^{-1} is proportional to the volume of crystallizable domains v and in addition to an exponential function of the temperature: [63, 64]

$$\tau_{nuc}^{-1} \propto exp\left(-\frac{\Delta U + \Delta F_c}{k_B T}\right) \cdot v \tag{2.6}$$

with the Boltzmann constant $k_B T$ and the temperature T. ΔU is an activation energy for polymer diffusion across the phase boundaries of crystallization that is dominating at lower temperatures. Dominating at higher temperatures is the critical free energy ΔF_c describing the gain in free energy upon formation of nuclei. A maximum nucleation rate is thus found for mediate temperatures. [65]

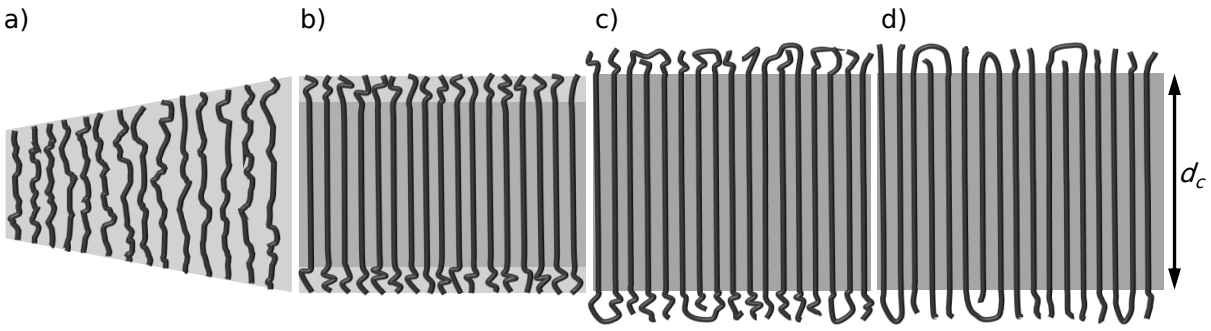

Figure 2.7: Multistage model for polymer crystallization proposed by Strobl. [62] (a) Growing mesomorphic phase around a nucleation agent. (b) Solidification by core crystallization and crystal growth (c) and (d) stabilization by surface ordering.

Growth kinetics The crystals start to grow from nuclei or from nucleating agents like impurities. In the initial stage of the model in figure 2.7a, a third phase, the mesomorphic (m) phase exists as intermediate phase next to the amorphous (a) and the crystalline (c) phase. The transition between the phases is described by three controlling temperatures:

- T_{am}^{∞}: transition temperature from amorphous melt to mesomorphic phase
- T_{ac}^{∞}: transition temperature from amorphous melt to crystalline phase
- T_{mc}^{∞}: virtual transition temperature from mesomorphic phase to crystalline phase,

which have the relation

$$T_{am}^{\infty} < T_{ac}^{\infty} < T_{mc}^{\infty}. \tag{2.7}$$

The mesomorphic phase rejects defects and spontaneously grows due to high inner mobilities. At a certain thickness, the core crystallizes and forms a block (figure 2.7b). The growth and surface ordering (figure 2.7c) finally stabilizes the crystal (figure 2.7d).

Based on this model, Strobel constructed a phase diagram dealing with four phases (figure 2.8). [62, 66, 67] The crystalline region (c) is divided into the native crystal (c_n) and the stabilized crystal (c_s) phase. The transition lines of the stable regions are shown as function of temperature T and inverse crystal thickness $1/n$. The crystallization and recrystallization lines were found to be independent of impurities, while the equilibrium melting temperature T_{ac}^{∞} is decreasing with impurities. The mesophase only exists up to T_{am}^{∞}. The triple points X_s (X_n) consist of equal Gibbs free energies of the amorphous melt, a mesomorphic layer and a stabilized (native) crystalline layer. Two routes for isothermal crystallization followed by heating are indicated in figure 2.8: *route (I)* is realized by crystallization at low temperatures. Starting at point (1), the chains from the amorphous melt are attached to the mesomorphous layer, that spontaneously thickens. On reaching

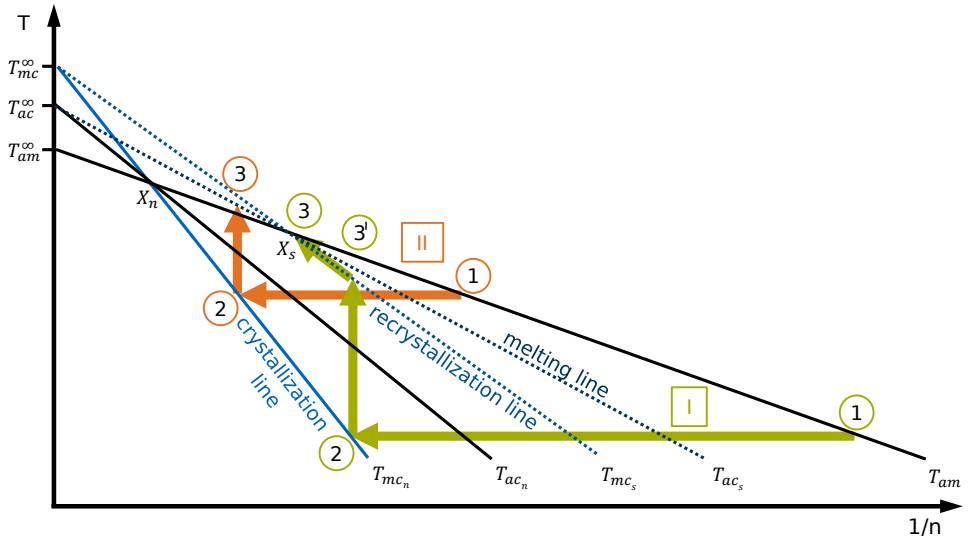

Figure 2.8: T/n^{-1} phase diagram of polymer layers in an amorphous melt (a) after Strobl. [62] Three phases are present: mesomorphic (m), stabilized crystalline (c_s) and native crystalline (c_n) phase. There are two routes for an isothermal crystallization: (I) for low crystallization temperatures and (II) for high crystallization temperatures.

T_{mc_n} at point (2), native crystals are formed followed by stabilization. Upon heating, they first stay stable until they meet the transition line T_{mc_s}. Instead of melting, the crystals transform into the mesomorphic state. A continuous recrystallization is mediated by the mesophase along point (3') to (3). The crystal finally melts at the triple point X_s. *Route (II)* is realized by crystallization at high temperatures. Starting at point (1), the chains from the amorphous melt are attached to the mesomorphous layer. The layer thickens spontaneously until point (2) on the T_{mc_n} transition line, at which native crystals form immediately. Upon heating, the system stays stable until the transition line T_{ac_s} is reached, associated with the melting of the crystal.

Phase separation

Blending different polymers leads to materials with new properties like mechanical stability. For organic solar cells, the mixture of p-type and n-type polymers is necessary to obtain satisfactory working devices due to an efficient charge transfer. [68] However, two polymers usually do not mix but phase separate. The discussion focus on polymeric systems. For other systems, the reader is referred to literature. The Gibbs free energy of mixing ΔG needs to be considered to describe the thermodynamic phase behavior. In the case of two polymers, the Flory-Huggins theory is well established to describe their-miscibility behavior using a mean-field approach. [69, 70] Mixing two components A and

B with the respective Gibbs free energies G_A and G_B of the isolated materials and G_{AB} of a fully intermixed blend yields the difference in Gibbs free energy upon mixing ΔG of

$$\Delta G = G_{AB} - (G_A + G_B). \tag{2.8}$$

At constant temperature and pressure of the environment, phase separation is favored for $\Delta G > 0$ while for $\Delta G < 0$, the mixed state is preferred. The difference in free energy can also be expressed in terms of the change of entropy ΔS and enthalpy ΔE due to mixing the components at temperature T:

$$\Delta G = -T\Delta S + \Delta E. \tag{2.9}$$

The entropy is increased upon mixing. Furthermore, the interaction between the two components influences the enthalpy of the system.

Entropic contribution: A rigid lattice model is used to obtain the change in entropy ΔS. From the number of possible arrangements Ω the entropy is calculated by $S = k_B ln(\Omega)$ with k_B the Boltzmann constant. This is used to formulate the change in entropy due to mixing $\Delta S = S_{AB} - (S_A + S_B)$ is

$$\Delta S = -k_B n \left(\frac{\Phi_A}{N_A} ln\Phi_A + \frac{\Phi_B}{N_B} ln\Phi_B \right) \tag{2.10}$$

with $N_{A,B}$ the degree of polymerization and $\Phi_{A,B}$ the volume ratio of component A and B, while n is the total number of molecules on the lattice and $\Phi_A + \Phi_B = 1$. Equation 2.10 describes:

- mixture of monomers ($N_A = N_B = 1$),
- mixture of polymers ($N_A > 1, N_B > 1$) and
- polymers in solution ($N_A = 1, N_B > 1$).

Enthalpic contribution: The interaction between the monomers of the components are described by the enthalpic contribution to the Gibbs free energy. The change in enthalpy ΔE due to mixing components A and B is given by

$$\Delta E = n k_B T \chi \Phi_A \Phi_B \tag{2.11}$$

with χ the Flory-Huggins interaction parameter.

The Gibbs free energy upon mixing ΔG (equation (2.9)) can be rewritten with equations (2.10) and (2.11), and normalized to one mol:

$$\Delta G = RT \left(\frac{\Phi_A}{N_A} ln\Phi_A + \frac{\Phi_B}{N_B} ln\Phi_B + \chi \Phi_A \Phi_B \right) \tag{2.12}$$

with $R = k_B N$ and N Avogadro's number.

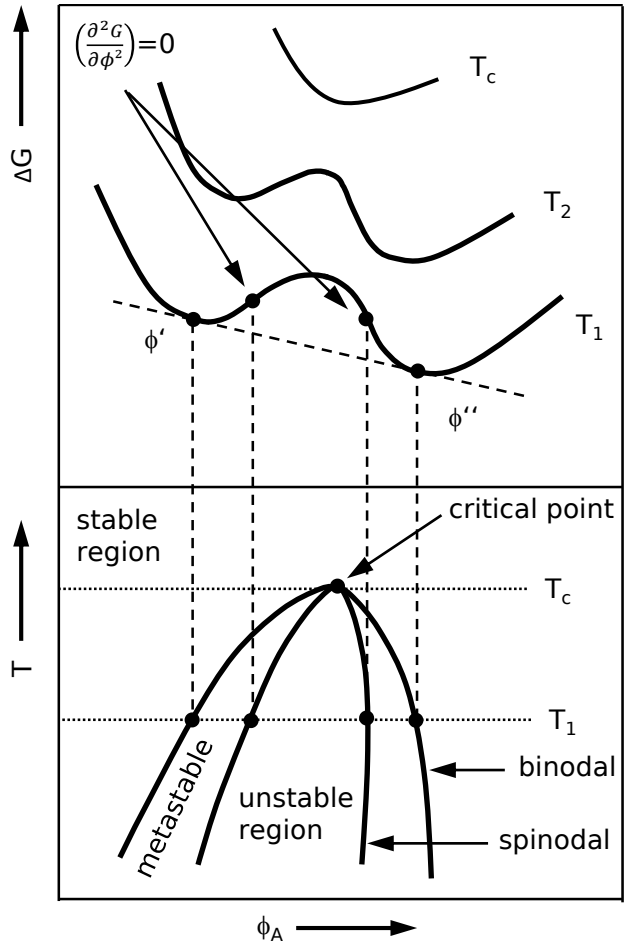

Figure 2.9: Construction of a phase diagram. Upper diagram: Gibbs free energy as function of the blend ratio $\Delta G(\Phi_A)$ for different temperatures T_i. The temperature increases from T_1 to T_2 to the critical temperature T_c. Φ' and Φ" are obtained from the tangent (dashed line). Lower diagram: The phase diagram $T(\Phi_A)$ derived from the projection of the tangent construction (binodal) and the turning points (spinodal) of the $\Delta G(\Phi_A)$ diagrams for different temperatures.

Flory-Huggins interaction parameter: The mean field formalism of the Flory-Huggins model assumes the interaction parameter χ to be only of enthalpic origin. However, experiments lead to corrections of the Flory-Huggins interaction parameter χ with an entropic contribution χ_S:

$$\chi = \frac{\chi_H}{T} + \chi_S \tag{2.13}$$

with the enthalpic contribution χ_H.

Phase diagram: Using Flory-Huggins theory, a phase diagram for polymer mixtures can be derived. The construction of such a phase diagram is shown exemplary in figure 2.9. The upper part shows the Gibbs free energy of mixing depending on the polymer ratio $\Delta G(\Phi_A)$ for different temperatures T_i obtained from equation (2.12). For high temperatures (T_c), a homogeneous mixture is stable as seen by the global minimum of the trajectory. Decreasing the temperature (T_1 and T_2) leads to phase separation. The transition line from homogeneous to separated phase (binodal) is obtained from Φ' and Φ" of the $\Delta G(\Phi_A)$ trajectories for different temperatures. Φ' and Φ" are tangential points of the trajectory. A mixture of two components at a temperature T_1 and a polymer

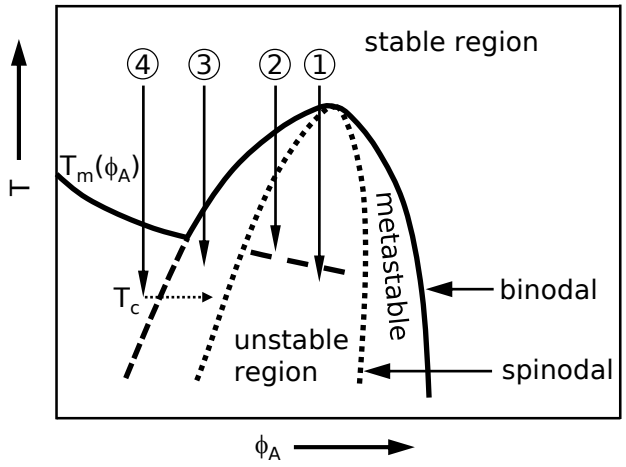

Figure 2.10: Modified phase diagram according to [71]. Additionally to the spinodal and binodal, the melting line $T_m(\Phi_A)$ of the crystalline component is shown. T_c is the crystallization temperature. The arrows and numbers (1)-(4) indicate different conditions for quenching from the melt.

ratio of $\Phi' < \Phi_A < \Phi''$ will phase separate into two phases with the polymer ratios of Φ' and Φ", respectively. Depending on the initial blend ratio, the phase separation occurs spontaneously (unstable region) or needs a nucleation step (metastable phase). The transition between metastable and unstable is the spinodal line and is obtained from the turning points of $\Delta G(\Phi_A)$. The critical point is the common point of spinodal and binodal transition lines. At this point, a second order phase transition occurs.

Phase separation of crystallizing polymers. In a polymer blend, in which one component is crystallizing, the structural evolution might be dominated by the crystallization process. The phase diagram needs to be modified to account for the melting temperature $T_m(\Phi_A)$ of the polymer (figure 2.10). [71, 72] Typical structural evolutions are described by different routes (1)-(4). The starting point for each route is well above the melting temperature $T_m(\Phi_A)$. Thus, the crystallizing polymer is still amorphous and the blend behaves like a standard blend. Below $T_m(\Phi_A)$, the structural length is defined by the dominating process. If the phase separation is faster than the crystallization, the crystal size is limited by the structural length of the phase separation. If on the other hand the crystallization is faster, the crystal size exceeds the structural length. In route (1), phase separation occurs via spinodal decomposition, while in route (3), it happens via nucleation and growth. During crystallization of a component B the surrounding gets depleted from component B, which hinders further crystallization. However, the phase separation process leads to regions with a higher content of component B, facilitating the crystallization. Route (2) indicates the case, in which the phase separation induces crystallization. A blend slightly above $T_m(\Phi_A)$ phase separates in the unstable region. As a result, local enrichments of component B occur. Due to the dependence of $T_m(\Phi_A)$ on the blend ratio, the $T_m(\Phi_A)$ line can be hit at the respective temperature inducing crystallization. Route (4) describes the crystallization induced phase separation. A blend

below $T_m(\Phi_A)$ in the stable, homogeneous region starts to crystallize. Impurities, including material from component A are rejected from the forming crystal. The local blend ratio at the growth front is consequently varied towards component A. If the local blend ratio shifts towards the unstable region, phase separation occurs.

2.2 Organic solar cells

The reason for the explanation of the morphology and crystallinity in the previous section becomes clear when explaining the principles of organic solar cells. Solar cells are in general devices that convert sun light into electrical energy. The main processes always include absorption of light, generation of free charge carriers and the transport of these charge carriers. The material in which these processes take place is the (photo-)active material. The main difference compared to inorganic solar cells is, that the active material in efficient organic solar cells consists of at least two components. The solar cells built within the scope of this thesis consist of a polymer donor and a fullerene based acceptor. In the following an overview on the basic principles involved in energy transfer as well as the main loss mechanisms are presented.

2.2.1 Basic principles

Organic solar cells consist of a multilayer stack. [25] Figure 2.11a shows the principle setup of an organic solar cell in standard geometry, where the top metal electrode serves as a cathode. The important light absorbing and energy converting part, the active layer, is sandwiched between the electrodes. In order to improve the efficiency, blocking layers are inserted between the active layer and the electrode. The figure only depicts an electron blocking layer between active layer and the transparent conductive oxide (TCO), in this case indium doped tin oxide (ITO). Often, also a hole blocking layer is inserted between the active layer and the metal electrode. The active layer used in thesis is a blend of poly(3-hexyl-thiophene) (P3HT) as donor material and [6,6]-phenyl-C_{61}butyric acid methyl ester (PCBM) as acceptor material.

The process of converting a photon to charge carriers is depicted in figure 2.11b in an energy level diagram. It shows the present energy levels of the donor and the acceptor material as well as the electrodes without blocking layer. The process of photon conversion to charge carriers is also depicted in figure 2.12 in the active layer profile. The steps (I)-(V) in figure 2.11b correspond to figure 2.12a-e, respectively. When light enters the active layer, it is absorbed by the polymer donor and an electron is excited from the HOMO to the LUMO, which results in a bound electron-hole pair, a so-called exciton. The exciton

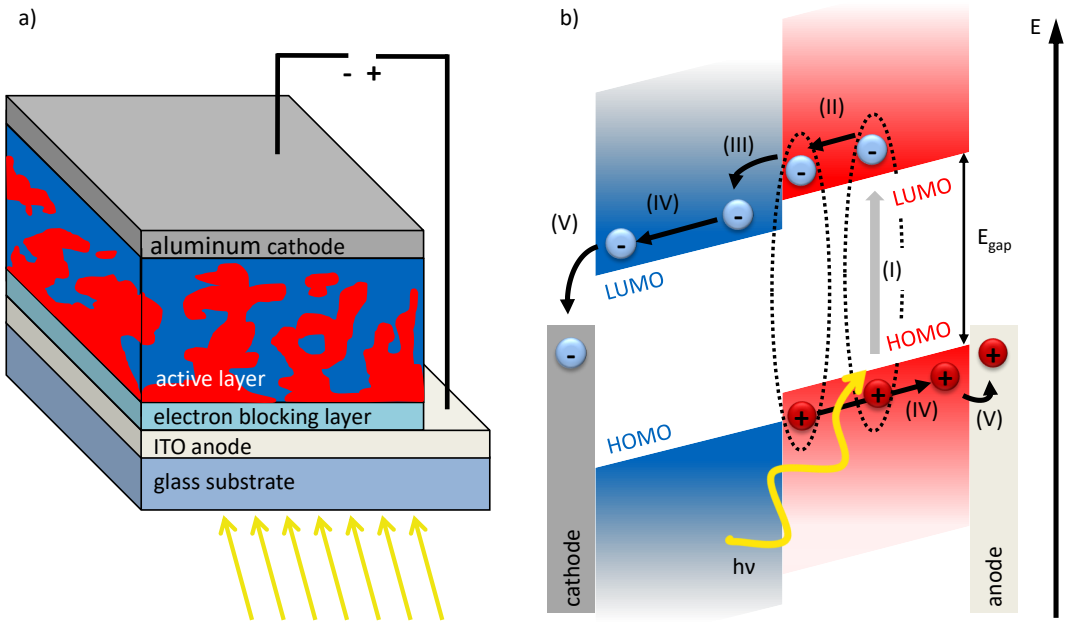

Figure 2.11: Sketch of a solar cell and the physical principle. (a) Schematic setup of an organic solar cell in standard geometry. The active layer consists of a donor:acceptor blend. Incoming light enters the solar cell from the bottom glass substrate to the active layer where it gets absorbed. b) Energy level diagram of an organic solar cell without blocking layers. (I) An incoming photon with energy $h\nu \geq E_{gap}$ is absorbed in the polymer, exciting an electron from the HOMO to the LUMO leaving a hole behind and being bound as an exciton. (II) The exciton diffuses to the donor-acceptor interface. (III) It dissociates at the interface to free charge carriers. The electron is transferred into the electron acceptor. (IV) Transportation of the free charge carriers to the respective electrodes. The electrons are conducted in the LUMO of the acceptor and the holes in the HOMO of the donor-polymer. (V) The charges are extracted at the respective electrodes.

has to diffuse to the donor-acceptor interface, in this case P3HT and PCBM. The LUMO of the PCBM "accepts" the electron of the exciton and provides the energy to split the binding. It is important to note, that an interface needs to be reachable within the lifetime of an exciton, determining its diffusion length. A common approach to achieve this is a so-called bulk-heterojunction (BHJ), depicted in the images. The intermixing of donor and acceptor material provides a higher interfacial area compared to a simple bilayer. The separated electron and hole are then transported to the electrodes via the LUMO of the acceptor and the HOMO of the donor, respectively. The involved processes are described in more detail in the following.

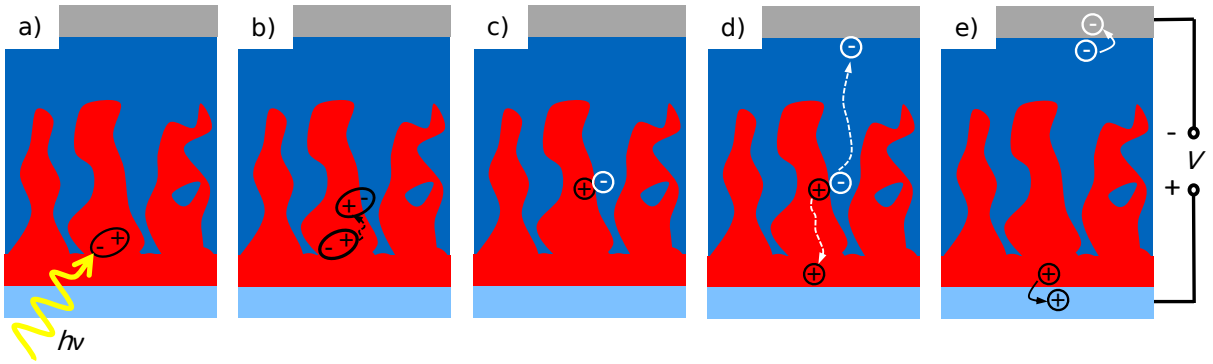

Figure 2.12: Schematics of an active layer profile of an organic solar cell. Depicted in blue is the electron accepting material PCBM, the electron donor material (red) is P3HT. The aluminum cathode is depicted in gray and the anode in light blue. (a) An incoming photon with energy $h\nu \geq \mathrm{E_{gap}}$ is absorbed by the polymer, creating a bound electron-hole pair, an exciton. (b) The exciton diffuses to a donor-acceptor interface where it (c) dissociates to free charge carriers. The electron is transferred into the electron acceptor. (d) Transportation of the free charge carriers to the respective electrodes. (e) The charges are extracted at the electrodes and recombine through an external load.

Absorption

The first step in producing electrical current out of sunlight is absorption. The transmission or absorption of light in a thin film can be described by the Lambert-Beer law:

$$I_T(\lambda) = I_0(\lambda) exp^{-\alpha(\lambda)d} \tag{2.14}$$

with I_T and I_0 the intensity of the transmitted and incident light, respectively, α the absorption coefficient and d the thickness of the material. The absorption process in polymers is described in the following. An incident photon can excite an electron from the HOMO to the LUMO leaving behind a hole. The absorption can only happen if the energy of the incident photon is equal or larger than the band gap energy E_{gap} of the polymer:

$$E_{photon} = h\nu = \frac{hc}{\lambda} \geq E_{gap} = E_{LUMO} - E_{HOMO} \tag{2.15}$$

with h being Planck's constant, c the speed of light, ν the frequency and λ the wavelength of the photon. The absorption spectrum of a polymer depends mainly on the type of monomer, degree of polymerization and its conformation. The spectrum exhibits broadened peaks due to the vibronic excitations leading to a splitting in the energy levels. Figure 2.13 shows the absorption process in an energy diagram showing two electronic states along with the vibrational excitations. The incoming photon with energy $h\nu$ is absorbed and excites an electron from the ground state ($n = 0$, $\nu = 0$) into an excited

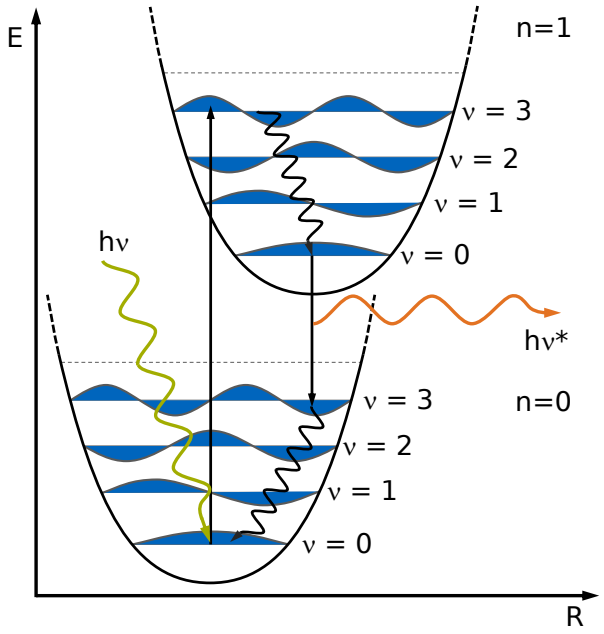

Figure 2.13: Diagram of the Franck-Condon principle for light absorption in organic solar cells. Two electronic states $n = 0$ and $n = 1$ are shown as function of the nuclear distance R. Additionally, the vibronic levels ν are exemplary shown with their wave functions. As the electronic transition is much faster than the nuclear motion, the transition is shown by vertical arrows. The internal relaxation (wavy arrow) to the lowest vibrational state is non-radiative.

one, here depicted as $n = 1$, $\nu = 3$. The excitation follows the Franck-Condon principle. It assumes the electron transition to be faster than the nuclear motion, so that for the time of excitation only the electrons are considered to move. The excited electron first dissipates energy by transition to the lowest vibronic state ($\nu = 0$) within the excited electronic state. Thereafter, it can relax back to the electronic ground state, but not necessarily to the vibronic ground state, under emission of a photon with energy $h\nu^*$. The relaxation to the vibrational ground state is again non-radiative. The energy that is transferred into vibrations is the difference of the energy of the emitted to the absorbed photon ($h\nu \geq h\nu^*$).

The absorption spectra of polymers show a fine structure, which originates from the properties of the polymer. Excitations can occur within one molecule or from one molecule to another one. [31] P3HT as semicrystalline polymer for example shows absorption lines in addition to the 0-0 vibronic intrachain excitation. [33] The absorption lines in P3HT originating from this intermolecular excitation can be calculated with the weakly coupled H-aggregate model. [32] There, the relation between the absorption of the 0-0 and 0-1 transition is calculated with

$$\frac{A_{0-0}}{A_{0-1}} = \frac{n_{0-0}}{n_{0-1}} \left(\frac{1 - 0.24 \frac{W}{E_p}}{1 + 0.073 \frac{W}{E_p}} \right) \tag{2.16}$$

with $n_{0-0}/n_{0-1} \approx 0.97$ as the ratio of the real part of the refractive indices, the phonon energy $E_p = 0.18$ eV and W the exciton band width for the sample system P3HT. [32] The observed relation yields information about the ratio of non-aggregated (amorphous) and aggregated (crystallized P3HT molecules). [32, 72, 73] Therefore, the difference of the

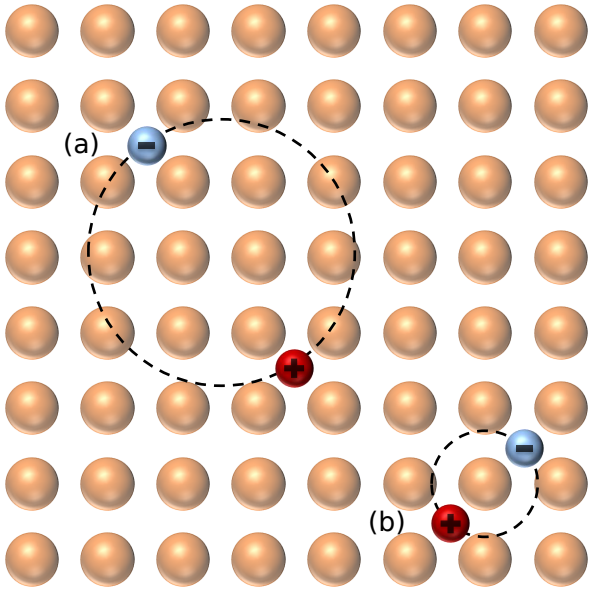

Figure 2.14: Illustration of two types of excitons via their size and thus energy. (a) The weakly bound Wannier-Mott exciton expands over several atoms, whereas the (b) strongly bound Frenckel exciton is located at one atomic position. The bright orange spheres depict the atoms of the material.

measured spectrum and the one calculated from the weakly coupled H-aggregate model is attributed to the absorption of the non-aggregated polymer chains. [73, 74]

Upon excitation of the electron, a hole is left behind in the HOMO. Due to Coulombic interactions, the electron is bound to the hole, whereby an exciton is created. The generated electron-hole pair is stronger bound as compared to inorganic semiconductors. This is due to the lower dielectric constant ($\epsilon_r \approx 3-4$) for organic materials as compared to inorganic ones ($\epsilon_r > 10$) leading to higher Coulomb attraction (around 1 eV). [75] Therefore, the thermal energy (around 25 meV) is not sufficient to dissociate the exciton. [75] Excitons are generally classified via their binding energies, relating to their sizes. Two types of them are depicted in figure 2.14. Weakly coupled excitons are called Wannier-Mott excitons and have accordingly a large size over several atomic distances. Frenckel excitons in contrast are strongly bound and thus very small in size, located at one atom. [43] In organic materials, the Frenckel excitons are typically found due to the low dielectric constants.

Exciton diffusion

An exciton is a bound quasi-particle and has no net charge. To contribute to charge transportation, it has to be separated. As mentioned above, the thermal energy is not sufficient to separate the exciton. To achieve this, it has to reach an interface of the hole- and electron-conducting material. The transport of the exciton takes place via energy transfer processes. The most important ones are the trivial transfer process (also photon reabsorption) and the Förster transfer. In the photon reabsorption process the exciton recombines under emission of a photon that gets reabsorbed by another molecule generat-

ing a new exciton. The Förster transfer (or fluorescent resonance energy transfer, FRET) is a non-radiative transfer from a donor to an acceptor via dipole-dipole coupling. [76,77] While the Förster transfer is the dominant process for short distances, the photon reabsorption is dominant for larger distances. The movement of an exciton has no preferential direction and can be understood as a random hopping process, described by a diffusion-like propagation. An important factor for this transport is the diffusion length l_d, as a radius in three dimensions within which the exciton moves:

$$l_d = \sqrt{ZD\tau} \tag{2.17}$$

with the diffusion coefficient D and the lifetime of the exciton τ. Z is a parameter describing the dimensionality d of the diffusion, $Z = 2d$. For polymers typically used in organic solar cells, like P3HT, the lifetime is only in the order of nanoseconds, resulting in a diffusion length of around 10 to 30 nm. [78,79] This limited diffusion length determines the optimal morphology of a donor:acceptor blend. If the distance to an interface is too large, the exciton will recombine without having the change to get separated. Thus, a preferred morphology is the bulk heterojunction.

Exciton dissociation

Once the material interface is reached by the exciton, the properties of the acceptor material influence the lifetime positively as the exciton is stabilized by the interface. Furthermore the binding energy is affected. An exciton experiencing the field of the acceptor material is called exciplex. Figure 2.15 depicts two possible ways to split an exciplex. One of them is a simple charge transfer from the donor polymer to the LUMO of the more electronegative material, the acceptor, figure 2.15a. The other way is a two step process, figure 2.15b. First, a Förster transfer leads to a complete transfer of the exciplex to the acceptor material. Subsequently, the hole is transferred back to the polymer. Both processes need to happen on a fast timescale, before the charges can recombine.

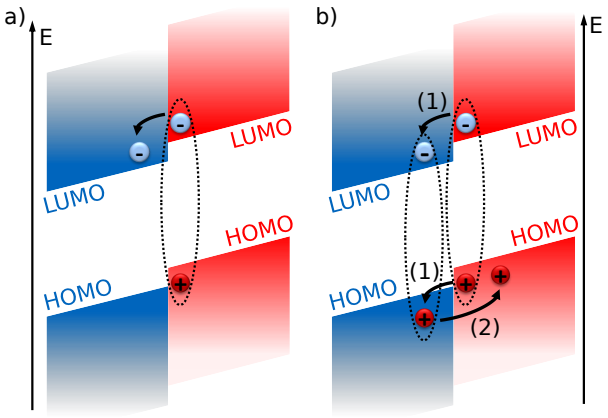

Figure 2.15: Energy diagram depicting the HOMO and LUMO energy levels of an acceptor (blue) and donor (red) interface showing two ways of charge transfer. (a) Direct transfer of the electron to the acceptor material. (b) Two step process, in which (1) the energy is transferred to the acceptor via Förster transfer followed by (2) a back-transfer of the hole to the hole-conducting polymer.

Charge carrier transport

Once the charge carriers are separated, they have to be transported to the respective electrodes. The holes and electrons are transported in the donor and the acceptor material, respectively. Due to the disorder of organic materials compared to inorganic semiconductors, the transport of the charges is generally characterized by the low mobilities, strong polaronic effects and a hopping transport. The process of charge transport is described in section 2.1.1.

Charge carrier extraction

When reaching the semiconductor interface, the charge carriers need to be extracted, which strongly depends on the device architecture. Furthermore, the recombination rate at the interface and therefore the charge carrier concentration is of importance. The photocurrent can be calculated using a model after Sokel and Huges, indicating that the photocurrent depends on the voltage across the device. [80] A mechanism influencing the charge carrier extraction are surface recombinations and imbalanced hole and electron mobilities. [79, 81]

2.2.2 Loss mechanisms

So far, the mechanisms describe the ideal way of exciton creation, charge carrier separation, transport and extraction. Next to the choice of the donor and acceptor material with suitable properties and matching work functions, further loss mechanisms have to be considered. The minimization of these loss mechanisms are one of the biggest challenges in the production of photovoltaic devices. The loss mechanisms according to figure 2.16 are:

I: Direct recombination of an exciton after photon absorption. This may happen if the distance to the next donor-acceptor interface is larger than the exciton diffusion length (equation 2.17). To prevent such a recombination, an optimization of the active layer morphology is necessary in terms of distance to the donor/acceptor interface.

II: Recombination of dissociated charge carriers. Usually, defects, chain end groups and side groups accumulate at the interface. These defects have a lower charge carrier mobility and slow down the charge transport. Therefore, it provides the possibility of recombination of already separated charge carriers. To avoid this recombination, a high mobility is necessary.

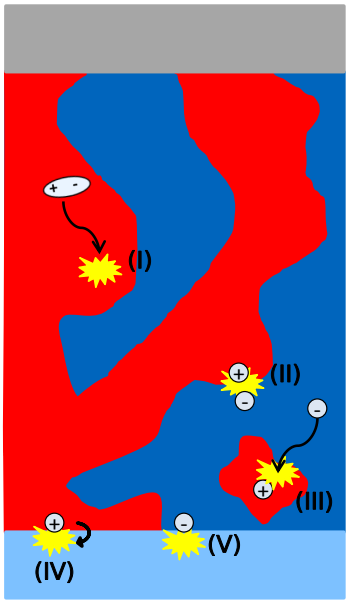

Figure 2.16: Sketch of possible loss mechanisms in organic solar cells. (I) Exciton recombination, (II) recombination of dissociated charge carriers, (III) trapping of a charge carrier on an island, (IV) reaching the wrong electrode of the respective charge carrier, (V) recombination of the charge carrier at the regular electrode.

III: A charge carrier can also be trapped on a material island. If no connection to an electrode is available, the charge carrier may recombine with a mobile charge carrier in the other material. Closed percolation paths to the electrode are necessary.

IV: Possibly, the electron or hole conducting material is connected with the anode or cathode, respectively. Then, a charge carrier can reach the wrong electrode and would therefore not contribute to the power generation. A blocking layer can prevent the contact of the wrong charge carrier to the electrodes.

V: A further loss mechanism is surface recombination, which may happen at the regular electrode by recombination. [81]

For many of the described loss mechanisms, the morphology of the active layer is crucial. There are competing restrictions on the morphology of the active layer and the performance of solar cell devices is strongly linked tot the morphology. However, controlling the morphology is a big challenge and is part of numerous research activities. [82–84]

2.3 Slot-die coating

One of the major issues to be addressed in organic electronics in general and organic photovoltaics specifically is the upscaling of production processes. One deposition method, that enables the transfer from lab scale devices to large area roll-to-roll processed solar cells is slot-die coating. It offers the possibility of sheet-to-sheet based coating which can be transferred to roll-to-roll processes. The advantage is the pre-metered solution supply,

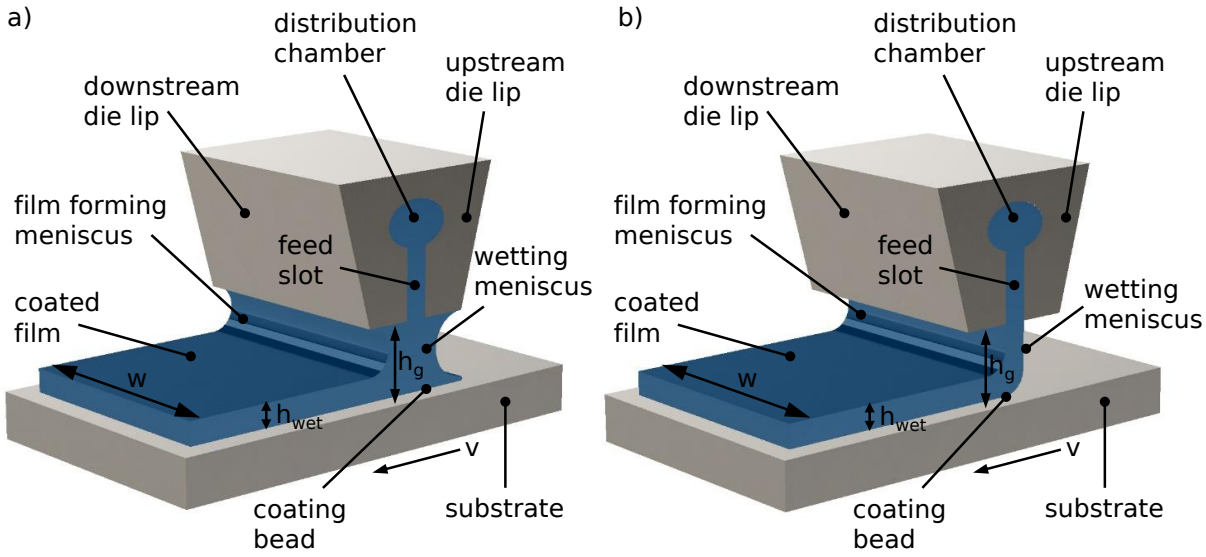

Figure 2.17: Differentiation between coating processes. (a) In slot-die coating, the gap clearance h_g is small and the solution forms a meniscus which fills the gap completely. (b) In extrusion coating, h_g is much larger and the liquid is deposited via a curtain. The die lips are not wetted. The film is coated with a speed v with a coating width w and a wet thickness h_{wet}.

for which all of the provided solution is deposited on the substrate without losses. In the following the basics of the coating process are introduced (section 2.3.1). Thereafter, the most important printing parameters (section 2.3.2) and their influence on the deposited films as well as typical defects (section 2.3.3) in the final films are discussed. More details about slot-die coating and printing processes are found in literature. [13, 14, 16, 49, 50, 85]

2.3.1 Basics

In slot-die coating processes, the solution is fed into the print head or coating die which distributes it onto the substrate. Two processes are to be differentiated, slot-die and extrusion coating. The principles of theses processes are depicted in figure 2.17. The coating liquid is guided to the substrate through a coating die. It consists of a distribution chamber and a feed slot, which provides a uniform liquid flow rate over the complete coating width w. The solution is provided from a pump with a certain flow rate f. The coating head consists of an upstream and a downstream die lip, which are separated by the feed slot. The distance between the die lips and the substrate is the gap clearance h_g. The film formation occurs in the coating bead, which is determined by the film forming meniscus at the downstream lip and the wetting meniscus at the upstream lip. The formed liquid bridge between the coating die and the substrate differs between the slot coating

process (figure 2.17a) and the extrusion coating operation (figure 2.17b). For the former one, the gap clearance is only a few times the final wet film leading to the meniscus filling the complete coating gap under the downstream lip and partially under the upstream lip. For extrusion coating, the gap clearance is larger and the liquid deposited to the substrate forms a liquid curtain. The following discussion focuses on slot-die coating as the main depositing technique within this thesis.

The center part of a coating system is its die. A manifold of different designs are known from publications, manufacturer brochures or patents. The internal as well as the external design are important and are often adapted to the coated liquid and applications. While the inner design ensures a uniform liquid flow rate over the complete coating width w, the external design defines the pressure distribution in the coating gap and thus the deposition quality. For the external design, the shape and the inclination of the die lips as well as the positioning of the coating head are varied. A challenge is the manufacturing of a coating die, as a high quality of surfaces and tolerances is necessary due to the narrow gap clearance. Next to the design of the print head, additional devices are applied to influence the pressure difference between upstream and downstream menisci. For stabilizing the meniscus and increasing the coating speed a vacuum device is applied at the upstream die lip or an over-pressure at the downstream meniscus. Latter one has to be designed very carefully as the applied air flow can harm the surface uniformity of the coated film.

2.3.2 Printing parameters

Coating active layers for organic solar cells requires precise control over the resulting film quality and thickness. Moreover, the film thickness cannot be chosen arbitrarily, but in a window providing films free of defects, the so called coating window. Figure 2.18 schematically depicts the influence of processing parameters on variations of the coating thickness. Several parameters are included in the coating window, like liquid properties, operating conditions and die geometry. A stable coating process demands a proper choice of parameters to balance the forces acting on the coating bead. Amongst these parameters are the following: [49]

I: Fluid and material properties:

- the wetting behavior of the coated solution on the substrate determines the contact angles to the substrate as well as to the coating die
- the rheological properties with the viscosity μ
- the surface tension σ of the coated solution
- the density δ
- substrate properties (dewetting, preparation, etc.)

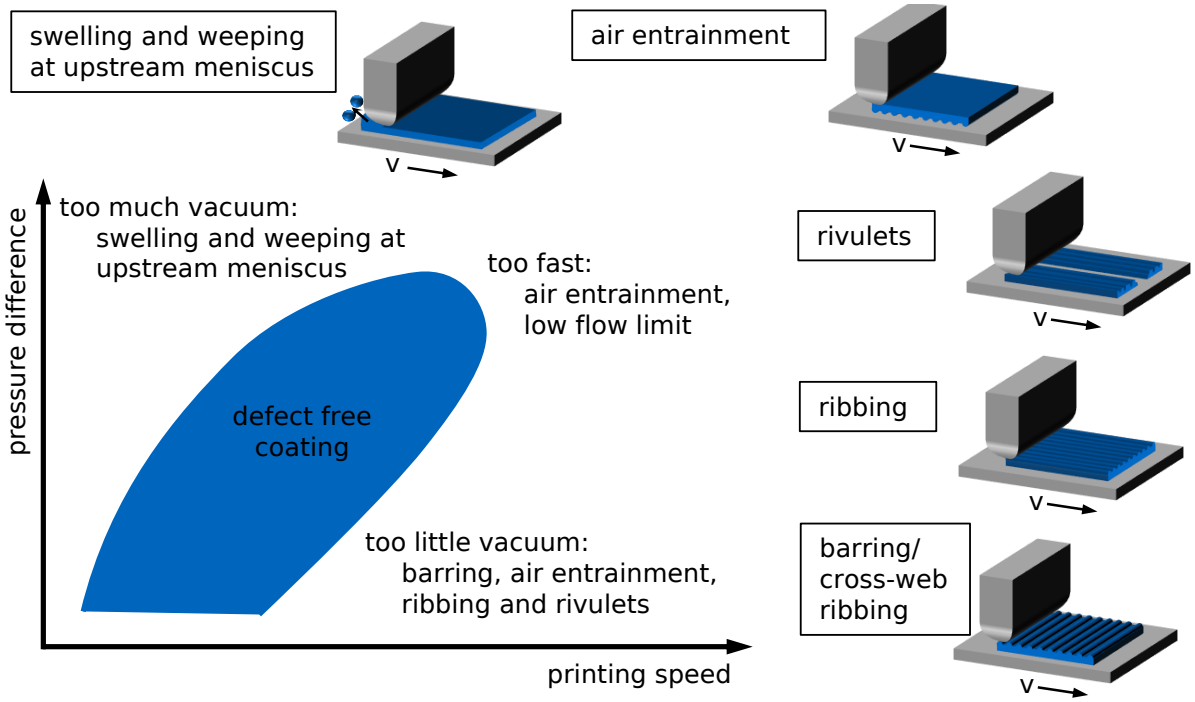

Figure 2.18: Schematic coating window for a slot-die printing process according to Durst and Wagner. [49] Depending on the pressure difference between upstream and downstream lip and printing speed, only a limited parameter space can be chosen to obtain a film, that is free of defects.

II: Geometric parameters:

- shape, dimensions, inclinations and position of die lips and feed slot
- shape of substrate and gap clearance

III: Operating parameters:

- print speed v
- wet film thickness h_{wet} determined by printing speed v, feed flow rate f and coating width w
- external forces (gravity, external fields, etc.)
- gas pressure at upstream and downstream menisci

An important influence on the formation of the coating bead is given by the feed flow rate f as exemplary depicted in figure 2.19 at constant printing speeds v. A low flow rate yields an unstable liquid bridge and no complete film on the substrate (figure 2.19a) or rivulets (figure 2.19b). For a stable film, the flow rate has to be increased. The coating gap is filled below the downstream lip (figure 2.19c). A further increase of the flow rate leads to an increasing pressure at the feed slot and hence to a movement of the wetting

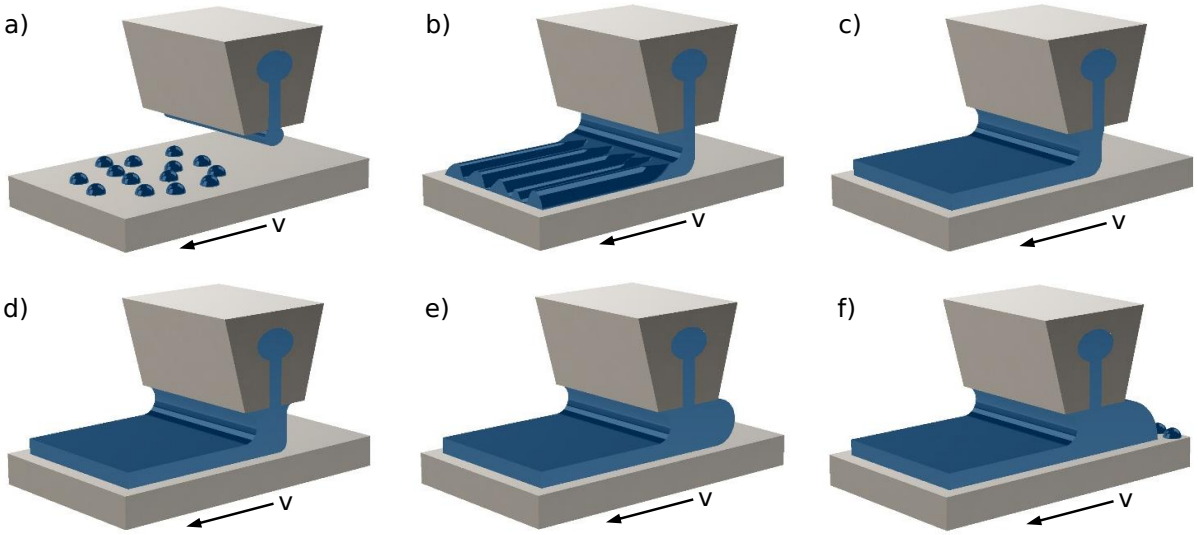

Figure 2.19: Qualitative variation of the coating bead with feed flow rate at constant printing speed v. The flow rate increases from (a) to (f).

meniscus along the upstream lip (figures 2.19d and 2.19e). The limit of stable coating is reached after further increasing the flow rate. Then, the wetting meniscus swells until the coating solution spills on the upstream substrate (figure 2.19f).

2.3.3 Defects

Next to the aforementioned instabilities, a number of additional defects may occur during or after printing, which might be due to a parameter choice out of the coating window, the pre-treatment of the substrate or the properties of the coated solution. [86] Figure 2.20 summarizes the most common defects in slot-die coated films.

Ribbing describes the formation of waves on the surface along the printing direction. It occurs at too low pressure differences or too high capillary number Ca, which describes

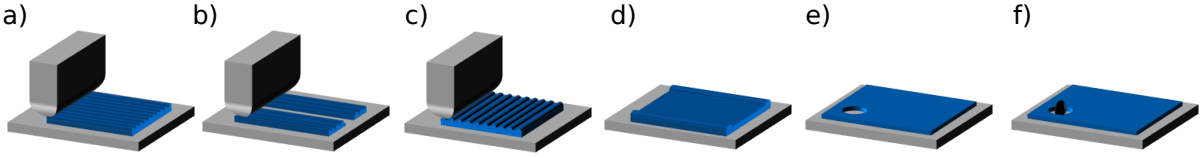

Figure 2.20: Schematic illustration of the most common printing defects. The observed defects are (a) ribbing, (b) rivulets, (c) barring/cross-web ribbing, (d) fat edges, (e) crater, (f) spotting.

the interaction of viscous forces due to the dynamic viscosity μ versus the surface tension σ at a given printing speed v:

$$Ca = \frac{\mu \cdot v}{\sigma} \tag{2.18}$$

Rivulets are stripe like patterns in coating directions. It is either uncoated areas or strong deviations of the coated material. A possible reason is a too low feed flow rate f or too fast printing speed v. Another origin might be blocking of the feed slot due to obstructing particles or dirt.

Barring/Cross-web ribbing are waves perpendicular to the printing direction. They might occur at too low pressure differences between upstream and downstream lips or high printing speeds.

Fat edges are the most common defects in slot-die coated films. Its origin lies in the drying behavior, which starts at the edges of the film, where the surface and thus contact to air is the highest. This leads to a concentration and surface tension gradient from the center to the edges, which induces a mass flow of the liquid.

Crater describe local deviation of thickness. It results mainly from inhomogeneities of the substrate or dirt particles. These yield to a gradient in surface tension which in turn leads to a mass flow towards high surface tension.

Spotting are defects similar to craters due to external surface inhomogeneities. This also includes local temperature deviations.

2.4 X-ray scattering

As explained in section 2.2, the inner morphology of organic active layers is of utmost importance concerning the device performance. Generally, there are two materials involved, the donor and the acceptor component. These two materials might phase separate upon solidification. Moreover, the polymer used in this thesis, P3HT, is of semicrystalline nature. The principle processes of crystallization and phase separation are described in section 2.1. X-ray scattering is a powerful tool to investigate the morphology of the film volume on different length scales with high statistical relevance. This section introduces the basic principles of elastic X-ray scattering, meaning scattering events under a pure momentum transfer without energy transfer. After the basic principles (section 2.4.1), the applications in the main techniques used within this thesis are discussed, namely X-ray reflectivity (XRR) in section 2.4.2 and X-ray scattering under grazing incidence in section 2.4.3.

2.4.1 Basic principles

The main physical process of X-ray scattering is the interaction of an electromagnetic wave with electrons in the sample under investigation. [51] An electromagnetic wave has the electric field vector

$$\vec{E}(\vec{r}) = \vec{E_0} \cdot exp(i\vec{k_i}\vec{r}). \tag{2.19}$$

Here, $|\vec{E_0}|$ is the constant amplitude, $\vec{k_i}$ the wave vector and $\vec{r}$ the position vector. The wavenumber is $k = |\vec{k_i}| = 2\pi\lambda^{-1}$ with the wavelength λ. The Helmholtz equation describes the electric field traveling through a medium with refractive index $n(\vec{r})$: [51]

$$\Delta\vec{E}(\vec{r}) + k^2 n^2(\vec{r}) \cdot \vec{E}(\vec{r}) = 0. \tag{2.20}$$

The refractive index is

$$n(\vec{r}) = 1 - \delta(\vec{r}) + i\beta(\vec{r}) \tag{2.21}$$

with the dispersion $\delta(\vec{r})$, which is always positive,

$$\delta(\vec{r}) = \frac{\lambda^2}{2\pi} r_e \rho(\vec{r}) \sum_{k=1}^{N} \frac{f_k^0 + f_k'(E)}{Z} \tag{2.22}$$

and the absorption

$$\beta(\vec{r}) = \frac{\lambda^2}{2\pi} r_e \rho(\vec{r}) \sum_{k=1}^{N} \frac{f_k''(E)}{Z} = \frac{\lambda}{4\pi}\mu(\vec{r}). \tag{2.23}$$

$r_e = e^2(4\pi\epsilon_0 c^2)^{-1}$ is the classical electron radius, also known as Thompson scattering length of the electron. $Z = \sum_k Z_k$ is the total number of electrons with Z_k the number of electrons of component k. $\rho(\vec{r})$ is the electron density as a function of space. Furthermore, $\mu(\vec{r})$ denotes the linear absorption. The atomic form factor is expressed as

$$f_k = f_k^0 + f_k'(E) + f_k''(E), \tag{2.24}$$

where f_k^0 depends on $\vec{q} = \vec{k_f} - \vec{k_i}$ with $\vec{k_i}$ and $\vec{k_f}$ the wave vectors of the incident and exiting wave. For small incident angles, $f_k^0 \approx Z_k$. For homogeneous media and far away from absorption edges, equation (2.21) can be simplified to

$$n = 1 - \frac{\lambda^2}{2\pi} r_e \rho + i\frac{\lambda}{4\pi}\mu, \tag{2.25}$$

which is independent of the position. $r_e\rho$ is called scattering length density (SLD). In the case of X-rays, the dispersion δ is of the order of 10^{-6} and the absorption β one or two orders of magnitude smaller. For that case, the critical angle α_c can be expressed as

$$\alpha_c \approx \sqrt{2\delta}. \tag{2.26}$$

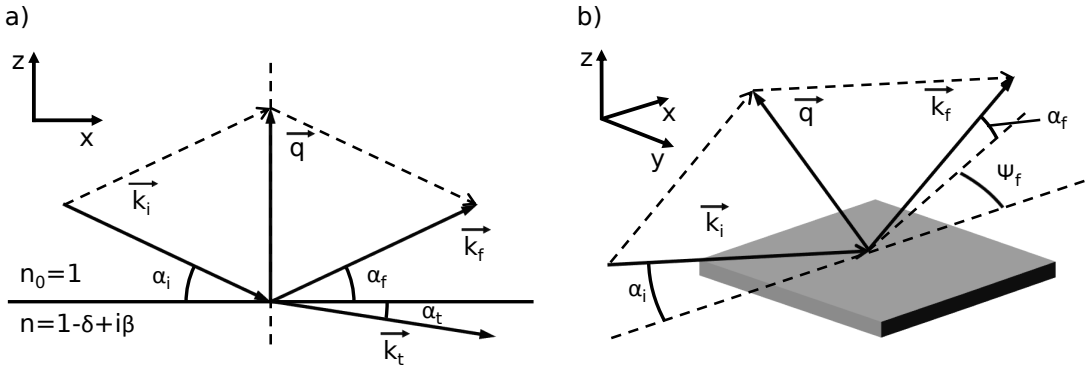

Figure 2.21: Definition of the notification for X-ray scattering. (a) Specular reflection within the plane of the incident X-ray beam and (b) diffuse scattering out of the scattering plane. $\vec{k_t}$ and α_t denote geometry for the transmitted beam.

In scattering experiments, the critical angle is of utmost importance. An anomalous surface scattering from thin films probed with grazing incident X-ray scattering was first observed by Yoneda. [87] He saw an intensity peak appearing at the critical angle, which is due to enhanced scattering intensities of the respective material corresponding to that specific critical angle. This phenomenon allows for investigations of material specific characteristics in blends of different materials.

For analysis and discussion, the basic geometry and the respective notification of angles and directions is important. Figure 2.21 schematically depicts two cases of scattering, the specular and the diffuse scattering. The incident X-ray beam $\vec{k_i}$ impinges the sample under a shallow angle α_i, which is - for X-rays - measured towards the sample surface. The exiting beam $\vec{k_f}$ is reflected under an angle α_f in vertical direction. For specular reflection, $\alpha_i = \alpha_f$ and the beam stays in the xz-plane, referred to as the scattering plane. In the case of diffuse scattering, $\vec{k_f}$ also possesses an angle Ψ_f in the xy-plane.

2.4.2 X-ray reflectivity

X-ray reflectivity (XRR) probes the vertical film composition using the specular reflection. In that geometry, the out-of-plane angle $\Psi_f = 0$ and thus the scattering vector $\vec{q}$ is normal to the surface and consists only of the q_z component:

$$q_z = \frac{4\pi}{\lambda} sin(\alpha_i). \tag{2.27}$$

The incident beam is reflected within the film at any interface of changing refractive indices. Snell's law defines the angle α_t of the transmitted beam, while its amplitudes

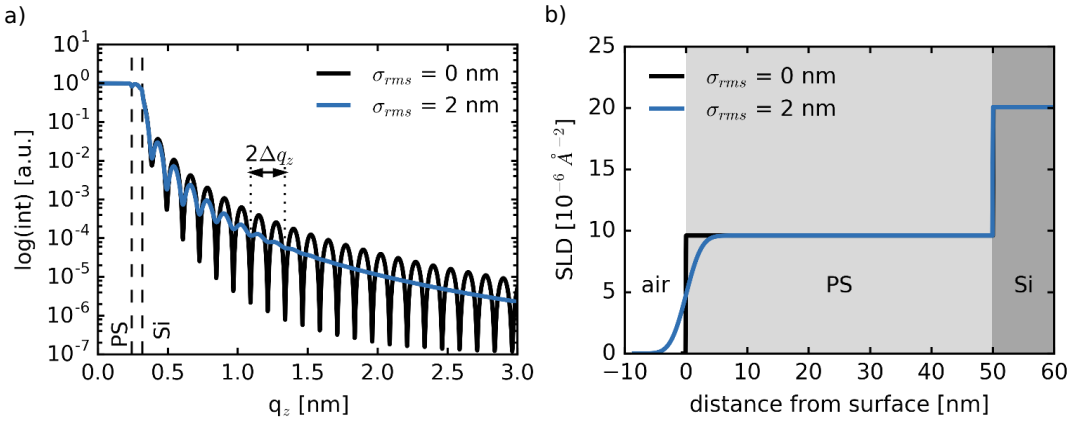

Figure 2.22: Influence of surface roughness on XRR data. (a) Simulated X-ray reflectivity data for a 50 nm thick PS film on a silicon substrate with different roughness $\sigma_{rms,k}$. The vertical dashed lines show the critical angles for PS and Si. (b) The corresponding SLD profiles of the PS sandwiched between the Si substrate and air. The surface roughness leads to the Gaussian broadening.

are described by the Fresnel reflection r_F and transmission coefficient t_F. With that, the reflectivity and transmission are defined by $R_F = |r_F|^2$ and $T_F = |t_F|^2$.

Analyzing the inner film structure is done by theoretically slicing the film in k layers, each with a reflective index n_k, a thickness d_k and a roughness $\sigma_{rms,k}$. The layer is sandwiched between an infinite substrate and an air interface. For each layer, the ratio of reflection and transmission is calculated. The reflectivity of the layer stack neglecting the interface roughnesses is then calculated using Abeles Matrix formalism or Parratts recursion formula. [88–90]

The interface between neighboring layers is defined by the root mean square roughness $\sigma_{rms,k}$, defined by:

$$\sigma_{rms} = \sqrt{\frac{1}{N_\sigma} \sum_{k=1}^{N_\sigma} \Delta z_k^2} \tag{2.28}$$

with the number of sampling points N_σ along the interface Δz_k as the deviation of the mean interface at the sampling point k. The reflectivity is corrected for the roughness by applying an exponential function to the Fresnel coefficient assuming Gaussian distributed heights. [91] In case of the roughness being comparable to the film thickness, the interface is approximated by several sub-layers. [92]

Figure 2.22a shows a calculated reflectivity curve of a 50 nm thick polystyrene (PS) film on a silicon (Si) substrate as comparison without and with surface roughness of 2 nm. The data are normalized such that for total reflection ($\alpha < \alpha_c$) the intensity is 1. At the

critical angle of PS, a dip and at the critical angle of silicon a steep decrease is observed. The intensity decreases with q^{-4} and additionally with the roughness. The oscillations in the scattering pattern are called Kiessig-fringes and are related to the film thickness d by [93]

$$d \approx \frac{2\pi}{\Delta q_z} \tag{2.29}$$

with the periodicity Δq_z. An increasing roughness dampens the oscillations. From the data, the SLD profile in dependence on the film depth is extracted (figure 2.22b). The SLD profile shows the change on the film surface upon variations of film roughness.

2.4.3 Grazing incidence X-ray scattering

A limitation when probing the inner structure of thin films in transmission is the film volume. To compensate for that, a very shallow angle below 1 ° is chosen for hard X-rays, and the sample is investigated in reflection geometry. The small angle results in a large footprint of the beam on the sample. The basic geometry and definitions are introduced in figure 2.21b. Grazing incidence X-ray scattering (GIXS) uses a fixed incident angle α_i and the diffuse scattering signal is recorded using a two-dimensional (2D) detector. For a given sample-detector distance (SDD), every pixel of the detector is assigned to a certain vertical α_f and horizontal Ψ_f exit angle. The angles can be transformed to the scattering vector $\vec{q}$ by

$$\vec{q} = \frac{2\pi}{\lambda} \begin{pmatrix} \cos(\Psi_f)\cos(\alpha_f) - \cos(\alpha_i) \\ \sin(\Psi_f)\cos(\alpha_f) \\ \sin(\alpha_i) + \sin(\alpha_f) \end{pmatrix}. \tag{2.30}$$

Two cases of GIXS are discussed in more detail, grazing incidence wide angle X-ray scattering (GIWAXS) and grazing incidence small angle X-ray scattering (GISAXS). The former one is also known as grazing incidence X-ray diffraction (GIXD) but with an area detector. The main difference between both techniques are the different SDD and thus the accessible scattering angles and q-range, respectively. A more detailed discussion on X-ray scattering is found in literature. [34, 51, 52, 94–98]

GIWAXS

A method to investigate the crystalline structure of a sample is X-ray diffraction (XRD). It uses a monochromatic X-ray beam, that is scattered at different lattice planes (hkl) within the sample under investigation. For thin films the diffraction is often performed under grazing incidence due to the aforementioned advantages. The method is then called grazing incidence wide angle X-ray scattering (GIWAXS) and is discussed in the

following. Figure 2.23a shows the diffraction of parallel X-rays with the lattice planes. The X-rays scatter at different lattice planes, which have a distance of d_{hkl}, and thus lead to a difference in the beam path length of Δs. The scattered X-rays interfere constructively or destructively depending on the incident angle θ. For constructive interference, the Bragg condition,

$$n\lambda = 2d_{hkl}sin(\Theta) \tag{2.31}$$

has to be fulfilled. This can be expanded to the Laue condition in three dimensions, which states, that constructive interference only happens, if the difference between incoming and scattered wave vector is equal to a reciprocal lattice vector ($\vec{q} = \vec{k_f} - \vec{k_i} = \vec{G}$). For visualization, the Ewald sphere is used as depicted in figure 2.23b. For elastic scattering events as discussed here, the momentum is conserved and $|\vec{k_i}| = |\vec{k_f}|$. The Ewald sphere has a radius $|\vec{k_i}|$ and thus, scatted points on the shell conserve the momentum. Diffraction patterns are observed, if a reciprocal lattice point touches the sphere. Looking at the Ewald construction (figure 2.23b) an important point concerning GIWAXS pattern is evident. 2D area detectors access only one specific surface of a sphere in reciprocal space. For a given incident wave vector $\vec{k_i}$, the scattered wave vector $\vec{k_f}$ does not solely contain a k_z-component without contributions of k_x or k_y. The scattering in the specular plane ($k_y = 0$) is always a combination of k_z and k_x. This leads to the inaccessible range in vertical direction for GIWAXS as depicted in figure 2.24b. Additionally to the

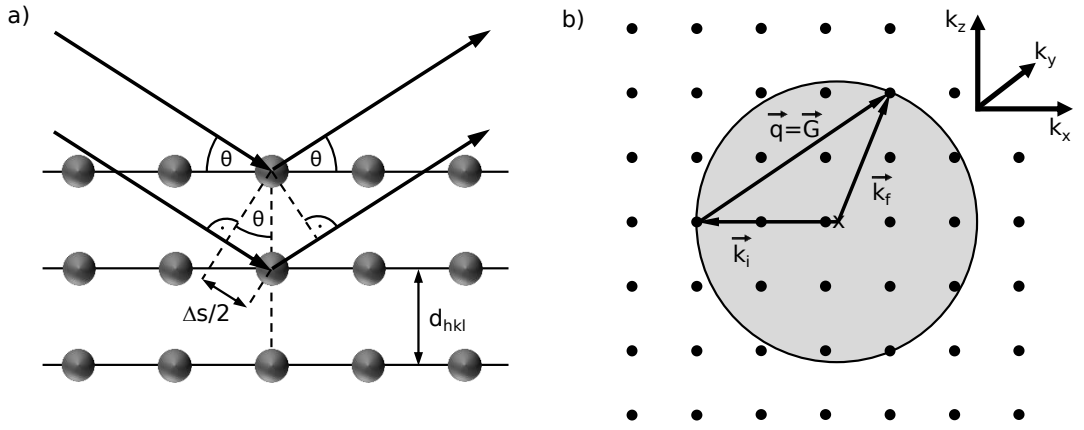

Figure 2.23: (a) Illustration of the Bragg condition. The horizontal lines represent the lattice planes separated by d_{hkl}. X-rays are depicted by the arrow that impinge the lattice planes under an angle Θ. Constructive interference occurs if the path difference Δs is an integer multiple of the wavelength. (b) Ewald construction: Constructive interference occurs for the intersections of the reciprocal lattice (dots) with the sphere around x with radius $|\vec{k_i}|$. $\vec{k_i}$ and $\vec{k_f}$ represent the wave vectors of incident and scattered X-rays.

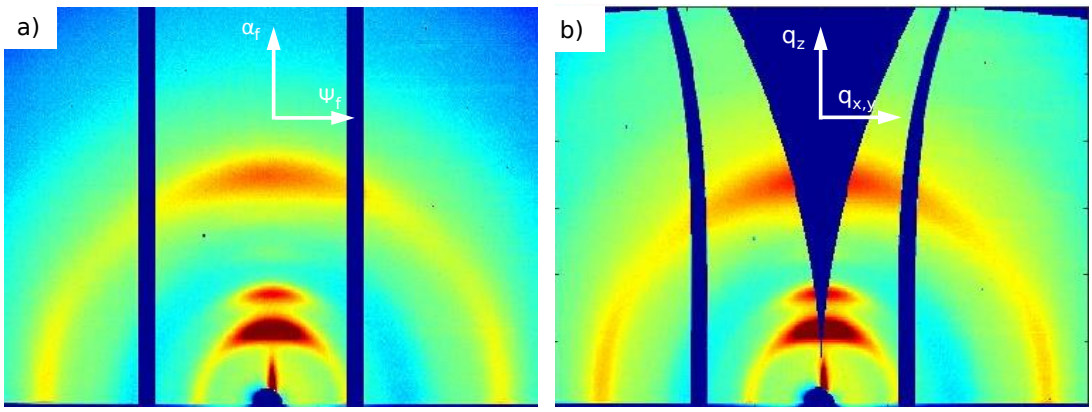

Figure 2.24: 2D GIWAXS scattering pattern. (a) Scattering intensity map as recorded. The vertical bars are due the intersection of detector modules. (b) Same pattern after application of corrections and recalculation to q_z and $q_r = \sqrt{q_x^2 + q_y^2}$. Signals at higher q_z without contributions of q_r, i.e. the momentum transfer with $q_r = 0$ are not accessible leading to the wedge.

constructive interference of scattering peaks from ordered layers, signals from amorphous parts of the polymer can be seen which are due to typical atom-to-atom distances within the polymer. [99, 100]

Further corrections that are applied before reducing and analyzing the data are necessary: X-rays that are scattered under different angles and thus have a difference in pathway between scattering center and the detector area. Additionally, the photons hitting the detector pixels under different angles are counted with different probabilities. This is taken into account by efficiency corrections. The variation in pixel sensitivity between the pixels is included in a flat field correction. The typical linear polarization of synchrotron radiation needs to be considered with polarization corrections. A further correction is of geometrical origin. Due to the flat detector and since all the pixels are of same size, they cover different solid angles. Figure 2.24b shows a scattering pattern after application of all the mentioned corrections and recalculation to momentum space. Details about the applied corrections and the effect on the scattering patterns can be found in literature. [94–96]

Scherrer equation From the diffraction peaks, information about the molecular arrangement can be extracted. The amplitude relates to the amount of crystals and the position to the average distance of scattering planes. The Scherrer equation relates the full width at half-maximum (FWHM) $\Delta(2\theta_{hkl})$ of a diffraction from the lattice planes (hkl) at the diffraction angle $2\theta_{hkl}$ to a lower limit of the crystallite size D_{hkl}:

$$D_{hkl} = \frac{K\lambda}{\Delta(2\theta_{hkl}) \cdot cos(\theta_{hkl})}, \tag{2.32}$$

where λ is the wavelength and K the Scherrer constant, which is most often cited to have a value of around 0.9 as derived from the original publication: [97]

$$K = 2 \cdot \left(\frac{2 \cdot ln(2)}{\pi} \right)^{\frac{1}{2}} \approx 0.93. \tag{2.33}$$

Transferring the formula to a representation in reciprocal space, we get

$$\Delta q_{hkl} = \frac{4\pi}{\lambda} \left[sin \left(\frac{2\theta_{hkl} + \frac{\Delta(2\theta_{hkl})}{2}}{2} \right) - sin \left(\frac{2\theta_{hkl} - \frac{\Delta(2\theta_{hkl})}{2}}{2} \right) \right],$$

which can be rewritten using the trigonometric identities for the sum and differences to

$$\Delta q_{hkl} = \frac{4\pi}{\lambda} 2cos(\theta_{hkl}) sin \left(\frac{\Delta(2\theta_{hkl})}{4} \right).$$

As the FWHM is rather small, we can make use of the approximation $sin(\theta) \approx \theta$, insert into equation (2.32) and obtain the Scherrer equation for the reciprocal space:

$$D_{hkl} = \frac{2\pi K}{\Delta q_{hkl}}. \tag{2.34}$$

The crystallite size calculated by the Scherrer equation is calculated without corrections for the peak broadening due to instrumental settings or paracrystalline disorder. It is therefore not the absolute value but a good estimation of the lower limit of the crystal size and in this work used for comparison of the structures or following its evolution.

GISAXS

The size of different domains is important for efficient solar cells. This phase separation usually happens at larger length scales compared to the ones observed in crystallinity investigations. Larger length scales in real space means smaller ones in the reciprocal space. Hence, the scattering signals at small angles is investigated by grazing incidence small angle X-ray scattering (GISAXS). It offers the possibility to investigate the film structure in both, the vertical and horizontal direction. Lateral structures contribute to diffuse scattering. Furthermore, reflections at the sample and the substrate occur. An approach to account for that is the distorted wave Born approximation (DWBA) as first-order perturbation of an ideal system. Figure 2.25 represents the cases, DWBA combines in its approximation. The exiting wave is a combination of directly scattered and the additionally reflected waves. Several analysis programs offer the possibility to simulate complete 2D scattering patterns in the framework of DWBA. [101–104] Another approach to analyze the lateral structures is to investigate the horizontal line cuts at the Yoneda position. The advantage is the reduced need of computing power. For that purpose the effective interface approximation is applied in which only lateral correlations in the film are considered, meaning q_z is considered as a constant. [105]

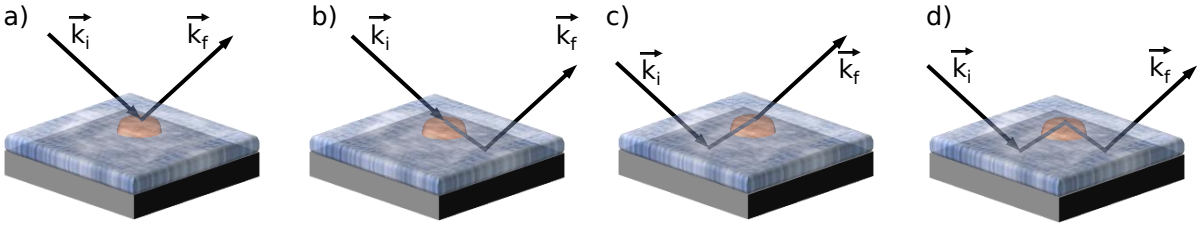

Figure 2.25: Illustration of the contributions of the DWBA. The incoming beam is scattered (a) directly to the outgoing wave or (b) before being reflected. Else, the incident wave is first reflected before scattering (c) directly to the outgoing wave or (d) followed by another reflection. In the framework of the DWBA, all four events are superimposed.

The differential cross section for diffuse scattering is given by

$$\frac{d\sigma}{d\Omega}|_{diff} = \frac{A\pi^2}{\lambda^4}(1-n^2)^2|T_i|^2|T_f|^2 P_{diff}(\vec{q}) \propto P_{diff}(\vec{q}) \tag{2.35}$$

with the illuminated area A, the Fresnel transmission coefficients $T_{i,f}$ for the incident and outgoing beam and $P_{diff}(\vec{q})$ the diffuse scattering factor as a direct measure for the scattered intensity. [106]

For modeling the horizontal intensity profiles, N identical objects of a certain size and spatial distribution are assumed. The size is described by a from factor $F(\vec{q})$, which is the Fourier transform of its electron density distribution. The spatial arrangement is defined by an interference function, the structure factor $S(\vec{q})$. [107] With that the diffuse scattering factor is characterized by:

$$P_{diff}(\vec{q}) \propto NS(\vec{q})F(\vec{q}). \tag{2.36}$$

The above mentioned contributions of the DWBA are contained in $F(\vec{q})$, which is most commonly assumed to be cylindrical to account for the rotational symmetry of the system. The corresponding structure factor $S(\vec{q})$ is usually a one-dimensional paracrystalline lattice. There, the objects are arranged periodically with an increasing deviation of the exact positions with increasing distance from the lattice's origin. This induces a short-range order. The lattice is independent of the orientation of the system and thus invariant towards rotation. [108] Several form factors and their independent spatial distribution are assumed to act in the local monodisperse approximation (LMA). This approximation considers each object to only scatter with objects of the same origin but not with the ones from other form and structure factors. Therefore, the final intensity is considered to be the sum of the intensity of each contributing form and structure factor. [109]

3 Characterization methods

This thesis aims to correlate structural properties of printed organic thin films with their photovoltaic performance and spectroscopic behavior. For that purpose, a number of characterization methods are necessary to access information about the organic films. This chapter introduces the applied methods on the spectroscopic and electronic level (section 3.1) as well as on the structural level (section 3.2). The used instruments, basic setups and working principles as well as the respective data analysis are described.

3.1 Spectroscopic and electronic characterization

Spectroscopic and electronic characterization techniques determine the functionality and properties of the organic thin films under investigation. In particular, UV/Vis spectroscopy (section 3.1.1) reveals information about the absorption behavior, and the electrophoretic mobility (section 3.1.2) allows for measuring the zeta potential of a polymer in solution. Information about the electronic properties and photovoltaic performance is obtained via mobility (section 3.1.3) and current-voltage (section 3.1.4) measurements.

3.1.1 UV/Vis spectroscopy

One of the most important prerequisites for transferring photon energy into electrical energy is the ability to absorb light as described in section 2.2. To characterize the thin film properties, the samples are probed in visible and ultra violet range using spectrometers. For this purpose, two instruments are used. For fast recording during *in situ* measurements, the sample is illuminated using white light, which is provided through an optical fiber and the transmitted signal is transferred to a spectrometer with another optical fiber. The data are then analyzed wavelength resolved as schematically depicted in figure 3.1a. The used instrument is a custom Nanocalc-XR-NIR and is purchased from Ocean Optics with the software OceanView. The second instrument is the Lambda 650S from PerkinElmer that enables to measure the transmitted or reflected light with an integrating sphere (Spectralon R highly reflective 150 mm spherical chamber) taking the scattered light into account. Figure 3.1b depicts the optical path of the instrument. The

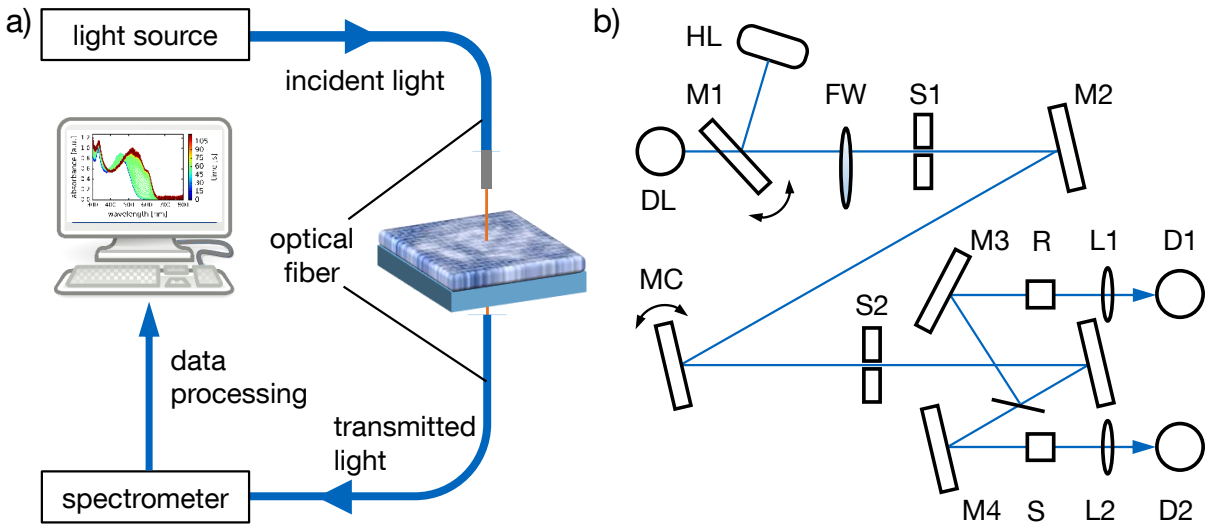

Figure 3.1: a) Illustration of the *in situ* transmission setup for fast recording of transmission spectra. b) Optical path for the static sample setup. A deuterium (DL) and a halogen (HL) lamp provide the light and are switched by the mirror M1. A filter wheel (FW) and a slit (S1) filter and refine the spectral width of the light which is then guided by mirror M2 to the monochromator (MC). After passing a second slit (S2), the monochromatic light is split into two paths guided via a mirror (M3 or M4) through the reference (R) or the sample (S) and a focusing lens (L1 or L2) to the respective detectors (D1 or D2).

combination of a deuterium (DL) and a halogen (HL) lamp provides a wavelength range of 190 nm $< \lambda <$ 900 nm by switching the light source at around 320 nm using the mirror M1. A filter wheel (FW) filters and collimates the spectrum before the slit (S1), which is set to 2 nm, focuses the beam. Another mirror (M2) deflects the light on a monochromator (MC) which determines the desired wavelength before passing another focusing slit (S2). The monochromatic light is split into two paths and respective mirrors (M3 and M4) guide the light through a reference (R) and the sample (S) before a focusing lens (L1 and L2) focus the light on the respective detectors (D1 and D2), which are located inside the integrating sphere.

For the static measurements, the intensity is measured for transmitted and reflected light. The absorbed intensity can be calculated by correcting the transmitted intensity with the reflected intensity. For the *in situ* measurements, the reflection could not be taken into account. Using the obtained intensity spectra, the absorbance $A(\lambda)$ can be calculated using Lambert-Beer's law (equation 2.14):

$$A(\lambda) = -log_{10}\left(\frac{I_T(\lambda)}{I_0(\lambda)}\right) = log_{10}I_0(\lambda) - log_{10}I_T(\lambda) = \alpha(\lambda)d \cdot log_{10}e \tag{3.1}$$

with the wavelength λ, the (reflection corrected) transmitted intensity I_T, the initial intensity I_0, the wavelength dependent absorption coefficient $\alpha(\lambda)$ and the thickness of the sample d.

The absorption coefficient $\alpha(\lambda)$ is an important material property, and can be calculated with the known absorbance $A(\lambda)$ and the exact thickness d of the layer:

$$\alpha(\lambda) = \frac{A(\lambda)}{d \cdot log_{10}e}. \tag{3.2}$$

As only photons with a wavelength λ exceeding the excitation energy E of the absorbing material are absorbed, the relation

$$E = \frac{h \cdot c}{\lambda} \tag{3.3}$$

with the Planck constant h, the speed of light c, can be used to determine the band gap of the probed material. [110] The optical band gap energy E_{gap} is related to the absorption coefficient α via the Tauc equation

$$(\alpha E)^n = B(E - E_{gap}) \tag{3.4}$$

with the constant B for different transitions and the energy E from equation 3.3. The exponent $n = 1/2$ for allowed indirect transitions and n = 2 for allowed direct transitions. In order to obtain the optical band gap E_{gap}, $(\alpha E)^n$ is plotted against the photon energy E and linearly extrapolated to obtain E_{gap} via equation 3.4. [111]

Further to the absorption behavior and the optical band gap of the material, information about the inter- and intramolecular ordering of the polymer can be obtained for P3HT in the frame of the weakly coupled H-aggregate model as described in section 2.2.

3.1.2 Electrophoretic light scattering

Depending on the interaction of a material in a surrounding solvent, the material might exhibit an electrophoretic mobility within the solution. Most commonly, this happens for surface charged particles that develop a zeta potential. The electrophoretic mobility μ_e of the material in solution is measured by its movement upon applying an electric field. Besides optical measurements using a microscope and a scale, acoustic or optical laser methods using the Doppler shift of moving particles are used. For the measurements within this thesis, a Zetasizer Nano ZS from Malvern instruments is used. The basic working principle is shown in figure 3.2.

A laser light with a certain frequency is split into two paths. One path serves as reference, while the other one is directed into the sample cell. This cell contains the particles or polymer within the respective solution. Depending on the interaction of the

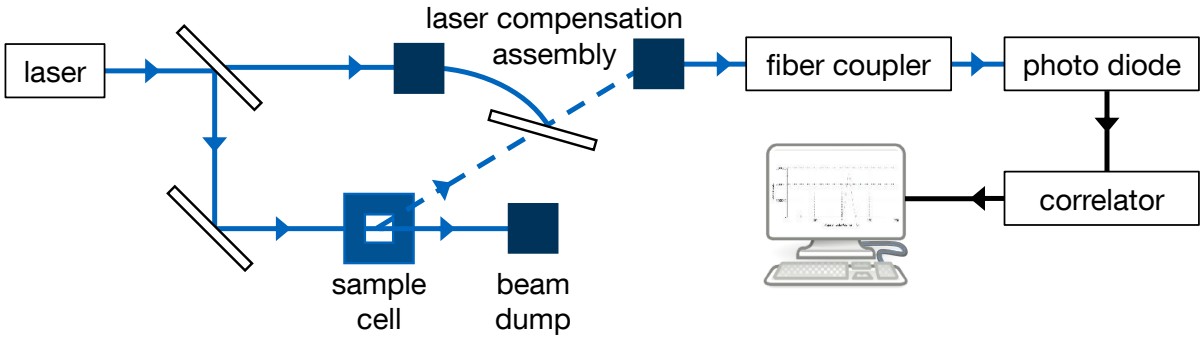

Figure 3.2: Schematic working principle of the electrophoretic mobility measurement setup. A laser light is split into a reference and the sample probing path. In the sample cell, the dissolved material under investigation is exposed to a varying electric field. The frequency of the laser light deflected in a certain direction is Doppler shifted depending on the speed of the particles in the sample cell upon the electric field. Both light paths are coupled after the sample and detected by a photo diode. Analyzing the correlations the obtained intensity spectra is then related to the mobility.

particles with the surrounding ions, a different strength of the zeta potential is developed. This zeta potential results in a movement of the particles upon an electric field inside the sample cell. By illuminating the sample with the laser light, the beam is scattered by the particle. Furthermore, the frequency of the laser light shifts depending on the speed and direction of the particle movement due to the Doppler effect. By combining the reference beam and the frequency shifted sample beam and knowing the applied electrical field, a characteristic superposition is obtained yielding the electrophoretic mobility μ_e of the particles in the respective solvent:

$$\mu_e = \frac{v}{E} \tag{3.5}$$

with the particle velocity v under the applied electrical field E. The zeta potential ζ can be calculated from the mobility μ_e by Henry's equation:

$$\zeta = \frac{3}{2} \cdot \frac{\mu_e \cdot \eta}{\epsilon \cdot f(ka)} \tag{3.6}$$

with the viscosity η of the solvent, the sample's dielectric constant ϵ and the Henry function $f(ka)$, which is commonly set to 1.5 in the Smoluchowski approximation for a thin double layer and 1 in the Hückel approximation for a thick double layer. [112]

3.1.3 Metal-insulator-semiconductor - charge extraction by linearly increasing voltage

For effectively working semiconductors, a high mobility of the charge carriers is necessary. To determine the mobility, a technique called metal-insulator-semiconductor - charge extraction by linearly increasing voltage (MIS-CELIV) is used. [113, 114] MIS-CELIV offers the possibility to selectively measure the hole or electron mobility in active layers applied in organic solar cells with thicknesses in the order of 100 nm. Depending on the location of the insulating layer (below top electrode or above bottom electrode) the hole or the electron mobility is measured. In figure 3.3 a hole mobility measurement setup is depicted.

Initially, an offset voltage is applied and the respective charge carriers gather in the semiconductor at the insulator interface. Afterwards, a linearly increasing voltage is applied which lowers the electric field and allows the charge carriers to move away from the insulator interface. The charge carriers need a certain time (transit time) to travel through the semiconductor. The time 0 is the start of the current increase. It passes the displacement current j_0 and increases further. The displacement current is a product of the device capacitance and the slope of the applied voltage. The device is again depleted,

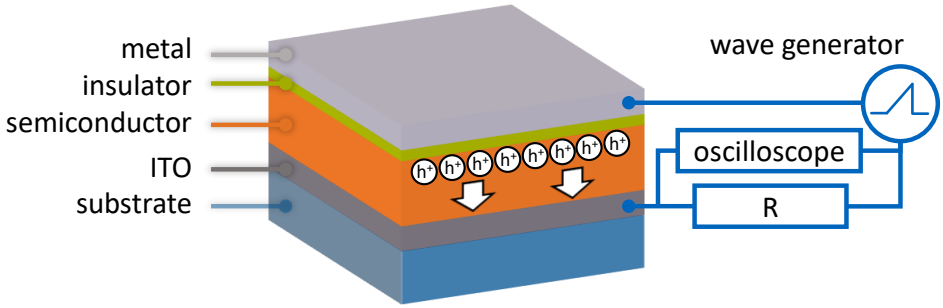

Figure 3.3: Schematic of a hole mobility measuring setup using MIS-CELIV. An insulating layer is inserted below the top electrode. By applying a voltage with a certain offset, the holes are assembled underneath the insulator layer and can not recombine with the electrons in the top electrode. Linearly increasing the voltage yields to a flow of the holes through the resistor which is recorded by the oscilloscope. With the semiconductor layer thickness and the time for the current to flow, the mobility of the respective charge carriers can be calculated.

when the current density reaches the displacement current density j_0 after passing a maximum. The mobility μ is calculated by

$$\mu = \frac{2 \cdot d_s^2}{(At_{tr}^2) \cdot \left(1 + \frac{\epsilon_s d_i}{\epsilon_i d_s}\right)} \tag{3.7}$$

with the semiconductor thickness d_s, the voltage slope $A = dU/dt$, the insulator thickness d_i and the dielectric constant of the semiconductor ϵ_s and the insulator ϵ_i. The transit time t_{tr} is obtained from the time at which the current density j is twice the displacement current j_0 via:

$$t_{tr} = t_{2j_o} \cdot \frac{4}{\pi}. \tag{3.8}$$

The mobility is measured for a number of offset voltages and averaged. For the analysis a self written python code is used. Details about the measurement and the procedure are found in the Bachelor's thesis of Salma Mansi. [115]

3.1.4 Current-voltage characterization

The most important specification of a solar cell is its current-voltage characteristics (I-V curves). For standard test conditions, a solar simulator (LOT0108, LOT-QuantumDesign GmbH) with electronic shutter is used to simulate the air mass 1.5 global (AM1.5G) solar irradiance. In figure 3.4 the AM1.5G solar spectrum as well as the spectrum of the used solar simulator is shown. The characteristic dips in the solar spectrum are due to the absorption in the earth's atmosphere. The solar simulator is set to an irradiance of 100 mW cm^{-2} with a calibrated standard solar cell (ReRa Solutions BV).

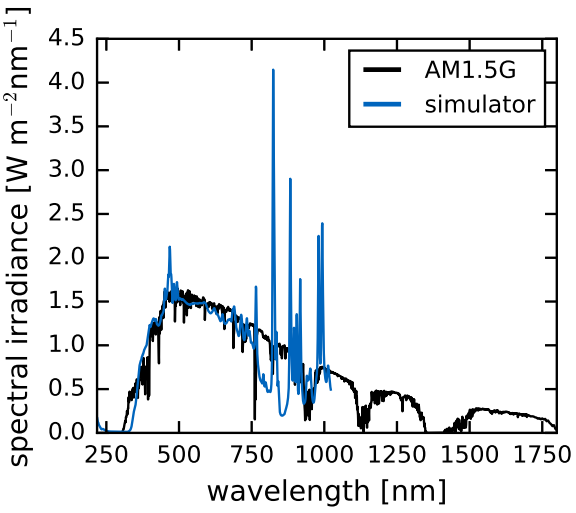

Figure 3.4: Wavelength dependent spectral irradiance of the sunlight under AM1.5G condition (black line) up to 1800 nm (data from NREL). The used sun simulator is calibrated in intensity to match the AM1.5G spectrum and shown in blue up to a wavelength of 1000 nm.

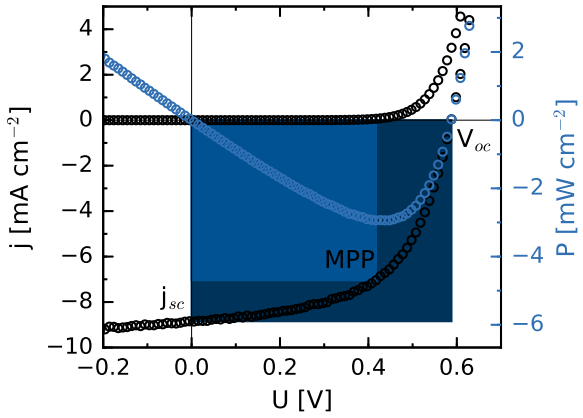

Figure 3.5: Typical current-voltage characteristic of a solar cell. The black open circles show the I-V characteristic of a solar cell in dark conditions (upper curve) and under simulated AM1.5G illumination (lower curve). The power-voltage curve is shown in blue and has its maximum absolute value at the maximum power point MPP. The open circuit voltage U_{oc} and the short circuit current density j_{sc} are indicated. The fill factor is calculated with the indicated rectangles at MPP and $j_{sc} \cdot U_{oc}$.

For measuring the I-V curves, a Keithley 2400 source meter is used and controlled by a self developed LabView program. The curves are recorded by sweeping the voltage from -1 V to 1 V in steps of 0.01 V, which can be varied, with a standard delay of 1 ms. Figure 3.5 depicts a typical I-V curve in dark and illuminated condition. The current is normalized to the pixel size, which is confined using a mask during illumination. The mask size is typically 0.1 cm^2 for small standard solar cells, for the printed solar cells it varies up to 0.6 cm^2. From the recorded I-V curves under illumination, the typical solar cell parameters are extracted, including the open circuit voltage U_{oc} at $j = 0$, the short circuit current density j_{sc} for $U = 0$ and the maximum power point MPP, where the power density $P = j \cdot U$ is maximum. The fill factor FF of a solar cell is defined as the ratio of the power at the MPP and the maximum power possible as the product of j_{sc} and U_{oc} depicted as rectangles in figure 3.5:

$$FF = \frac{U_{MPP} \cdot j_{MPP}}{U_{oc} \cdot j_{sc}} = \frac{P_{max}}{U_{oc} \cdot j_{sc}}. \tag{3.9}$$

An ideal solar cell should therefore highlight an almost rectangular curve, which would result in a fill factor of close 100%. For that purpose, the serial resistance of a solar cell determined from the slope at j_{sc} should be as low as possible. The shunt resistance, however, should be as high as possible. It indicates leakage of charges and is determined from the slope at U_{oc}. All the parameters together result in the efficiency η of the solar cell. It is defined as the ratio of the extracted power P_{out} to the incident power P_{in} from illumination:

$$\eta = \frac{P_{out}}{P_{in}} = \frac{U_{oc} \cdot j_{sc} \cdot FF}{P_{in}} \tag{3.10}$$

with the incident power set to $P_{in} = 100$ mW cm^{-2}.

3.2 Structural characterization

For information about the structure-function relationship, next to the electronic properties, characterizing the morphology is necessary. The structural investigation methods can be divided into real space and reciprocal space techniques. The used real space techniques optical microscopy (OM, section 3.2.1), atomic force microscopy (AFM, section 3.2.2) and profilometry (section 3.2.3) image the surface directly on different length scales without the need of further transformations. Vis-NIR reflectometry (section 3.2.4) yields information about film thickness and optical film properties like refractive indices in vertical direction. The reciprocal space scattering techniques reveal information in momentum space which has to be converted to obtain information about the film structure. The used techniques like X-ray reflectivity (section 3.2.5) and grazing incidence X-ray scattering techniques (section 3.2.6) are introduced along with the basics in data analysis.

3.2.1 Optical microscopy

To investigate the homogeneity and film surface structure on a micrometer scale as well as to determine the active area of a solar cell pixel, optical microscopy (OM) is used (figure 3.6).

Using visible light the achievable resolution R is limited according to the Rayleigh criterion,

$$R = \frac{1.22 \cdot \lambda}{2 \cdot NA}, \tag{3.11}$$

where NA is the objective's numerical aperture and λ the used wavelength.

The optical microscope used within the scope of this thesis is a DM2700 from Leica combined with a charged coupled device (CCD) camera (Leica MC170HD). Using a high precision grid, the pixel size for each objective is obtained and listed in table 3.1 along with the resolution calculated from equation 3.11 for a wavelength of 700 nm.

The recorded images are processed using the software ImageJ. [116]

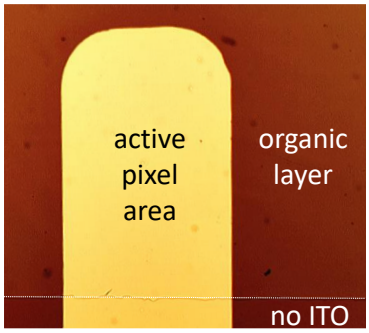

Figure 3.6: Exemplary optical micrograph of a solar cell pixel. The bright area is the active solar cell pixel determined by the evaporated aluminum contact and the lower line which shows the edge, at which the ITO is etched. The dark area is the organic active layer.

Table 3.1: Characteristics of different objectives of the optical microscope DM2700 from Leica used for this thesis.

magnification	NA	resolution [µm]	pixel size [µm]
1.25x	0.04	10.7	11.7 ± 0.1
5x	0.12	3.6	2.9 ± 0.1
10x	0.25	1.7	1.5 ± 0.1
20x	0.40	1.1	0.7 ± 0.1
50x	0.50	0.9	0.3 ± 0.1
100x	0.85	0.5	0.2 ± 0.1

3.2.2 Atomic force microscopy

With an atomic force microscope (AFM) the surface of a film can be probed with a higher resolution compared to an optical microscope. A principal setup of an atomic force microscope is depicted in figure 3.7. The used AFM is the Nanosurf FlexAFM with an Isostage from Nanosurf AG.

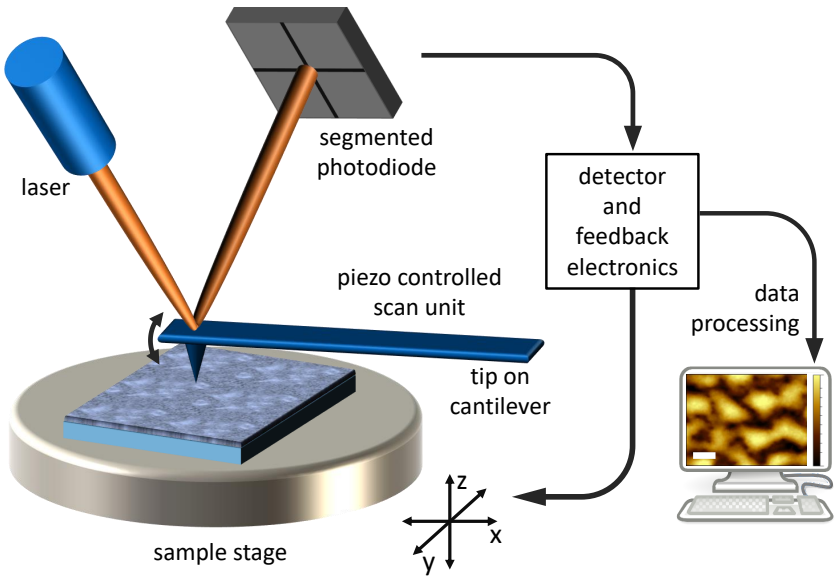

Figure 3.7: Schematic of an atomic force microscopy setup. The tip is mounted on an oscillating cantilever and probes the sample surface while it is moved with a piezo controlled scan unit. The deflection of the cantilever is detected with the reflection of a laser beam, that is monitored with a segmented photodiode.

When the tip mounted on the cantilever approaches the sample surface, the interactions between tip and surface result in a deflection of the cantilever. A laser is focused on the top of the cantilever and reflected to a segmented photodiode. Deflections of the cantilever result in a shift of the reflected laser beam which is detected by the photodiode and corrected via the feedback electronics.

Different modes for the AFM are available, which can be divided into contact and non-contact modes. For the contact mode, the tip touches the sample and the deflection force of the cantilever is measured. The sample is then scanned at a constant, pre-set deflection force and accordingly adjusted by the feedback electronics. Measuring the lateral force on the tip gives insight into the friction forces on the sample surface and can be used to differentiate the materials. In case of the non-contact (or tapping) mode, a piezoelectric drive excites the cantilever with a frequency ω. Interactions with the sample in close vicinity result in deviations from the frequency, amplitude and phase. With the feedback electronics, the distance is kept constant. The software records both, the sample topography as well as the phase, which reveals information about the material composition.

As tips, ContAl-G are used for the lateral force mode and Tap19Al-G for the tapping mode. The images can be processed using the software Gwyddion v2.43 to post treat and analyze the data.

3.2.3 Profilometry

Profilometry is an efficient method to obtain the thickness of a polymer film. For that purpose, the film is scratched before placing it under the stylus. The stylus scans perpendicular over the scratch and from the resulting height profile, the film thickness is obtained. Figure 3.8 shows the stylus while probing the sample surface over a scratch.

The sample is placed on a movable stage and the stylus (a diamond tip) approaches the sample surface. During the scan, the sample stage moves in one direction. A constant force of the tip results in a height profile of the sample. In this thesis, a DektakXT by Bruker Nano Surfaces Division is used. The diamond tip has a radius of 2 µm and presses

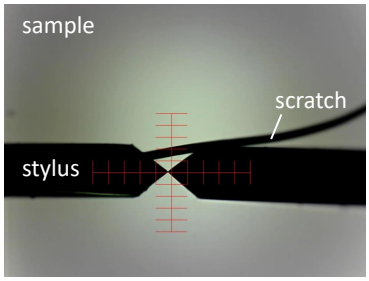

Figure 3.8: Micrograph of the profilometer while recording an image. The stylus (left) is mirrored (right) on the sample surface. The red cross shows where the stylus is located during the measurement. The dark line is a scratch, required to determine the film thickness.

on the sample surface with a corresponding weight of 1 mg. For thickness measurements, the height is averaged over at least 3 spots per scratch and several scratches on different positions on the sample. As the tip slightly penetrates into the soft polymer film, the measurements provide only a rough estimation of the thickness. The data analysis is performed using Vision64 which is included in the profilometer system.

3.2.4 Vis-NIR reflectometry

Reflectometry with visible (Vis) and near infrared (NIR) light, also known as white light reflectometry, is used to track the film thickness of thin films. It is especially suited for measuring the changes in film thickness during processing of the thin films. In figure 3.9 a schematic of the Vis-NIR reflectometry system is depicted.

The principle of Vis-NIR reflectometry is based on interfering light from different depth and interfaces in the probed thin film. The incoming light penetrates into the film and is partially reflected at the interfaces inside the film. In case of absorbing materials, not the complete spectrum of the incident light can be used. However, the NIR part of the spectrum is not absorbed for most of the utilized polymers and can therefore be used for characterizing the sample. The reflected waves interfere in a constructive or destructive

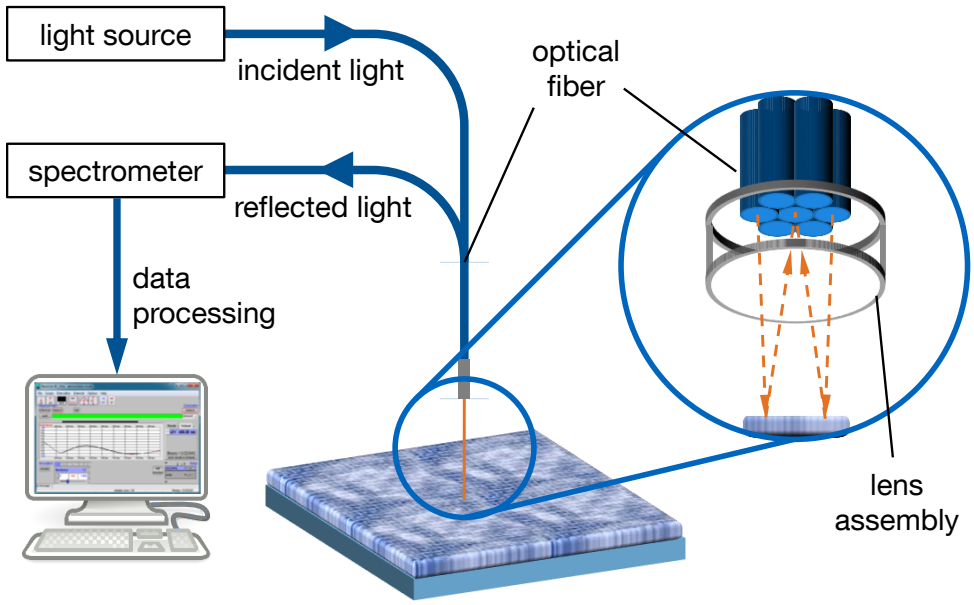

Figure 3.9: Schematic setup of a reflectometer. The light is guided to the sample via optical fibers and focused on the sample using a lens assembly. The reflected light is caught by another optical fiber located in the middle of the light guiding fibers. The reflected light is then guided to a spectrometer and processed by the software.

way depending on their respective optical paths. It is dependent on the film thickness d, the index of refraction $n(\lambda)$ and the extinction coefficient $k(\lambda)$. The interference pattern is analyzed by fitting with a suited model.

The measurements in this thesis are performed with a F20-UVX thin-film analyzer (Filmetrics Inc.) and a custom Nanocalc-XR-NIR from Ocean Optics. The wavelength range is 220 nm - 1700 nm. Both provide an internal fitting software. Additionally, the software Scout is used for an exact spectrum analysis and fitting.

3.2.5 X-ray reflectivity

The vertical film composition can be probed by X-ray reflectivity (XRR), which allows to determine the film thickness and roughness, too. It is suitable for finding enrichment layers in thin organic films. XRR measurements are performed with a Bruker Advance D8 Reflectometer with a copper anode. The schematic setup is shown in figure 3.10.

A copper anode provides the X-ray spectrum of Cu-K$_\alpha$ ($\lambda = 1.541$ Å). The monochromatic light is obtained by a Göbel mirror that is located directly after the source. The beam is collimated by a slit system in front of the sample. The X-ray source has an angle θ to the sample, which is varied during the scan. After scattering at the sample and passing further slits, the beam intensity is detected by a point detector as a function of θ. The angle between the incoming beam and the point detector is kept constant at 2θ during the scan. The scan range is typically in the range of 0.01° to around 6°. A knife-edge directly above the sample is narrowed to the surface to a very close distance to cut off a part of the beam at low angles to avoid over-illumination. By using the knife edge, a

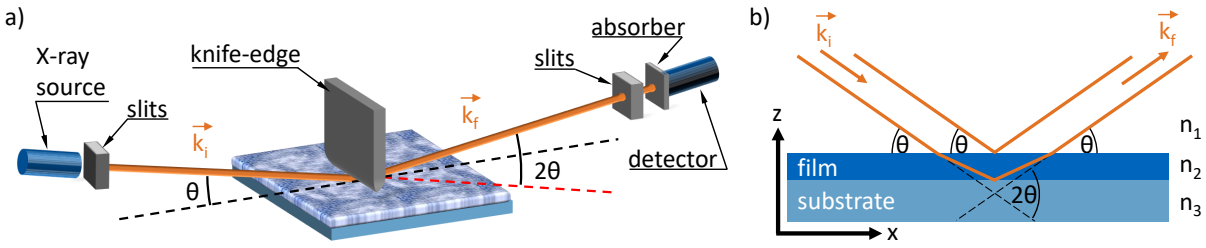

Figure 3.10: a) Schematic setup of X-ray reflectometry. X-rays are generated by a Cu-anode, monochromatized by a Göbel mirror in the X-ray source and collimated by slits. The X-rays impinge the sample under an angle θ and are reflected with an angle of 2θ with respect to the incoming beam. After passing further optics, the beam intensity is detected. A knife edge restricts the footprint of the X-ray beam. Both, the X-ray source and the detector are moved around the sample always keeping the $\theta/2\theta$-configuration. b) The X-ray beam is reflected at each layer interface and an interference pattern occurs due to constructive or destructive interference.

high angular resolution can be achieved without loosing beam intensity for higher angles, which would be the case if smaller exit slits would be used instead. The intensity over the complete angular range varies by around six orders of magnitude. Therefore, the scan range is split up into different overlapping regions with adjusted counting times ranging from a few seconds at low θ up to 100 s at high θ. The different measurement regions are merged to a complete reflectivity curve using the software Diffrac.EVA. The scattering length density (SLD) profiles of the films are modeled and fitted to the experimental XRR data to receive information about vertical film composition. For that purpose the MOTOFIT software package from Nelson, that makes use of Abeles Matrix formalism or Parratts recursion formula is used. [88–90]

3.2.6 Grazing incidence X-ray scattering

Grazing incidence X-ray scattering (GIXS) is the method of choice to obtain information about crystallinity, crystal orientation and inner morphology of thin organic films. The basic theoretical background is given in section 2.4. The principal setup of a GIXS experiment is schematically depicted in figure 3.11.

X-rays highlight the potential to probe the inner film morphology without destruction. For thin films, the scattering volume in transmission is small and the resulting scattering signal would be extremely low. The samples are therefore measured in reflection geometry with X-rays impinging the sample under a very shallow angle. Therefore, the footprint of the beam and thus the probed volume is very large and an average information about a large film volume is obtained.

The accessible length scales are determined by the size of the 2D-detector and its sample-detector distance (SDD). For short SDDs of about 10-30 cm, wide angles can be detected, which correspond to small distances up to a few nanometers. The corresponding technique is called grazing incidence wide angle X-ray scattering (GIWAXS). It yields information about the molecular arrangement and crystal packing. For long SDDs of 300-400 cm, small angles below 5° can be resolved corresponding to length scales of around 1 nm up to 1 µm. The technique is therefore called grazing incidence small angle X-ray scattering (GISAXS) and used to probe the inner morphology on the mesoscale, for example for phase separation of the materials or aggregation of domains. The choice of SDD depends on the question to be answered and can be varied for each experiment.

The scattering pattern is detected on a 2D-detector. At the Advanced Light Source (ALS) of the Lawrence Berkeley National Laboratory (LBNL), two detectors are used, a Pilatus 1M and a Pilatus 2M from Dectris. The detector is set up with different amount of segments. A segment exhibits 487 x 195 pixels with a pixel size of 172 x 172 µm^2.

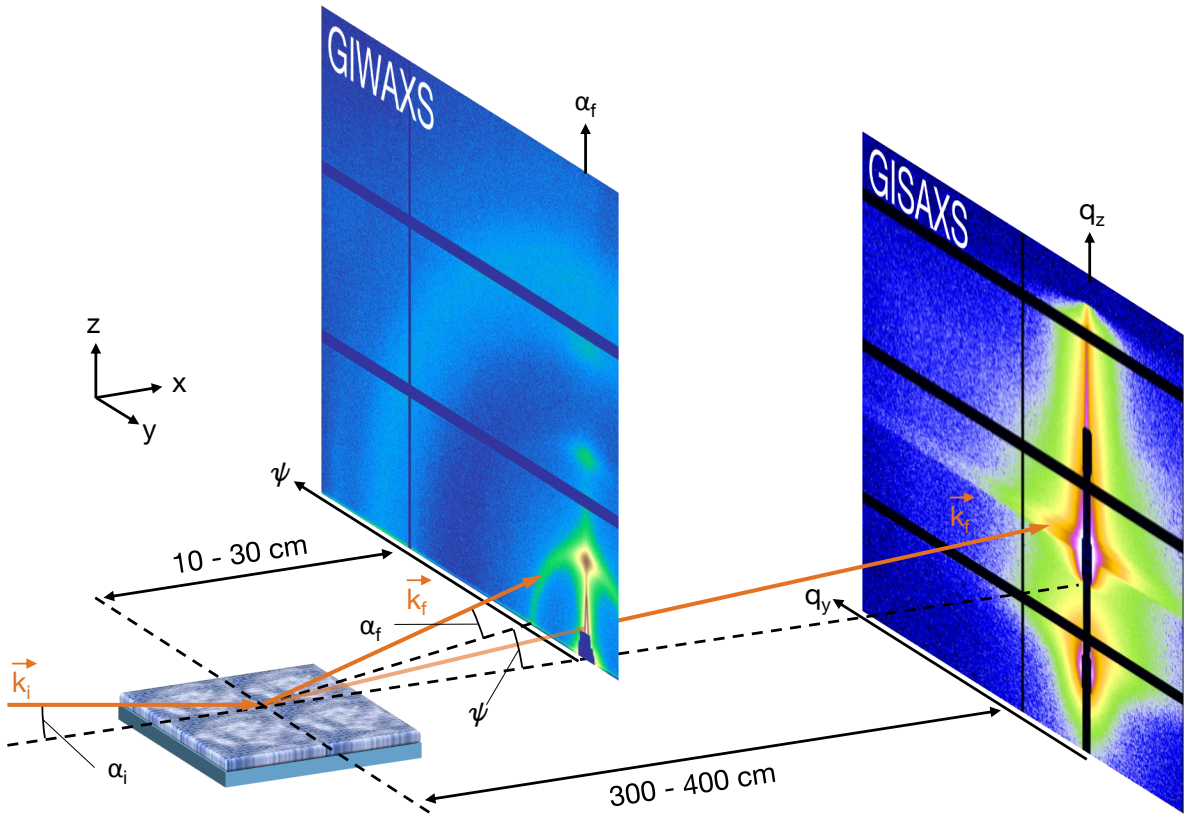

Figure 3.11: Schematic setup for grazing incidence X-ray scattering measurements. The incident X-ray beam $\vec{k_i}$ impinges the sample under a shallow angle α_i. The beam is scattered at the sample and the final beam $\vec{k_f}$ with the angle α_f in the xz-plane and ψ in the xy-plane. The scattering signal is detected on a 2D-detector at a distance of 10-30 cm for grazing incidence wide angle X-ray scattering (GIWAXS) and 3-4 m for grazing incidence small angle X-ray scattering (GISAXS). Depending on the distance, different length scales are accessible. A rod beamstop blocks the direct and the specularly reflected beam to protect the detector from over-saturation.

The Pilatus 1M consists of two columns with five segments each. Its area is therefore 168.7 x 179.4 mm^2 with 981 x 1043 pixels. The Pilatus 2M has three columns with eight segments each, and therefore a size of 253.7 x 288.8 mm^2 with 1475 x 1679 pixels. The connection of the segments results in a gap which misses the scattered data at this spot. With a maximum count rate of 10^7 photons s^{-1} pixel^{-1}, the detector is protected against over-illumination from the direct and specularly reflected beam by a beamstop. Due to the missing background noise and a read out time of less than 3 ms, the Pilatus detectors are highly suitable for low scattering intensities and time resolved measurements.

GIWAXS and GISAXS measurements are performed at the beamline 7.3.3 at the ALS. The wavelength is 1.24 Å, which corresponds to an energy of 10 keV. Details about the beamline can be found in literature. [117]

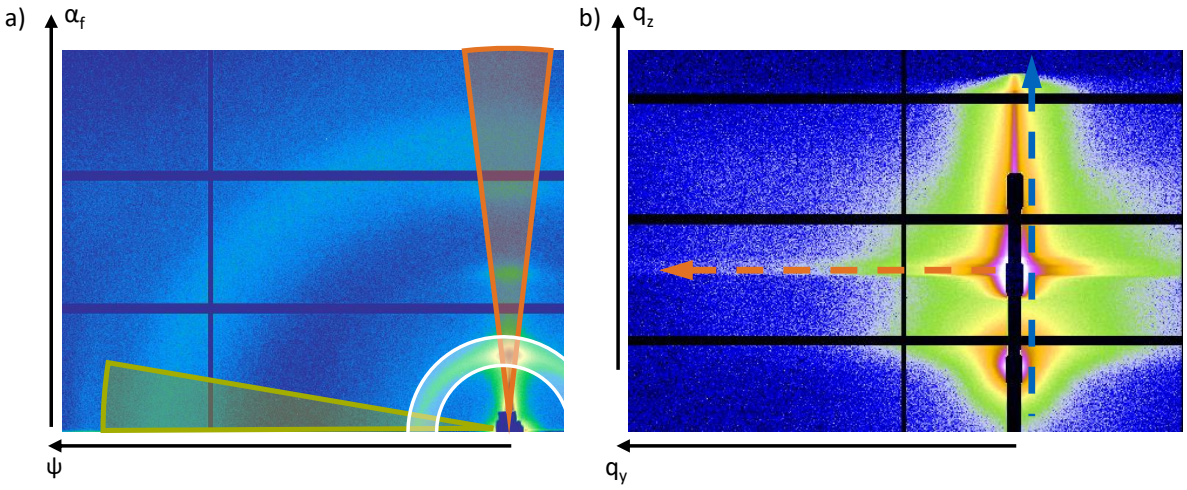

Figure 3.12: Sample 2D data to exemplify data analysis for GIWAXS and GISAXS. a) For GIWAXS analysis, radially integrated intensity profiles (orange and green) yield information about out-of-plane and in-plane structures, respectively. Azimuthally integrated intensity profiles lead to information about the orientation of a certain length scale. The data are shown as detector patterns without transferring into momentum space. All the integrations need certain corrections. b) For GISAXS, line cuts in vertical (blue) and horizontal (orange) direction reveal information about vertical and lateral structures, respectively. If a rod beamstop is used, the vertical cuts are performed next to the rod.

GIWAXS

The basic setup of grazing incidence wide angle X-ray scattering (GIWAXS) is shown in figure 3.11. The incident X-ray beam impinges the sample under a shallow angle of around 0.2°. The scattered signal is detected on a 2D-detector, that is close to the sample with a distance of 10-30 cm to resolve the large angles. If applicable, the sample environment is placed in a helium atmosphere to suppress scattering from air. Further than that, no flight tube is installed between the sample and the detector. The advantage of GIWAXS data on a 2D-detector is the possibility to extract information about the crystal orientation.

For analyzing the GIWAXS data, a number of corrections need to be applied before further processing, which are explained in section 2.4 in more detail. The data are reduced to one dimensional intensity profiles, to obtain quantitative information about the sample in a certain directions. For reducing the data, the software GIXSGUI is used. [94] Depending on the direction of integration of the 2D data, different information are accessed, see figure 3.12a. Vertical, radially integrated intensity profiles along q_z at lowest accessible q_r yield information of the molecular packing perpendicular to the substrate. In figure 3.12a, this integration sector is indicated in orange with an azimuthal angle of

around $\chi = 85°$ to $\chi = 95°$. Horizontal, radially integrated intensity profiles along q_r provided information about the molecular packing parallel to the substrate. The horizontal intensity profile is highlighted in green in figure 3.12a with an angle of $\chi = 0°$ to $\chi = 10°$.

Additional information about the crystal orientation are obtained by azimuthally integrated intensity profiles, indicated with the white tube in figure 3.12a. The integration is done from $\chi = 0°$ to at least $\chi = 90°$, if possible to $\chi = 180°$. If the sample behaves like an in-plane powder, the reduced data are $\sin(\chi)$ corrected to account for the tilted Ewald sphere. [96, 118, 119]

The reduced and corrected data contain material characteristic peaks which are fitted with a sum of Gaussians and an adequate background function using self written Python scripts. From the fitting parameters, conclusions about the crystal properties can be derived and the crystal size is estimated using the Scherrer equation 2.34.

GISAXS

The setup used for grazing incidence small angle X-ray scattering (GISAXS) is similar to the one used for GIWAXS as depicted in figure 3.11. The difference is the increased sample to detector distance (SDD) to 300-400 cm to resolve the small angles. As the long path to the detector would result in strong air scattering, a flight tube is installed in the path from the sample to the detector. It contains either helium or is evacuated to avoid scattering with air. The large SDD allows to probe structure sizes in the mesoscale between a few nm up to µm. To protect the detector from over-saturation, a beamstop is installed in front of the detector to block both, the direct and the specularly reflected beam. For the experiments at ALS, a rod beamstop is used, which completely shields the signal around $q_y = 0$.

For the analysis, scattering signals in vertical and in horizontal direction are of interest. Line integrals are performed as indicated in figure 3.12b in the respective directions with blue and orange arrows. The horizontal integral is typically obtained at the materials Yoneda position, which is a material characteristic depending on its critical angle. [87] From these integrals, information about the film composition perpendicular and parallel to the substrate are obtained. The reduction of the data is performed using the software package DPDAK from DESY. [120] Custom made macros are used for data modeling to analyze the reduced data. The models assume up to three spherical or cylindrical form factors with a Gaussian distribution of their size, each together with 1d paracrystals as structure factor in the local monodisperse approximation (LMA). It assumes, scattering only occurs from objects of the same size, independent from the presence of other structures.

4 Sample preparation

The basic materials and processing steps for the substrates and the thin film deposition are presented in this chapter. Details for each experiment are noted at the beginning of the respective chapters. The materials and solvents are introduced in section 4.1. The cleaning procedure of the substrates is explained in section 4.2.1. Section 4.2.2 shows the thin film deposition methods and introduces the printing parameters used in this thesis. The solar cell fabrication is then elucidated in section 4.2.3.

4.1 Materials

The structural formulas of the materials used in this thesis are depicted in figure 4.1.

Poly(3-hexyl-thiophene) (P3HT)

Commonly applied as donor in the active layer of organic solar cells is poly(3-hexyl-thiophene) (P3HT), $(C_{10}H_{14}S)_n$. It is used as hole conducting polymer with lowest unoccupied molecular orbital (LUMO) level at -3.3 eV and highest occupied molecular orbital (HOMO) level at -5.2 eV. The reported band gap is 1.9 to 2.0 eV and therefore it absorbs in the visible light range. [55, 56] Its hole mobility μ_h is $5.6 \,\mathrm{x}\, 10^{-4}$ $\mathrm{cm^2\, V^{-1}\, s^{-1}}$ and the electrical conductivity is 10^{-9} to 10^{-7} $\mathrm{S\, cm^{-1}}$, which can be improved by doping. [121, 122] The reported mass density is 1.1 $\mathrm{g\, cm^{-3}}$. [123, 124] The P3HT used in this work is purchased from Rieke Metals Inc. with an average molar mass M_W of 53 $\mathrm{kg\, mol^{-1}}$.

[6,6]-phenyl-C61-butyric acid methyl ester (PCBM)

Widely used electron acceptor material in organic photovoltaics is [6,6]-phenyl-C61-butyric acid methyl ester (PCBM), which is a derivative of buckminster fullerenes. The high electron mobility of around $2 \,\mathrm{x}\, 10^3$ $\mathrm{cm^2\, V^{-1}\, s^{-1}}$ originates from the large number of delocalized π-orbitals. [125] The LUMO level is at -4.3 eV and the HOMO level at -6.0 eV, which results in an electronic band gap of 1.7 eV. [126] PCBM absorbs in the UV-range and thus

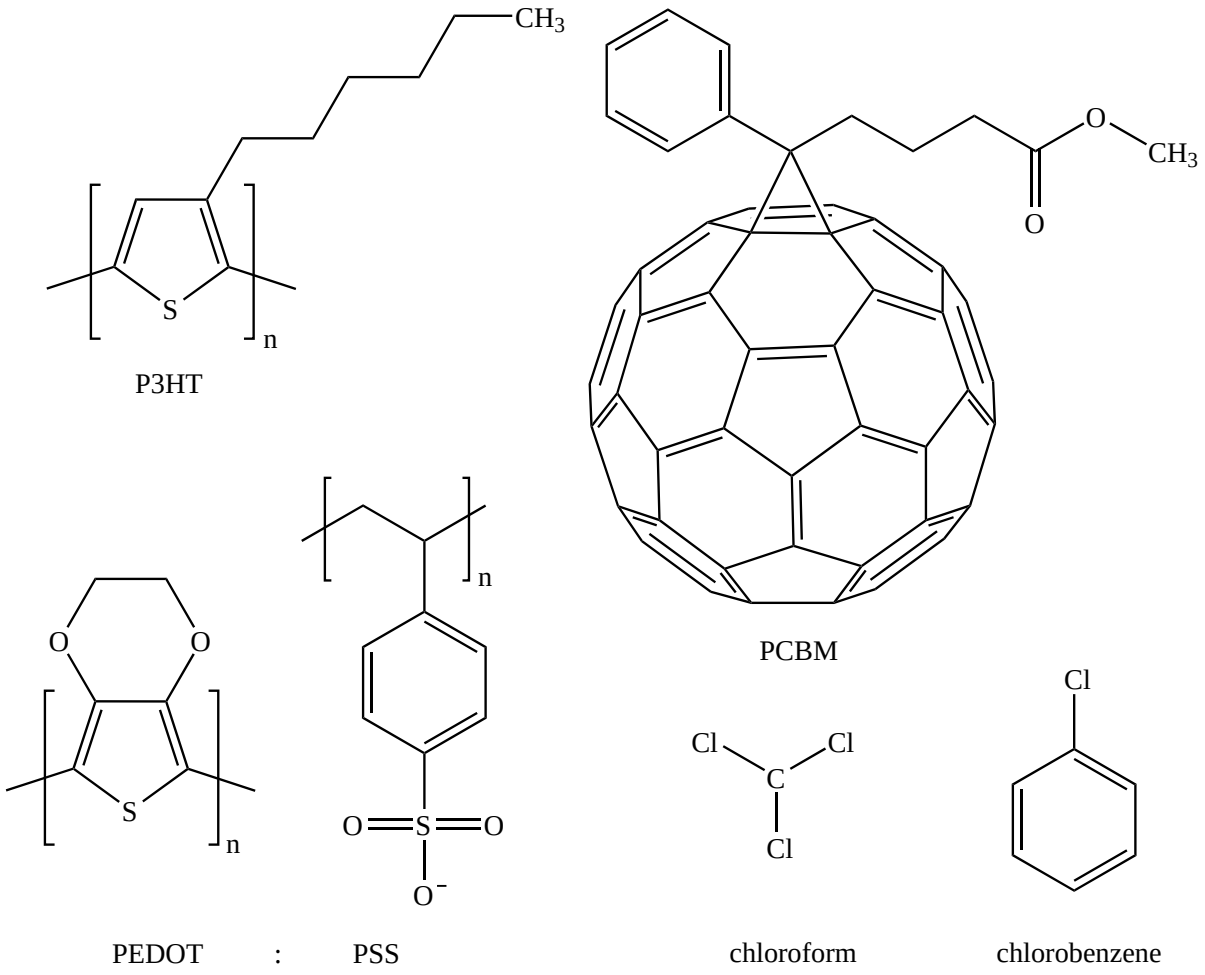

Figure 4.1: Structural formulas of the materials used in this work.

only marginally contributes to the total light absorption in solar cells. The reported density is between 1.3 and 1.5 $\mathrm{g\,cm^{-3}}$. [123,124] The used PCBM is purchased from 1-Material Inc.

Poly(3,4-ethylenedioxythiophene):poly(styrenesulfonate) (PEDOT:PSS)

For organic electronics, poly(3,4-ethylenedioxythiophene):poly(styrenesulfonate), or short PEDOT:PSS, is an important water soluble and electrically conductive complex of two polymers. The conductive part is fulfilled by PEDOT, whereas PSS is used as counterion to provide water solubility and therefore the easy processability of PEDOT:PSS. It is optically nearly transparent and its hole conducting and electron blocking properties provides the possibility to apply PEDOT:PSS in organic solar cells, although not as active

material. The used PEDOT:PSS (AI 4083, M121) (PEDOT:PSS ratio 1:6) purchased from Ossila, is kept in the refrigerator at 4 °C.

Solvents

Chlorobenzene: For the bulk heterojunction, both, the conjugated polymer (P3HT) and the fullerene (PCBM) are dissolved in chlorobenzene which has a boiling point of 131 °C and a density of 1.1 $g\,cm^{-3}$. Chlorobenzene used within this thesis is purchased from Carl Roth with a purity of $\geq$ 99.5 %.

Chloroform: Since P3HT and PCBM do not exhibit an electrophoretic mobility in chlorobenzene but in chloroform, the materials are dissolved in the latter for electric field investigations (chapter 7). Chloroform has a boiling point of 61 °C and a density of 1.5 $g\,cm^{-3}$. Chloroform used within the scope of this thesis is purchased from Sigma-Aldrich.

Substrates

Silicon: For experiments performed with samples on a silicon substrate, a wafer with a diameter of 100 mm (Si-Mat, p-doped, (100) orientation) and a thickness of 525 µm is used. The wafer is cut to the desired size using a diamond cutter. Subsequently, it is broken over a defined metal edge.

Glass: For measuring the optical properties of thin films in transmission, an optical transparent substrate like glass is needed. The used glass slides (Carl Roth) with a size of $76 \times 26 \times 1$ mm^3 are scratched on the backside using a glass cutter and broken at this particular scratch over a defined metal edge.

ITO coated glass: For the standard solar cell setup, glass coated with indium doped tin oxide (ITO), SnO_2:In_2O_3, is used. It is a transparent conductive oxide for contacting the solar cell. The used substrates are purchased from Solems with a size of 75×20 mm^2. The glass is 1 mm thick and coated by a 100 nm thick ITO layer with a sheet resistance of 25-35 $\Omega\,sq^{-1}$.

4.2 Sample processing

A certain routine needs to be fulfilled to obtain homogeneous and thus reproducible thin films. This routine includes the preparation of the substrates, the deposition of thin films and the steps to apply the films in solar cells. In the following, each step is described.

4.2.1 Substrate preparation

The used substrates have to be in a defined state before further processing in order to get reproducible results. Therefore, the glass or silicon substrates are cleaned in an acid bath. [105] The ingredients, which are deionized water (DI H_2O), hydrogen peroxide (H_2O_2, Carl Roth) and sulfuric acid (H_2SO_4, Carl Roth), are successively added in a glass beaker using the amounts listed in table 4.1 and heated to 80 °C.

Table 4.1: Composition of the acid bath for cleaning the substrates.

chemical	**amount [ml]**
DI H_2O	54
H_2O_2	84
H_2SO_4	198

The cut samples are immersed in the acid bath for 15 min and subsequently placed in deionized water. Directly after that, the samples are separately rinsed with deionized water to remove acid traces and dried with nitrogen. With that, the samples have a defined oxide layer with a hydrophobic surface.

4.2.2 Thin film deposition

For deposition within the scope of this thesis, two methods are used, spin coating and slot-die coating.

Preparation of blend solution

P3HT:PCBM: For the production of a standard solar cell active layers, a solution of P3HT:PCBM with a 1:1 weight ratio is prepared. Therefore, the utilized welted glasses are each cleaned with the later used solvent to ensure the removing of all residuals that are soluble in the respective solvent. After drying the glasses with oil-free nitrogen, the desired amount of P3HT and PCBM are directly put into separated glasses and measured using an analytical balance (Sartorius CPA 225D). Having measured the amount of polymer, the particularly needed volume of solvent (chlorobenzene or chloroform) is added with a microliter pipette to obtain the concentration of 16 $mg\,ml^{-1}$. This solution is stirred until dissolving. The same is done for PCBM to get a concentration of 16 $mg\,ml^{-1}$ of the solution. Thereafter, the glasses are sealed using Parafilm® to avoid solvent evaporation.

The separate solutions are placed on a shaker (IKA-Vibrax-VXR) over night before the solutions are combined.

PEDOT:PSS is already dissolved in water upon receiving. Before application, PEDOT:PSS is placed in a ultrasonic bath for ten minutes in order to dissolve aggregates and subsequently filtered with a 0.45 µm poly(vinylidene fluoride) (PVDF) filter to remove big clusters.

Spin coating

Spin coating is a common technique to produce thin homogeneous films out of solution with controllable and reproducible thicknesses. For spin coating, the cleaned substrate is placed on the rotation chuck. The sample is fixed either by vacuum or by pins. For spin coating (Ossila, E441), the rotational speed in revolutions per minute (rpm), the time and the acceleration is set. After setting the needed parameters the solution is dispersed over the substrate to completely cover it. During spin coating, first the excessive solution is removed followed by evaporation of the solvent. The obtained film thickness d depends on the molecular mass M_W, the initial concentration c_0 and the rotational speed ω and can be calculated using the Schubert equation [127]:

$$d = A \cdot \left(\frac{1950 \frac{1}{min}}{\omega} \right)^{\frac{1}{2}} \left(\frac{c_0}{20 \frac{g}{l}} \right) \left(\frac{M_W}{100 \frac{kg}{mol}} \right)^{\frac{1}{4}}, \tag{4.1}$$

with the scaling factor A including environmental parameters like temperature and humidity. A linear relation between the thickness and the concentration of the polymer solution is found for the case of pure polymer films within certain regimes. There, the viscosity of the solution can be neglected. [127] Generally, the thickness depends on the viscosity of the solution as well. Thus, a higher viscosity yields a larger film thickness.

Slot-die coating

For the printing experiments in this thesis, a lab-scale printer is developed. It facilitates the implementation into a synchrotron beamline and is therefore suitable to perform fundamental investigations on the film solidification process. The printer is described in detail in chapter 5. An overview of the setup with the most important components is depicted in figure 4.2a.

The solution is provided via a syringe pump with variable pump rate. A suitable pump rate is found to be 0.25 $\mathrm{ml\,min^{-1}}$ for a solution concentration of 16 $\mathrm{mg\,ml^{-1}}$. The distance between print head and sample, the gap clearance, is controlled using two systems. One is an optical one, using a 10x-magnification objective and a CMOS camera. The print

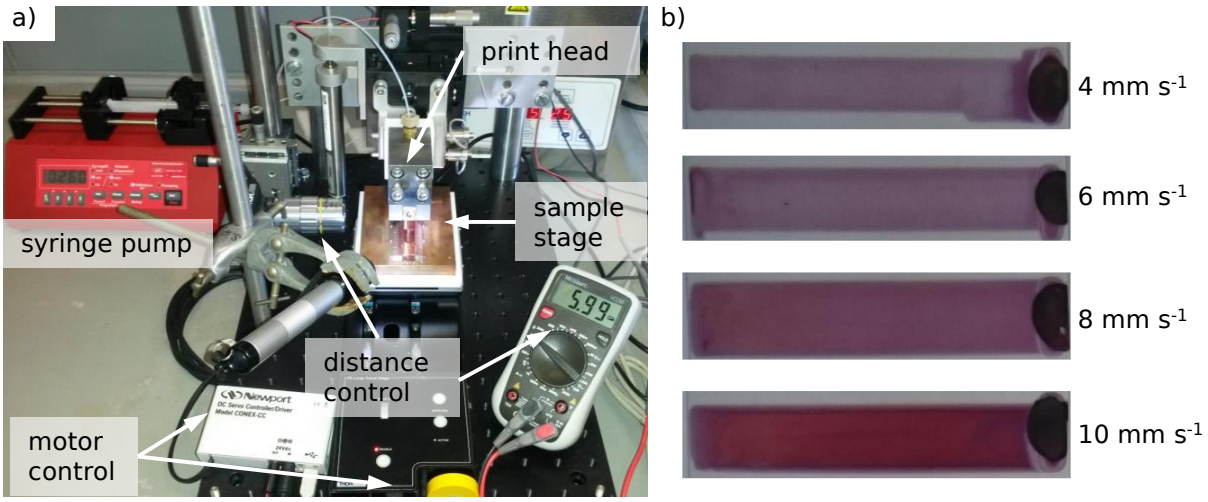

Figure 4.2: (a) Overview over the slot-die setup used in this thesis with the most important components. Two motor control units for the vertical and horizontal motor. The print head distance is controlled with two systems, a camera watching the distance and a force sensor in the vertical mounting to detect the moment the print head is touching the substrate. (b) Photographs of films printed with a gap clearance of 300 µm at different horizontal printing speeds.

head lip face is followed and a distance to the sample can be read through calibration. The second one is a force sensor mounted on the contact point of the vertical motor. The force is measured continuously and the force due to the weight of the print head is measured. Once it touches the sample surface, it becomes smaller, which yields the zero gap clearance. The exact distance is set via the vertical motor. The gap clearance is chosen to allow a meniscus formation between print head and sample before starting the printing process. In this thesis, a gap clearance of 300 µm is commonly used. The horizontal motor moves the substrate underneath the print head and is thus responsible for transferring the meniscus onto the substrate. Figure 4.2b shows photographs of films printed at different horizontal velocities. The pump rate was 0.25 $\mathrm{ml\,min^{-1}}$ and the gap clearance 300 µm. Well reproducible films are obtained for a printing speed of 10 $\mathrm{mm\,s^{-1}}$, which lead to a final film thickness of around 150 nm.

A detailed investigation on the printing parameters and the influence on the final films was performed by Oliver Filonik and Fabian Englbrecht. [128, 129]

4.2.3 Solar cell fabrication

The fabrication of solar cells involves five different steps as depicted in figure 4.3. As

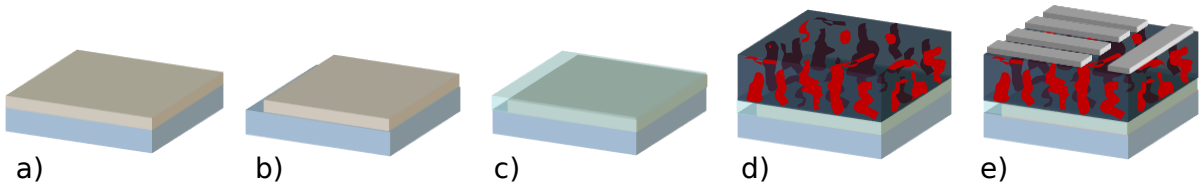

Figure 4.3: Schematics of solar cell assembly: (a) The glass substrate coated with ITO is (b) partly etched to remove the ITO at one side before cleaning. (c) PEDOT:PSS is spin coated onto the ITO before (d) the active layer is applied using slot-die coating. The samples are thereafter cut to a size of 2 x 2 cm^2 before (e) evaporating aluminum contacts.

substrate, ITO coated glass is used, which already requires a slightly different procedure as normal glass described above.

Substrate preparation

As substrates for solar cells in standard geometry indium doped tin oxide (ITO) coated glass is used due to its high conductivity (figure 4.3a). The ITO layer is partly etched away from the substrate as depicted in figure 4.3b. Therefore, ITO is partly covered with a Scotch tape. For etching, zinc powder is distributed on the non-covered part of the ITO. Hydrochloric acid (HCl, 37 %) is applied on the distributed zinc powder. After completion of the reaction, the remaining parts are rinsed away with deionized water and the tape is removed.

Cleaning

As acid cleaning would etch away the ITO, another cleaning method is applied for the solar cell substrates. The cleaning process includes four steps each of them containing a ten minutes ultrasonic bath followed by rinsing of the substrates.

First, the substrates are placed in a Teflon holder and rinsed with deionized water. Thereafter, they are subsequently immersed in Alconox® dissolved in deionized water (10 $g\,l^{-1}$, Sigma-Aldrich), ethanol (Carl Roth), acetone (Th. Geyer) and isopropyl alcohol (IPA, Carl Roth), in between a ten minutes ultrasonic bath and rinsing of the samples with the appropriate solvent (in case of Alconox®, they are rinsed by deionized water). After finally rinsing the samples with IPA, they are dried with nitrogen.

Right before continuing with the next preparation step, the sample surface is treated in an oxygen plasma. This aims to remove all organic traces and to improve the wetting of the surface with the following solution of the blocking layer. Therefore, the samples are

placed on a glass plate in between the electrodes in a plasma oven (SmartPlasma from plasma technology GmbH). The chamber is evacuated to 0.3 mbar before filling with oxygen. The plasma is applied for 3 minutes.

Application of electron blocking layer

The first applied layer is PEDOT:PSS to improve the contact and as blocking layer of electrons, figure 4.3c. Therefore, PEDOT:PSS is put into the ultrasonic bath for 10 min. The solution ($\approx$ 1-2 ml) is then filtered with a PVDF filter with a pore size of 0.45 µm to remove big clusters directly before spin coating. The spin coating parameters are 3000 rpm for 60 s leading to a film thickness of around 50 nm. Directly after spin coating, the samples are put on the heating plate at 150 °C for 10 min to remove the remaining water.

Application of active layer

As active layer, only non-water based solvents can be used since otherwise the applied PEDOT:PSS layer would be re-dissolved. Within the scope of this thesis, P3HT:PCBM dissolved in chlorobenzene or chloroform as described previously is used. Around 0.1 ml is slot-die coated on the electron blocking layer with a substrate speed of 10 $mm\,s^{-1}$, a print head to substrate distance of 0.3 mm and a pump rate of 0.25 $m\ min^{-1}$ (figure 4.3d).

Aluminum contact evaporation

Before evaporating aluminum contacts the samples are cut into $20\,x\,20\ mm^2$ pieces to fit into the evaporation pockets. The aluminum (ChemPUR, 99.99 % purity) is evaporated at a pressure below 10^{-5} mbar using a CREAMET 301 V2 evaporation system from Creative Vakuumbeschichtung GmbH in a nitrogen filled glovebox. The deposition controller SQC-122c from Sigma Instruments allows for precise thickness control. The evaporated aluminum contact has a thickness of 100 nm (figure 4.3e).

5 Design and construction of an experimental printing setup

Thin film deposition and its control became more and more important over the last few decades. It is not only the functional coating of surfaces which gains interest, but also organic thin film deposition which is used in organic electronic (OE) applications. For OEs, the most common deposition method to date is spin coating. A lot of progress in the field of OEs is due to the easy reproducibility of spin coated films. [130] However, a drawback of this technique is the limited surface size that can be coated. A further progress in the development of organic solar cells (OSCs), organic light emitting diodes (OLEDs) or organic field effect transistors (OFETs) demands a homogeneous coating on large surfaces. With a film thickness of around one hundred nanometers, the deviations should be in the lower nanometer scale. [13] These requirements cannot be faced by lab scale techniques like spin coating, but rather by different kind of printing techniques. [16] Next to the homogeneous deposition of the functional material, the inner film morphology is of utmost importance for the performance of the organic functional layer. [82, 131, 132] Therefore, several attempts aim to influence the inner morphology after producing the devices, the so called post-production treatment. Among these attempts, the most prominent ones are thermal annealing, external magnetic or electric fields or temperature gradients. [133–135] As it is beneficial to accelerate the total production time of the devices, the treatment during device processing comes more and more into focus. For organic solar cells, for example, force fields, different solvents, solvent additives or a reduced solvent evaporation rate via solvent annealing is applied during processing. [136–138] Especially the latter approach shows a notable improvement of the device performance. [137, 138]

Insight on the inner morphology is regularly obtained by characterization using X-ray scattering techniques. For thin organic films, X-ray scattering under grazing incidence is applied in order overcome the limited scattering volume due to the low film thickness (see 2.4). [34,139] Hereby, the incoming X-ray beam impinges the sample under a shallow angle which leads to a large probed volume. The scattered signal is then detected and, depending on the distance of the detector to the sample and the wavelength of the X-ray, different length scales are accessed. For many polymers, especially the widely used poly(3-hexyl-

Figure 5.1: Diagram to show the structure of the thesis. This chapter explains the experimental setup that was constructed and built. Based on this setup, the further experiments are performed.

thiophene) (P3HT) the spacing between the backbones is the most relevant information on the smallest length scale and therefore the respective high scattering angles need to be accessible in any experiment. Recent investigations in the field of OE focus on the kinetics playing an important role during device fabrication or operation. [38, 140, 141] Current interest is put on the investigations of the kinetics in up-scalable techniques which still lacks fundamental experiments. Thus, knife and slot-die coating have become one of the most widespread large-scale processing techniques to be investigated. The first attempts of a slot-die coater that is adaptable to synchrotron beamlines have been introduced and the initial studies showed the mechanisms of the structure formation of printed photoactive layers. [142, 143] The experiments show the importance of the control of numerous parameters while processing and their enormous impact on the molecular assembling. To investigate the complex assembling process, in thin organic films while printing, more effort needs to be put on the experimental conditions. In particular, advanced setups for *in situ* characterization are necessary. These setups have to be adjusted in order to be implemented in synchrotron beamlines while still being able to control a wide number of parameters. The definition and construction of such a setup is therefore the first step to be fulfilled before deeper investigations on the kinetics can take place. Thus, the setup presented in this chapter is the base of the complete work presented in this thesis (figure 5.1).

This chapter describes in detail the concept and construction of a slot-die coater that can be implemented into a synchrotron beamline. The project is an ongoing collaboration with the group of Dr. A. Hexemer at the Advanced Light Source (ALS) of the Lawrence Berkeley National Laboratory (LBNL), in particular with Dr. C. Wang and Dr. C. Zhu. It starts with the basic printer setup (section 5.1). This section gives an overview on the printer scaffold, the print head and the motors along with their control. This section also investigates the meniscus forming process at the print head lip. Using this basic setup it is already possible to print thin organic films applied in solar cells and thus the parameters for printing are defined. It furthermore offers the possibility to vary the substrate temperature and therefore the drying speed of a printed thin film. In the following section 5.2 the printer is equipped with electrodes for the application of an electric filed during

printing. With this modification, new possibilities on the manipulation of the morphology arise. A further improvement of the printer is the equipment with an atmosphere control chamber described in section 5.3. This chamber is capable of providing a defined flow of different saturated gases containing organic solvents and keeping the atmosphere. Thus, the setup allows for solvent annealing during processing. It is constructed in away that allows for accessing the freshly printed films with X-rays for *in situ* structure formation investigations. Another implementation are optical fibers for probing the film during solidification with transmission or reflection measurements. The functionality of the setup is demonstrated by implementing it into a synchrotron beamline where the solidification process of a printed thin organic film is tracked with grazing incidence small angle X-ray scattering (GISAXS). Furthermore, another experiment is performed measuring the transmittance of the samples during solidification. For both experiments, the influence on the film drying process of a saturated gas stream is observed. Parts of this chapter are published in "Note: Setup for chemical atmospheric control during in situ grazing incidence X-ray scattering of printed thin films", Review of Scientific Instruments 2017, 88 (6), p. 066101. [144]

5.1 Basic printer setup

A printer setup, that was previously introduced by collaborators serves as template for the experimental setup presented in the following. [143, 145] In particular the principle of the vertical translation and the print head mounting are used for the first version of the setup. The drawbacks of this setup were the low flexibility to modify with customized equipment, the limited printing area of less than 20 mm x 100 mm and the sensitive motor. The following most important requirements are defined to overcome this drawbacks:

- low weight for setting on a goniometer stage (< 15 kg)
- printing area of more than 20 mm x 100 mm
- heatable sample stage up to 140 °C
- accessibility of the printed film for *in situ* GISAXS and GIWAXS
- high reproducibility of the coated films
- flexibility to modify setup

In the following the single parts of the basic printer are described, starting with the printer scaffold, followed by the print head together with an investigation of the meniscus formation process and afterwards the software control.

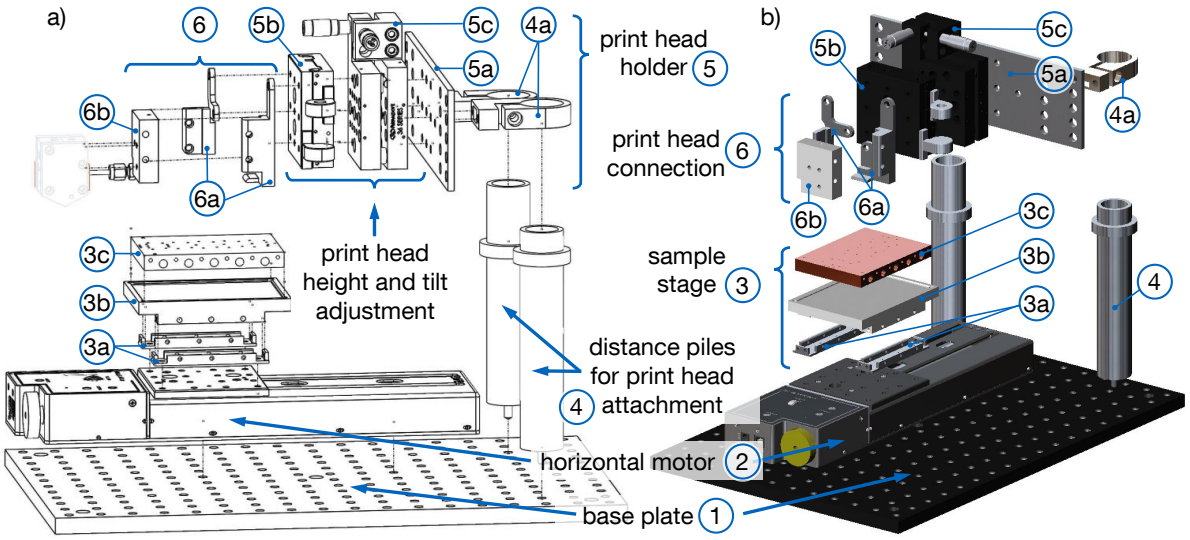

Figure 5.2: Exploded view of the base printer setup a) drawing and b) 3d CAD model without the print head. The system consists basically of two parts, the sample stage on the horizontal motor and the mounting for the print head. For flexibility, the print head position can be varied in height and tilted. The numbers are explained in the main text.

5.1.1 Printer scaffold

The basic setup of the printer is shown in figure 5.2. The base plate (1) is a breadbord with size 300 mm x 450 mm x 12.7 mm, on which all of the subsequent equipment is mounted. Directly connected to the base plate are a horizontal motor (2) for the sample stage (3) and two distance piles (4), on which the print head holder (5) is mounted.

The sample stage (3) of this basic printer version consists of three parts. Two mounting rails (3a) are fixed on the horizontal motor (2). They serve to fix a heat buffer (3b) for the copper sample stage (3c). The heat buffer (3b) is made of poly(tetrafluoroethylene) (PTFE), a thermoplastic polymer, better known under the trade name Teflon®. This material has a melting point of 327 °C (glass transition temperature T_g = 115 °C) and a coefficient of thermal expansion of 112-125·10^{-6} K^{-1} and a thermal diffusivity of 0.124 mm^2 s^{-1}. [146–148] It is therefore suitable to serve as heat buffer of the copper sample holder (3c), which can be heated up to 150 °C using heating cartridges. The copper plate features five clearance holes for the heating cartridges and blind holes in between for the temperature sensors. On top of the sample holder, several M2 threads serve to fix the sample using headless screws. The arrangement of the threads offers a variety of possible substrate sizes, especially for the used lengths and widths of ITO glasses and microscopic slides (see chapter 4).

The print head holder (5) is mounted on the distance piles (4). The print head con-

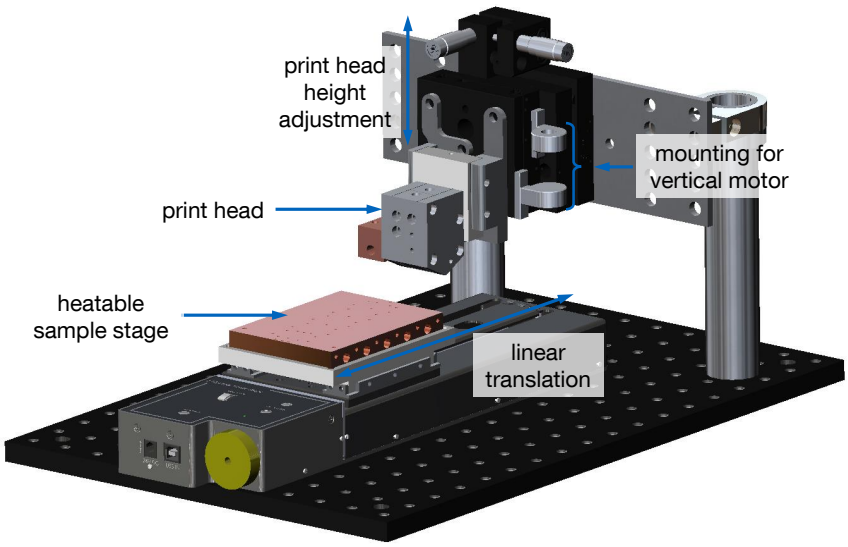

Figure 5.3: Complete assembly of the basic printer setup including the print head and a heatable sample stage. For coating, the latter one is linearly translated underneath the print head, which is adjustable in height via a vertical motor (not shown in this image).

nection (6) needs to be adjusted in an accurate way, meaning the height and tilt. For the height adjustment, two systems are used. First, a rough height adjustment is done with the clamps (4a) on the distance piles and the attachment plate (5a). Second, a ball bearing linear stage (5b) with travel length of 25.4 mm purchased from Newport (M-423) is used for the fine attachment of the height. This stage is mounted on a tilt and rotation platform (5c). It features a tilt adjustment of -4.3° to +7.0° and a rotational adjustment of ±2.5°, which is sufficient to account for different substrate and coating conditions. The platform is purchased from Newport (M-36). To connect the print head, a system (6) consisting of three parts is used. Two aluminum holders (6a) are mounted on the linear stage (5b) and serve as positioning system of a PTFE block (6b), on which the print head will be directly mounted. This block with the print head is then connected to the aluminum holders with ball lock pins.

The completely assembled printer is shown as a CAD drawing in figure 5.3. For the fine adjustment of the head height, instead of a manual micrometer screw, a motorized actuator is used.

In order to set the accurate height of the print head, two methods are used. The first one is an optical control, the second one a force sensor. The former one consists of a CMOS camera (Thorlabs DCC1645C) with a Mitutoyo objective (M Plan APO) purchased from Edmund Optics GmbH with a 10 fold magnification and a working distance of 33.5 mm. With this camera system the print head and sample are monitored and the distance can be set via a calibration of the optics or by using the substrate surface as zero position of the print head height and moving the vertical motor to the desired absolute position. An image of the print head and sample seen by the camera system is shown later in figure 5.5. The force sensor as the second system is attached to the vertical mounting of the

actuator. The sensor detects the change of weight between the print head being above the sample and touching it, which is then set as the zero position.

5.1.2 Print head

The most important part of the printer is the print head. It needs to provide a homogeneously distributed amount of solution over the complete lip. A number of studies on the influence of the lip on the meniscus forming process shows the complexity of the construction. [49, 149] A first cooperation on the development of a suitable slot-die print head was with UNAV Coating Technologies, Switzerland. The first version of the print head is seen in the assembly of the slot coater in figure 5.3. Further improvements of the print head came with the cooperation with Jema Technologies LLC, USA, California. A technical drawing of the principle setup of the print head and an isometric exploded view is given in figure 5.4.

The solution is fed into the print head via an inlet with a 1/8-27 NPT thread on top of the print head. A tube connected to the syringe pump provides the solution with a given pump rate through an adapter. The solution flows through a channel (1) to the

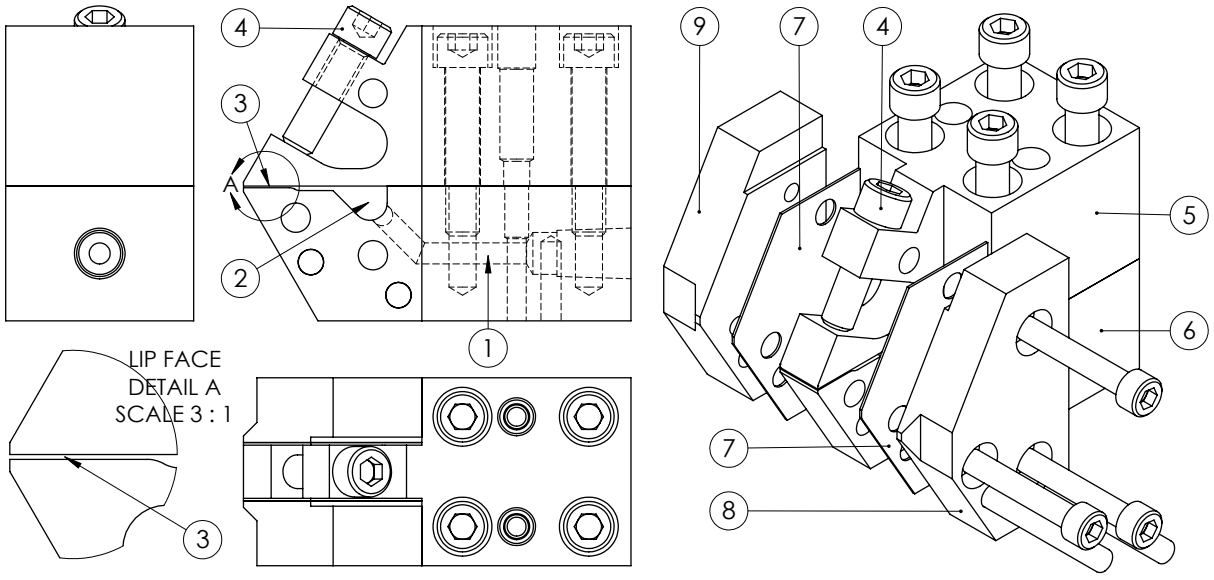

Figure 5.4: Technical drawing of the print head including an exploded isometric view. The solution is provided via an inlet on top of the print head through a channel (1) to the distribution chamber (2). The solution is then brought to the substrate through the feed slot (3), which is adjustable with a screw (4) at the front part (5) of the print head, while the solution feed is located in the rear part (6). Two shim masks (7) limit the feed slot width and are fixed with a right (8) and a left (9) bracket. Drawing based on Jema Technologies LLC.

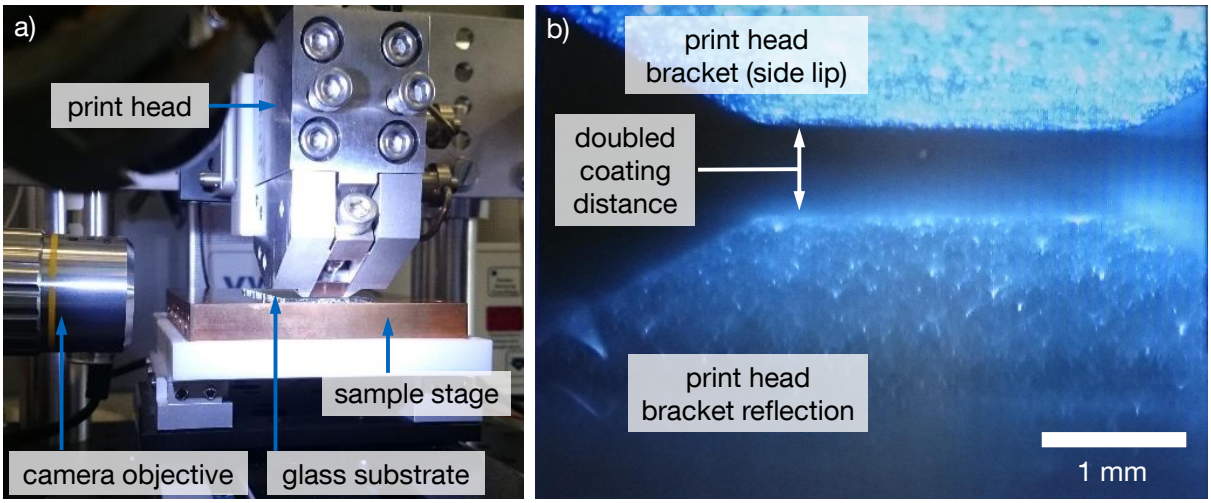

Figure 5.5: a) Photograph of the basic printer setup from the front view including a camera for watching the meniscus forming. (Photo: Oliver Filonik) b) Record of the camera image looking from the side onto the left print head bracket (as mounted in (a)). The coating distance of the print head to substrate, known as gap clearance, is adjusted using a vertical motor.

solution distribution chamber (2). This chamber provides the solution through the feed slot (3) to the substrate. The width of the feed slot can be varied between 0 and 0.3 mm via an adjustment screw (4) at the front part (5) of the print head. The solution feed and distribution chamber is located in the rear part (6) of the slot-die head. Two shim masks (7) on each side of the feed slot provide the boundary for the solution. The shim masks are fixed with a right (8) and a left (9) bracket.

The print head is mounted to the basic printer setup using the print head connection. A picture of the setup with a substrate directly before the printing process is shown in figure 5.5a.

The camera observes the left print head bracket, which is used to set the clearance gap as described previously using the vertical motor. In the recorded image (figure 5.5b) the lower part of the bracket as side boundary of the lip is shown. This record serves not only for setting the head-to-sample distance, known as gap clearance, but also to watch the meniscus forming and determine the start of the coating process.

The initial wetting of the surface is recorded with the camera from the front (figure 5.6), to get a rough idea about the meniscus formation. A detailed study on the starting process of slot-die coating is performed by Chang et al. [150] They found, how the starting process influences the film quality and how a stable meniscus is reached.

Once the distribution chamber is filled, it is only one tenths of a second, that the meniscus is formed over the complete width of the lip. Further pumping leads to an

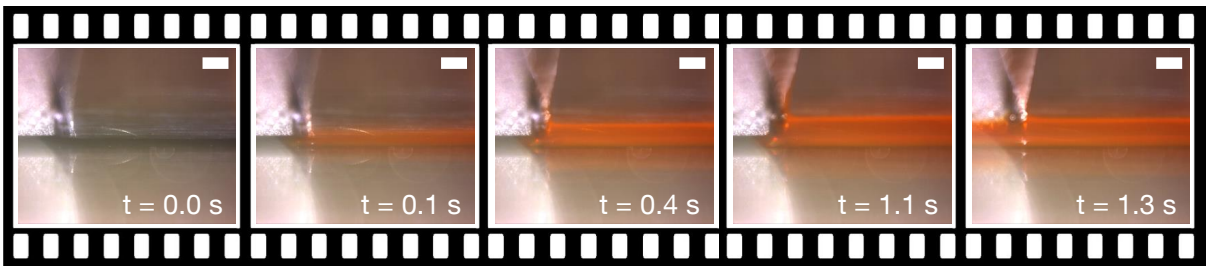

Figure 5.6: Snapshots from a movie watching the forming meniscus from the front. Initially, the meniscus is kept at the lip for around 1 s during which the meniscus height increases. After a certain amount of material is pumped through the print head, the meniscus moves over the side of the lip. The scale bar in each image represents 1 mm. (gap clearance: 300 µm, pump rate: 0.25 ml min^{-1})

increase of the wetting meniscus which covers the full width of the lip. This increase of the meniscus leads to an increased volume in the upstream die lip and thus to a change of the coating bead. For the pump rate of 0.25 ml min^{-1} and a clearance gap of 300 µm, there is only a time window of 1 s, in which the meniscus is kept within the lips. Afterwards, the meniscus moves sideways over the brackets of the slot-die head.

The increase of the meniscus height after it ranges over the side of the feed slot is shown in figure 5.7, in which each frame represents additional 0.2 s of pumping.

With a pump rate of 0.25 ml min^{-1} each of these 0.2 s of pumping yields to additional

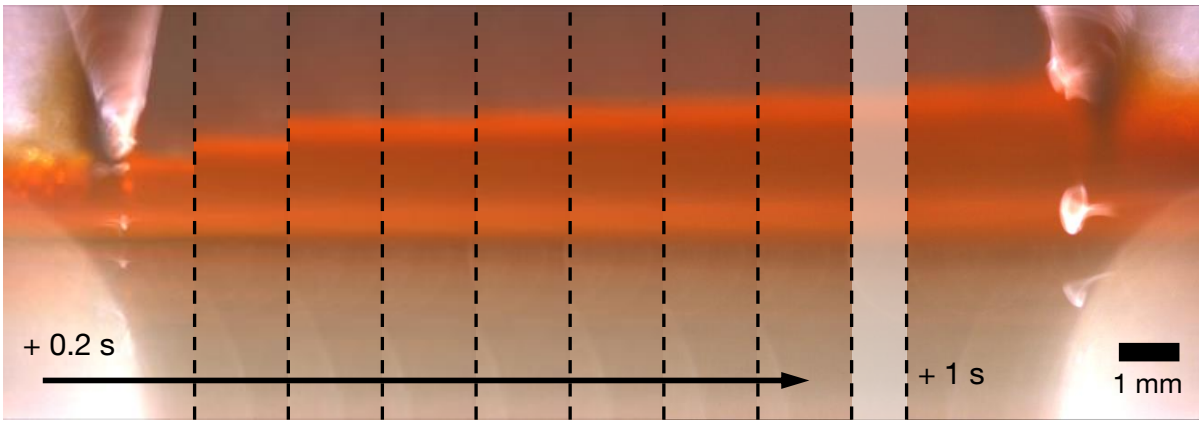

Figure 5.7: Selected pictures from a video of the meniscus formation at the print head showing the growth of the meniscus once it moved over the side of the feed slot. Each frame represents a progress of 0.2 s, the last one of 1 s. With a pump rate of 0.25 ml min^{-1}, each 0.2 s frame contains additional 0.8 µl solution. Shown in the picture is a polymer solution at the side of the feed slot.

0.8 µl of the solution which is contained in the meniscus. This excess of solution has then an influence on the film thickness and quality, which needs to be reproducibly controlled. The starting point of the printing procedure needs therefore be set to a certain time after the initial meniscus is formed.

5.1.3 Linear motors and software control

The movement of the sample stage as well as the vertical adjustment of the print head height is motorized. As actuator of the vertical adjustment of the print head with micrometer accuracy, CONEX-CC from Newport is used. The motor has a travel range of 25 mm with a guaranteed absolute accuracy of ±5.0 µm and a minimum incremental motion of 0.20 µm. The properties are sufficient for setting the print head height (gap clearance) to around 300 µm. For the horizontal translation, a 150 mm translation stage with stepper motor purchased from Thorlabs (LTS-150/M) is used. It has a horizontal velocity of up to 50 mm s^{-1} with an absolute on-axis accuracy of 20 µm with a bidirectional repeatability of ±2 µm. The remote control of each of these motors is done with their respective manufacturer software. For the Thorlabs motor this is the APT software. For the horizontal motor, the speed, the start and the end position of the printing process are set. The Newport CONEX-CC motor is delivered with a software for remote control as well. This is used for setting a minimum end of run, i.e. the minimum print head position, to ensure that the print head lips can not accidentally crash into the substrate holder,

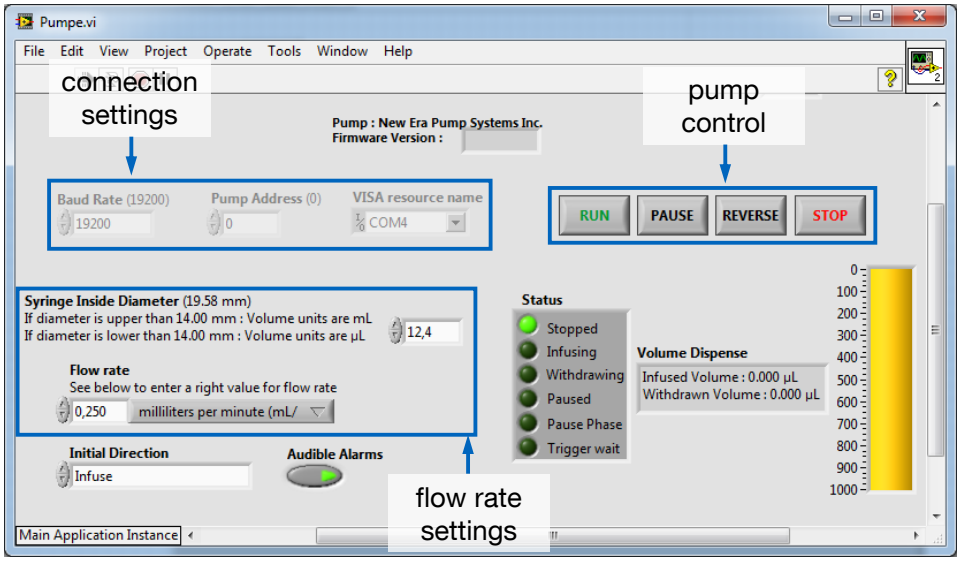

Figure 5.8: Graphical user interface of the LabView program to remotely control the pump.

which would lead to scratches and thus malfunctions of the print head. Furthermore, the height of the print head is set accurately and reproducible to have the same distance to the substrate during the complete experiment.

For feeding the solution into the print head, the Aladdin Syringe Pump AL-1000 purchased from World Precision Instruments is used. Its dispensing accuracy is ±1 % and a wide range of flow rates can be covered by using different syringe diameters. A LabView user interface allows for remotely controlling the syringe pump (figure 5.8). With the pump control software, the flow rate is set, which transfers with the given syringe diameter to a certain feed rate. Using the software, the infusing process is started and towards the end of the printing process, the pump is set to withdraw a certain volume.

A detailed experiment with the basic printer setup and the influence of the sample stage temperature on the morphological evolution of organic thin films can be found in chapter 6.

5.2 Electric field implementation

The printer in the basic version already opens a variety of parameters to control, that possibly influence the inner film morphology. For further manipulations of the structure, an additional parameter is implemented. The printer setup is therefore modified, to implement an electric field while printing. Using this modification the basic principles for an electrophoretic printing process can be studied. Figure 5.9 shows the modified setup as a photograph and a schematic CAD drawing.

In figure 5.9a, the complete setup including the syringe pump is shown. The voltage for the electric field is provided by a power supply, which is set with the desired voltage

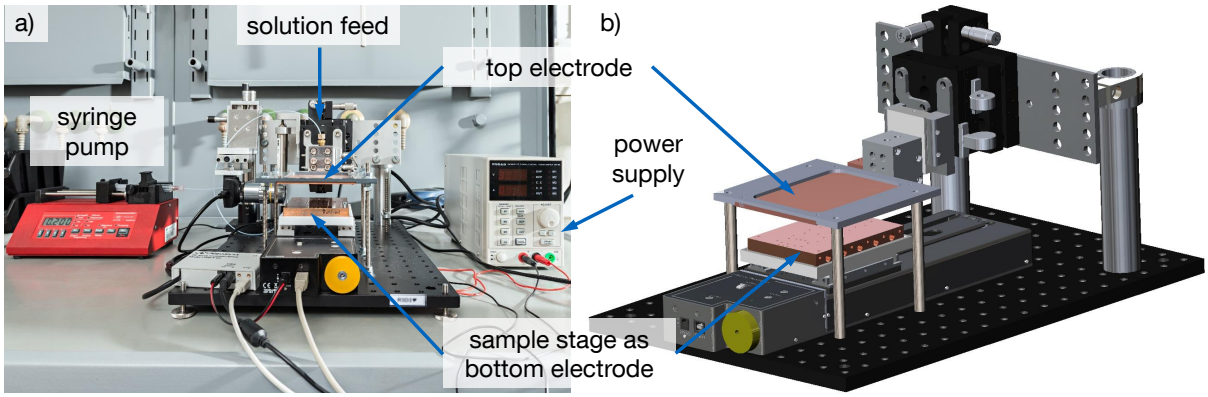

Figure 5.9: a) Photograph of the modified printer setup including an electric field application. (Photo: Ulrich Benz) b) 3d CAD model of the respective setup including the top electrode.

for the field and which limits the current that is allowed to flow. The copper plate of the sample stage serves as bottom electrode. It is directly connected to the power supply. The conductive top part of a substrate (indium doped tin oxide, ITO) can be contacted using conductive screws that are fixed in the copper sample stage. The top electrode is fixed on a non-conductive holder. This top part is mounted on four piles that are adjustable in height via threads. With this adjustment the electric field strength can be varied at constant voltage by changing the distance between top and bottom electrode. It is possible to contact the print head with the top electrode to further increase the electric field during printing. By doing so, the distance of the electrodes is only as big as the substrate thickness plus the gap clearance. If the ITO of the substrate is connected as well, a current flow during printing is possible.

A 3d drawing of the printer setup (figure 5.9b) clarifies the implementation of the electrodes. The mounting of the top electrode is shown in this figure.

A detailed experiment with the modified printer and the ability to apply electric field during printing to influence the structure of organic thin films is given in chapter 7.

5.3 Atmospheric control chamber

The evaporation process of the solvent while solidification of the thin organic film has an enormous impact on the structure formation. [142] As a consequence, the ability to manipulate and even control the atmosphere surrounding the drying film is highly desirable. With further modifications of the printer setup it is important, that the initially mentioned requirements (section 5.1) are fulfilled, especially concerning the weight and the ability to perform *in situ* investigations. This section describes the construction, test and verification of a chamber to control the printing atmosphere.

5.3.1 Construction

The chamber needs to be able to handle chemically aggressive atmospheres and is therefore generally made of aluminum for its ability to resist organic solvents with a relatively low specific weight and easy processability. An overview of the chamber is shown in figure 5.10. The size of the chamber is as small as possible to minimize the influence of the residual atmosphere. The outer dimensions are around 13 cm x 30 cm at a height of 8 cm. Only the scattering window exhibits a slight extension to 10 cm height in order to reach a sufficiently large scattering angle during the *in situ* experiments. The length of the chamber is determined by the length of the sample stage plus the travel range of the linear motor (150 mm). To keep the low weight limits, all the side plates exhibit milled

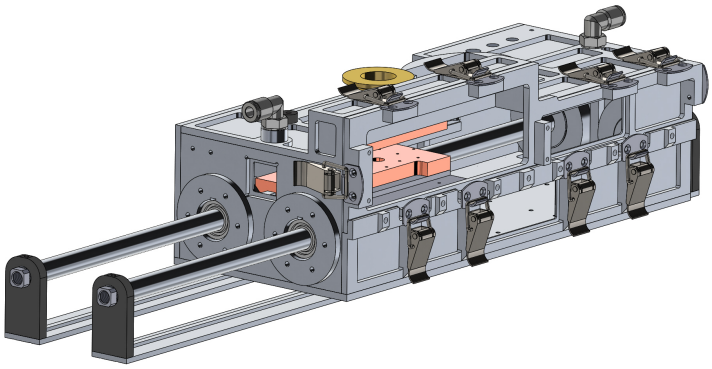

Figure 5.10: Overview of the atmospheric control chamber which can be implemented in the printer described previously. The chamber is made of aluminum plates, which exhibit milled pockets for weight reduction.

pockets. The stability of the chamber is guaranteed by the webs. They also offer the possibility for welding together all the sides for a high tightness and for drilling holes and threads. The linear movement of the sample stage underneath the print head is achieved by two hollow pistons that are fixed to rails mounted on the linear motor. A removable cover that allows for the exchange of samples is sealed with an area seal and fixed with snap locks during operation to ensure the tightness.

Details of the single parts of the chamber and its implementation in the printer are shown in the exploded view of the chamber in figure 5.11a. A challenge in constructing the chamber is the tightness of the moving parts. The pistons are therefore sealed with

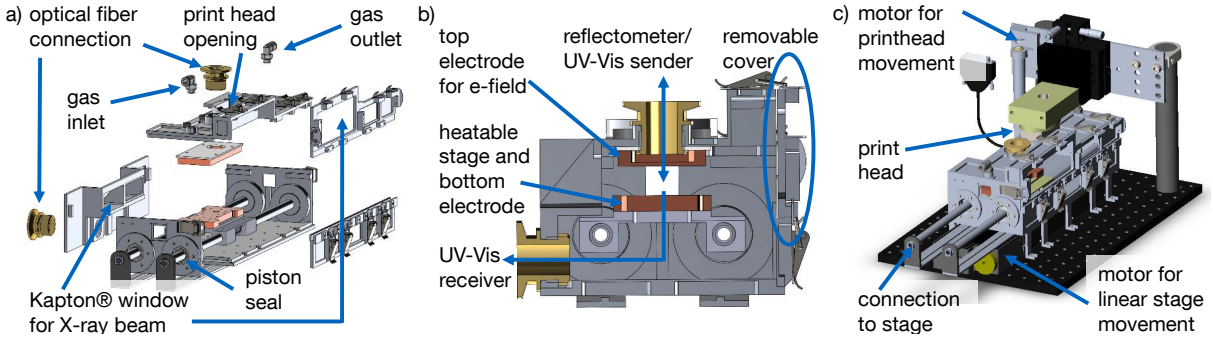

Figure 5.11: Schematic drawings of the atmosphere control chamber and the assembled slot-die coater. a) Exploded view of the chamber showing the inner setup of the chamber. The lid contains a gas in- and outlet as well as the opening for the print head and an optical fiber connection. On the left and right side, Kapton® windows offer the possibility for X-rays to enter and exit the chamber with minimum scattering. The sample stage is mounted on pistons that are sealed at the chamber entrance. b) Sectional front view of the chamber. The UV-Vis connection is depicted as well as the sample stage and the top electrode. The right side consists of a cover that is removable for sample exchange. It features a sealing as well as quick connections for tightening. c) 3d CAD model of the assembled complete slot-die printer. Reproduced from [144], with the permission of AIP Publishing.

solvent resistant seals made of Zurcon® Z20 purchased from Trelleborg Sealing Solutions. The material is resistant against many organic solvents and therefore suitable to be implemented as piston sealing. The construction with the motor being outside the chamber and transferring the linear movement to the inner part of the chamber via the pistons prevents the motor or electronic parts from being exposed to the solvent atmosphere.

The desired atmosphere is obtained by mixing a saturated with a dry gas flow. Therefore, the gas tubing coming from a neat gas supply is split into two paths. Each of the paths contains a mass flow meter, which allows to regulate the gas volume through each path. One of the split tubes passes then a washing bottle, which contains the target solvent for the respective atmosphere. The path passing the washing bottle is saturated afterwards and merged with the other path containing dry gas. By adjusting the volumes in each path, a mixture of saturated and dry gas can be set. The merged path is directed into the chamber via the gas inlet, which is a nozzle purchased from Lechler GmbH (flat fan nozzle 686.408.16.CA.00.0). It provides a defined gas flow above the sample.

The ability to perform *in situ* X-ray measurements while printing is one requirement to be fulfilled. Therefore, on either side of the chamber, 25.4 µm thick Kapton® foils from DuPont™ are inserted. This material is frequently used as window for X-ray experimental setups as it only scatters weakly. [151, 152] The height extension at the exit window to 10 cm is designed to achieve scattering signals up to 40°, which allows to observe the main characteristic peaks of most polymers of interest. The other windows, that are not functional for the X-ray scattering experiments are covered with glass. They serve as access of illumination and video cameras to follow the printing process. Further features of the chamber are the KF flanges mounted on top of the chamber and on its left side. With these flanges, optical fibers can be attached which are connected to a spectrometer either for reflectometry or UV-Vis transmission measurements. Thus the film thickness or the absorption properties during solidification can be probed, respectively.

A closer look to the sectional front view of the chamber is shown in figure 5.11b. It highlights the path for optical characterization of the printed films. The optical fiber connected to the top KF flange is guided through a PTFE buffer and a copper plate. This plate is used as the top electrode for application of an electric field and the PTFE buffer ensures the screening of the chamber from the applied voltage. The sample stage has a hole to allow an optical path for the characterization. A 90°-bended fiber mounted in the KF flange at the side of the chamber collects the transmitted light and guides it to a spectrometer. The copper sample stage acts as bottom electrode for the electric field. It is mounted on a holder made of poly(ether ether ketone) (PEEK). This material offers a high solvent resistivity, a melting point at (389 ± 4) °C (glass transition temperature T_g = 140-155 °C) and a low coefficient of thermal expansion of $58 \cdot 10^{-6}$ K^{-1}. [153–155] The copper

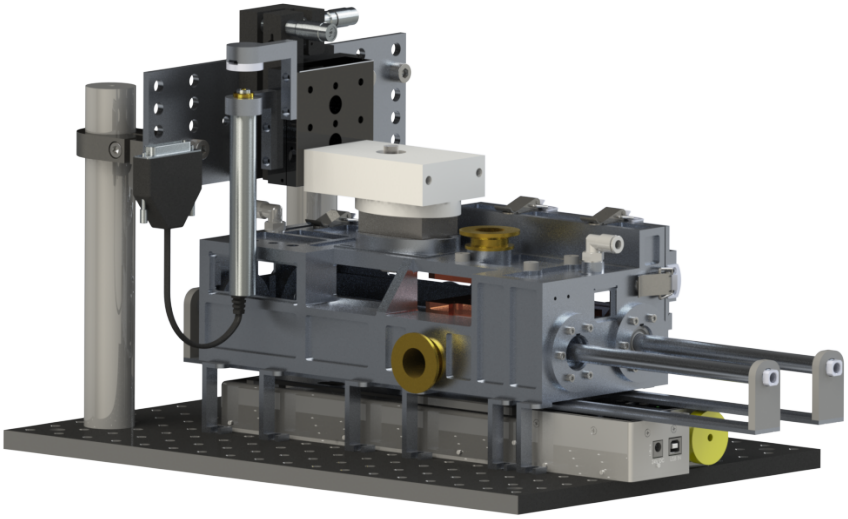

Figure 5.12: Drawing of the assembled slot-die coater including the atmospheric control chamber, the vertical and horizontal motors and the print head.

stage can be heated up to 150 °C with high-performance resistors, that are connected to electrical plugs, mounted into the hollow pistons and sealed by casting epoxy. The PEEK holder prevents the heat to diffuse to the pistons, which might generate a malfunction.

A 3d drawing of the complete printer setup including print head and holder is depicted in figure 5.11c. The chamber is mounted on stages above the horizontally moving motor. The rails connected to the pistons are fixed on the motor stage. The print head is inserted into the chamber through an opening at the top of the chamber. It is fixed and sealed using area seals in a holder made of PEEK which reduces heat conduction to the mounting. The print head holder and the top of the chamber are sealed using bellows to seal the chamber against the atmosphere. With that, a vertical movement of the print head and therefore an accurate setting of the gap clearance is possible while no contamination from the surrounding atmosphere is entering the chamber.

An overview over the completely assembled printer is given in figure 5.12, in which all parts, including the motors are shown. In order to produce the gas mixture that is lead into the chamber, the stream of neat gas is split up and one path passes a washing bottle as described previously. In order to accurately set the volume of the respective streams, mass flow meters purchased from Vögtlin Instruments AG (red-y smart controller, GSC-B9SA-BB23) are used. A LabView program controls the mass flow meters (figure 5.13).

Settings for the flow rate (in ml min^{-1}) need to be given for the complete volume flow of nitrogen. By setting the desired saturation of the gas, the respective percentage of the volume is directed through the flow meter connected to the washing bottle. Check valves ensure the protection of the flow meters against the saturated gas and thus the correct direction of the flow.

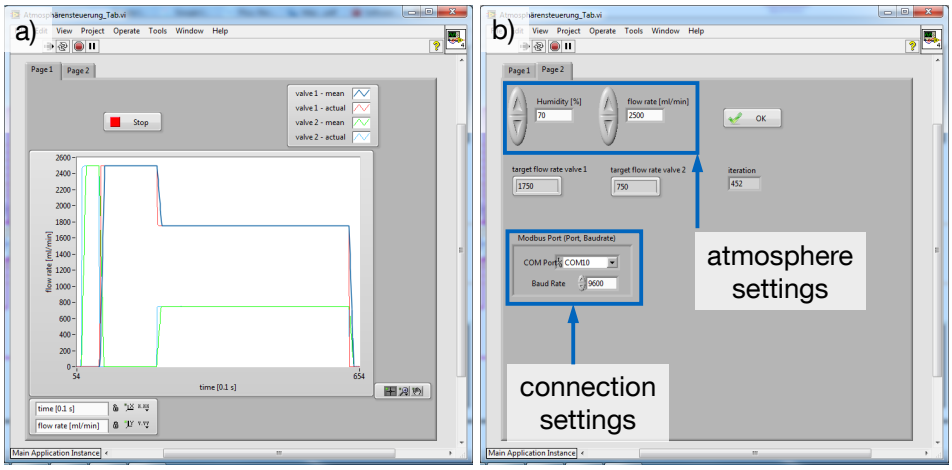

Figure 5.13: LabView user interface for the remote control of the flow meters. The first tab (a) shows the actual and the mean flow through both of the flow meters. The settings are defined in the second tab (b).

5.3.2 Concept testing

The functionality of the chamber and the fulfillment of all requirements is tested in two experiments. The ability to measure UV-Vis spectra is tested outside a beamline in the laboratory. The suitability to perform *in situ* measurements is tested by implementing the printer into the beamline 7.3.3 of the Advanced Light Source (ALS) at the Lawrence Berkeley National Laboratory.

The test of an optical characterization during solidification is performed by printing a polymer:fullerene film on a glass substrate. As polymer, poly(3-hexyl-thiophene) (P3HT) and as fullerene [6,6]-phenyl-C_{61}butyric acid methyl ester (PCBM) is used. The gap clearance is 300 µm and the printing speed 10 mm s^{-1}. An exemplary record of the *in situ* UV-Vis spectra for a sample printed under a dry gas flow is shown in figure 5.14a.

The frame rate of the spectra are 200 ms^{-1}. At a wavelength of around 605 nm, the crystallization process of the polymer can be followed by the evolving shoulder. After the initial evaporation of the solvent, the polymer crystallizes within 10 to 20 seconds, seen by the evolving shoulder. This rapid crystallization is known to be due to a critical concentration of the polymer in the solution, once most of the solvent has evaporated. [142] Using a saturated gas stream during the printing process, the onset of crystallization can be delayed. In figure 5.14b, the normalized intensity of the shoulder at 605 nm for different atmospheres is depicted. It shows, that for printing under a purely saturated gas stream, the growth of the crystallization absorption shoulder is delayed by around 20 s from 50 s to 70 s. This onset can be further delayed, by letting the atmosphere inside the

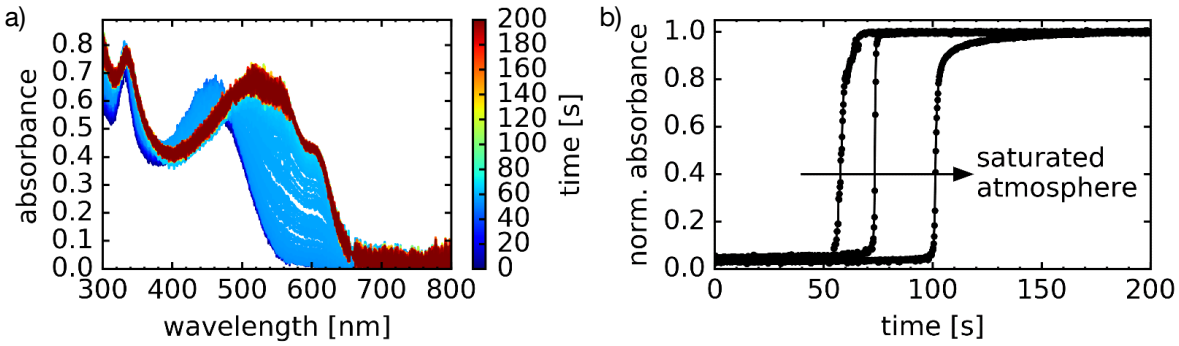

Figure 5.14: a) Exemplary *in situ* absorbance data of a P3HT:PCBM sample printed under dry gas flow with a frame rate of 0.2 s^{-1}. At around 605 nm, the shoulder indicating crystallization of the polymer during the film solidification can be followed. b) The intensity of the crystallization shoulder at 605 nm for samples printed under a dry flow of nitrogen, a saturated flow and a saturated flow with a saturation time of 10 min before printing. Each of them leads to a further delay of the intensity increase. Reproduced from [144], with the permission of AIP Publishing.

chamber saturate. If the saturated gas flow is switched on 10 min prior to printing, the crystallization is delayed to nearly doubled the time of the film printed under a dry gas stream.

In a second experiment, the atmospheric chamber and its ability to influence the drying kinetics on a nano-morphological scale, is tested. Therefore, *in situ* GISAXS measurements are conducted. The complete setup is implemented into beamline 7.3.3 of the Advanced Light Source (ALS) at Lawrence Berkeley National Laboratory. Figure 5.15 shows a photograph of the connected setup within the beamline. The incoming X-ray beam impinges the sample from the right side of the chamber and scattered beam exits the right Kapton® window into the flight tube (conus in figure 5.15) to the detector. At

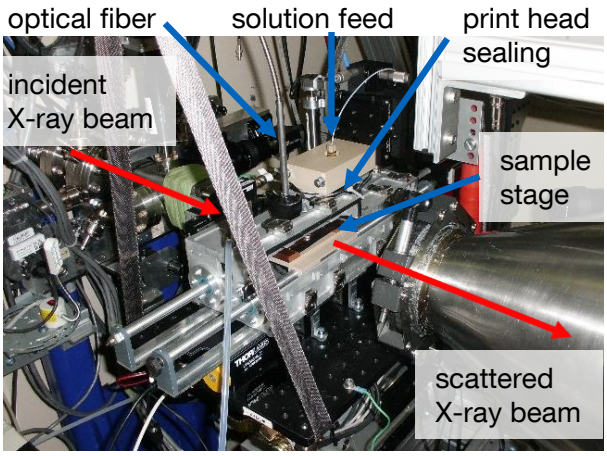

Figure 5.15: Photograph of the printer setup implemented in the endstation of the synchrotron beamline 7.3.3 of the Advanced Light Source. The red arrows pointing to the right show the path of the X-ray beam before and after the scattering event. The detector is behind the flight tube on the right (not shown in this image)

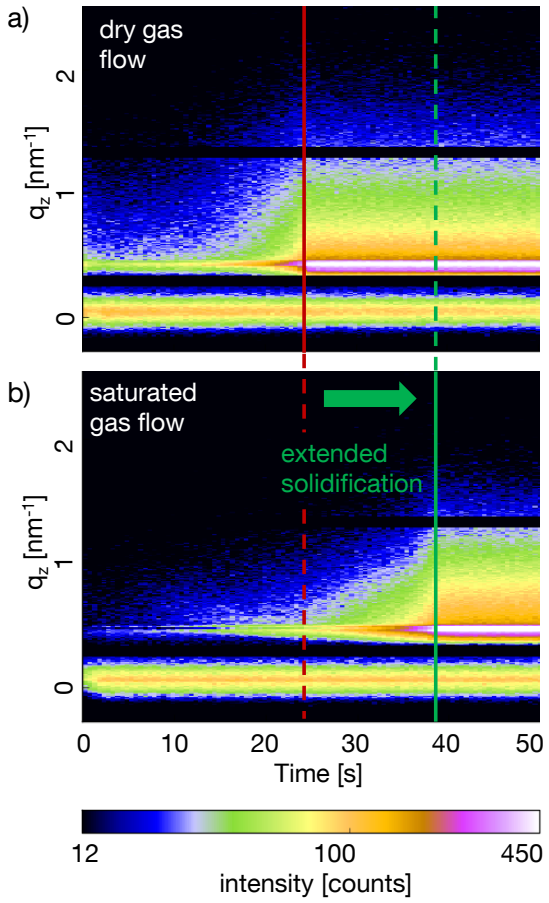

Figure 5.16: Vertically integrated intensity profiles of GISAXS 2D data versus time with differently saturated gas streams above the sample. a) The vertical cuts of a scattering experiment of a P3HT:PCBM film printed under a flow of dry helium versus time. The final structure seen in the 2D color plot is reached after around 24 s. b) Using a saturated gas flow, the solidification process is extended by around 15 s. The red line roughly indicates the final film structure for the film printed under a dry gas stream, while the green line roughly indicates the end of the structure formation of the film printed under a saturated gas flow. Reproduced from [144], with the permission of AIP Publishing.

the top KF flange, an optical fiber is connected for reflectometry measurements. The glass windows in the chamber allow for monitoring the meniscus formation process via cameras, so that the printing process can be started remotely.

The samples are printed as before under differently saturated gas streams. Helium is used as gas instead of nitrogen to lower scattering from the atmosphere. The sample system is P3HT:PCBM, which is coated on a silicon substrate under the same conditions as the previously described UV-Vis spectra. The incident angle for the experiment is 0.35° and the sample-to-detector distance is around 1.8 m, which results in an observable q-range of 0.08 - 2.50 nm^{-1}. This q-range corresponds to a real space distance of 2.5 - 78.5 nm. Figure 5.16 shows the resulting vertical line cuts of the time resolved measurements for printing under a dry gas stream (figure 5.16a) and a saturated gas stream (figure 5.16b). The vertical line cuts contain information about the vertical size distributions in the sample and are performed next to the rod beam stop.

A clear delay in the solidification is observable when comparing the vertical scattering development with time. A flow of saturated gas slows down the complete solidification process by approximately 15 s. Printing under a dry gas flow shows a rapidly increasing scattering signal, while printing under a saturated gas stream initially shows a decelerated

process. After a rapid increase in the vertical scattering intensity, the sample already reveals its final structure. A slower drying of the printed films is expected to positively influence the device performance if implemented in organic solar cells. [137, 142]

Comparing the results of the UV-Vis measurements with the scattering experiments, it is evident, that the chamber is able to influence the atmosphere as intended. The structure evolution can, in both cases, be delayed by nearly 20 s just by using a saturated gas stream over the sample while printing. A detailed experiment and the impact of a saturated atmosphere on the film structure can be found in chapter 8.

5.4 Summary

An experimental setup for printing organic solar cells and simultaneously characterizing the films *in situ* while drying is built. Using this setup, numerous parameters while printing can be controlled. The basic setup already offers the possibility to vary the sample stage temperature which influences the drying speed of the printed films. This can be used to understand the impact of the drying dynamics on the structure formation.

A modification of the setup yields to the possibility to apply an external electric field while printing. By varying either the applied voltage or the distance between the top and the bottom electrode, a wide range of electric fields can be applied. The possibility to connect the print head to the top electrode and the conducting ITO to the bottom electrode furthermore allows a current flow while processing. This feature enables to influence the structure formation of thin organic films.

In order to control the solidification process an atmospheric chamber for the slot-die coater is designed and built, that can be implemented into a synchrotron beamline. An *in situ* characterization of the nano-structure evolution is possible. With the setup, the fabrication of solar cells can be transferred into a synchrotron beamline offering a detailed analysis of the fundamentals of structure formation while controlling the environment to approach optimized film production conditions. It is furthermore possible to characterize the optical properties of the drying films *in situ* by either reflection or transmission in a wide range of wavelengths. The setup is tested and for both, optical and scattering experiments, a delay in solidification of a sample P3HT:PCBM film is observed upon the variation from a dry to a saturated gas stream while printing.

The proposed sophisticated experimental setup enables to tailor the nano-structure of freshly printed thin organic films while tracking its formation on a nano-scale. Using this setup, the self-assembly process in thin films can be influenced by tuning several macroscopic thermodynamic parameters (temperature, humidity, printing speed, flow rate) which enable the production of functional films with enhanced properties.

6 Structure formation dynamics in printed films

The morphology of polymer:fullerene bulk heterojunction (BHJ) thin films has an enormous impact on the organic solar cell devices and is thus of significant interest. [34,36,156] As described in chapter 2.2, a BHJ generally consists of a donor and an acceptor. Typical and widely studied materials are poly(3-hexyl-thiophene) (P3HT) as donor polymer and [6,6]-phenyl-C_{61}butyric acid methyl ester (PCBM) as acceptor fullerene. [21] The materials are blended together in solution and while the solvent evaporates, the materials may phase separate forming an interpenetrating network, the BHJ. A key for improving organic solar cells is to control the nanomorphology. Several approaches aim to tune the morphology after processing, for example thermal or solvent annealing. [157–160] The thermodynamics involved during evaporation of the solvent play an important role in generating the BHJ. Thus, the final film structure and the energetic ordering might be influenced by the choice of solvent or solvent additives. [38, 83, 161–164] The influence of a processing additive on the polymer's crystallization was investigated using X-ray scattering of slot-die coated and roll-to-roll processed films. [136, 165] All the information so far, however, are gained out of static measurements. Accessing the formation process of such an organic thin film is still an open problem which to solve is highly desirable. A particular interest in the dynamics is upon moving from lab-scale processing methods towards industrially scalable processes like spray coating or printing methods. A lot of work deals with the dynamics on lab scale processes which lead to a significant knowledge. Still, transferring to large-scale is difficult as the drying kinetics differ for latter ones. [13, 16, 166] Each and every coating process differs possibly even fundamentally with respect to the solvent evaporation rate and thus might deviate in the solution driven self-assembling of the active layer. [167–169] For solution cast and blade coated as well as for spin coated films the development of the morphology upon solidification has been probed. [37, 39, 40, 140, 166, 170, 171] It was observed, that initially edge-on oriented crystals form, followed by less oriented ones which lead to the conclusion that the crystallization starts at the interfaces. [37,39,172] Slot-die coating exhibits a huge potential for organic electronics as it is already widely established in the printing industry. Time-resolved measurements of the structure evolution in slot-

die coated P3HT:PCBM active layers are so far missing. [173] However, with respect to tailoring the film assembling process, a deeper knowledge about the structure formation process is of utmost importance and thus the next step in this thesis (figure 6.1).

Figure 6.1: This chapter deals with the formation of the nano-structure in order to understand the necessary processes.

This chapter is based on the publication "Following the Morphology Formation In Situ in Printed Active Layers for Organic Solar Cells", Advanced Energy Materials 2016, 6 (1) 1501580. [142] It presents *in situ* scattering measurements of the drying dynamics of slot-die coated thin organic films. The experiment is an ongoing collaboration with the group of T. P. Russell at the Department of Polymer Science and Engineering at University of Massachusetts Amherst and Material Science Division of the Lawrence Berkeley National Laboratory (LBNL) as well as the group of Dr. A. Hexemer at the Advanced Light Source (ALS) of the LBNL. They serve to demonstrate the capabilities of the printer with a model system and serve asa basis for further examinations. Two different sample preparation routes are used to study the film formation process. Details about the experimental procedure are given in section 6.1. It describes the used setup as well as the sample preparation routes and the specific scattering settings. The following section 6.2 presents the results of the experiments. First, *in situ* GIWAXS experiments reveal information of the polymer crystallization process. Tracking the thickness gives further insight into the possible concentrations and helps to classify the different observations in the crystallization and phase separation process. To understand the phase separation process, the fullerene aggregation is monitored using GISAXS. The results of these experiments are presented subsequently. The following section shows the influence of the different preparation routes on the solar cell performance. Section 6.2.4 combines the experiments and concludes with the proposition of a model of the structure evolution as an outcome of the experiments.

6.1 Experimental details

Slot-die coating offers the possibility of depositing a thin film on a substrate while controlling several parameters like amount of deposited material or drying temperature.

Real-time monitoring of the drying kinetics is challenging and state of the art imaging techniques like atomic force microscopy (AFM) or transmission electron microscopy (TEM) face severe limitations with respect to the time resolution. For this study we therefore made use of indirect imaging via grazing incidence X-ray scattering, described in sections 2.4 and 3.2.6. For the experiments presented in this chapter, a custom made slot-die coater is used. The printer is the first generation of the coater described in section 5.1 and details can be found there. It was recently presented by Feng Liu et al. who successfully implemented the printer at the synchrotron beamline at the Advanced Light Source (ALS) of the Lawrence Berkeley National Laboratory (LBNL). They were able to map the morphology formation process of the copolymer of diketopyrrolopyrrole and quaterthiophene (DPPBT) and [6,6]-phenyl C71-butyric acid methyl ester ($PC_{71}BM$). [143] The setup was also used to follow the structure formation of poly(3,4-ethylenedioxythiophene):poly(styrenesulfonate) (PEDOT:PSS) films, which showed the impact of ethylene glycol (EG) treatment on the molecular arrangement of PEDOT crystals. [145] Figure 6.2 shows a picture of the used printer setup with the main components, the print head and the heatable sample stage.

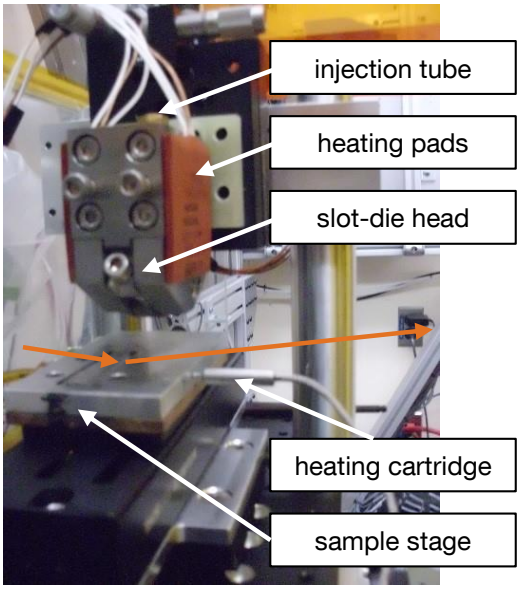

Figure 6.2: Photograph of the slot-die coater used for the experiments in this chapter. The substrate is positioned on the heatable sample stage which is driven past the slot-die head. The heating cartridge offers the possibility to heat up and keep the temperature of the sample stage during the complete experiment. The heating pads for the print head were not used for this experiment. The solution is fed into the printing head via the injection tube. The complete setup is placed into a helium box for reduction of the air scattering during the experiments. The orange arrow shows the rough direction of the X-ray beam.

Materials and sample preparation: The solution for the active layer is produced as described in chapter 4. Acidic cleaned silicon wafer spin coated with PEDOT:PSS serve as substrates. The wafer were cut in approximately 100 mm long and 20 mm broad stripes before placing on the printer's sample stage. The substrate is fixed on the stage with a vacuum chuck. For the experiments, the prepared solution is then fed into the slot-die head using a syringe pump with a pump rate of 0.2 $ml\,min^{-1}$. The distance of the slot-

die head to the substrate is set to around 100 µm and the printing speed to 10 mm s^{-1}. These settings result in a film thickness of the P3HT:PCBM films of around 100 nm. In order to keep the high time resolution for the scattering experiments for GISAXS, the film thickness is increased to around 300 nm by adjusting the printing parameters. As seen by Parnell et al., a thicker sample shows similar effects to those found in slower dried films. [174] This justifies the the change in parameters for the experiments.

To correlate the structure to the performance, solar cells are fabricated on a cleaned ITO substrate coated with a 30 nm thick PEDOT:PSS layer (section 4.2). The active layer is printed with the two preparation routes at room temperature and 40 °C substrate temperature, yielding a thickness of around 100 nm. Aluminum contacts with a size between 0.23 cm^2 and 0.65 cm^2 are evaporated and the devices are sealed using epoxy glue and a glass slide. The data are averaged over six to nine pixels.

In situ scattering experiments: The *in situ* scattering experiments are performed at the beamline 7.3.3 at the Advanced Light Source (ALS). [117] The wavelength for this experiments is $\lambda = 1.24$ Å which corresponds to an energy of 10 keV. The signal is detected by a Pilatus 1M detector with a frame rate of 1 s^{-1}. This frame rate includes data recording of 0.97 s and a readout of 0.03 s. In order to suppress background scattering from air, the printer is placed inside a helium box. Directly after the coating process, the incident X-ray beam impinges the sample continuously at a fixed distance from the print head and follows the drying process. Recording the final film for more than 200 s at the same position ensures that no beam damage occurs which would influence the organic film and thus the results of the experiment.

For *GIWAXS*, the incident angle is set to 0.18° and the sample to detector distance is 294 mm. The data reduction of the 2D-scattering patterns is performed using GIXS-GUI 1.6.1 from the Argonne National Laboratory which can be used to perform all the corrections necessary for a correct reduction as described in section 2.4. [94–96]

For *GISAXS*, the sample to detector distance is set to 356 cm and the incident angle is 0.3°. The data reduction was performed using the software DPDAK from the Deutsches Elektronen-Synchrotron (DESY) in Hamburg. [120] The horizontal cuts are performed at the PCBM Yoneda position. [87] In order to obtain high statistics, the cuts are performed over 19 pixels in height, all checked for not deviating concerning their scattering features. The data are then modeled in the framework of the distorted wave Born approximation (DWBA) and the local monodisperse approximation (LMA) based on contributions from three substructures each described by a certain shape of a form factor (average structure sizes) and a structure factor (average center-to-center distance) according to a 1d paracrystal as proposed by Hosemann et al. [108] More details about the model function can be found in section 2.4.

6.2 In situ characterization

Two preparation routes are chosen for the *in situ* experiments. Films prepared with route 1 are printed with the sample holder kept at room temperature (RT) while the samples prepared with route 2 are printed with the substrate holder at 40°C. Two different experiments are performed, GIWAXS, to follow the polymer crystallization, and GISAXS to follow the phase separation and picture the process at a larger size scale. In the following subsections, both experiments are presented separately from each other and for each preparation route. After presenting the results of the solar cells prepared using both preparation routes, the results are combined and discussed in a broader context which will then lead to a model of the structure evolution process.

6.2.1 Polymer crystallization process

The 2D-GIWAXS data collected during the experiments are shown in figure 6.3 for the sample prepared via route 1, at room temperature (RT). The raw scattering patterns are converted to present the q-range, which gives rise to the missing wedge at low q_r. The black bars in between the scattering patterns are due to the detector gaps, which can not be avoided due to construction constraints of the detector.

Directly after the coating process, there is still an excess of the solvent, chlorobenzene (CBZ). The contributions of CBZ on the scattering patterns can be seen in the first pattern at 0 s in figure 6.3. As CBZ shows no preferred orientation with respect to the substrate plane, it occurs as a bright ring, which is due to the average separation distance between the molecules. [143] At the same q-range, scattering from randomly oriented PCBM clusters is expected. [39, 172, 175] With time, the scattering signal of the the CBZ is decreasing in intensity due to the evaporation and hence the reduced amount of scattering centers in the film. As time proceeds, the solvent scattering signal further decreases until it is replaced by the scattering of the aforementioned PCBM clusters. A highly intense scattering signal mainly in vertical direction can be observed in the lower left corner. This signal results from the GISAXS pattern and is shielded with a beam stop in order to protect the detector from oversaturation. After around 8 s, a scattering contribution directly above the GISAXS signal occurs, which is attributed to the (100) reflection of the first forming P3HT crystals. As time proceeds, the scattering signal of the (100) peak becomes more and more intense. The signal of the (100) peak broadens in azimuthal direction at 21 s, which indicates a higher angular distribution of the P3HT crystals within the film. [30,98] Once the scattering signal of the solvent disappears, higher order peaks of the (100) P3HT peak becomes visible. After 31 s no changes are seen on the 2D scattering patterns any more, indicating that the structure formation process is

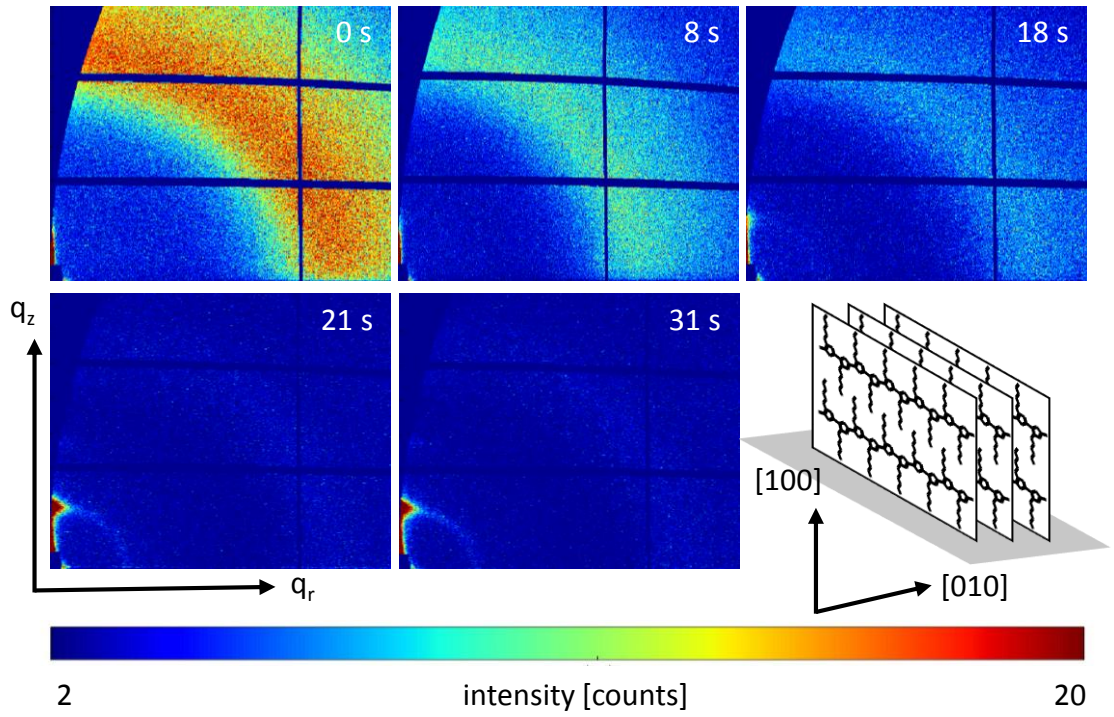

Figure 6.3: Two dimensional GIWAXS patterns of the films coated at room temperature at five distinct stages during the drying process. Initially, the signal mainly consists of a non oriented ring which is attributed to the solvent, chlorobenzene. Later on, a higher intensity occurs in the lower left corner, which broadens in the following to a more ring-like structure. The drying time is mentioned in each of the scattering patterns. The schematics on the lower right shows an edge-on oriented P3HT crystal. The lamellar backbone spacing in [100] and the π-π stacking in [010] direction are indicated.

completed. The intensity of the (100) reflection is mainly in the vertical direction, which means the scattering vector is mainly in the direction perpendicular to the sample surface. This scattering direction of the (100) peak is known from other deposition methods like doctor blading or spin casting. It is due to the edge-on configuration of a polymer crystal and results from the scattering of the ordered backbones of the polymer. [30, 39, 170] The edge-on configuration is quite common in polymers used in organic photovoltaics. The schematics in figure 6.3 depicts exemplary a P3HT crystal in the edge-on configuration, in which the backbones are parallel and the side chains perpendicular to the substrate. The (100) peak resulting from the backbone spacing in the [100] direction is characteristic for the P3HT crystal. It can be seen as an indicator of the polymer's crystallinity and is therefore used later on to quantitatively describe the backbone stacking during the film formation process.

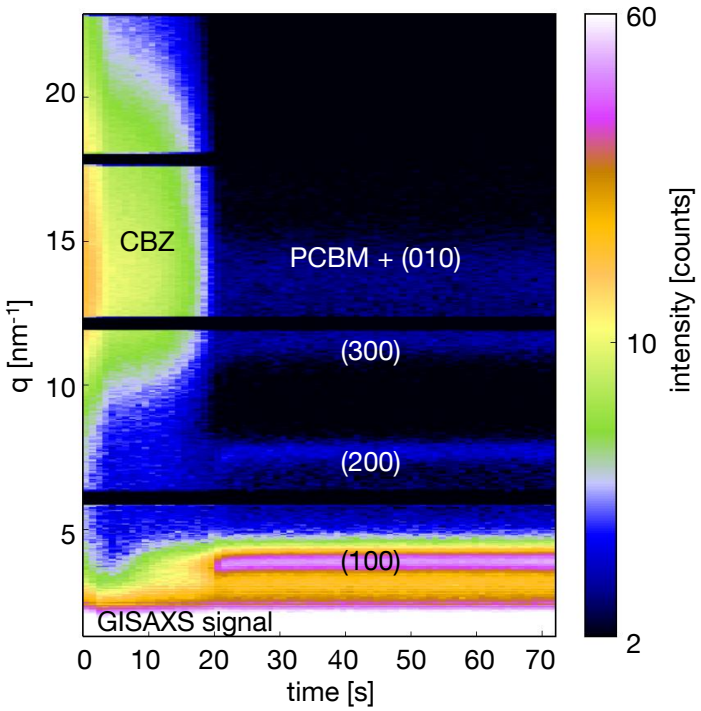

Figure 6.4: Two dimensional colormap of the structure formation of the film printed at room temperature. It shows the development of the scattering signal in vertical direction along the missing wedge with time. The contributions of the main scattering planes of the polymer crystal as well as the PCBM are depicted. The higher orders (200) and (300) can clearly be seen. The colorscale is set for optimally recognizing the GIWAXS signals, which results in the GISAXS signal at low q being oversaturated.

Following the development of the intensity along the missing wedge, at lowest accessible q_r, presents a clearer image of the development of the scattering signals. Figure 6.4 shows a two dimensional colorplot of the vertical scattering intensity against the time.

The initial scattering from the chlorobenzene is again clearly visible, which then vanishes at around 21 s. The contribution of the (100) scattering peak as the main characteristic peak is observed at a q value of roughly 4 nm^{-1}, showing the highest intensity of the GIWAXS pattern, once the solvent is evaporated. In the colorplot, the development and the contributions of the higher order peaks (200) and (300) are seen. The PCBM and the (010) contribution are superimposed and not easily differentiated.

The time development of the integrated intensity profiles in vertical direction along lowest q_r for the sample coated at RT is depicted in figure 6.5 to extract information from the vertically stacked P3HT backbones. Similar to the colorplot in figure 6.4 the figure shows the vertically integrated intensity profiles. The intensity is plotted against the scattering vector q, with the colors showing the time development.

The evolution of the scattering intensities can clearly be followed in a quantitative manner. The (100) peak at $q \approx 3.8$ nm^{-1} is clearly visible and it can be seen, that the scattering of this peak is independent of the scattering intensity resulting from the chlorobenzene. In contrast, the scattering of the higher order peaks (200) and (300) as well as the (010) reflection resulting from the π-πstacking are superimposed by the chlorobenzene scattering signal at $q \approx 13$ nm^{-1}. Similarly, the signal arising from the PCBM crystals at $q \approx 14$ nm^{-1} is superimposed by the CBZ signal.

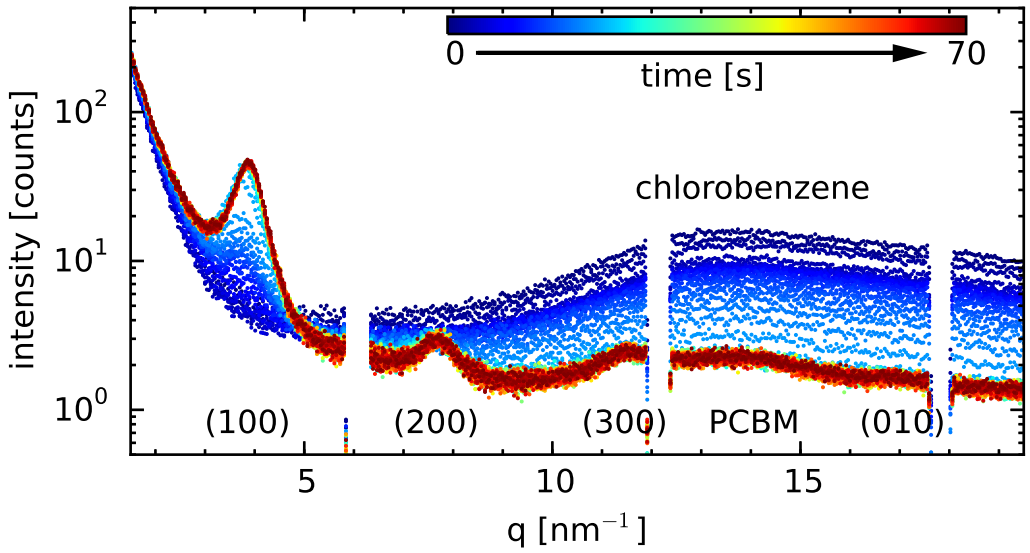

Figure 6.5: Time development of the integrated intensity of the GIWAXS signal in vertical direction along q_z at lowest possible q_r of the sample printed at room temperature. The colorcode indicates the drying time with each curve representing a 1 s measurement. The broad peak at the initial stages (bluish colors) at higher q represents the scattering of the chlorobenzene. The contributions of the polymer crystal are seen at later stages (redish colors). All the scattering contributions are marked with their origin of the polymer crystal planes or PCBM.

An important aspect in terms of crystallographic characterization is the orientation of a polymer crystal. As mentioned, the azimuthal broadening of the (100) peak indicates a higher angular distribution. The development of the crystal orientation is monitored using this azimuthal dependence of the integrated intensity of the (100) scattering peak. Figure 6.6 shows the azimuthally integrated intensities of the (100) peak with time.

Initially, only a low intensity is observed mainly resulting from the outliers of the GISAXS signal. As the P3HT (100) peak intensity increases, the azimuthally integrated intensity profile does as well. Within the first 20 s, the peak is narrow. This is a clear indication of the P3HT crystals being well aligned in edge-on configuration. The initial strong orientation is well known in other drying processes and is referred to as a crystallization at the interfaces, either of the film/substrate or the film/air interface. [172] After 21 s of solvent evaporation, the peak broadens in azimuthal direction. Thus, the crystal orientation shows a higher angular distribution.

In order to quantify the changes, the intensity profiles are fitted with gaussian functions around 0°. Figure 6.7 shows the resulting FWHM of the fits over time. The complete process can be divided into different stages, which will be refined in the analysis of the vertically integrated intensity profile afterwards.

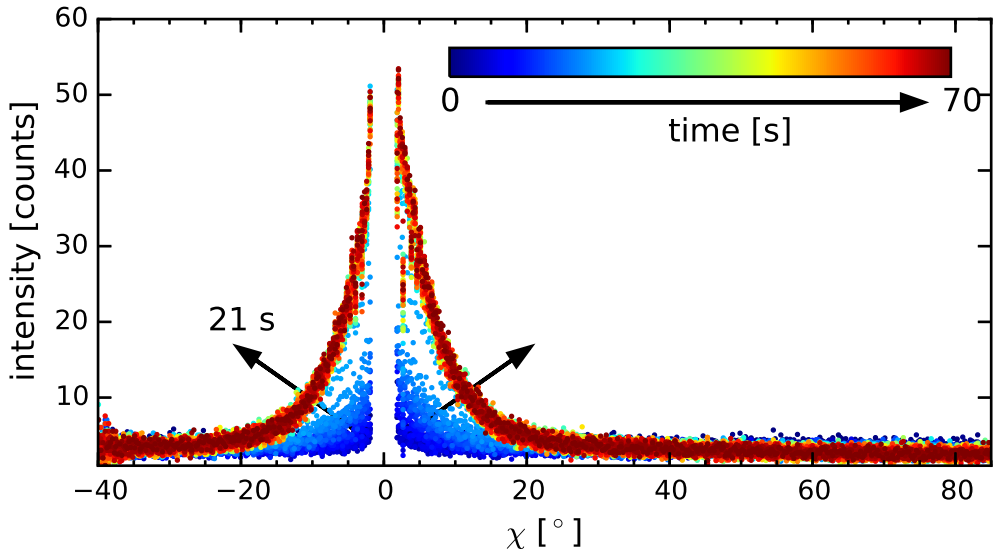

Figure 6.6: Azimuthally integrated scattering intensities of the (100) peak at q = 3.8 nm^{-1} of the sample coated at room temperature with time. The peak starts to broaden after 21 s indicating a higher angular distribution of the polymer crystals. The missing data points around 0° are due to the non accessible q range (missing wedge).

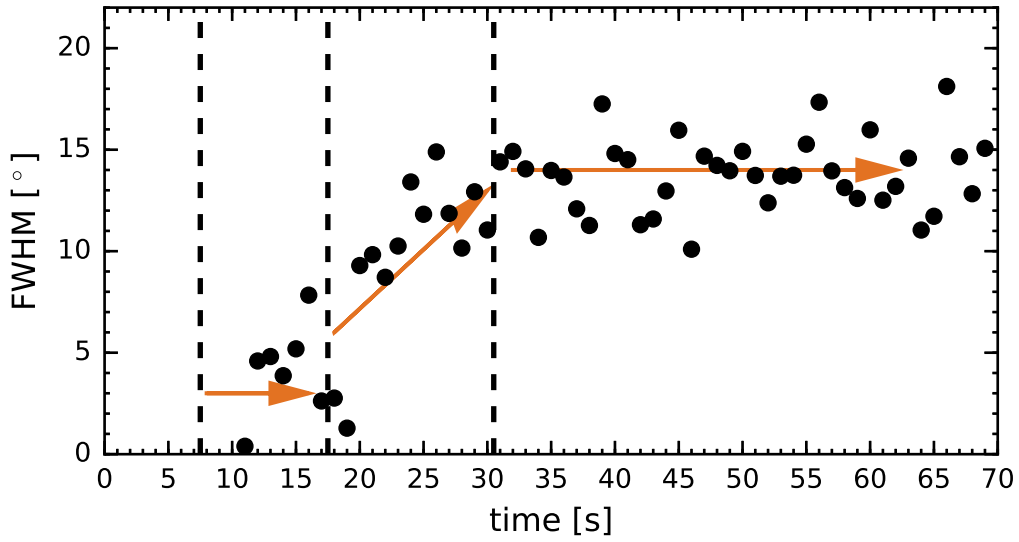

Figure 6.7: FWHM of gaussian functions fitted to the azimuthally integrated GIWAXS cuts of the (100) crystal plane around 0°. The orange arrows are guide to the eyes to see the rough development of the FWHM. Different phases are identified in the development of the FWHM and marked by the vertical dashed lines.

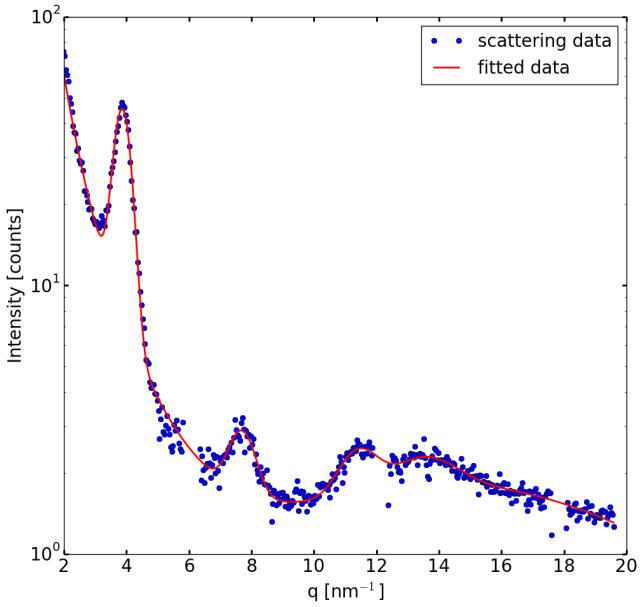

Figure 6.8: Exemplary complete fit of the GIWAXS scattering data at 60 s of the sample prepared at room temperature. The peaks can be attributed to the (100), (200), (300) lattice planes of the polymer backbones, the (010) plane of the π-π stacking as well as the PCBM scattering signal. The missing scattering points at q ≈ 6 nm^{-1}, 12 nm^{-1} and 18 nm^{-1} are due to the detector gaps.

In the beginning, no peaks could be fitted as the intensity is too low. No crystals have formed yet during this initial phase. The first results are obtained for the curve slightly later than 8 s but the FWHM is still very volatile in width and hardly increases in the next stage. A strong increase is observed starting shortly before 21 s, when the FWHM slightly increases to roughly 14°, at which it then stays constant in the final phase, yet with strong deviations. The classification of the stages will be refined and become more clear in the following.

Subtracting the q^{-4} dependent intensity decrease in the vertically integrated scattering profiles, the contributions of the peaks can be followed by fitting the curve with a Gaussian for each peak using a Levenberg–Marquardt algorithm. Figure 6.8 shows an exemplary fit of the scattering curve at 60 s. All the peaks of the polymer crystal can be depicted and thus show the quality of the fitting procedure. By fitting all the data using the fitted parameter of each frame as input parameters for the subsequent fit, the scattering development is tracked.

As the (100) peak is clearly distinguishable from the other scattering signals and as it contains the necessary information of the vertical crystal packing, the development of this particular scattering feature is followed. Using the peak position, which is related to the real space backbone spacing d by d = 2πq^{-1}, the amplitude indicating the amount of formed crystals and the full width at half maximum (FWHM) correlated to the crystal size via the Scherrer equation 2.34, an image of the crystal formation will be produced. The FWHM of the fitted Gaussian is related to the persistence length of the lattice. This length is usually converted to the crystal size using the Scherrer equation 2.34, which is

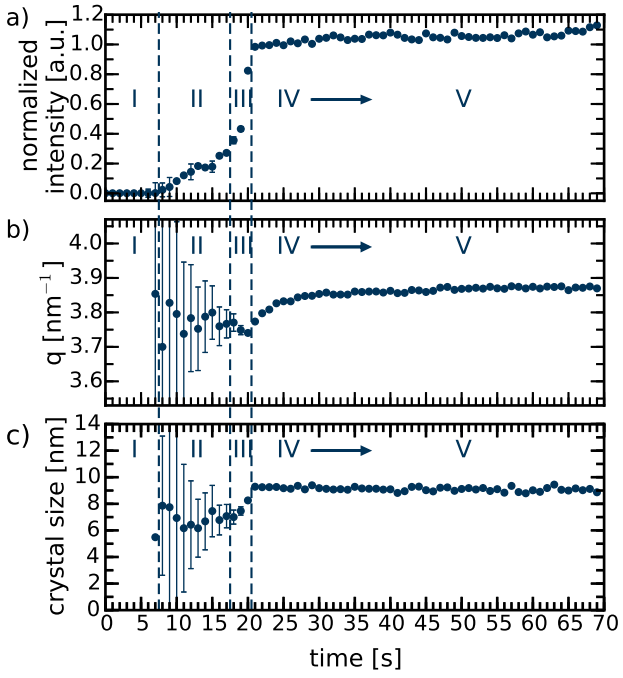

Figure 6.9: Extracted parameters from Gaussian fits of the (100) P3HT peak of the GIWAXS data with time for the sample printed at room temperature. a) The peak intensity, normalized to the final film's intensity. The intensity can be seen as an indication of the amount of crystals present in the film. b) The peak position in nm^{-1} is inversely proportional to the backbone spacing of the crystal. c) The crystal size is obtained via the FWHM of the fit and calculated using the Scherrer equation. Five stages of the crystal development are identified and denoted as I to V and marked with dashed lines.

strictly true only for a perfectly ordered crystal. [176] Furthermore, corrections for the peak broadening due to instrumental settings or paracrystalline disorder are not taken into account. Thus, the crystal size is not the absolute size, but a useful estimation of the lower limit and can be used as relative size for the structure evolution. For the sample printed at room temperature the parameters obtained from the peak fitting are depicted in figure 6.9.

Overall, five different stages can be identified, where stage V corresponds to the final film. The intensity of the fitted Gaussian is related to the volume fraction of crystalline polymers within the organic thin film and its development with time is shown in figure 6.9a. The first P3HT crystals exhibit a scattering intensity of the (100) planes after around 8 s. It is known, that this initial crystallization usually occurs, when the solubility limit is reached. [40, 172] Hence, until this point, only the excess solvent has been evaporated. This point, the onset of crystallization is set as the beginning of stage II. During stage II, the (100) peak intensity increases moderately. The peak position is depicted in figure 6.9b. In stage II, the peak initially is found at q $\approx$ 3.75 nm^{-1} with very high uncertainties due to the low intensity of the peak. During stage II, the tendency of the peak position shift is not obvious. While solvent is evaporating, the thickness of the printed film is shrinking which causes a shift in the sample to detector distance. This change is not taken into account for the q-values shown in 6.9. However, these changes are merely on the order of 0.02 nm^{-1} and thus smaller than the error bars. Even though the error bars do not allow for a clear statement, we suggest that the initially formed crystals are not yet optimally

packed and thus show a larger backbone spacing. The increase of the calculated size with time is shown in figure 6.9c. Similarly as for the peak center, the crystal size shows big uncertainties in the beginning (stage II). In stage III however, a rapid growth of crystal size along with a sharp increase of the scattering intensity is observed. In stage IV, the coherence length and scattering intensity saturate. Only the peak position of the (100) P3HT peak gradually shifts to larger values. This is related to a decrease of the backbone spacing at the beginning of stage IV of d = (1.68 ± 0.01) nm to (1.62 ± 0.01) nm. This is in the range of previous studies of P3HT crystals before annealing. [39, 175] The smaller backbone spacing can be explained by a reduction of stacking defects of the polymer backbones leading to denser packed polymer crystals. The crystal size estimated by the Scherrer equation is around (8.4 ± 0.3) nm and smaller than solution cast or doctor bladed films. [39, 40] The end of this optimization process which is also referred to as self-annealing is the transition to stage V, the last stage consisting of the finally obtained structure.

In order to test the findings again a faster fiml evolution and to bring the above observations to a more general view, the same experiments are performed with samples at the second preparation route. These samples were printed using the same parameters, but a slightly higher temperature of the sample stage, namely 40°C, for which we expect different drying kinetics. [169] Equivalent to the sample coated at room temperature, the resulting integrated scattering intensity profiles along q_z at lowest q_r are fitted with Gaussians. Figure 6.10 shows the resulting parameters with time.

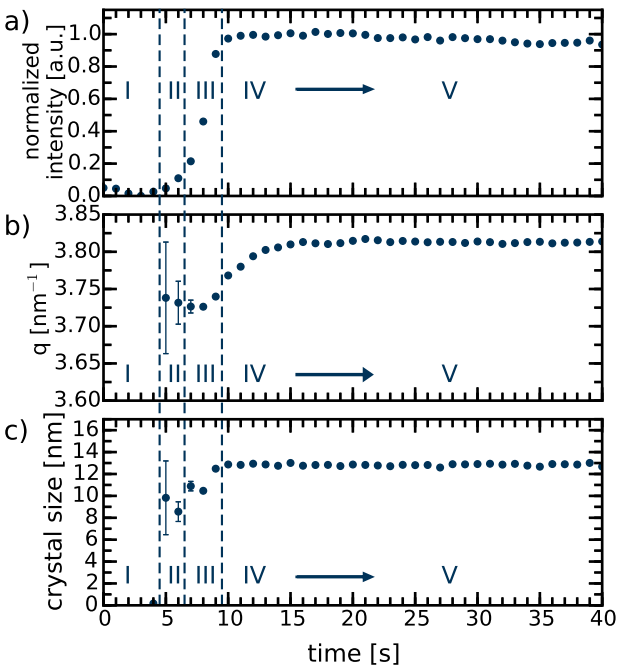

Figure 6.10: Extracted parameters from the Gaussian fits of the (100) peak of the GIWAXS data with time for the sample coated at a substrate temperature of 40 °C. a) The peak intensity normalized to the final film's intensity. b) The peak position in nm^{-1} is inversely proportional to the backbone spacing of the crystal. c) The crystal size is obtained via the FWHM of the fit and calculated using the Scherrer equation. The structure formation process is faster compared to the structure formation at room temperature. Similarly as for the sample at room temperature, the process is divided into five different stages, which are labeled accordingly.

The structure formation process is accelerated as it is expected for the elevated temperature of 40 °C. As for the sample prepared at room temperature, the structural evolution can be split up into five stages. Stage I is again dominated by the solvent evaporation as seen by a rapid decrease of the CBZ scattering signal. In stage II the initial crystals form. This process is, compared to the sample prepared at room temperature, much faster. Parallel to this formation, much better defined q-values of the peak center (figure 6.10b) as well as the crystal size (figure 6.10c) are observed. The initial crystal size is larger compared to the crystal size of the samples coated at room temperature. As for the sample coated at RT, the initial lower peak center in stage II indicate the formation of not yet optimally packed crystals. During stage III, the peak position becomes well defined, along with a rapid increase of scattering intensity and further crystal growth, comparable to the sample printed at RT. The final intensity is reached in stage IV. The crystal size is (12.2 ± 0.2) nm and the final backbone spacing reached towards stage V is (1.64 ± 0.01) nm.

In the following, the results of the two preparation routes are compared. A larger crystal size in [100] direction is observed for the sample coated at higher temperature. This is even though the crystal formation process is much faster compared to the RT sample. A possible reason for this is the increased mobility of the polymer due to the higher temperature. The packing of the final crystals in the sample coated at 40 °C is, however, slightly larger showing a less optimal packing possibly due to the rapid crystal formation process.

Comparing to different coating methods, the temperature dependency is similar in doctor bladed films. [39] The growth process in the presented experiment, however, exhibits two growth rates which is different to the known one in solution cast films. [40] One should keep in mind, that the drying kinetics of slot-die coated films differs from the slower drying solution cast films. For slot-die coated films, the drying front is following the printing direction, as the initially deposited material starts the drying process.

The scattering results of the presented GIWAXS studies are reproducible within the respective preparation routes and they all show similar stages for the respective temperatures. Hence, we see the described formation process to be a more general case in slot-die coated films.

Thickness tracking

When talking about the crystallization, an interesting information are the solution properties that are present, when certain crystallization phases occur. In the vertical scattering profiles shown in figure 6.5, the contribution of the scattering from chlorobenzene (CBZ)

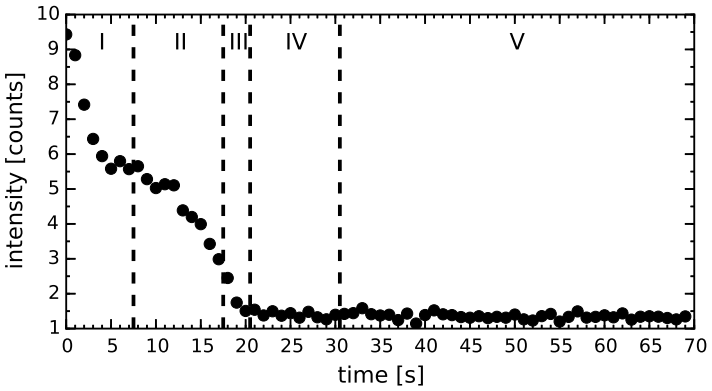

Figure 6.11: Tracking of the chlorobenzene's scattering intensity from the GIWAXS data of the sample coated at room temperature with time. The intensity at q = 19.6 nm^{-1} of the scattering profile is not superimposed by scattering signals from PCBM or polymer. The stages according to the ones described for the GIWAXS measurements are marked.

is observed. The scattering signal is due to the average separation distance between the CBZ molecules. [143] Furthermore, the solvent does not have a preferred orientation as seen in the two dimensional scattering patterns (initial stage in figure 6.3). This means, that the solvent content can be estimated in the vertical scattering profile. At higher q-values (q = 19 nm^{-1}), the signal is not superimposed by scattering from the PCBM or from contributions of the polymer. Thus, tracking the intensity at this q-value gives a rough idea about the solvent content present in the sample. For the sample printed at room temperature, the development of the signal with time is shown in figure 6.11.

The stages marked in the intensity development picture are the ones found for the GIWAXS scattering profiles (figure 6.9). The initial stage exhibits mainly evaporation of CBZ, seen by the rapid decrease in intensity. The onset of crystallization starting with stage II leads to a slower evaporation rate of chlorobenzene, as indicated by the decreased slope of the intensity versus time (figure 6.11). This is also seen in solution cast samples. [40] It is thought, that the formation of crystals hinders the diffusion of CBZ molecules to the film surface, where they are able to evaporate. Therefore, the observation of crystallization at the interfaces is supported by the decelerated evaporation rate. The intensity further decreases and reaches a low value in stage III, in which a rapid crystal growth has been observed. This might be due to the high concentration of polymers left in the film. To estimate the concentration of solid materials in the film, the thickness was tracked simultaneously using Vis-NIR reflectometry. The obtained thickness from the film dried at room temperature is depicted in figure 6.12.

Although the initial measurements are not accurate, a good idea of the initial thickness is obtained by recalculation and comparison with other measurements. The film thickness reaching the final value at around 15 s and thus slightly earlier than the scattering signal of CBZ is explained by the sensitivity of the measurement technique. The scattering signal is still present with a low amount of CBZ molecules, whereas this amount of molecules

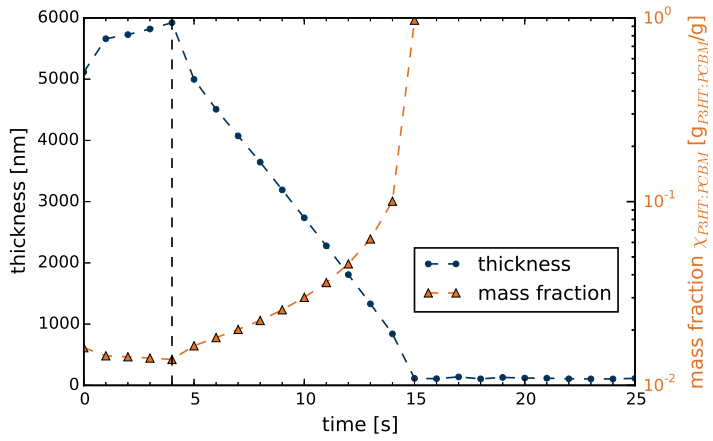

Figure 6.12: Thickness values obtained from Vis-NIR reflectometry (blue points) and the calculated mass fraction (orange triangles) in logarithmic scale. The measurements of the initial thickness are not accurate and recalculated for the calculation of the mass fraction.

can not be resolved by Vis-NIR reflectometry. The fitted refractive index was around n ≈ 1.3-1.5 for the dissolved film and n ≈ 1.7-1.9 for the final film, which is a mean value over the complete wavelength range. Out of the resulting thickness $d(t)$ the mass fraction of the active layer's solids $\chi_{P3HT:PCBM}$ is calculated by:

$$\chi_{P3HT:PCBM}(t) = \frac{m_{solid}}{m_{solid} + m_{solvent}(t)} \tag{6.1}$$

where m_{solid} is the mass of the solids (P3HT and PCBM) and $m_{solvent}$ is the mass of CBZ, which depends on the film thickness at given time t with:

$$m_{solvent}(t) = m_{solvent}(t=0) \cdot \frac{d(t) - d(t \to \infty)}{d(t=0) - d(t \to \infty)}. \tag{6.2}$$

The initial film thickness is $d(t=0)$ and the final film thickness is $d(t \to \infty)$. Initially, the mass concentration is

$$\frac{m_{solid}}{m_{solvent}(t=0)} = 16\frac{\text{mg}}{\delta \cdot \text{ml}} = \frac{16}{1110}\frac{\text{mg}}{\text{mg}}$$

with the density of chlorobenzene $\delta = 1.11$ g ml^{-1}. Thus, the mass fraction of the solid is calculated from the measured thickness with:

$$\chi_{P3HT:PCBM}(t) = \frac{m_{solid}}{\frac{m_{solid}}{\frac{16}{1110}} \cdot \frac{d(t)-d(t\to\infty)}{d(t=0)-d(t\to\infty)}} = \left(1 + \frac{16}{1110} \cdot \frac{d(t) - d(t \to \infty)}{d(t=0) - d(t \to \infty)}\right)^{-1} \tag{6.3}$$

The calculated mass fraction of the solid materials with time is plotted in figure 6.12 in logarithmic scale. This calculation serves only as an estimation, but it still is evident, that the solid mass fraction increases rapidly once most of the solvent is already evaporated. This rapid increase happens during stage III, when the crystallization shows a strong acceleration as well. Combining the thickness measurements with the results of the GIWAXS experiments leads to the suggestion, that the final crystals form after

a significant portion of the solvent has evaporated and the solubility limit is reached. This onset of crystallization yields a deceleration of the evaporation rate. From the azimuthal peak width we draw the conclusion, that these crystals are well oriented with the backbone parallel to the substrate, yet not well packed as seen from the Gaussian fits of the vertical intensity. Before the solvent is fully evaporated, the crystal size strongly increases together with a sharp intensity increase. That shows the significant improvement of ordered crystals in the not yet fully dried film.

6.2.2 Phase separation and fullerene aggregation

A further important aspect in terms of nano-morphology of organic thin films, besides the crystallization, are the kinetics on a larger length scale, the phase separation. In order to probe the formation process on this scale, a second scattering experiment, GISAXS, is performed. Therefore, a q-range of q $\approx$ 0.25-0.3 nm^{-1} is probed during the film solidification. This q-range is chosen, as contributions from PCBM clusters are expected to occur on that scale. [34, 37, 177, 178] The highest material contrast is contained in the Yoneda region, which is related to the material's critical angle. [87] Thus, horizontal cuts in $q_{x,y}$-direction are performed at this position, to follow the lateral evolution of the material with time.

Figure 6.13 shows the intensity development with time of these horizontal cuts in a 2D colorplot for the sample undergone preparation route 1 at RT.

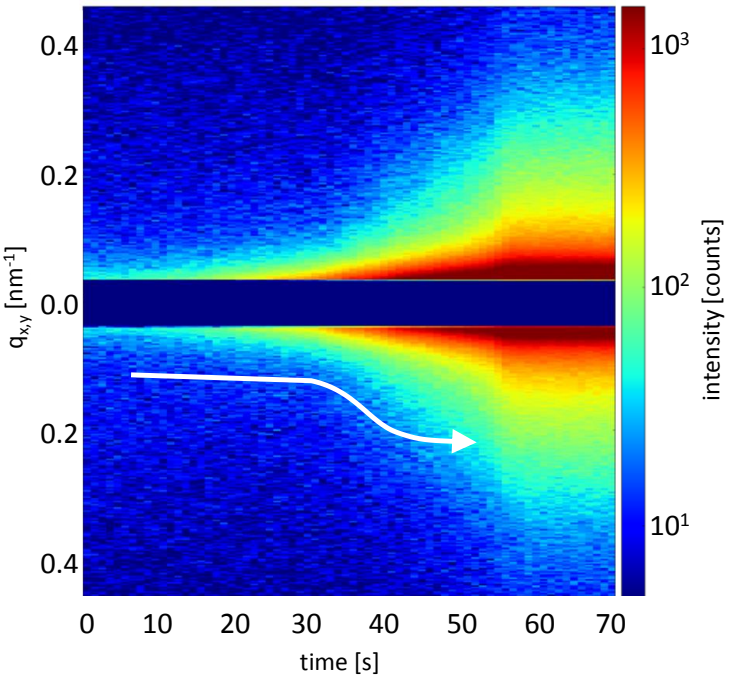

Figure 6.13: In plane GISAXS cuts of the sample coated at room temperature as a two-dimensional colormap of the temporal evolution. The development of the prominent shoulder at $q_{x,y} \approx$ 0.25-0.3 nm^{-1} is highlighted by the arrow. The dark region at $q_{x,y} = 0$ nm^{-1} is due to the beamstop protecting the detector from over-illumination.

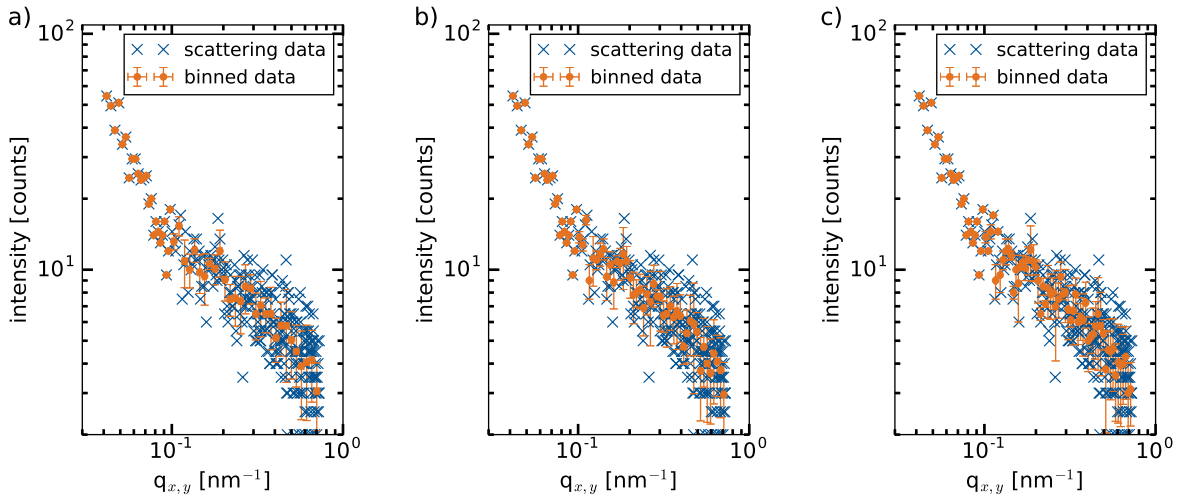

(a) 10 s, 30 bins **(b)** 10 s, 45 bins **(c)** 10 s, 60 bins

Figure 6.14: Effect of logarithmic binning on the horizontal line cut at the 10 s frame with different number of bins. The blue crosses represent the original scattering data and the orange points the binned data with their error bar. The higher the number of bins, the closer the original data are mapped having a high q-resolution, a low number of bins might induce artifacts that are not present in the data.

Initially, only a low intensity is observed. this is due to the well dissolved material, which does not yet show a regular ordering. It then slowly increases, starting around 10 s after recording, until approximately 30 s. Thereafter, a rapid increase of intensity for the next about 20 s occurs until the final structure is observed. It is already obvious, that especially in the beginning the intensity of the scattering is very weak. In order to overcome this challenge of low statistics, the data needs to be treated before further processing. A method established in neutron scattering, where a low flux is well known, is data binning. [179] As the low scattering intensity only becomes an issue at higher q-values, only these values need to be taken into account for binning. For the data treatment presented here, a logarithmic binning is applied to the data. Figure 6.14 shows the data at an early stage (10 s) after the start of the printing process.

The bins are evenly spaced on a logarithmic scale beginning at q = 0.1 nm^{-1} until the last data point. Starting at that particular q-value keeps the q-resolution at low q, at which the scattering intensity is still high enough for good statistics. Choosing logarithmic bins on the other hand, varies the bin size and thus keeps a higher initial q-resolution, at which the scattering intensity is still reasonably high. Towards higher q-values, the high q-resolution is not necessary anymore, but the fluctuations due to the low intensity of the scattering data become an issue. By increasing the bin size accordingly, theses data points are accordingly considered. Figure 6.14a-c shows the effect of changing the

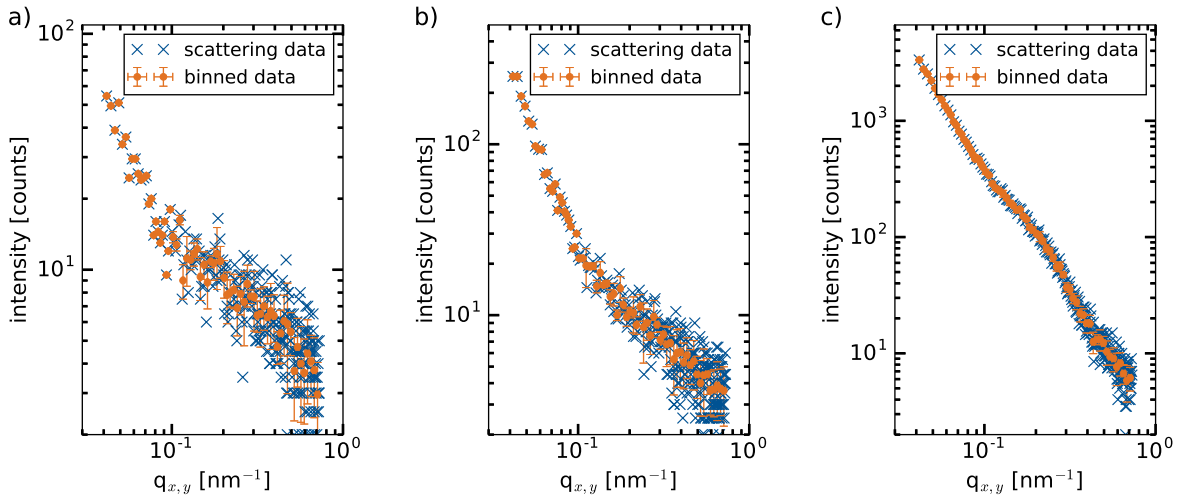

(a) 10 s, 45 bins **(b)** 30 s, 45 bins **(c)** 60 s, 45 bins

Figure 6.15: Scattering curves at three different times (blue crosses) and their respective binned data (orange points), each of them having 45 bins. Especially at later stages, the scattering features seen in the horizontal line profiles exhibit the same characteristics as the original data.

number of bins. A high number of bins (figure 6.14c) pictures the real scattering data more accurate, but no further advantage or clear structure can be obtained. On the other hand, a low number of bins (figure 6.14a) might result in artifacts, that are not present in the real scattering data (see for example at q $\approx$ 0.2 nm^{-1}). This can be due to defective detector pixels, the detector gap or other errors, which would overestimate the number of scattering events. For analysis of the data, a medium number of bins, namely 45 bins, is chosen (figure 6.14b).

To check the accuracy of the data treatment with the logarithmic binning using the start value q = 0.1 nm^{-1} and a number of 45 bins, scattering profiles at different times are investigated concerning the correct representation of scattering features. Figure 6.15 shows exemplary how the binned data coincide with the original scattering data.

Especially for later stages, at which binning of the data is not urgently necessary, it can be seen that the binned data do not contain features that are not present in the original scattering data (figure 6.15c). The choice of the bin size is therefore considered as reasonable for analyzing the data without a loss of the high time resolution and are therefore considered for the analysis of the GISAXS data in the following.

Figure 6.16 shows the horizontal cuts every 10 seconds with their respective modeled data. Furthermore, the final film, as obtained from the sum of in total 100 second record time is shown with its model. The structure development, appearing as the shoulders in

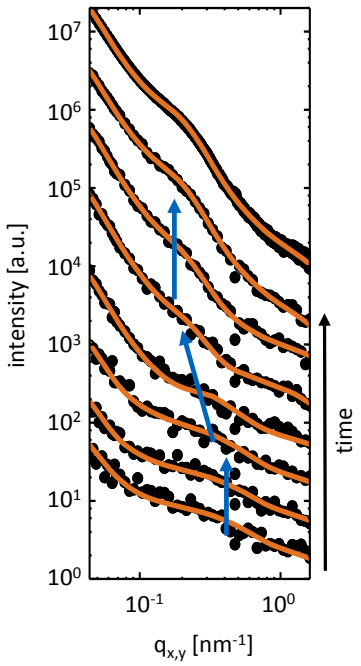

Figure 6.16: Horizontal GISAXS cuts of the sample coated at room temperature. The black points are the data obtained from the scattering patterns every 10 s from 0 s (bottom) to 60 s and the cut of the final film (top). The data of the time evolution from 0 s to 60 s are logarithmically binned for statistical improvements without change of scattering features present in the original data. The final film is obtained by summing up the scattering data of in total 100 s after the structure formation process was terminated. The orange lines represent the modeled data for each of the scattering curves. The prominent shoulder and its movement with time is depicted by the blue arrows. For clarity, the data are shifted along the intensity axis.

the scattering data can be followed as highlighted by the blue arrows. With time, theses features shift towards smaller q-values, meaning to larger structures.

The final film (top scattering curve in figure 6.16) is unbinned and shows high statistics. Therefore, modeling this scattering curve with the same features as found by modeling the binned data of the structure evolution, supports the choice of parameters applied during modeling the structure formation. The used model consists of a form and a structure factor of the main feature. These factors can be related to cluster radii and their respective lateral distance.

The resulting structure sizes obtained from modeling the scattering curves at room temperature are depicted in figure 6.17. The film formation is divided into five stages, which are marked in the figure.

Already in the beginning of the process, some structures in the intermediate q-regime are observed (figure 6.17a). Due to the low intensity of the scattering signal, a rare occurrence of these clusters is concluded. The large separations (figure 6.17b) found for this clusters further support this argument, which is expected for a well dissolved system still containing a lot of solvent. This is denominated stage I of a five stage process. The solvent evaporation continues during stage II, in which the cluster radius increases slowly from (2.1 ± 0.6) nm. A rapid decrease of the lateral distances is found in this stage which is attributed to a nucleation process that takes place in that phase. This nucleation process continues until a minimum lateral cluster distance is reached which is marked as the transition towards stage III. Different clusters aggregate in this stage which yields

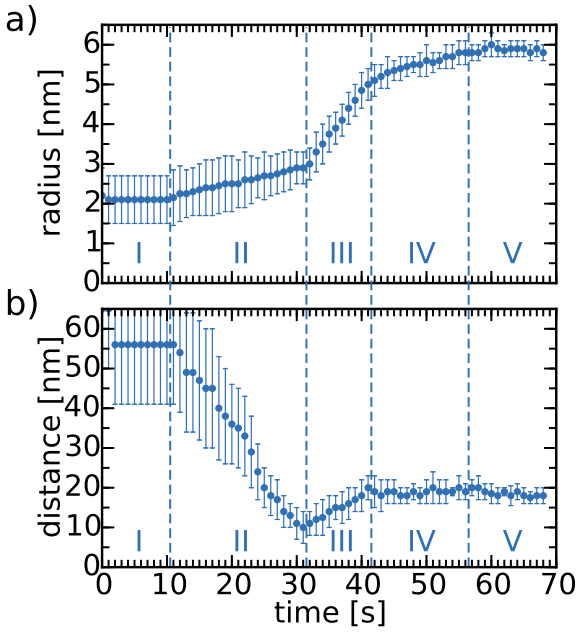

Figure 6.17: Parameters applied for modeling the horizontal GISAXS cuts of the sample coated at room temperature. a) The development of the cluster radii with time along with their respective lateral distances (b). Five stages (I-V) are identified out of the combined parameters and marked with dashed lines.

a quick increase in diameter along with a slight drift of these clusters apart from each other. This behavior is characteristic for a ripening process. The final separation of the aggregates has a distance of (18 ± 2) nm and is reached already in stage IV. During that stage, the cluster radius still slightly increases. The final cluster radius is obtained in stage V and found to be (5.8 ± 0.3) nm.

The same experiment is performed for a sample in preparation route 2, which is coating at a substrate temperature of 40 °C, for which the solidification is monitored using GISAXS. The development of the parameters with time obtained from modeling the horizontal GISAXS cuts are depicted in figure 6.18.

The structure formation can be divided into five stages, similar to the film coated at room temperature. Generally, the cluster evolution is accelerated compared to the sample coated at RT, due to the higher temperature. Already in the still well dissolved film, small clusters are observed (figure 6.18a). As the shoulder's intensity increases, the radius can be determined to be (2.4 ± 0.7) nm, which initializes stage II. Simultaneously, the lateral distance of the observed clusters decreases (figure 6.18b). A smoothly growing cluster radius is characteristic for stage II, while it rapidly increases in stage III. A minimum in the cluster distance is found to occur at the transition to stage III, which again indicates a ripening process. The second to last stage shows a constant lateral spacing, while the cluster radius in this stage IV slowly grows. The final separation is found in stage IV with a lateral distance of (17 ± 4) nm. The cluster growth is terminated in stage V, having a radius of (4.7 ± 0.4) nm.

Comparing the samples prepared under the different preparation routes, RT and 40 °C

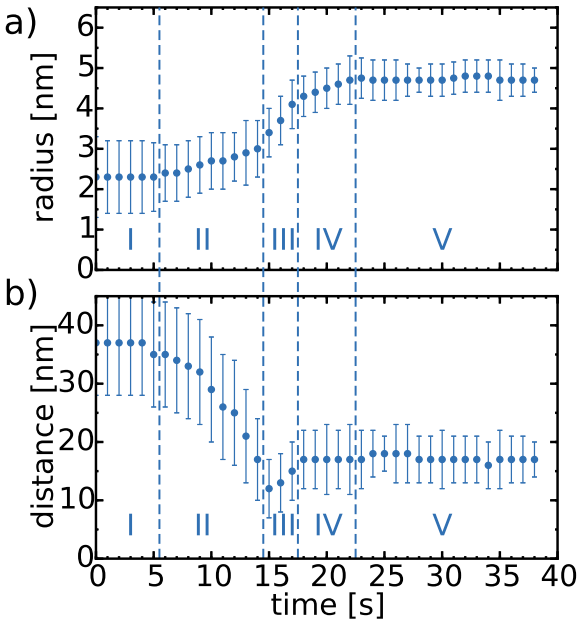

Figure 6.18: Cluster radius (a) and lateral distance (b) with time, obtained from modeling the horizontal GISAXS cuts of the sample coated at a substrate temperature of 40 °C. The structure formation is accelerated compared to the sample prepared at room temperature but still shows the characteristic five stages (I-V), which are marked with dashed lines.

substrate temperature, very similar morphological evolution is found. For both samples, five characteristic stages are seen, each of them containing the same underlying processes. The sample prepared at higher temperature exhibits smaller cluster sizes as the one prepared at RT while the lateral spacing is similar. Due to the parallel development within the respective stages, the observed structure formation process can be generalized. The behavior of the cluster sizes with temperature is different as seen for the crystallization of the polymer crystals. There, the P3HT crystals were larger at higher temperatures. Out of this inverse behavior, we can conclude, that the clusters observed with GISAXS are PCBM aggregates, not P3HT crystals. As P3HT in the amorphous phase also contains a certain fraction of PCBM, the observed clusters might also be a result of scattering from a mixed phase of P3HT and PCBM. [72, 180, 181] With a higher degree of crystallinity, the miscibility of PCBM is lowered. [182] Compared to other studies, the sizes and lateral distances found for the clusters in GISAXS are in good agreement for P3HT:PCBM films. [72, 131, 177, 183, 184] The observations of inverse size to temperature dependence of P3HT crystals and PCBM aggregates is consistent with the concept of a crystallization driven phase separation. As the larger P3HT crystals in films prepared at elevated temperatures hinder PCBM diffusion, these molecules are prevented to aggregate. This diffusion is even further suppressed as the solvent evaporation rate is increased compared to the RT sample. Resulting from the competition of crystallization kinetics and PCBM diffusion and aggregation, the formed PCBM aggregates are smaller for samples with larger crystallites.

6.2.3 Solar cell performance

The impact of the different production routes on the device performance is tested in solar cells. The cells are measured as prepared and after thermal annealing at 110 °C for 10 min. Figure 6.19 shows the parameters obtained from the characterization.

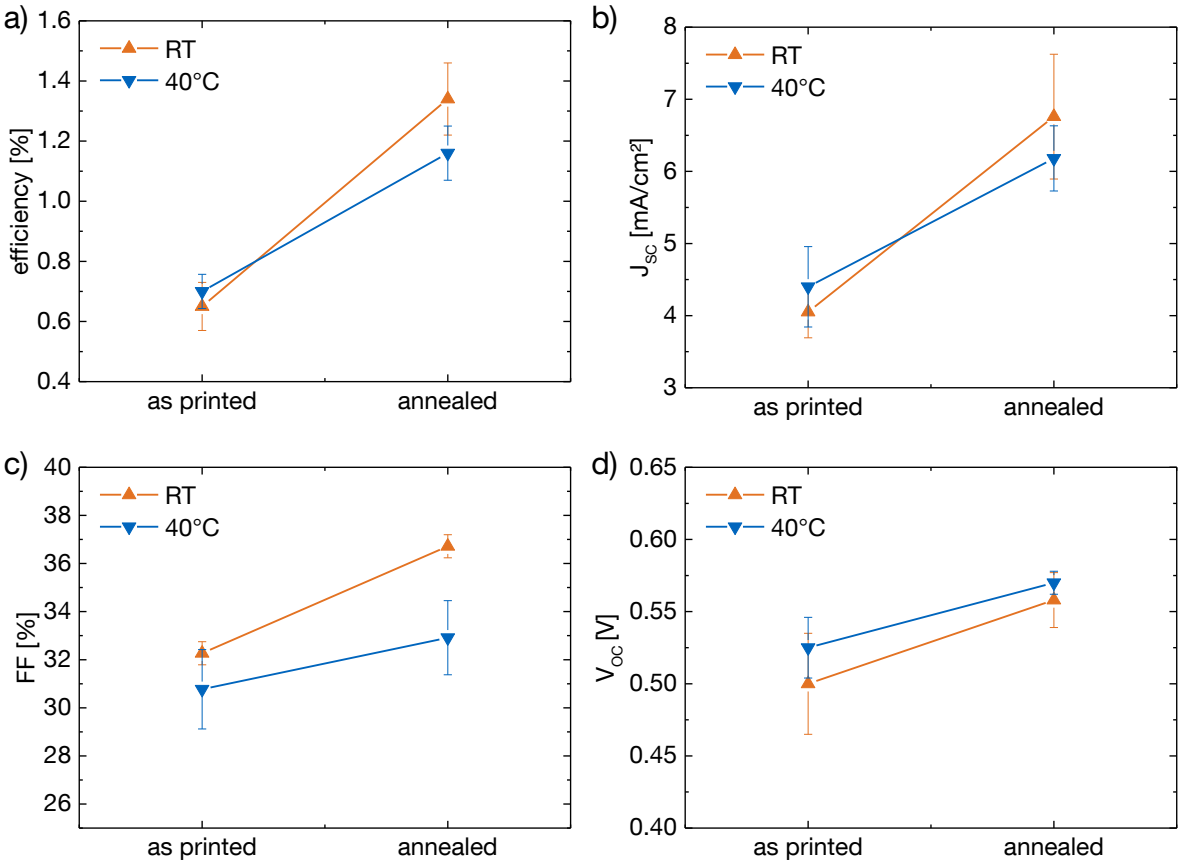

Figure 6.19: Characteristics of the solar cells prepared with the different preparation routes before and after thermal annealing showing the efficiency (a), the short circuit current density (b), the fill factor (c) and the open circuit voltage (d). Samples printed under RT conditions are pictured with the orange upward triangle, samples printed at 40 °C with the blue downward triangle. The data are averaged over six to eight pixels.

As known for organic solar cells with P3HT:PCBM active layer, the device performance is extremely improved by thermal annealing due to an optimized packing. [158, 185] The *in situ* scattering experiments performed in this work show the samples before annealing at high temperatures, although the sample prepared at 40 °C already underwent a slight annealing procedure. The data show, that the devices produced at room temperature exhibit a lower power conversion efficiency of $\eta_{\mathrm{RT}} = (0.65 \pm 0.06)$ % compared to the 40 °C sample with $\eta_{40\,^{\circ}\mathrm{C}} = (0.70 \pm 0.06)$ % before thermal annealing. The same is true

for the open circuit voltage V_{oc} and the short circuit current density J_{sc}, which is around 8 % higher for the 40 °C sample. While the former one stays at a lower value as for the 40 °C sample even after annealing, the latter one as well as the efficiency gain a higher improvement ($\eta_{\mathrm{RT}} = (1.3 \pm 0.1)$ %) from the annealing process compared to the one of the 40 °C sample ($\eta_{40\,^\circ\mathrm{C}} = (1.1 \pm 0.1)$ %). The fill factor of the solar cells prepared at RT is slightly higher than for the one coated at an elevated temperature and the improvement due to annealing is even stronger for the RT sample. For printed solar cells using this active layer, typical power conversion efficiencies are in the range of 1.6 - 2.1 %. [85]

6.2.4 Structure evolution model and conclusion

The performed measurements can be combined to get a complete picture of the structure formation process in slot-die coated P3HT:PCBM photoactive layers. In general, all the performed experiments exhibit five stages of structure evolution, fully independent of the drying speed. This leads to the assumption of a general film formation process that is pictured by the experiments. An important outcome of the investigations is a structure evolution model based on the previously described observations. Figure 6.20 schematically shows the complete formation process of the nanostructure. In the model, the solvent is shown as green points, the polymer backbone chains are represented by the dark lines, which are - in case of crystallinity - framed by a black box. The PCBM aggregates are highlighted by blue cylinders, PCBM molecules however are not shown.

In summary, the experiments are combined to get the following picture of the five stages of the structure formation process:

Stage I: During the first stage, mainly the solvent evaporates. This evaporation does not yet have an influence on the polymer/fullerene aggregation or crystallization as it is only a matter of excess solution and the critical concentration is not yet reached. [40] A occurrence of small PCBM aggregates is however already observable in the solution.

Stage II: The first ordered P3HT structures form in the early phase of stage II, when the critical solution concentration is reached. The onset of crystallization is seen in the reduced solvent evaporation rate. The crystals hinder the solvent molecules from diffusion to the surface, from where they would evaporate. The initially formed structures are highly edge-on oriented. The reason for this good alignment is the crystallization at either the solvent/air or the solvent/substrate interface and is known to appear in blade-coated films. [172] PCBM molecules start to aggregate and the forming P3HT crystals consist of not optimally packed backbones with a larger spacing. In the ongoing process, the PCBM cluster size increases, while their lateral distance shrinks. This observation is explained by a crystallization induced phase separation rather than driven by spinodal decomposition.

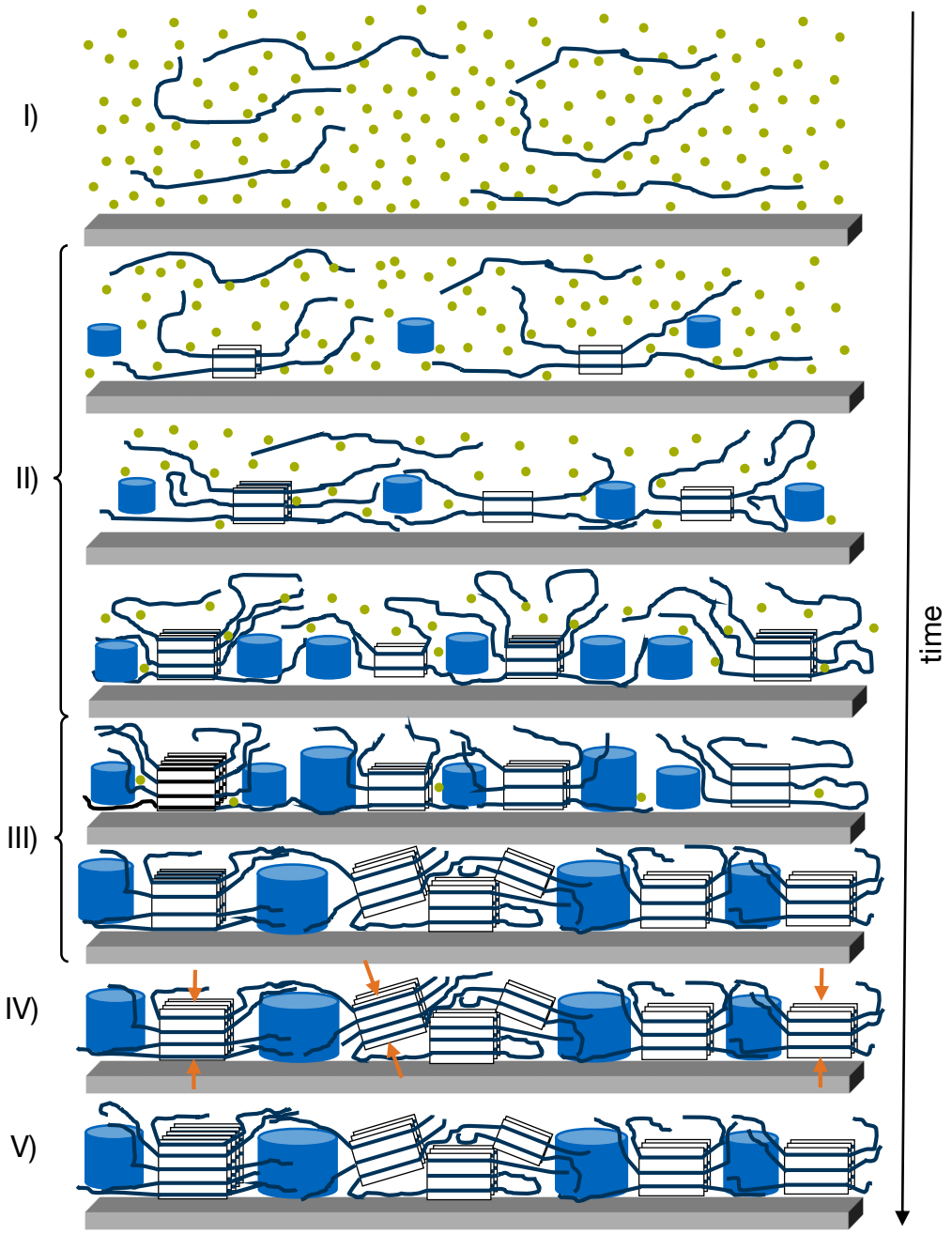

Figure 6.20: Model of the structure formation process with time for slot-die coated P3HT:PCBM films. On the left the stages are indicated. Very active stages are split up into initial to final phase. The green points represent the solvent, the dark lines the polymer backbones. The black frames around the polymer chains represent crystallized polymer. The fullerene aggregates are shown by blue cylinders. For simplicity, only one layer of the complete bulk is shown. The substrate is indicated as the gray bottom.

[172] It is well known, that the P3HT crystals can not enclose PCBM molecules due to their limited space. The maximum amount of PCBM within a crystal part of the P3HT is found to be 3 - 4 %. [181, 184] Schmidt-Hansberg et al. investigated blade-coated films, for which they saw indications of PCBM molecules that are squeezed out of the polymer crystallization areas, followed by fullerene aggregation. [172] Furthermore, Kohn et al. observed a crystallization induced structure formation which they related to the limited miscibility of P3HT and PCBM. [180] Our interpretation of stage II, that the increasing size of the P3HT crystals drives the PCBM molecules away from the growth area, which induces further aggregation, are supported by these findings. This is seen in the GISAXS data, at which the lateral distances of the PCBM, containing P3HT crystals that determine the separation length as spacer, decreases while their size increases. In spin coated films, that are post annealed, it was seen that the diffusion of PCBM away from the crystal growth front and the growth rate determine a characteristic size. [186] The P3HT crystal does not contain PCBM molecules, the amorphous phase, however, might contain PCBM molecules. That is why the polymer chains depicted in figure 6.20 overlap with the PCBM aggregates.

Stage III: A rapid further polymer crystallization occurs during stage III. The not yet optimized packing of the crystals is seen by the larger backbone spacing compared to the final film. The rapid crystal growth forces the PCBM clusters to move together yielding a fast increase of PCBM cluster radii and a slight increase of their according lateral distance.

Stage IV: During stage IV, the crystals improve their packing, which is referred to as a self-annealing process. The increasing q-value to the final one is related to the shrinking of backbone spacing. The final reformation of the polymer crystals and the evaporation of the final solvent molecules induces the PCBM clusters to further move together, which is seen by the slight growth of cluster size.

Stage V: The transition from stage IV to stage V, in which the final film morphology is obtained, is an ongoing relaxation process. Collins and coworkers found a solubility of 16 - 22 % of PCBM in amorphous P3HT regions, which was confirmed by Ruderer et al. [72, 181] Therefore, the findings presented in this chapter are in good agreement with the coexistence of the three phases of pure P3HT crystals, pure PCBM aggregates and an intermixed phase of amorphous polymer and PCBM molecules. [37, 83, 174, 180, 187]

Solar cells: The reason for the higher short circuit current J_{sc} and thus power conversion efficiency of the untreated 40 °C sample can be found in the crystallite sizes for each of these samples, which was smaller for the RT sample. The crystallinity is an important factor influencing the mobility within a polymer. [30, 188] It is possible, that the larger crystals are beneficial for the 40 °C sample. With thermal annealing, however, the improvement of the RT sample is better compared to the 40 °C sample, yielding higher

efficiencies. The initially larger crystals of the latter sample might be problematic for the diffusion and thus hinder the morphology to further optimize. The findings in these experiments suggest to keep the drying kinetics on a slower time scale. Similarly, Li et al. found the control of the active layer growth rate to be beneficial for the hole mobility and thus the device performance. [137, 189]

6.3 Summary

The crystallization process of P3HT is monitored with *in situ* GIWAXS, while the PCBM aggregation is investigated with *in situ* GISAXS during the solidification of slot-die coated P3HT:PCBM thin films. Therefore, a custom made slot-die coater is implemented into a synchrotron beamline. To improve the statistics and keep the high time resolution, a logarithmic binning procedure is introduced. this data treatment is evaluated and allows for an improved data modeling of the GISAXS data. The findings of both experiments show, that in general, five stages of structure development are found, independent of the investigated length scales or drying temperature. All the five stages are interpreted and the findings yield to the proposition of a structure formation model.

The crystallization starts at the critical solution concentration. The forming polymer crystals are well aligned in an edge-on orientation. When the initial crystals form, they hinder the solvent molecules from diffusion to the surface and thus slow down the evaporation process. In the solution, already a few fullerene aggregates are present. The following stage exhibits a further rapid crystal growth, forcing the PCBM aggregates to move apart from each other and increase in size. We thus see a crystallization induced phase separation, which results in length scales, that are dominated by the sizes of the polymer crystals.

The crystal size of films printed at room temperature is found to be smaller compared to the sample printed at 40 °C. This is the reason for the better performing solar cells of the 40 °C sample before thermal annealing. However, the findings show, that these bigger crystals hinder the PCBM diffusion during the thermal annealing step, which lowers the improvement of the power conversion efficiency of these samples. Based on these findings, a low solvent evaporation rate during printing is proposed in order to improve the final solar cell performance.

This work provides an important part to understand the mechanisms taking place during solidification of slot-die coated thin organic films. It is an essential contribution towards tailoring the thin film morphology, which is a necessary step with respect to device optimization during fabrication.

7 Impact of electric field on active layer

The possibility to process organic solar cells out of solution led to a significant increase of investigations in the last years, since it allows high throughput at low cost and potentially short payback time. [13,15] As described in chapter 2.2, the active layer of an organic solar cell generally consists of a blend of two materials forming an inter-penetrating network called bulk heterojunction with a high interfacial area between the components. [29] A key challenge to address is the nanoscale morphology of bulk heterojunctions of conjugated polymers, regarding both, the phase separation of the active layer materials and their molecular packing. [28, 30, 190–192] The nanoscale order influences the charge carrier generation as well as the charge carrier mobility. A created exciton needs to reach an interface between the materials within its lifetime in order to possibly be separated. Furthermore, the crystallinity and its orientation with respect to the substrate highly influences the directionality of high mobility. [30] Then, the charge carrier needs a percolation path within the material to its respective electrode, else it gets trapped and might yield to charge accumulation. A model system for organic photovoltaics, that is well characterized is a blend of poly(3-hexylthiophene) (P3HT) and [6,6]-phenyl-C61-butyric acid methyl ester (PCBM). [21] The inner morphology is commonly influenced by the choice of solvents, solvent additives or solvent annealing. [83, 137, 157, 160, 193] Another widely used approach is thermal annealing as a post production method. [158, 159] It is further improved by simultaneously applying an electric field over the active layer. [194–202] In order to reduce the processing time of devices, approaches to influence the structure formation *in situ* become the focal point of interest. Some examples are the use of shear forces, temperature and reduced solvent evaporation rates. [138, 142, 189] Molina-Lopez and coworkers recently found a positive influence on the molecular packing of organic thin films by applying an electric field during solution shearing. [191] Electric fields were furthermore used to create lateral structures in the polymer film. [203] Several investigations show the impact of an electric field on the orientation of polymer crystals and the influence on organic thin films. [198, 204–206]

In industry, electric field applications for improved toner transfer in printing systems are commonly installed. The use of electrophoretic forces is for example known from liquid toner. There, it is utilized to move the toner and reuse the solvent after transferring the

toner. [207,208] On this basis, the printer setup is modified to facilitate the application of an external electric field during the deposition of the organic film as described in section 5.2. The aim of the present chapter is to actively influence the structure formation of the printed thin organic film (figure 7.1).

Figure 7.1: This chapter describes a possibility to actively influence the structure formation of a printed film.

To this end, P3HT and PCBM are dissolved in chloroform, a solvent, in which P3HT and PCBM exhibit an electrophoretic mobility. This effect is used to actively induce vertical material composition gradients. The experimental procedure to investigate the effect of the processing under external electric field is introduced in section 7.1. The influence on the electronic properties is studied by charge carrier mobility measurements and organic solar cells in section 7.2. The inner morphology is thoroughly investigated using scattering methods and the results are discussed in section 7.3. The findings are interpreted in a schematic representation of the film structure presented in section 7.4. The findings in this chapter are the basis of a manuscript entitled "Electrophoresis assisted printing: a method to control the morphology in organic thin films".

7.1 Experimental details

The used printing setup is introduced in chapter 5. Figure 7.2 schematically shows the printing process during which the solution is coated, and, an external voltage between the print head and the ITO of the substrate is simultaneously applied. The print head is thereby connected to an additional top electrode. The film is exposed to the electric field for 30 s. Low (±10 V), medium (±50 V) and high (±100 V) voltages are applied between the print head and the ITO. The proximity of the print head to the ITO ($d \approx$ 0.3 mm) leads to high electric fields (0.3 – 3.3 $\mathrm{kV\,cm^{-1}}$) in its vicinity. The attached top electrode has a distance of 2.5 cm to the ITO. The direction of the external electric field is pointing forward (towards the ITO) as depicted in figure 7.2 for positive voltages and backward (towards the liquid/air interface) for negative applied voltages. Printing without an external electric field is performed as reference film, showing the intrinsic tendency of the material composition.

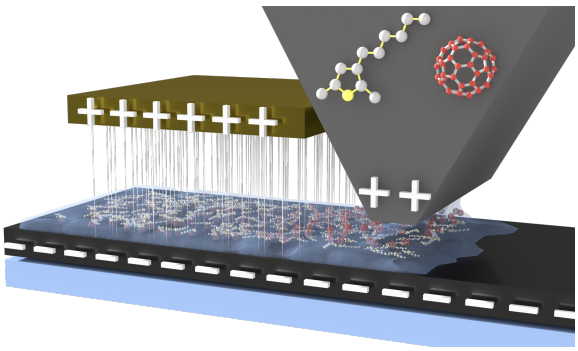

Figure 7.2: Sketch of the print head and attached electrode with the indium tin oxide (ITO) coated glass as substrate and counter electrode for the external electric field treatment while processing. The figure shows the application of a positive voltage, meaning the electric field is pointing in forward direction towards the substrate. In the vicinity of the print head, the field is extremely high due to the proximity of both electrodes.

Slot-die coating: The P3HT:PCBM solution is deposited on the PEDOT:PSS coated substrates in ambient atmosphere. The distance of the print head to the sample is set to 0.3 mm, the solution is injected into the print head via a syringe pump with a rate of 0.25 ml min^{-1}. The horizontal speed of the substrate underneath the print head is 10 mm s^{-1} resulting in average final film thicknesses of around 150 nm. During the printing process a voltage is applied between the print head and a connected top electrode (2.5 cm above the sample) and the ITO of the substrate. The applied voltages are 0 V as reference, ±10 V, ±50 V and ±100 V, positive voltages result in the electric field pointing towards the substrate (forward direction), whereas negative voltages result in the electric field pointing away from the substrate (backward direction). The highest electric fields in the vicinity of the print head (distance 0.3 mm) are 0 V cm^{-1}, ±0.3 kV cm^{-1}, ±1.7 kV cm^{-1} and ±3.3 kV cm^{-1} for the respective applied voltages if air is counted as dielectric. The observed current is less than 10 µA for the highest applied voltage. The films are subsequently annealed at 140 °C in a nitrogen atmosphere before further processing.

Electronic and spectroscopic characterization: Solar cell devices are produced as described in section 4.2 and measured according to section 3.1.4. The electrophoretic mobility is measured with a Zetasizer ZS from Malvern (section 3.1.2). For that purpose, two separate 12 mg ml^{-1} solutions with P3HT and PCBM, respectively, dissolved in chloroform are used. Hole mobility is measured using metal-insulator-semiconductor - charge extraction by linearly increasing voltage (MISCELIV, section 3.1.3). The active layer is therefore printed directly on ITO without the use of PEDOT:PSS, with else the same conditions as above. The samples are cut into 2 x 2 cm^2 pieces and a 50 nm thick MgF_2 insulating layer and 100 nm thick aluminum contacts are evaporated. The mobility measurements are performed using different offset voltages and averaged over all used offsets, the error is due to the standard deviation.

X-ray scattering and reflectivity measurements: Grazing incidence wide and small angle X-ray scattering (GIWAXS/GISAXS) measurements are performed at beamline 7.3.3 at

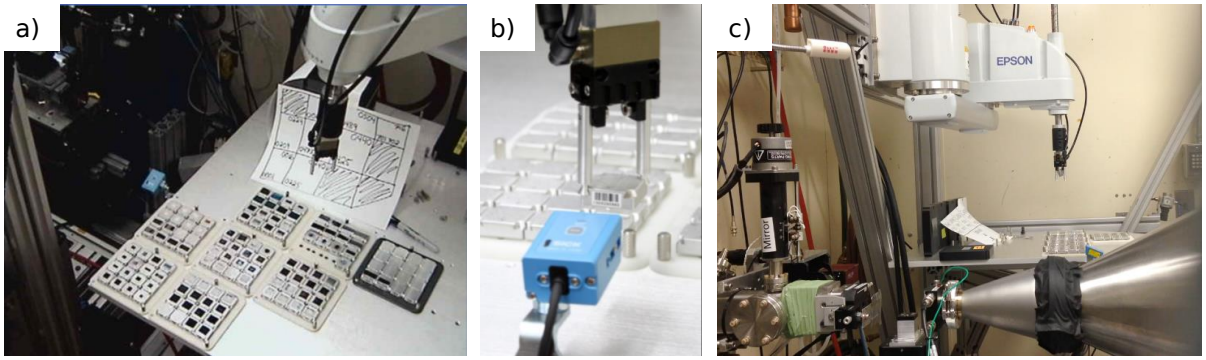

Figure 7.3: The grazing incidence X-ray scattering experiments are performed in a remote access beamtime using a robot. The samples are provided on sample boxes containing 4 x 4 chucks on which the probe is fixed (a).The robot picks up the chucks and a bar code scanner identifies the sample under investigation (b). After placing the chuck with sample to the appropriate position the robot moves back to the home position and the sample is aligned and measured (c).

the Advanced Light Source (ALS) of the Lawrence Berkeley National Laboratory (LBNL) with a wavelength of $\lambda = 1.24$ Å. [117] The scattering experiments are conducted using a robot and remote access to the beamline. Figure 7.3 shows the robot setup at the beamline. The samples are provided on separate chucks, each equipped with a bar code to clearly identify the sample. A robot picks up the chucks with the sample, passes a bar code reader and places the sample into the beam path. After the robot moved back to its home position, the alignment and measurement are started.

For GIWAXS, the sample-to-detector distance is 270 mm and the incident angle 0.17°, above the critical angle of the active layer materials. For the analysis, azimuthally integrated intensity profiles are extracted from the solid angle corrected 2D scattering data using the GIXSGUI 1.6.1 software of the Argonne National Laboratory, taking into account the necessary corrections. [94, 96] The azimuthal integrals are $\sin(\chi)$ corrected to account for the in-plane isotropy. GISAXS measurements are performed under an incident angle of 0.25° at a sample-to-detector distance of 380 cm. The horizontal line profiles are obtained at the Yoneda position of PCBM to obtain the respective material sensitivity and modeled as described in section 3.2.6.

X-ray reflectivity is measured and analyzed as described in section 3.2.5. The reflectivity is modeled using a layer model, where the P3HT:PCBM blend is assumed to consist of three parallel layers, each with an individual thickness, constant scattering length density (SLD) and a roughness accounting for the interlayer mixing with an error function. The model is fitted to the data using Motofit software, which calculates the reflectivity using Abeles matrix method. [88, 90] For the SLD of pure P3HT and PCBM, films made of

the bare materials are used. The overall SLD within each film is preserved and so is the integrated PCBM volume concentration as expected for films produced from the same solution and a 1:1 weight ratio.

7.2 Electronic and spectroscopic characterization

An insight into the functionality of thin films printed under different applied external voltages is seen by probing the electronic and spectroscopic properties of the respective films. Focus is put on the photovoltaic performance of the films implemented into an organic solar cell as an example application.

7.2.1 Solar cell performance

Controlling the inner film structure is desirable for a number of applications, amongst others for organic solar cells. The presented printing procedures are applied into films for organic solar cells in standard geometry (ITO/PEDOT:PSS/P3HT:PCBM/Al). The measured current voltage characteristics are shown in figure 7.4. The I-V curves of the

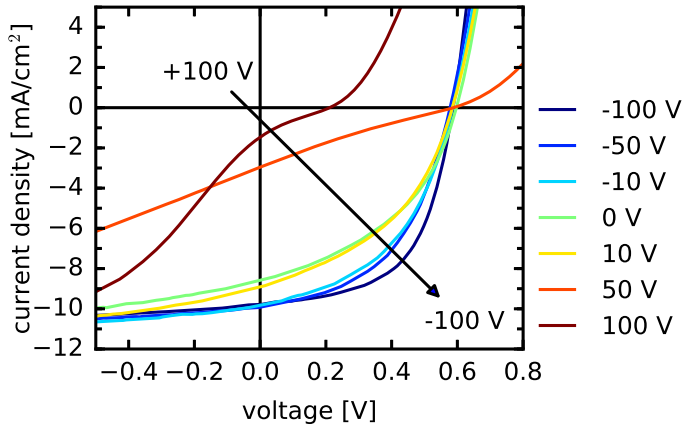

Figure 7.4: Device performance data showing the current-voltage characteristic of ITO/PEDOT:PSS/P3HT:PCBM (1:1)/Al devices printed with different strength and direction of the electric field. The arrow depicts the tendency from highest forward electric field to highest backward directed electric field.

films printed under medium and high forward electric field show a strong s-shape. This already indicates a restricted charge transport and an accumulation of charge carriers as known from enrichment layers. [209] The s-shape of the I-V-curve vanishes for low and backward directed electric fields. The solar cell parameters obtained from the measurements are listed in table 7.1.

The forward directed fields downgrade the performance which as seen in the I-V curves due to the strong s-shape. It even leads to a drop in the open circuit voltage for a high forward directed e-field. For illustration of the development of the parameters, figure 7.5

Table 7.1: Solar cell parameters obtained for the devices printed under application of an external electric field while processing.

applied external voltage [V]	$\mathbf{V_{OC}}$ **[V]**	$\mathbf{j_{SC}}$ **[mA cm^{-2}]**	**FF [%]**	**PCE [%]**
+100	0.21 ± 0.02	1.4 ± 0.2	21 ± 1	0.1 ± 0.1
+50	0.59 ± 0.01	2.4 ± 0.7	18 ± 4	0.3 ± 0.2
+10	0.59 ± 0.01	8.7 ± 0.5	43 ± 2	2.2 ± 0.2
0	0.60 ± 0.01	8.0 ± 0.4	43 ± 2	2.1 ± 0.2
-10	0.59 ± 0.01	9.4 ± 0.7	46 ± 2	2.6 ± 0.3
-50	0.58 ± 0.01	9.4 ± 0.6	48 ± 3	2.6 ± 0.3
-100	0.59 ± 0.01	9.2 ± 0.5	57 ± 2	3.0 ± 0.3

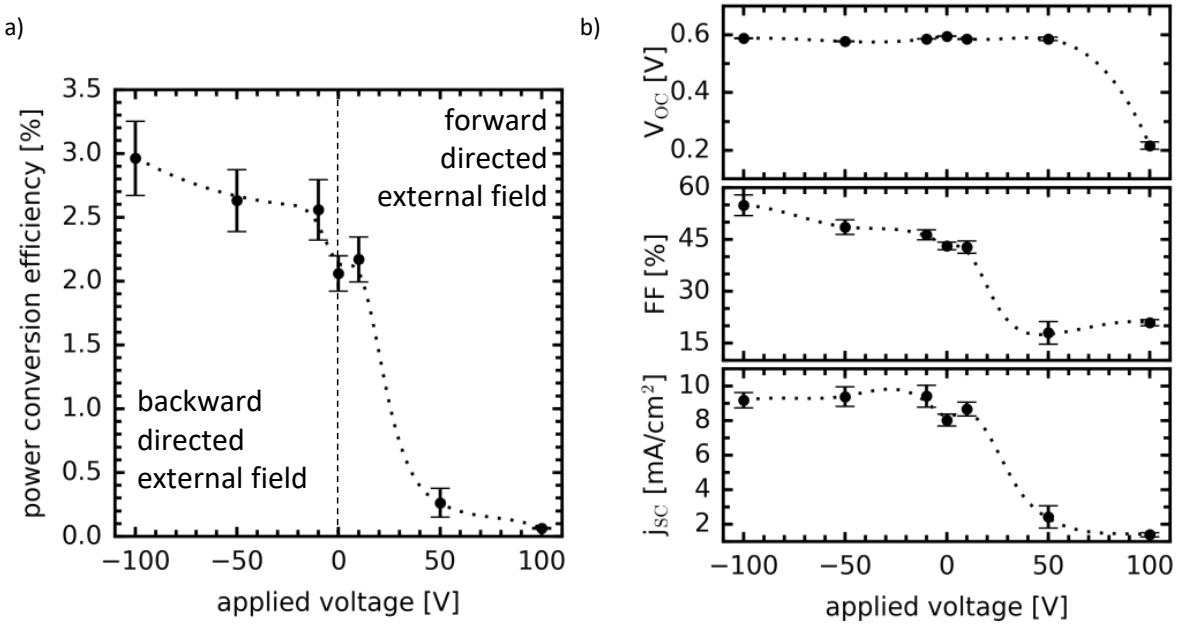

Figure 7.5: Solar cell parameters of the devices for different applied external voltages between print head/top electrode and the ITO while printing. The (a) power conversion efficiency and (b) open circuit voltage (V_{OC}), fill factor (FF) and short circuit current density (j_{SC}) are depicted. The error bars result from standard deviations of the experimental values. The dotted lines are guides to the eye.

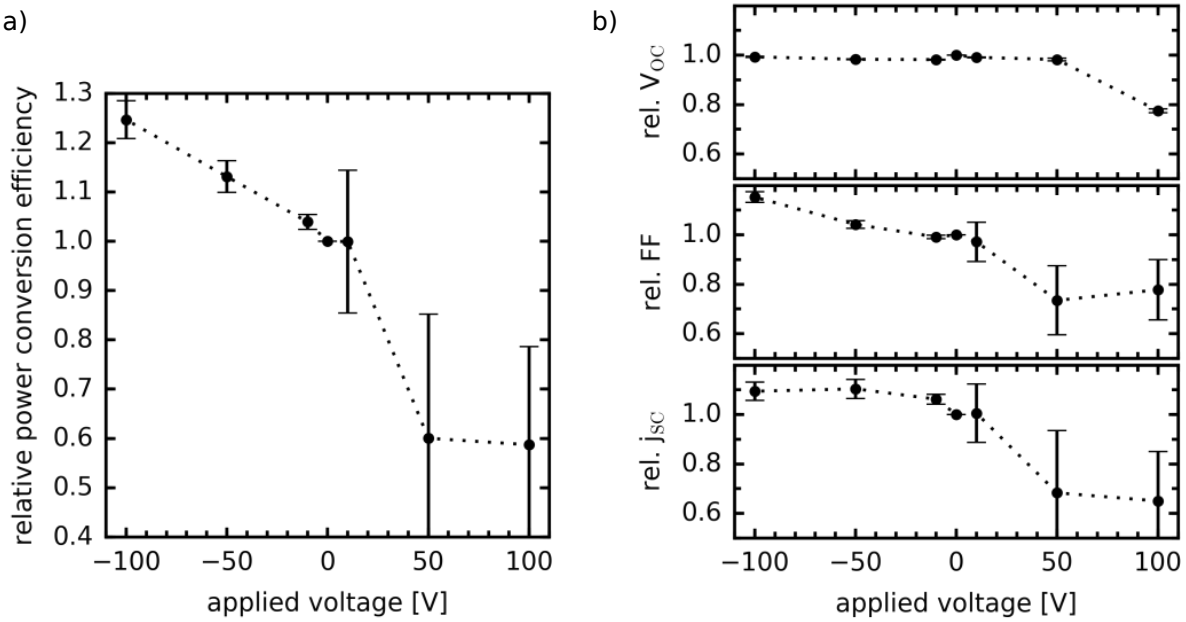

Figure 7.6: Relative solar cell parameters of ITO/PEDOT:PSS/P3HT:PCBM (1:1)/Al devices for different applied voltages between print head/top electrode and the ITO while printing. The (a) power conversion efficiency and (b) open circuit voltage (V_{OC}), fill factor (FF) and short circuit current density (j_{SC}) are each normalized to the intrinsic device printed without application of an external electric field. The error bars result from averaging over three batches of solar cells. The solar cell parameters in (b) are plotted with equal ordinate range for ease of comparison. The dotted lines are guides to the eye.

depicts the dependency on the applied external electric field while printing. As directly seen, the backward e-field is beneficial for the device performance. The power conversion efficiency of a solar cell printed under high backward electric field improves to (3.0 ± 0.3) % in comparison to the reference cell (2.1 ± 0.2) %. The main influence occurs in the short circuit current density (from (8.0 ± 0.4) mA cm^{-2} to (9.2 ± 0.5) mA cm^{-2}) and the fill factor (from (43 ± 2) % to (55 ± 3) %) of the respective devices. The parameters are in a good range for printed solar cells with this standard material system. [85, 210]

For more statistics, three batches of solar cells are produced and the resulting parameters show a similar tendency as depicted in figure 7.6. The three individually processed solar cell devices are characterized and each batch is normalized to its reference device without applied external voltage. The errors within a batch are due to the standard deviation of the respective devices. The errors after normalization to the sample without applied external voltage (V=0) are calculated using error propagation:

$$\Delta\left(\frac{b_i(V)}{b_i(V=0)}\right) = \left(\frac{\Delta b_i(V)}{b_i(V)} - \frac{\Delta b_i(V=0)}{b_i(V=0)}\right) \cdot \frac{b_i(V)}{b_i(V=0)} \tag{7.1}$$

with $b_i(V)$ the samples of the ith-batch and their respective standard deviation $\Delta b_i(V)$ as absolute errors. The error of the reference cell after normalization to itself is zero. The error after averaging all independent solar cell batches is then calculated as the mean value of the individual absolute errors.

In average, the improvement of the power conversion efficiency is as high as 25 % for the highest applied backward directed field compared to the reference cell. The main driving force is the fill factor, that increases by 15 % in average and the short circuit current with a mean increase of 10 %.

7.2.2 Absorption behavior

The functionality of the polymers after deposition under an electric field is tested via their absorption properties. The measurements are depicted in figure 7.7. The spectra show no strong deviations, which leads to the conclusion that the polymer properties remain unchanged and thus the material is not harmed by the electric field. An indication of the non-destructive intervention of the electric field was already given by the preserved open circuit voltage of the devices fabricated under the electric field. Further to that, the absorbance of all printed films exhibits the same typical features for P3HT:PCBM blends, namely the 0-0 transition at around 600 nm and the 0-1 and 0-2 absorption bands at around 550 nm and 510 nm.

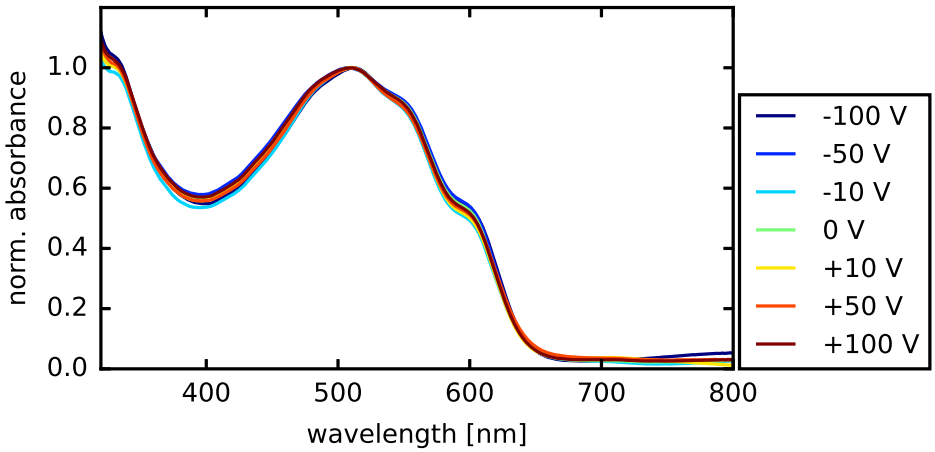

Figure 7.7: The absorbance spectra of the P3HT:PCBM films printed under different applied voltages between print head/top electrode and the ITO normalized to the main absorption peak at around 510 nm. All curves exhibit the typical crystalline peaks for P3HT.

7.2.3 Mobility measurements

Since the charge carrier mobility is of utmost importance for the functionality of organic electronics, its dependency on the preparation routes is investigated. The vertical hole mobility is measured using metal-insulator-semiconductor - charge extraction by linearly increasing voltage (MIS-CELIV). The resulting mobilities are depicted in figure 7.8.

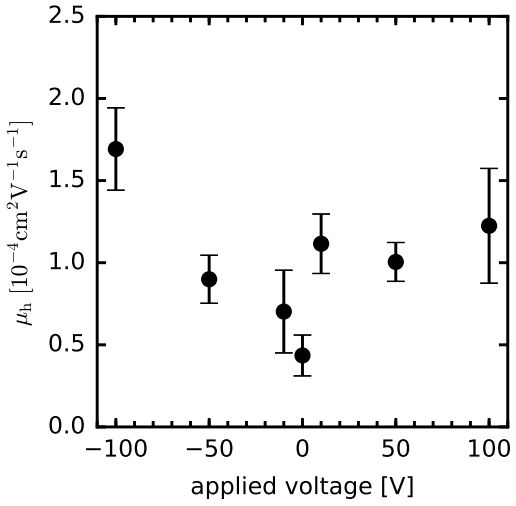

Figure 7.8: Vertical hole mobility of the active layers printed under different applied external electric fields. The mobility increases for applied electric fields compared to the one of the intrinsic active layer.

Already a low applied external electric field leads to a strong increase of the hole mobility. The direction of the applied field does not alter the mobility but the strength does. A reason might be found in the crystal properties of the respective films, as they strongly influence the charge transport and are thus subject of further investigations.

7.3 Morphological analysis

The inner morphology has an enormous impact on the functionality of organic solar cells (section 2.2). The presented I-V-curves show an s-shape for medium and high forward directed electric fields. This already indicates charge accumulation and might be due to changes in the inner structure. Furthermore, the charge carrier mobility increases with application of an electric field while deposition. To analyze the reason for this behavior, the inner morphology is investigated.

7.3.1 Crystallinity investigations

The charge transport in P3HT:PCBM films is well known to depend on its crystalline properties. [30, 192] A reorientation of the polymer crystals in an electric field was previously observed due to dielectric forces acting on the polymer. [191, 195] P3HT crystals

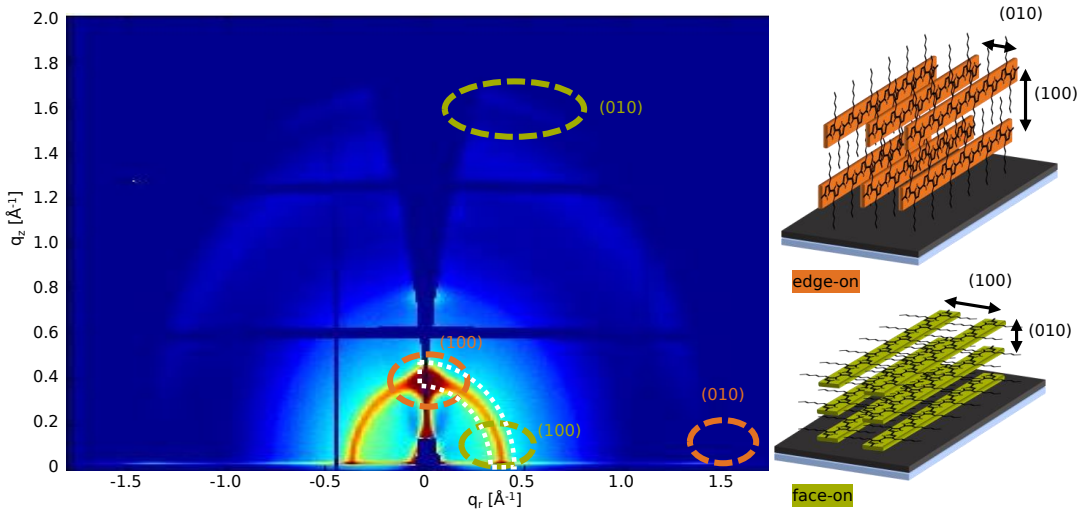

Figure 7.9: 2D GIWAXS pattern of P3HT polymer crystals exhibit typical diffraction patterns that allow to identify the orientation of the crystals. An edge-on crystal is schematically depicted in the top right corner. They exhibit a higher scattering intensity of the (100) planes in vertical direction and of the (010) peak resulting from the π-π stacking in horizontal direction. In contrast, the face-on oriented crystal (depicted in the bottom right corner) results in higher scattering intensities of the (100) plane in horizontal direction and of the (010) planes in vertical direction. The white dotted semicircle is the region at which the orientation analysis is performed.

typically orient in a face-on or edge-on orientation as schematically depicted in figure 7.9. In both configurations the polymer backbone is parallel to the substrate. For the former one, however, the side chains are oriented parallel to the substrate, while they are perpendicular for the latter one. The final orientation depends on the processing conditions. [30, 192] To obtain the crystal orientation, grazing incidence wide angle X-ray scattering (GIWAXS) experiments are performed. In a 2D scattering pattern as shown in figure 7.9 each of the configurations exhibit typical scattering signals.

The direct beam at $|\vec{q}| = q = 0$ Å^{-1} is blocked together with the signals of the grazing incidence small angle X-ray scattering (GISAXS) signal. The scattering signal from the (100)-planes of P3HT is found at $q \approx 0.38$ Å^{-1}. The (100)-planes of an edge-on oriented crystal are parallel to the substrate and the [100]-direction perpendicular, respectively. Therefore, a pronounced scattering is seen in the pattern in vertical direction at $q_z \approx 0.38$ Å^{-1}. On the other hand, for a face-on oriented crystal, the (100)-planes are perpendicular to the substrate and the [100]-direction parallel. Consequently, the 2D scattering pattern shows a contribution in horizontal direction at $q_r \approx 0.38$ Å^{-1}. Similarly, the scattering occurs in different directions for the (010)-planes. Isotropically oriented crystals, that exhibit no preferred orientation result in a scattering ring at the respective

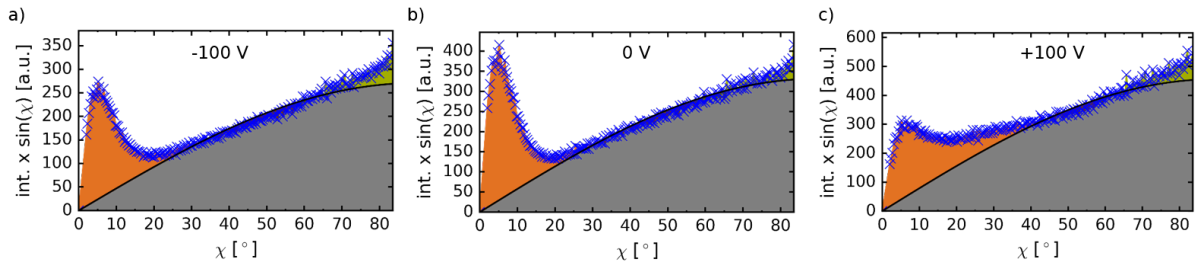

Figure 7.10: Azimuthally integrated intensity profiles along the azimuthal angle from 0° to 85°. Due to the in-plane isotropy of the P3HT crystals, the intensity profiles are sin(χ) corrected. Exemplary shown are the azimuthal profiles for (a) -100 V, (b) 0 V and (c) +100 V applied voltage. They gray lower area represents the isotropic crystals, the orange area at low χ results from the edge-on oriented crystals and the green area at high χ from face-on oriented crystals.

q-value of 0.38 Å^{-1}. To quantitatively analyze the orientation of the crystals, azimuthally integrated intensity profiles are extracted from the 2D patterns at q = 0.38 Å^{-1} as indicated by the white semicircle in figure 7.9. The obtained intensity profiles are exemplary depicted in figure 7.10 for the reference sample and the samples with highest electric field in forward and backward direction. The intensity profiles are background corrected to account for the amorphous material. Since P3HT behaves like an in-plane powder, which means that in the x-y-plane no preferred orientation occurs, the profiles are sinus corrected. [96, 118, 119] The isotropically oriented crystals result in the gray shaded area in figure 7.10, while the edge-on oriented and face-on oriented crystals result in orange and green shaded areas, respectively. The differentiation in edge-on or face-on is dependent on the azimuthal angle χ. It is split into vertical scattering ($\chi < 45°$) from the edge-on oriented and horizontal scattering ($\chi > 45°$) from face-on oriented crystals. Due to the inaccessible q-range at small angles χ, the values are interpolated to 0 for $\chi \to 0°$to calculate the area of edge-on oriented crystals.

The resulting ratios of face-on and edge-on oriented crystals and their sum to all crystals is shown in figure 7.11a. The sum of oriented crystals has an overall similar ratio to all crystals of a round 0.16 with a moderate drop after application of a low electric field. The ratio of edge-on oriented to all crystals however, strongly drops upon the application of an external field. On the other hand, the ratio of face-on oriented to all crystals strongly increases with electric field. From the data it is concluded, that the application of an external electric field reorients the crystals from edge-on to face-on orientation. The observations are in agreement with the findings in spin cast and solution sheared films in the presence of an electric field. [191, 195] The authors attribute the reorientation to dielectric forces acting on the polymer.

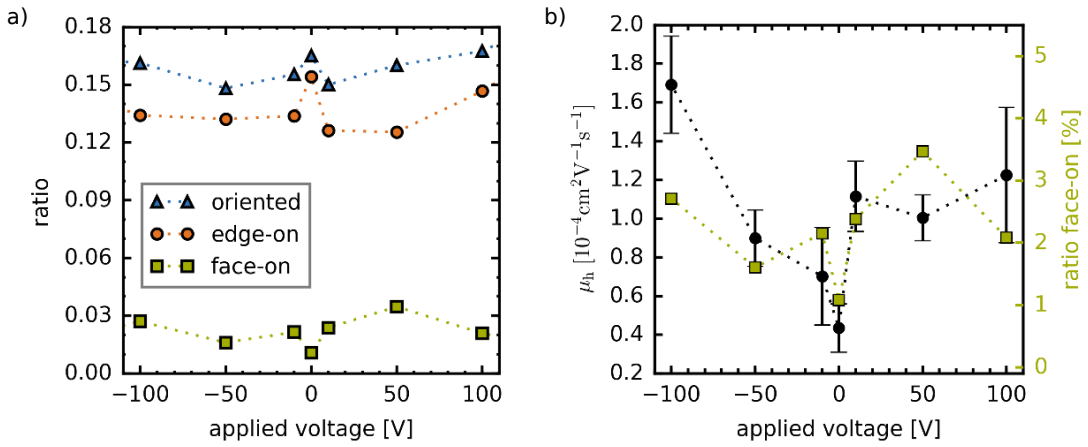

Figure 7.11: Results from the orientation analysis and their connection to the mobility. (a) The ratio of P3HT crystals oriented face-on (green squares), edge-on (orange circles) and the sum of both (blue triangles) to all crystals for different applied external voltages while printing. (b) Hole mobility of the devices (black circles, left axis) as determined in figure 7.8 for different applied voltages and the corresponding ratio of face-on oriented crystals (greens squares, right axis). Data points are connected by dotted lines to guide the eye.

The charge transport in polymer crystals is favored along the π-π-stacking in the [010]-direction. [30, 211] For a solar cell device with the charge transport perpendicular to the substrate, a face-on orientation of the polymer crystals is therefore preferred. To investigate the correlation between the mobility and the crystal orientation deduced from the GIWAXS analysis both are plotted in figure 7.11b. Similar to the reorientation of the polymer crystals, the vertical hole mobility increases with electric field as expected due to the favored charge transport in π-π-stacking direction.

7.3.2 Vertical material composition

The current voltage characteristics of the solar cells printed under the experimental conditions showed a strong s-shape for the forward directed electric field. The shape is explained by charge carrier accumulation and possibly due to enrichment layers of the materials in the active layer. Therefore, the vertical phase separation is investigated using X-ray reflectivity (XRR). The method allows to differentiate between variations in scattering length density (SLD) within the film. The SLD is related to the material composition. Figure 7.12a shows the characteristic reflection curves of the different films. The specular reflection of the X-ray beam is tracked. Depending on the SLD distribution within the film, the X-ray beam is reflected at interfaces of varying SLDs. This yields to fringes, the Kissing oscillations and a roughness dependent slope of the reflectivity data.

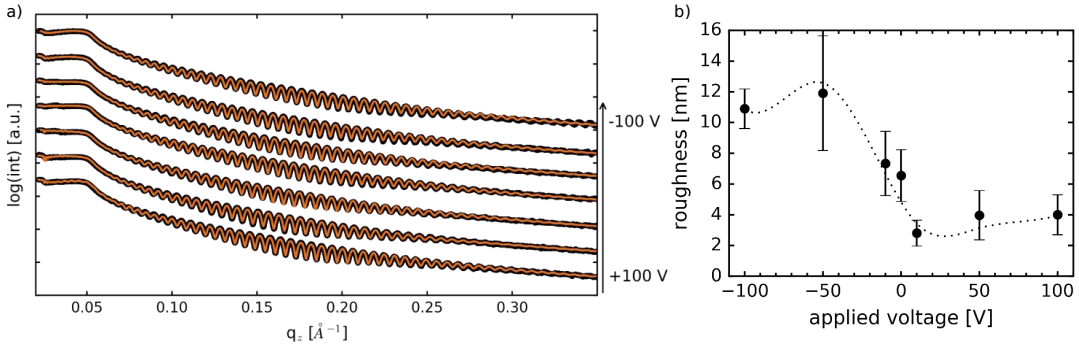

Figure 7.12: (a) XRR data for the different applied voltages with their respective fit (orange line) shifted along the intensity axis for clarity. (b) The roughness is obtained from the fits and the error bars are the corresponding fitting uncertainties. The dashed line is a guide to the eye.

The experimental data are fitted to a stacked layer model which accounts for the SLD, the roughness and the thickness of each layer. The respective fits to the data are shown in figure 7.12a. From the modeled data, the film roughness is obtained (figure 7.12b). The roughness upon application of a backward electric field increases from (7 ± 2) nm for no applied field to (11 ± 2) nm. In contrast, the roughness for a high forward electric field decreases to (4 ± 2) nm.

With the model, a vertical SLD profile is extracted as shown in figure 7.13a. It shows the SLD profile in a gray-scale coded composition model from the substrate (normalized depth 0) to the air interface (normalized depth 1). Measuring the pure P3HT and PCBM films provide the SLD of 10.9 x 10^{-6} Å^{-2} and 3.0 x 10^{-6} Å^{-2}, respectively. These values are in agreement with the calculated ones for a density of the materials of 1.2 g cm^{-3} for P3HT and 1.5 g cm^{-3} for PCBM and therefore of reasonable range. The presented SLD profiles can therefore be seen as material composition profiles in which black represents pure PCBM and white pure P3HT. The SLD profiles are transfered to volume concentrations of each material. The volume fraction χ_{PCBM} of PCBM in vertical direction is calculated from the fitted SLD profiles for each depth by:

$$SLD_{blend} \cdot 100 = \chi_{PCBM} \cdot SLD_{PCBM} + (100 - \chi_{PCBM}) \cdot SLD_{P3HT}$$

$$\Longleftrightarrow \chi_{PCBM} = \frac{(SLD_{blend} - SLD_{P3HT}) \cdot 100}{SLD_{PCBM} - SLD_{P3HT}}$$

The resulting depth profiles with the PCBM volume concentration are shown in figure 7.13b. As for the mean SLD of the XRR fits, the mean PCBM volume concentration is the same (52 ± 1) % for all differently prepared films. The intrinsic tendency of the films printed without electric field exhibits a PCBM enrichment at the film/air interface of up to 80 vol.-% accompanied by a very thin P3HT enrichment at the substrate interface. Ap-

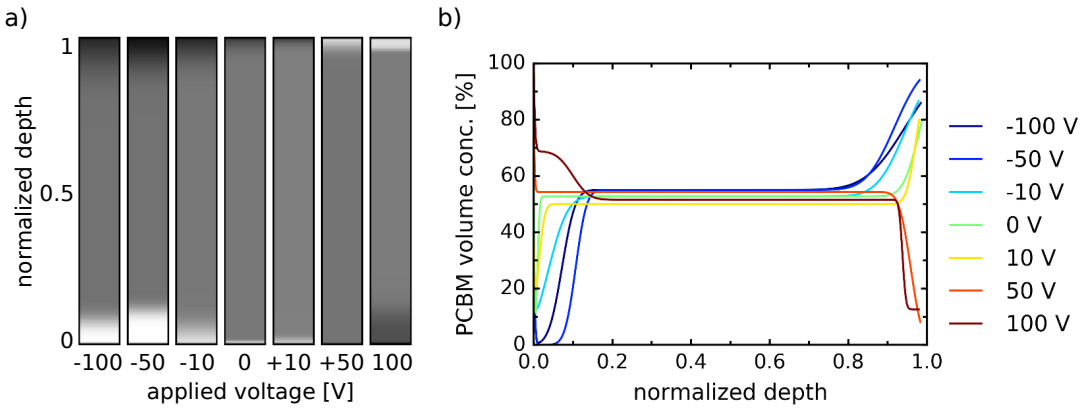

Figure 7.13: (a) Vertical material composition profiles obtained from the analysis of X-ray reflectivity (XRR) data for different applied voltages. Depicted are the scattering length density (SLD) profiles along with the film depth in gray scale code. In the representation, black depicts the SLD of PCBM and white the one of P3HT. The normalized depth 1 is the film/air interface, while 0 is the interface of the active layer to ITO. (b) Calculated volume concentration of PCBM as a function of the depth in the film derived from the scattering length densities of the XRR fits. The film/air interface is the normalized depth 1. An average of 50 % PCBM is conserved for all fits as expected for the prepared samples with a 1:1 P3HT:PCBM solution.

plying a reverse electric field (negative voltages) enhances the observed intrinsic tendency and the enrichment layers become more pronounced. For higher reverse fields, the P3HT layer at the substrate/film interface contains in average only P3HT while the film/air interface exhibits a high volume concentration of PCBM up to 90 vol.-%. In comparison, the forward electric field yields to an inversion of the intrinsic tendency. The substrate/film interface shows a PCBM enrichment up to 70 vol.-% and only around 10 vol.-% of P3HT at the film/air interface. Based on the geometry of the built solar cells, the enrichment is beneficial concerning the fill factor of the devices and therefore explains the observed changes in the produced solar cell devices. [212]

The origin of the varied vertical film composition is found in the electrophoretic mobilities μ_e of the involved materials in chloroform. The materials are separately measured in solution using electrophoretic light scattering. The found mobilities are 1.9 x 10^{-9} $m^2\,V^{-1}\,s^{-1}$ for P3HT and 4.0 x 10^{-9} $m^2\,V^{-1}\,s^{-1}$ for PCBM in chloroform. Thus, PCBM moves nearly double the speed of P3HT at a given electric field. In the vicinity of the print head, the electric field is very strong which results in a wide movement of the materials. Both P3HT and PCBM exhibit enough electrophoretic mobility to move through the entire film thickness within the experimental time. The experimental conditions are chosen such, that the material is fixed by electrophoretic forces against the forces due to evaporation. Similar

experiments using chlorobenzene instead of chloroform do not exhibit measurable electrophoretic mobilities. Hence, the findings suggest, that a specifically chosen combination of material and solvent enables the clearly observable vertical composition modification, which might be transferable to other material systems, including small molecules.

7.3.3 Lateral phase separation

For a complete insight into the inner film morphology, information about the lateral structures are needed. For that purpose, grazing incidence small angle X-ray scattering (GISAXS) is performed. Figure 7.14 shows the horizontal line cuts of the 2D scattering patterns at the Yoneda position of PCBM. Therefore, the scattering intensities are sensitive to PCBM and can be attributed to it. [87] To extract quantitative information, the reduced line profiles are modeled with two cylindrical form and corresponding structure factors. The respective models are plotted in figure 7.14 in orange color.

The form and structure factors are interpreted as sizes and corresponding distances of PCBM clusters inside the film in lateral direction. Figure 7.15a shows the structure sizes and figure 7.15b its corresponding distances. The larger structure size, which corresponds to PCBM rich domains, increases for backwards directed electric fields from (18.3 ± 0.8) nm (without field) to (19.3 ± 0.8) nm (-100 V), while it slightly shrinks for the highest forward field (+100 V) to (17.5 ± 1.0) nm. Their distances are barely influenced by the electric field and are around 50 nm.

The found changes in the structure size are - together with the knowledge of the ver-

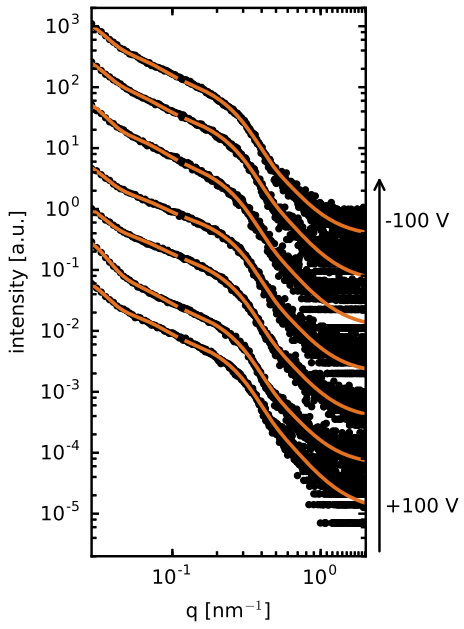

Figure 7.14: Horizontal GISAXS line profiles with fits obtained at the Yoneda position of PCBM to be sensitive for the respective material. The intensity profiles contain information about lateral structures inside the film. The orange lines are the modeled data of the GISAXS cuts.

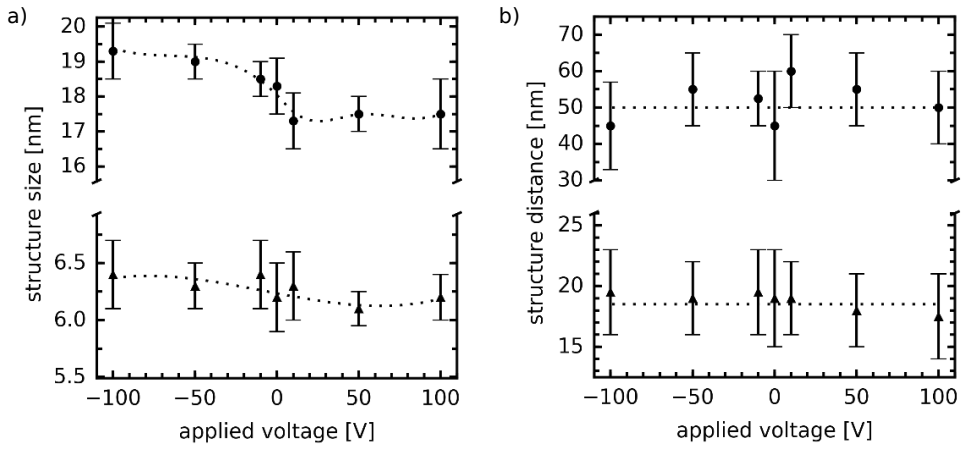

Figure 7.15: Lateral domains obtained from the GISAXS measurements. (a) The structure sizes are obtained from the form factors of the fits. (b) The corresponding structure distances obtained from the structure factors. The domains are attributed to PCBM domains in the film. the dashed lines are guides to the eye.

tical composition from XRR measurements - interpreted as compression and stretching of PCBM domains for backward and forward directed electric field. The enhancement of the backward directed electric field pushes the PCBM domains towards the film/air interface. On the other hand, forward directed electric fields, pull the PCBM domains towards the films/substrate interface leading to a stretching of the domains, that are intrinsically rather present at the film/air interface.

7.4 Resulting reconstruction of inner film morphology

The findings from the investigation of the inner structure via X-ray methods together with the functionality of the produced organic solar cells, are interpreted in a reconstruction of the inner film morphology to visualize the impact of the electric field. The findings are summarized in a schematic illustration of the morphology in figure 7.16. The model is chosen to represent the percolation paths of the charge carriers as necessary for the functionality of the solar cells. The film thickness is around 150 nm. The black areas correspond to PCBM rich domains, while the white areas represent the P3HT rich domains. PCBM enrichment layers are found for the intrinsic sample printed without electric field as well as for the sample printed under backward electric field at the film/air interface. For latter one, this tendency is enhanced with around 90 % of PCBM at the surface. Printing under forward directed electric field, on the other hand, causes an inversion of the vertical structure and a PCBM enrichment at the substrate/film interface is observed.

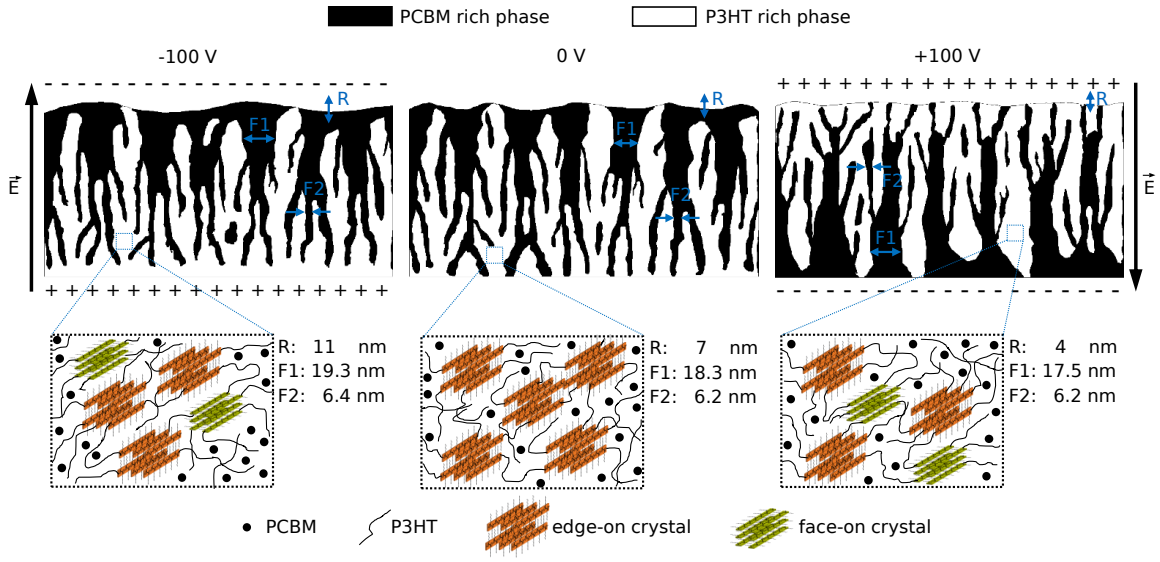

Figure 7.16: Schematic illustration of the influence of electric field application on the morphology of the organic thin films. Depicted are the morphologies of the films for the intrinsic tendency obtained by printing without electric field, and forward and backward directed electric field with highest applied voltage. The illustrations are reconstructed from GIWAXS, GISAXS and XRR data and are displayed to show the percolation paths of the film. The black/white representation in the upper row shows the phase segregation, vertical film composition and roughness as reconstructed from GISAXS and XRR data. Black color represents the PCBM rich domains, while white color represents the P3HT rich parts. The magnifications of the P3HT rich phases in the bottom row illustrate the reorientation of P3HT crystals towards face on orientation upon application of an electric field as seen by GIWAXS investigations.

All the found enrichment layers do not contain one type of material, but a mixture in different ratios. An exception is found for the high backward electric field, for which the enrichment of the P3HT at the substrate/film interface consists purely of P3HT. The top film roughness is obtained from modeling the XRR data and increases for backward directed electric fields. The representation of the PCBM domains shows the vertical compression and stretching of the material under backward and forward fields, respectively. Looking closer into the P3HT rich domains presents the reorientation of edge-on oriented P3HT crystals to face-on oriented ones. This representation clearly shows the positive influence of the backward directed electric field on the photovoltaic performance of the standard solar cells. An intrinsic blocking layer of both, P3HT and PCBM at the bottom and top interface, respectively, prevents charge carrier recombination at the electrodes and enables an improved charge carrier transport to prevent accumulation.

In conclusion, a possible process including the application of an electric field during printing is introduced. The process is adapted to known methods in industry and there-

fore well suited for an applied, up-scalable technique. Applying the process to a model system, the crystal orientation is influenced and edge-on oriented crystals reorient to face-on orientation. Furthermore, the vertical film composition is tuned by a proper choice of material and solvent, that, in combination, exhibit an electrophoretic mobility. This yields to an enhancement or an inversion of the intrinsic tendency of the film structure, depending on the direction of the applied electric field while lateral structures are conserved. This optimization is implemented into organic solar cells and leads to a power conversion efficiency increase of 25 %. The findings suggest that, by a proper choice of material and solvent, different combinations can be treated using a similar process. This also includes small molecules with the potential to further increase their performance in organic solar cells. Electrophoresis assisted printing therefore provides an efficient and low cost approach to optimize the active layer morphology.

7.5 Summary

One of the major advantages of organic solar cells and therefore a unique selling point is the possibility to process out of solution. This allows for advanced printing and spraying techniques. In focus are methods, that are industrially relevant. In this chapter, a method is presented, that is transfered from an industrial coating process to the production of organic solar cells. Electrophoretic assisted printing enables to actively influence the structure formation process. With a model system of a blend of poly(3-hexylthiophene) (P3HT) and [6,6]-phenyl-C61-butyric acid methyl ester (PCBM) the influence of an electric field on the structure formation is investigated. The application of the field during thin film deposition leads to a reorientation of the polymer crystals from edge-on to the more favorable face-on orientation. Along with that, the hole mobility is increased and the dependency of face-on orientation with the changes in charge carrier mobility is analyzed. Due to the intended combination of P3HT:PCBM in chloroform as solvent, the material exhibits an electrophoretic mobility. This property is used to actively move the polymer and fullerenes within the wet film. It is shown that a vertical modification of the thin films is possible, which leads to intrinsic blocking layers in the active film. Along with that, the lateral structures are preserved and a stretching and compression of PCBM domains are found for forward and backward directed electric fields, respectively. The optimization of the inner film morphology yields an improvement of the fill factor of the solar cells by 15 % and the short circuit current density by 10 %. The overall performance of the solar cells is thus improved by 25 %. The findings indicate that electrophoretic assisted printing can be transferred to different material combinations, including small molecules, that exhibit an electrophoretic mobility in the respective solvent.

8 Influence of solvent atmosphere on film evolution

Printed organic solar cells have gained tremendous interest over the last years. [13,15,213, 214] A lot of progress in terms of power conversion efficiency (PCE) was achieved during that time, exceeding 10 % efficiency. [215–217] The combination of the high PCE with the low cost and the ease of large area printing led to a high interest in academia and industrial research. One of the most investigated material systems for organic solar cells consists of poly(3-hexyl-thiophene) (P3HT) as donor polymer and [6,6]-phenyl-C_{61}butyric acid methyl ester (PCBM) as acceptor fullerene. [21,22,137,189,218,219] For a better device performance, a key factor to address is the inner morphology as described in chapter 2.2. Several approaches intend to influence the active layer morphology in terms of crystallinity and phase separation. Thermal annealing has shown to be an efficient route to improve the morphology and thus the device performance. [28,158,159,220,221] Moreover, the simultaneous application of an electric field during annealing is highly beneficial for the systems under investigation. [194–197] The choice of solvent and solvent additives influences the active layer morphology. [83,162,222–224] Another approach is the controlled slow growth of the active layer, which is also referred to as solvent annealing. [137,189,225] The slow growth rate results in an improved power conversion efficiency upon an increased absorption and hole mobility. [189] It is found that the π-conjugated structure of P3HT is improved upon reduced growth rates. [137, 226] To achieve the improved structure, Li et al. covered the samples after spin coating. [137] This approach using spin coating as deposition method, however, is not easily up-scalable, which is necessary for commercial applications of organic solar cells. So far, a lot of effort has been spent on understanding the mechanisms of film formation. Most of these investigations were performed using *in situ* characterization methods like reflectometry, absorption measurements or X-ray scattering. [40, 142, 218, 227, 228] Here, the process of a slow growth rate of the photoactive layer is transferred to an up-scalable printing process, allowing high throughput of the produced solar cells. We monitor the structure formation *in situ* with highly time resolved X-ray scattering experiments. The findings are transfered to a model representing the evolution of the film structure.

Figure 8.1: This chapter describes how to control the solidification process using defined atmospheres while printing.

To manipulate the drying kinetics of the printed thin film, the printer setup is modified with an environmental chamber, allowing full control of the chemical vapor composition surrounding the deposited film as explained in chapter 5 and respective reference [144]. A detailed description of the chamber is found in chapter 5.3. The aim of the work presented in this chapter is to control the solidification process in printed organic thin films (figure 8.1) with defined atmospheres surrounding the sample under investigation.

The film drying time is doubled upon the usage of a solvent enriched gas stream compared to the dry gas stream. The structure evolution is divided into four stages. The results show the differences in stage two and three of films printed under different atmospheric conditions. The experimental procedure is described in detail in section 8.1. The crystallization of the polymer in the different atmospheres is followed *in situ* using GIWAXS (section 8.2.1). Moreover, the phase separation and fullerene aggregation is investigated with GISAXS (section 8.2.2). The findings are combined and their influence on the structure formation model is described in section 8.2.3. The findings of the investigations on the influence of a solvent atmosphere on the film evolution are finally summarized in section 8.3.

8.1 Experimental details

For *in situ* studies, the time resolution of state-of-art imaging techniques like atomic force microscopy (AFM) or transmission electron microscopy (TEM) is not sufficient to follow the drying kinetics of thin organic films. For the study in this chapter, we used X-ray scattering under grazing incidence (section 2.4.3). To control the solidification process a custom slot-die coating setup is constructed. It is shown in section 5.3 and the respective reference [144]. The utilized setup is shown in figure 8.2.

Materials and sample preparation: The solution for the active layer is produced as described in chapter 4. The solution is slot-die coated on acidic cleaned silicon wafers spin coated with PEDOT:PSS with a thickness of around 40 nm. The wafers are cut into approximately 100 mm long and 20 mm broad stripes and placed on the printer's

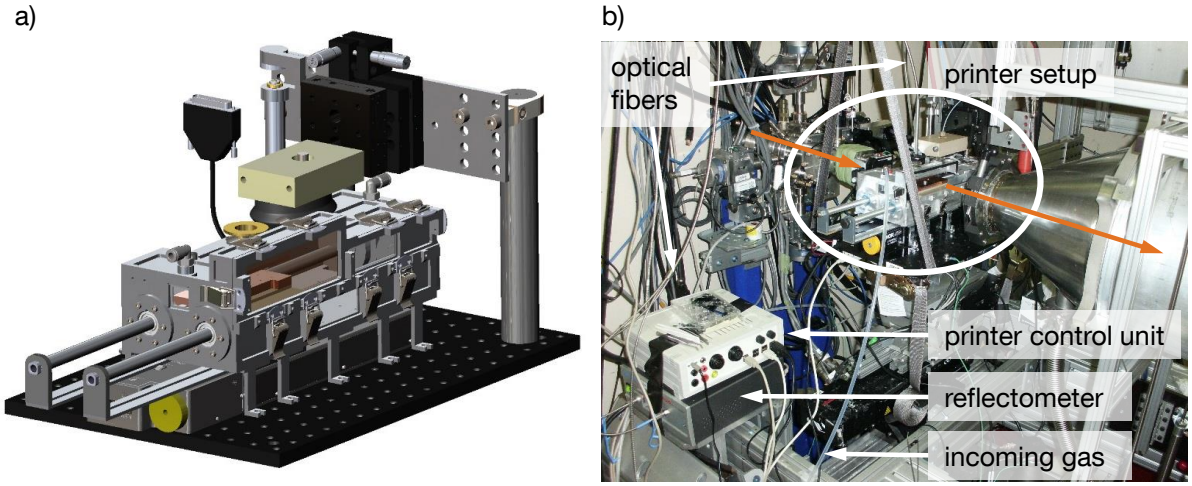

Figure 8.2: The utilized experimental setup. (a) Drawing of the printing setup including the atmospheric control chamber. The view allows to identify the large exit window for the X-ray scattering signal. Reproduced from [144], with the permission of AIP publishing. (b) Photograph of the experimental setup in the synchrotron beamline. The orange arrows schematically depict the X-ray path.

sample stage. The substrates are fixed on the sample stage with headless screws without application of a vacuum. The solution is fed into the slot-die head with a syringe pump at a rate of 0.2 $\mathrm{ml\,min^{-1}}$. The distance of the slot-die head to the substrate is set to around 300 µm. A printing speed of 10 $\mathrm{mm\,s^{-1}}$ results in a film thickness of around 300 nm. The solvent atmosphere in the chamber is controlled by combining dry helium with solvent-saturated helium in the desired ratio. For this purpose, two gas tubes are connected to the chamber. One contains the dry gas and the other one solvent-saturated gas after passing a washing bottle filled with chlorobenzene. For the experiments presented here, two environmental settings are used, comparing a completely dry helium gas with a chlorobenzene vapor enriched helium gas streaming above the sample. The flow rate of the helium is set to 5 scfh (2.36 $\mathrm{l\,min^{-1}}$).

In situ scattering experiments: The *in situ* scattering experiments are performed at beamline 7.3.3 at the Advanced Light Source (ALS). [117] The wavelength for these experiments is λ= 1.24 Å which corresponds to an energy of 10 keV. The signal is detected by a Pilatus 2M detector with a frame rate of 0.5 $\mathrm{s^{-1}}$. This frame rate includes data recording of 0.47 s and a readout time of 0.03 s. Directly after the coating process, the incident X-ray beam impinges the sample continuously at a fixed distance from the print head and follows the drying process. The time 0 is set to the occurence of the first scattering pattern, which occurs around 1-3 s after the deposition of the solution through the slot-die head. Recording the final film for more than 200 s at the same position on the

sample shows no changes in the scattering pattern. This ensures that no beam damage occurs which would influence the organic film and thus the results of the experiment.

The incident angle for the experiment is set to 0.35°. To detect both the GIWAXS and the GISAXS signal at the same time, an intermediate sample to detector distance (SDD) of 177 cm is chosen. This setting allows to follow the (100) peak of the P3HT polymer, which is sufficient for the characterization of the crystallization process. The data treatment of the GIWAXS signal is performed with GIXSGUI 1.6.1 from the Argonne National Laboratory which performs all the corrections necessary for a correct reduction as described in section 2.4. [94–96] To analyze the GISAXS signal, the data are reduced using DPDAK version 1.2.0 from the Deutsches Elektronen-Synchrotron (DESY) in Hamburg. [120] For the analysis, the shoulder in the horizontal cut is tracked by plotting Iq^2 versus q after background subtraction and fitting a Gaussian function. [228–231] With the center of the shoulder, the average center to center distance of the scattering centers is determined. The results of the shoulder tracking serve as input for modeling the data in the framework of the distorted wave Born approximation (DWBA) and the local monodisperse approximation (LMA) based on contributions from three substructures each described by a certain shape of a form factor (average structure sizes) and a structure factor (average center-to-center distance) according to a 1d paracrystal as proposed by Hosemann et al. [108] Two structures are kept constant as local background of the scattering signals and the main feature arising from PCBM aggregates is followed. More details about the model function can be found in section 2.4. Before modeling, the data are logarithmically binned with 45 bins as introduced in chapter 6.

8.2 In situ characterization

The influence of the surrounding atmosphere on the thin film solidification is investigated for two cases. The first one is a film printed under fully dry gas conditions (DGC), whereby a steady flow of dry helium gas is present during the solidification. The second case is a film printed under solvent enriched gas conditions (SGC), whereby the helium gas is enriched with chlorobenzene vapor by passing a washing bottle filled with solvent before streaming above the printed film during solidification. The structure formation process is followed on different length scales. Therefore, an intermediate sample to detector distance is chosen, allowing for simultaneously measuring grazing incidence small angle X-ray scattering (GISAXS) and the main grazing incidence wide angle X-ray scattering (GIWAXS) peak arising from the (100) planes of poly(3-hexyl-thiophene) (P3HT) crystals. Figure 8.3 shows the 2D detector patterns of the final films summed up to in total 60 s illumination for the film printed under DGC (figure 8.3a) and under SGC (figure

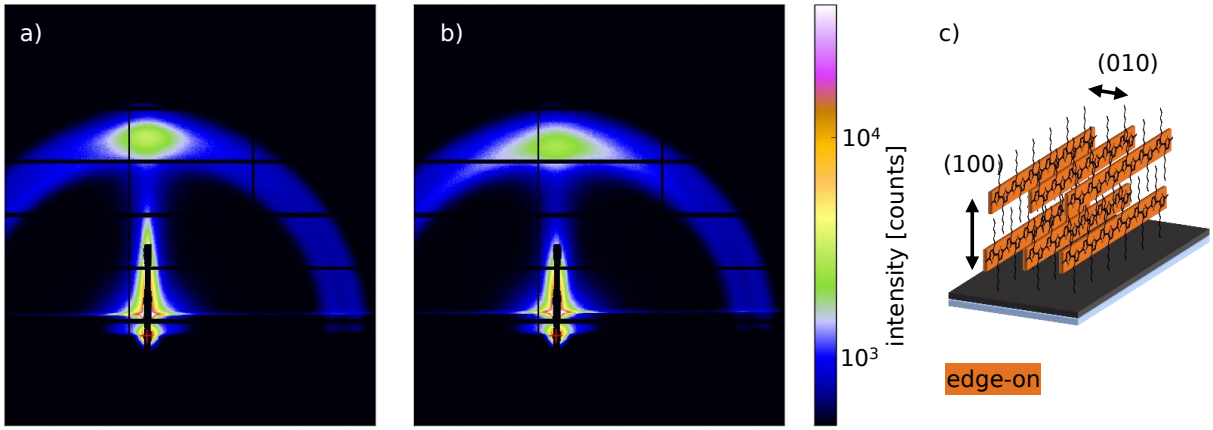

Figure 8.3: 2D detector patterns of the summed final films. (a) The pattern of the film printed under dry gas conditions (DGC). (b) The film dried under solvent enriched gas conditions (SGC). (c) Schematic drawing of a P3HT crystal in edge-on configuration with the lattice plane directions.

8.3b). Differences between both experimental routes are already visible in the detector patterns. The blue ring results from signals of Kapton® used for the entry and exit windows of the environmental chamber and the flight tube. This signal is superimposed by the scattering of the polymer backbones. In vertical direction, the (100) signal resulting from edge-on oriented P3HT crystals is visible as green-yellow scattering peak. At first view, the (100) peak of the sample printed under SGC (figure 8.3b) exhibits a wider azimuthal distribution compared to the sample printed under DGC. The schematics in figure 8.3c depicts an edge-on oriented P3HT crystal with the lattice planes. Moreover, the GISAXS signal shows differences, especially in vertical direction. At the same film thickness, the film printed under DGC exhibits a higher intensity especially visible above the beam stop.

In the following, the scattering patterns are investigated in detail. The focus is put on the time development of the patterns. First the (100) peak related to the crystallization process of the polymer is analyzed (section 8.2.1). Thereafter, the phase separation is investigated in section 8.2.2. The findings are then discussed and implemented into a structure evolution model in analogy to the one obtained for the temperature investigations in section 6.2.4.

8.2.1 Polymer crystallization process

An eye-catching feature in the final film scattering patterns in figure 8.3 is the azimuthal broadening upon printing under SGC. The first closer look is therefore to the time development of the azimuthal scattering intensity. Figure 8.4 shows a 2D color plot of the azimuthally integrated intensity for the film printed under DGC (figure 8.4a) and the film printed under SGC (figure 8.4b).

While the maximum intensity for the film printed under DGC is reached after approximately 24 s, it needs further 14 s to reach a wide azimuthal spread in the case of SGC. The positions in the 2D color map are marked with white dashed lines in the respective

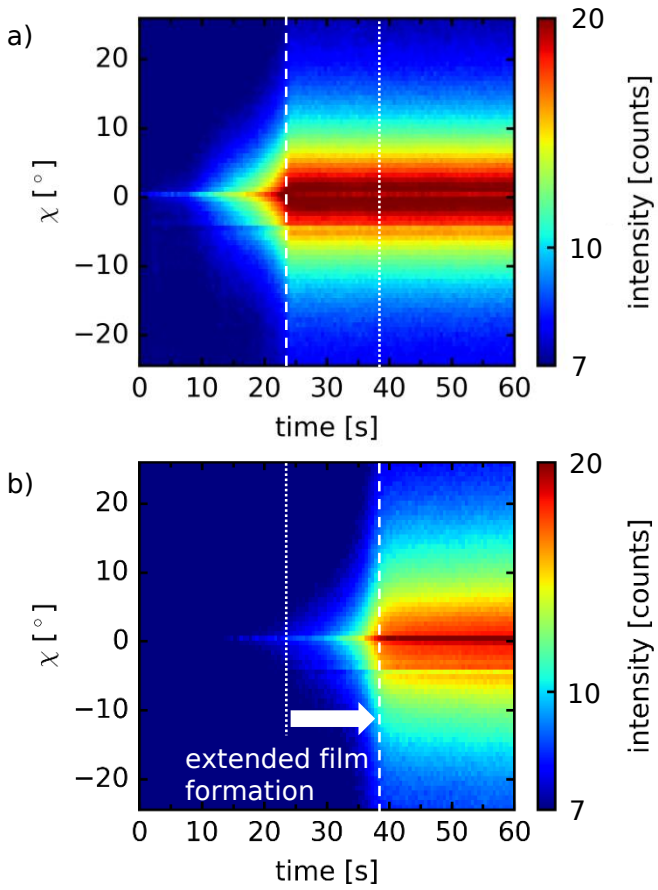

Figure 8.4: 2D color plots of the azimuthally integrated (100) signal with time. (a) Azimuthal intensity versus time for the film printed under dry gas conditions (DGC). The maximum χ-distribution of the signal is reached after around 24 s (white dashed line). (b) Azimuthal intensity versus time for the film printed under solvent enriched gas conditions (SGC). The maximum χ-distribution of the signal is only reached after around 38 s (white dashed line). For comparison, the maximum distribution of each film is indicated with the white dotted line.

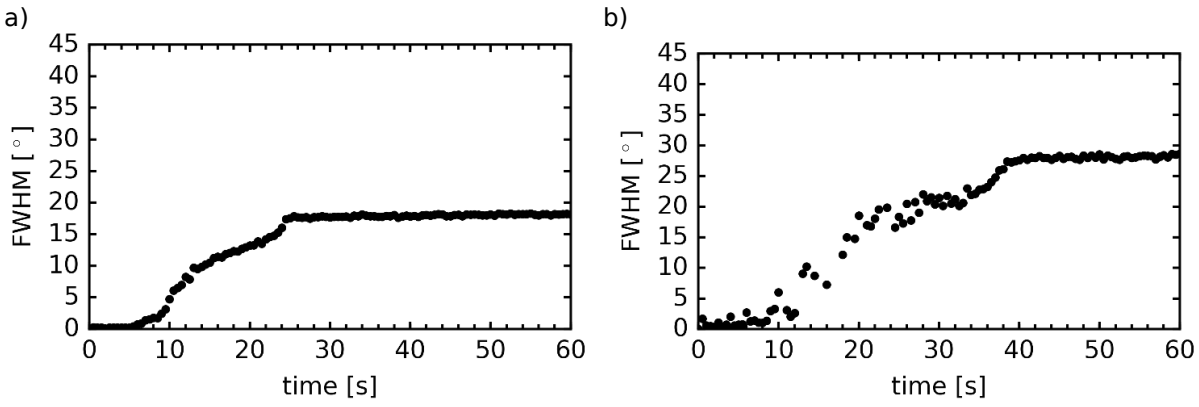

Figure 8.5: Full width at half maximum (FWHM) of the azimuthally integrated (100) peaks of (a) the film printed under dry gas flow and (b) the film printed under solvent enriched gas flow. The final broadness is found at the plateau after approximately 24 s and 38 s for the dry and solvent enriched environment, respectively. The FWHM of the film printed under enriched gas flow exhibits a larger FWHM compared to the one printed under dry gas flow.

pattern. A further noticeable feature for the azimuthal broadening of the film printed under SGC is the softer transition between initial and final azimuthal spread. The azimuthal distribution continues to broaden even until 60 s, while it instantly reaches the final χ-distribution in the case of dry gas.

The development of the azimuthal distribution is quantified by fitting the intensity versus the azimuthal angle χ with a Gaussian peak. The time development of its full width at half maximum (FWHM) is plotted in figure 8.5. The highest FWHM is reached after 24 s for the DGC printed film (figure 8.5a), while it is delayed to 38 s for the SGC film (figure 8.5b), as already estimated in the 2D GIWAXS pattern. The FWHM of the SGC printed film with 28° is around 10° larger compared to the one of the film printed under DGC. The investigated peak in vertical direction is a feature of the edge-on oriented P3HT crystal (as depicted in figure 8.3c). The broader azimuthal signal is an indication of higher disorder in orientation of the polymer crystals.

The polymer crystal orientation is further investigated by integrating over the complete azimuthal intensity profile. Analyzing the area under the scattering curve yields information about the ratio of edge-on vs. face-on and isotropically oriented crystals ($\chi < 45°$) of the complete crystallized polymer. The resulting time development of the edge-on ratio with time is shown in figure 8.6. As indicated by the FWHM of the curves, the film printed under SGC exhibits a 15 times higher ratio of edge-on oriented polymer crystals

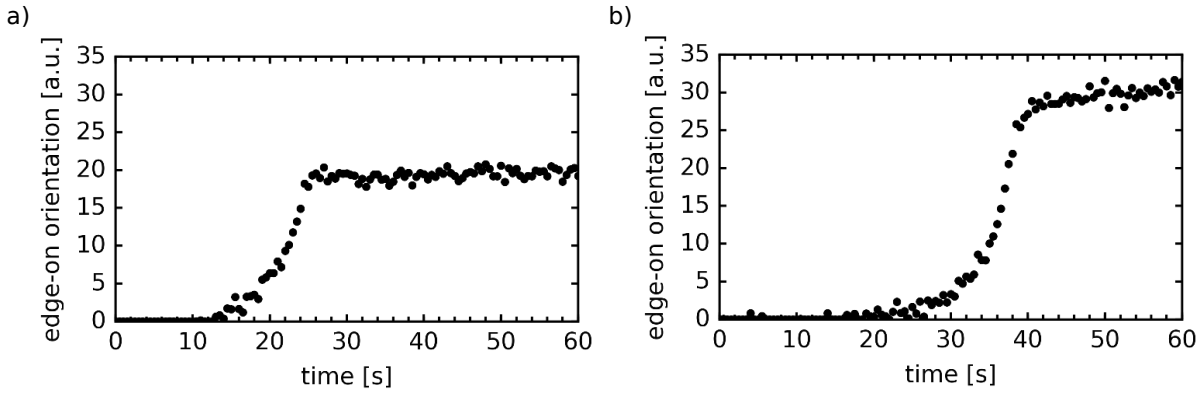

Figure 8.6: Calculated edge-on orientation of the films with time. (a) For the DGC film, the plateau is reached after around 24 s. In comparison, the SGC film (b) shows a higher edge-on orientation, which increases even further after 38 s.

compared to the DGC film. It should be noted that the time resolution and the involved low scattering intensities do not facilitate the determination of the face-on oriented ratio.

Interestingly, the development of the edge-on ratios shows different behaviors. While the DGC sample rapidly reaches the final state at around 24-26 s (figure 8.6a), the SGC sample highlights a softer transition around 38-46 s (figure 8.6b). This most likely is due to the decreased evaporation rate, after portions of the solvent have already evaporated into the atmosphere, which further increases the solvent content in the environment surrounding the sample. This leads to a deceleration of evaporation and thus leaves enough mobility to the polymer crystals to further rearrange. An increasing azimuthal distribution called mosaicity for slowly dried films at lower temperatures was also observed by Sanyal and coworkers. [39]

Apart from the crystal orientation, the packing of the crystals themselves and their formation are of interest. The time development of the vertical intensity profiles of the (100) peak is tracked and depicted in figure 8.7. Initially, two signals arising from the Kapton® before and after the sample are seen at 3.6 nm^{-1} and 4.1 nm^{-1}. These signals are clearly seen in both scattering patterns, of the DGC and SGC sample, respectively. The film printed under DGC develops its (100) signal within the time span of 12-25 s (blue-turquoise scatter points in figure 8.7a). On the other hand, for the SGC sample, the (100) signal arises between 20-44 s (yellow-orange scatter points in figure 8.7b) and thus clearly at a later stage with a longer duration. Interestingly, the q-position of the developing (100) peak shifts to smaller q-values for the SGC sample compared to the DGC sample indicating a larger spacing of the polymer backbones.

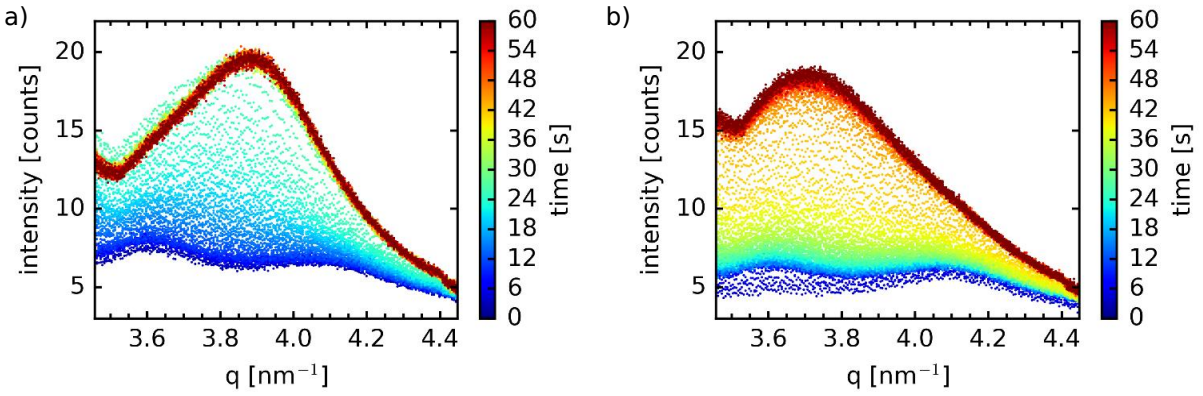

Figure 8.7: Development of the scattering profile in vertical direction with time during the first 60 s after printing. (a) Vertical scattering intensity profiles for the DGC film. The peak evolutions occurs in the blue-turquoise time regime corresponding to 20-30 s. (b) Scattering intensity profiles for the SGC film. The peak evolution is shifted towards the yellow-orange time regime between 30-45 s. The time scale is the same for both figures.

For quantification of the scattering peak development, the peak is fitted with a Gaussian function. Therefore, the local background is subtracted, which consists of the tail of the GISAXS signal at low q and the scattering of the Kapton® windows. The resulting parameters of the Gaussian fits with time are shown in figure 8.8. The intensity is normalized to the final value and is interpreted as a measure of the crystallization. The peak center is inversely related to the spacing of the (100) planes of the backbones d via $d = 2\pi q^{-1}$. The full width at half maximum (FWHM) can be related to the crystal size D with the Scherrer equation 2.34:

$$D = \frac{2\pi \cdot 0.9}{FWHM}. \tag{8.1}$$

As described in section 2.4.3, this size only provides a lower limit, as effects like instrumental broadening and paracrystalline disorder are not taken into account.

For the DGC sample (figure 8.8a), the final d-spacing of the polymer backbones is around (1.62 ± 0.01) nm and the lower limit of the crystal size in vertical direction approximately (14.7 ± 0.4) nm. For the SGC sample, (figure 8.8a), the final d-spacing of the polymer backbones is around (1.67 ± 0.01) nm and the lower limit of the crystal size in vertical direction approximately (14.3 ± 0.8) nm. The values are in agreement with other studies. [142, 218, 232, 233] It was also shown that solvent vapor leads to an increase in the d-spacing. [137, 229, 231]

Focusing on the development of the scattering signal of the DGC sample (figure 8.8a), it can be divided into three distinct stages. Initially, no scattering peak from the crystal

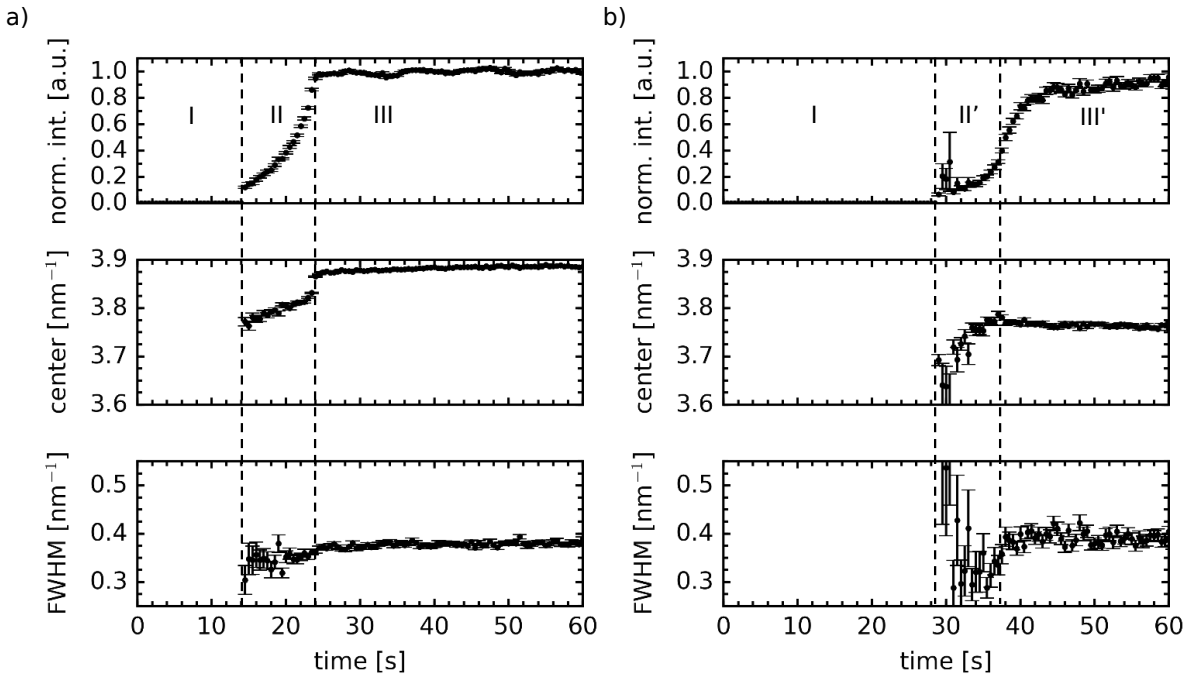

Figure 8.8: Fitting parameters for the vertical intensity of the (100) peak for (a) the DGC sample and (b) the SGC sample. Depicted are the parameters of the Gaussian fit; its amplitude normalized to the final intensity, the center and the FWHM. The onset of the scattering signal is indicated by the first vertical dashed line after stage I. The subsequent stage II ends after reaching the final intensity. For the sample printed under enriched atmosphere, this stage differs (denoted as II') and ends when the maximum of the peak center is reached. While the peak position shifts during stage III for the sample printed under dry gas flow, the intensity increases for the sample printed under solvent enriched gas (stage III').

is detected due to the well dissolved solution. This first stage is dominated by the evaporation of the solvent. The evaporation yields an increase in solid concentration until the solubility limit is reached. This limit was seen to be around 160-190 mg ml^{-1} in chlorobenzene and 70-130 mg ml^{-1} in dichlorobenzene. [172, 218] During that stage I, the molecules can freely move in the solution. The first scattering signals arising from the (100) spacing of the polymer backbones are seen after 14 s. This is the initialization of stage II, during which a nucleation and crystal growth process takes place. The peak center is initially found at q $\approx$ (3.77 $\pm$ 0.08) nm^{-1} or a d-spacing of (1.67 $\pm$ 0.04) nm. The q-position first slightly increases with time, and then rapidly increases towards the end of stage II. The rapid increase at the end of stage II was also observed in previous experiments and assigned a stage on its own in chapter 6. [142] The larger d-spacing of the initial nuclei is assigned to the formation of solvent swollen nuclei. With ongoing solvent evaporation,

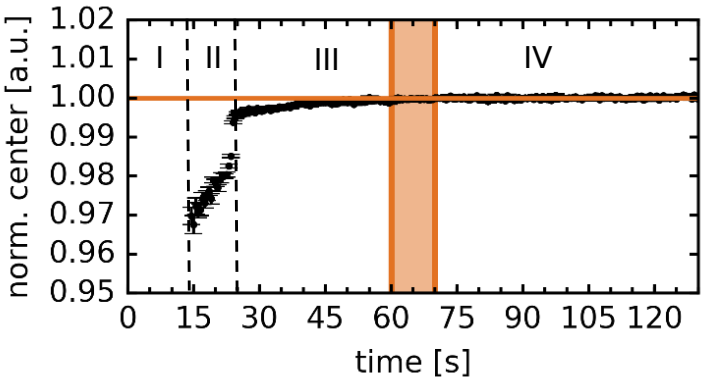

Figure 8.9: Peak center position normalized to the final peak center of the film printed under dry gas flow. The peak position shifts to higher q-values indicating a self-annealing process. The final crystal structure is obtained at stage IV.

the crystallite packing becomes more dense as seen in the shifting q-position of the peak during stage II. The evaporation consequently leads to a reduced mobility of the P3HT polymer chains in the solution. Gu et al. explain the change in mobility by the glass transition temperature T_g, which describes the transition temperature for the polymer chains to transit from the glassy to the rubbery state. [218, 234, 235] The evaporation of the solvent from the film steadily increases T_g of the polymer solvent mixture, thereby consequently reducing the polymer mobility. The latter one is required for polymer crystallization in terms of mass transport and rearrangement of the polymer chains. [236] The maximum in amplitude is reached after 24 s indicating the end of the crystallization process in stage II, which takes around 10 s, and the beginning of stage III. During stage III, the residual solvent escapes the film as known from several studies. [40, 142, 218] This yields to an improvement of crystal packing. Figure 8.9 shows the development of the normalized peak position of the DGC sample for a longer time scale normalized to its final value. After the strong increase of the peak position at the end of stage II, it further slightly increases during stage III. This was previously also referred to as self-annealing of the polymer crystal. [40, 142] While the crystal growth has already ended, the packing of the crystals improves until around 60-70 s. The formation of the final film is completed in stage IV.

The SGC sample exhibits the same stage I (figure 8.8b), during which the solvent in the freshly printed film evaporates. Due to the surrounding atmosphere, which contains solvent enriched gas, the partial pressure of chlorobenzene is already quite high. This leads to a significant decrease in the evaporation rate of the solvent from the coated film. This is clearly seen by the extended stage I, which, instead of 14 s for the DGC sample, lasts for 28 s. Interestingly, the structure formation in the next stages differs completely

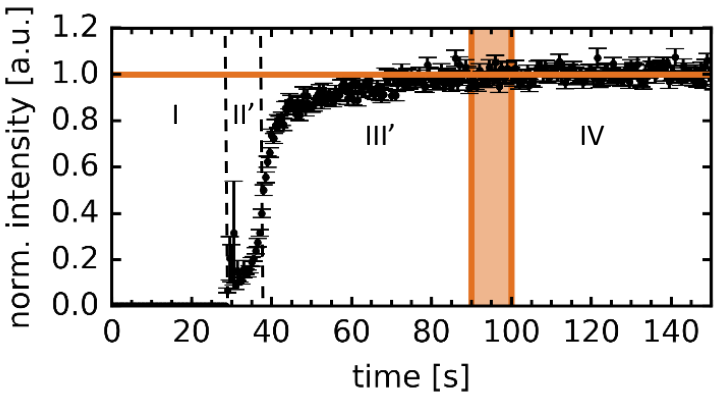

Figure 8.10: Normalized intensity of the Gaussian peak fit of the sample printed under solvent enriched gas flow. The horizontal orange line indicates the final amplitude. The vertical bar shows the time span, at which the final amplitude is roughly reached, initializing stage IV.

from the one in the DGC sample. After the solubility limit is reached, the first polymer nuclei form, initializing the next stage II'. Similarly to stage II for the DGC sample, the initial nuclei exhibit a larger backbone spacing of (1.80 ± 0.5) nm, at $q \approx (3.5 \pm 0.1)$ nm^{-1}. The nuclei are more loosely packed compared to the DGC samples. Most likely, this is due to the stronger swollen state of the polymer crystals that arises due to the slower escaping solvent molecules. During stage II', the q-value steadily shifts to larger values, until it reaches a maximum at $q \approx (3.78 \pm 0.01)$ nm^{-1} after around 28 s. This corresponds to a real space distance of the polymer backbones of (1.662 ± 0.005) nm, which is the packing of the initially formed nuclei in that sample. However, this point is not characterized by a maximum in intensity. Moreover, the intensity has yet only reached around half of its final intensity. Hence, the crystallization process has not yet ended, but the crystals already exist in their closest packing. The next phase, stage III', therefore starts with the crystals reaching their closest packing at approximately 38 s. The duration of stage II' of the SGC sample is of similar duration (10 s) with the DGC sample. During stage III', the intensity of the scattering peak increases further, while the FWHM, related to the crystal size, stays constant. This indicates the ongoing formation of crystals rather than a growth of crystals already present. Due to the low evaporation rate of the residual solvent, this process continues for a longer time, as seen in figure 8.10 in the zoom in of the normalized intensity of the SGC sample. The final amplitude is reached after 90-100 s, which leads to the final morphology in stage IV. As already observed for the mosaicity in figure 8.6b, the transition to the final stage is very smooth due to the slowly evaporating solvent.

8.2.2 Phase separation and fullerene aggregation

To further investigate the crystal growth, information about the phase separation and especially the fullerene aggregation are of interest. The phase separation is a critical point concerning the possibility to split excitons in organic solar cells, as described in section 2.2. For that purpose, the horizontal scattering profiles are of interest, as they contain information about the lateral phase separation. Figure 8.11 shows the 2D color plot of the horizontal scattering intensities versus time. The profiles are extracted at the critical angle of PCBM to be sensitive for that material. The color plot shows the evolution of a horizontal scattering feature around 0.2 nm^{-1}. For the DGC sample (figure 8.11a), the feature arises after approximately 24 s. The development of the scattering event for the SGC sample starts later, after around 38 s at a similar q-value of around 0.2 nm^{-1}.

To quantify the scattering events in the horizontal GISAXS signal, the data are processed in the scope of Kratky-style plots. Therefore the intensity profiles are plotted as Iq^2 versus q after the subtraction of a linear background and the peak position is tracked with time. [228–231] The resulting parameters of the fit are plotted in figure 8.12. Similar to the data obtained from the GIWAXS investigations, the evolving features of the SGC sample (figure 8.12b) are shifted to later times compared to the DGC sample (figure 8.12a). The stages depicted in the figure are the ones that are extracted from the GIWAXS analysis. The intensity of the scattering feature is related to the phase-separated volume fraction. The q-value is inversely proportional to the correlation distance Λ_c of the aggregates, $\Lambda_c = 2\pi q^{-1}$.

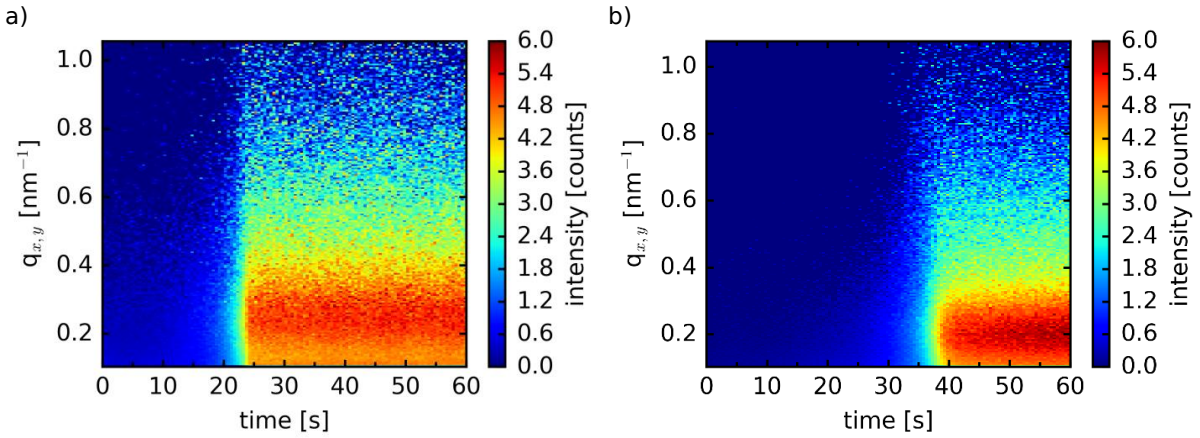

Figure 8.11: 2D color plot of the horizontal GISAXS pattern for $q_{x,y}$ versus time. (a) Intensity development for the sample printed under dry gas atmosphere. (b) Intensity development for the sample printed under a solvent enriched gas stream.

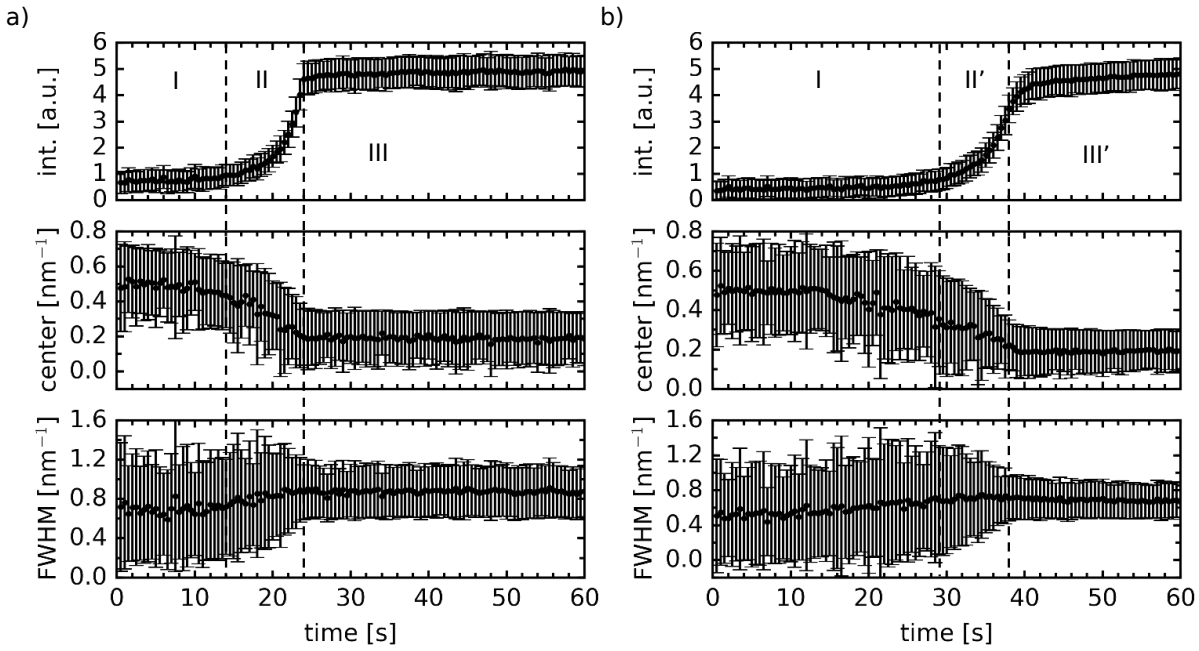

Figure 8.12: Fitting parameters for the peak position of the horizontal intensity profiles after subtraction of a linear background for (a) the sample printed under dry gas flow and (b) the sample printed under solvent enriched gas flow. The vertical dashed lines indicate the transition of the stages identified during the GIWAXS investigations. The error bars represent the fitting uncertainties.

For the DGC sample (figure 8.12a), the intensity of the scattering shoulder in the GISAXS signal is low during the initial stage I indicating a well dissolved system. The initial correlation distance is (15 ± 6) nm and slightly increases during stage I as seen by the decreasing center of the scattering peak. However, it should be mentioned, that in a highly diluted system, the cluster interaction is very weak. The low intensity already indicates the poor reliability of the correlation distance found in the initial stages. Former studies (chapter 6) have shown that already in the dissolved stage, small agglomerates of fullerene are present. [142] It was suggested that the agglomerates grow via an Ostwald ripening process towards the end of the following stage II. There, the intensity as well as the correlation distance increase rapidly and reach their maximum at the end of stage II. This is consistent with former investigations (chapter 6.2), for which this stage was split into two stages (II and III), for a slow and rapid formation of the structures. [142] In the present investigation, the peak center is located at (0.2 ± 0.1) nm^{-1} towards the end of stage II, corresponding to the distance of the PCBM aggregates of (41 ± 20) nm. This peak position stays constant during the further structure evolution process as seen previously.

A similar tendency in the development of the PCBM structures is found for the SGC sample, as shown in figure 8.12b. The stages are defined as the ones obtained from the GIWAXS investigations. Stage I is characterized by a generally low intensity of the structural peak. This is again assigned to the highly diluted solution and thus the weakly interacting clusters with no defined correlation length. The intensity increases towards the end of stage I in combination with a slight decrease of the peak position to q $\approx$ (0.4 $\pm$ 0.2) nm^{-1}. During stage II', the peak intensity gradually increases, which emphasizes the ongoing formation of PCBM clusters and thus the process of phase separation. At the same time, the peak position moves to smaller q-values. Hence, the correlation distance increases during stage II' from initially (21 $\pm$ 10) nm to (42 $\pm$ 21) nm towards the end of stage II'. This distance stays constant during the rest of the film formation. In the beginning of stage III', the peak intensity still increases, which is interpreted as a further optimization of the PCBM aggregation.

For a better comparison to the former studies in chapter 6 and reference [142] the data are analyzed in the framework of the distorted wave born approximation (DWBA) and the local monodisperse approximation (LMA). The evolution of one main structure representing the PCBM aggregates is followed. Figure 8.13 shows the horizontal scattering profiles for every 10 s from 0 to 60 s shifted along the intensity axis along with the final horizontal scattering curve summed over 60 s. The scattering curves are depicted for the DGC sample in figure 8.13a and for the SGC sample in figure 8.13b. Except for the final film, the horizontal scattering curves are logarithmically binned with 45 bins. The details of the procedure are explained in chapter 6. The purpose of binning the data is to increase the statistics of the scattering signal without loosing relevant information, in particular q-resolution. The orange lines for the respective scattering data in figure 8.13 depict the modeled scattering function. The evolution of the main scattering feature, as already seen in the color plot (figure 8.11), is highlighted by blue arrows. Modeling the final scattering curve with the same features as found during structure evolution gives proof of the accuracy of the model parameters due to the high statistics of the final scattering pattern.

From the modeled horizontal scattering profiles a form and structure factor are extracted. They represent the average cluster size and respective distance. The extracted parameters of the main feature corresponding to PCBM aggregates are depicted in figure 8.14 for the sample printed under DGC (figure 8.14a) and the one printed under SGC (figure 8.14b). The stages found during *in situ* GIWAXS experiments are marked.

For the sample printed under dry gas conditions (DGC, figure 8.14a), some structures - although very weak - are already visibly in the beginning of the process. The lateral distance is weakly defined and shows large error bars. The correlation distance is already

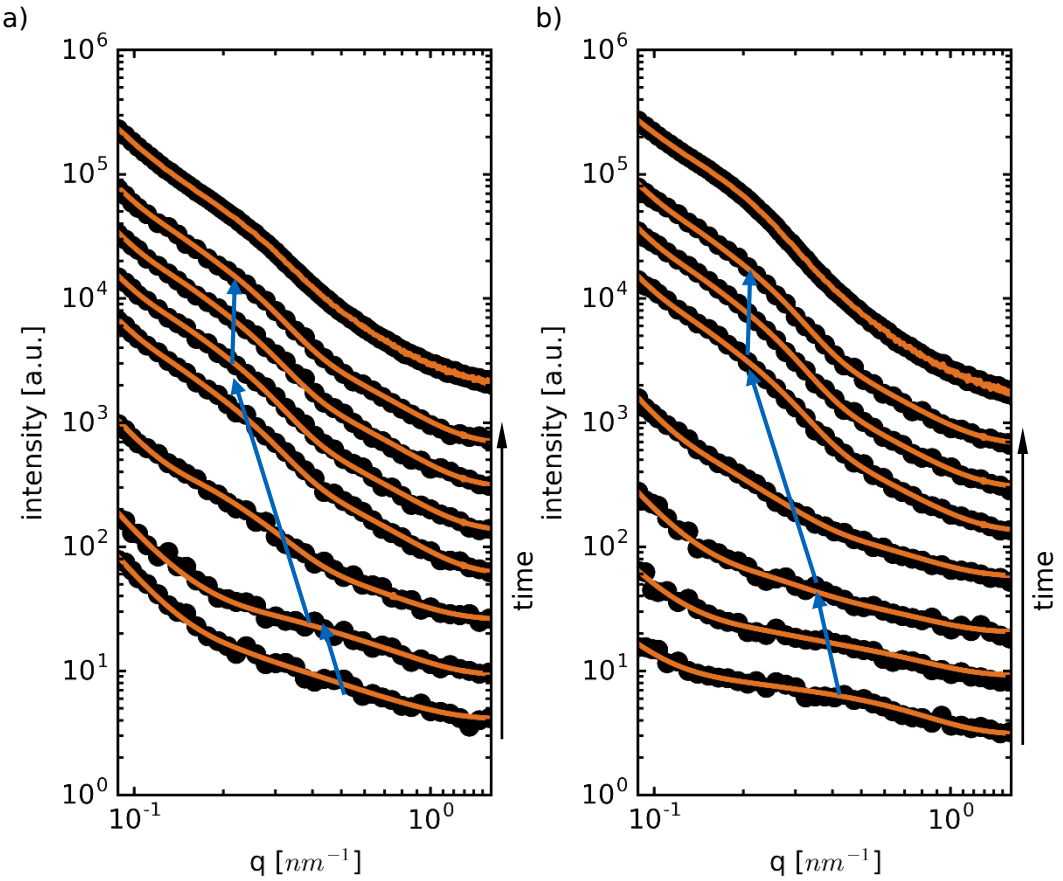

Figure 8.13: Horizontal GISAXS scattering data with modeled function for (a) the sample printed under dry gas flow and (b) the sample printed under solvent enriched gas flow. The black points are the scattering data and the orange lines the respective modeled scattering curves. Depicted are the scattering data every 10 s from 0 to 60 s (from bottom) with the binned scattering data and the final film with the unbinned data (top curve, summed over 60 s). The blue arrows depict the evolution of the scattering shoulder arising from PCBM aggregates. The curves are shifted along the y-axis for clarity.

seen in the Kratky-style analysis which served as input for the data modeling. The low intensity and the large, weakly defined distances are typical for a well dissolved system. The initial cluster radius is found to be (3.2 ± 0.8) nm with a lateral distance of (18 ± 10) nm. During the initial phase, the nucleation, the distance shrinks until it reaches a minimum at around 10-12 s with (11 ± 5) nm, after which also the aggregate radii start to grow. The following increase of the lateral distance and the cluster radii has been discussed in chapter 6, occurring from an Ostwald ripening process. Once the first polymer crystals are observed (start of stage II), the lateral distance further increases

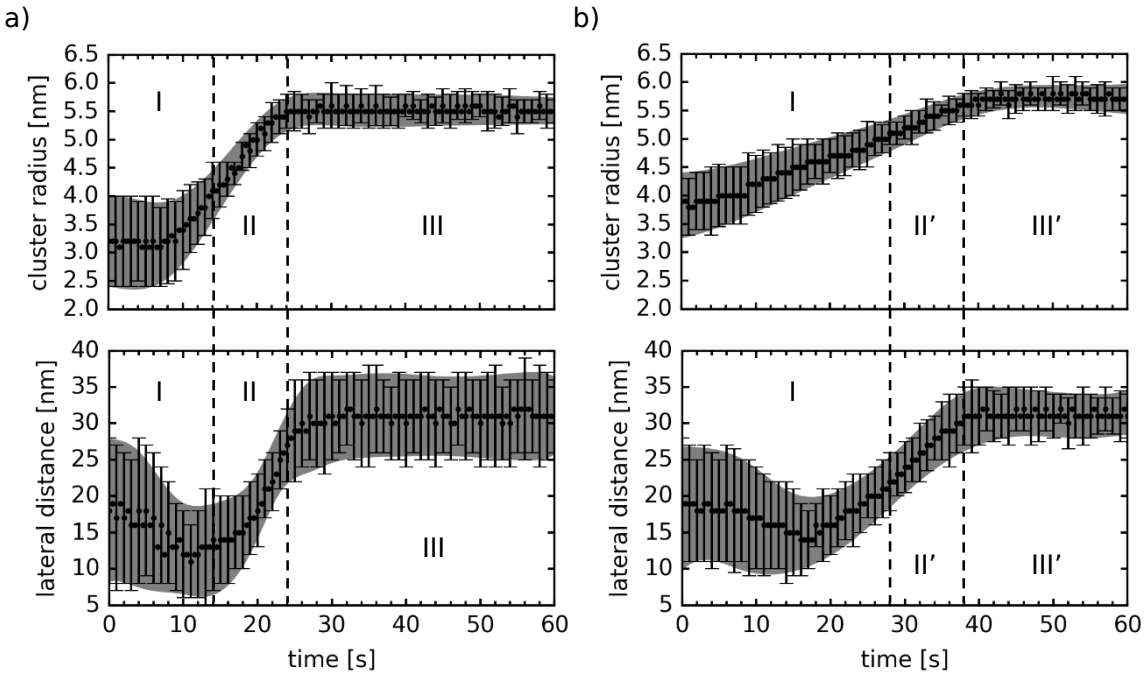

Figure 8.14: Extracted sizes from modeling the main feature of the horizontal GISAXS signals of (a) the sample printed under dry gas flow and (b) the sample printed under solvent enriched gas flow. The top graphs depict the size of the PCBM aggregates and the bottom graphs their distance. The error bars are shown for every second data point for clarity and the gray tube depicts the averaged range of the modeled sizes. The vertical dashed lines indicate the transition of the stages identified during the GIWAXS investigations.

along with a growth of the cluster radius. The cluster radius grows during stage II from (4.1 ± 0.5) nm with a lateral distance of (14 ± 7) nm to (5.5 ± 0.3) nm with a lateral distance of (27 ± 5) nm. During the crystal rearrangement in stage III, the PCBM aggregates only slightly vary and reach a final size of (5.5 ± 0.3) nm at a distance of (31 ± 6) nm.

The extracted parameters of the sample printed under solvent enriched gas conditions (SGC) are depicted in figure 8.14b. The initial parameters obtained from a very weak signal are a average cluster radius of (3.8 ± 0.6) nm and only weakly defined lateral spacing of (19 ± 9) nm. The initial phase is characterized by a nucleation and a subsequent ripening process; during both processes the PCBM aggregate size as well as the distance increases. At the end of stage I, when the first polymer crystals are found, the cluster radius is (5.1 ± 0.2) nm with a lateral distance of (22 ± 4) nm. During stage II', both the cluster size and the distance increase and reach a value of (5.6 ± 0.2) nm with a lateral spacing of (30 ± 4) nm. During stage III', the cluster size slightly growths at a rather

constant lateral spacing. The final cluster size is (5.7 ± 0.2) nm with a lateral distance of (31 ± 3) nm.

When comparing both preparation routes, very similar PCBM aggregation development is observed. It starts with a nucleation process followed by a ripening process shortly before the first polymer crystals are found. The rapid growth of structures and their distance during the polymer crystallization phase (stage II and II') is interpreted as crystallization-driven phase separation and was observed in previous studies (chapter 6 and [142]). The formation of polymer crystals is pushing the PCBM aggregates apart, which leads to an increased lateral spacing. Moreover, the miscibility of PCBM in P3HT crystals is lowered with increasing degree of crystallinity and mixed phases mainly consist of amorphous polymer and PCBM. [72, 180–182] Hence, the PCBM molecules are pushed along the crystallization front and forced to form aggregates as seen in increasing cluster radii. The final PCBM aggregates are slightly larger for the SGC sample, while the respective lateral spacing is similar. This is in agreement with the smaller P3HT crystals observed in the GIWAXS experiments, which act as spacer between the PCBM aggregates. Similar results were observed for the different drying speeds upon substrate temperature in chapter 6 and [142].

8.2.3 Discussion of a structure evolution model and conclusion

The characterization of the films printed under different atmospheric conditions are combined to obtain an image of the structure formation. In general, the structure formation development is divided into four stages, whereas the second stage, during which the main structure growth takes place, consists of subphases of slow and fast growth. Figure 8.15 depicts the development of the structure based on the scattering experiments and highlights the differences between the two atmospheric conditions while printing. In the model, the P3HT polymer backbone is depicted as black lines, its crystalline state is shown as bended parallel backbones. The solvent is indicated by green color, which gets less intense during evaporation. The solvent evaporation was not recorded during the experiments, but is extracted from literature knowledge and given as estimation during the single phases. PCBM is shown in groups when aggregated. Arrows indicate the repulsion (black) of PCBM aggregates or the optimization of crystal packing (orange).

The following picture of the structure formation is obtained. In summary, four stages are found:

Stage I (DGC and SGC): The first stage is characterized by the evaporation of the excess solvent. P3HT and PCBM in the solution exhibit a high mobility and can initially freely move through the film. The GISAXS intensity is low, indicating the low degree

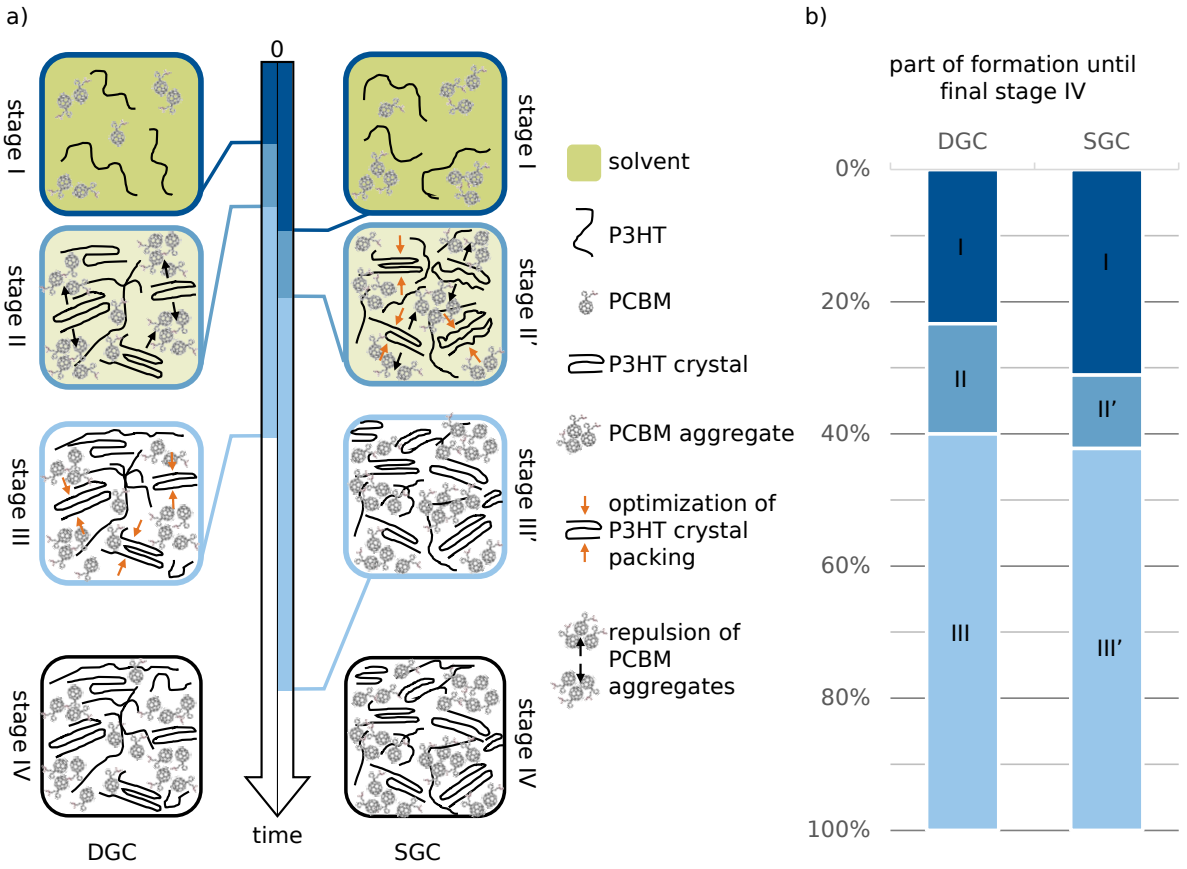

Figure 8.15: Schematic of the structure formation of films printed under dry gas conditions (DGC) and solvent enriched gas conditions (SGC). a) Picture of the drying process for the DGC sample (left) and the SGC sample (right). The time axis shows the shift of the different stages. The film formation differs in the stages II/II' and III/III'. b) Shares of the different stages until the final film (stage IV) is obtained.

of phase separation. [228] However, indications of small PCBM clusters are found in the horizontal scattering profiles. The aggregate radius with (3.8 ± 0.6) nm for the SGC sample is found to be larger than for the DGC sample with around (3.2 ± 0.8) nm. The evaporation of solvent leads to an increase of the solid concentration during that phase. Towards the end of stage I, the intensity of the GISAXS signal rises, indicating the further formation of PCBM clusters.

Stage II (DGC): Once the critical solution concentration is reached, the first polymer crystals form. The formed crystals are initially strongly edge-on oriented and reorient towards the end of stage II. Moreover, the first crystals exhibit a high spacing between their backbones indicating their swollen character. With time, the distance shrinks along with

a crystal growth and the formation of further crystals. Additionally, a growth of the size of the PCBM aggregates is seen, accompanied by an increase of their correlation distance. The limited miscibility of PCBM in P3HT is well known. [181, 237] The observations of simultaneous measurements of different length scales presented in this work indicate that the phase separation is driven by the formation and growth of P3HT crystals. This is in good agreement with other studies, which showed the movement of the PCBM driven by the crystallization front. [142,172] The amorphous phase of P3HT on the other hand may contain PCBM as indicated in the model. [180, 238, 239] Towards the end of stage II, the crystallization rate strongly increases along with an enormous improvement of the crystal packing, although the latter is not yet optimized. This also leads to a further repulsion of the PCBM aggregates, forcing them to grow to their final size of (5.5 ± 0.3) nm with a lateral distance of (27 ± 5) nm.

Stage III (DGC): After the completion of the crystallization process, the packing of the crystals further improves in a self-annealing process. This leads to the finally optimized packing of the P3HT crystals with a backbone spacing of (1.62 ± 0.01) nm. The intensity of the GISAXS signal slightly increases, indicating a further phase separation of the material, which is explained by the final rearrangement and packing of the polymer crystals and the final evaporation of solvent molecules. The PCBM aggregates finally show a size of (5.5 ± 0.3) nm at a distance of (31 ± 6) nm.

Stage II' (SGC): The initial phase of stage II' of the SGC sample is similar to the one observed in stage II of the DGC sample. The solvent evaporates until a critical solution concentration is obtained. The P3HT starts to crystallize with a large spacing between the backbones. With increasing crystal size and number of crystals, the backbone spacing shrinks, until it reaches an optimized packing towards the end of stage II' with (1.67 ± 0.01) nm. However, the crystallization is not yet finished as compared to stage II of the DGC sample as seen by the increasing intensity of the GIWAXS scattering signal. As for the DGC sample, the growing crystals during stage II' lead to an increase of the PCBM aggregate spacing. The PCBM aggregates initially exhibit a radius of (5.1 ± 0.2) nm and grow slightly with ongoing crystallization. At the end of stage II', the PCBM aggregates exhibit a size of (5.6 ± 0.2) nm with a lateral spacing of (30 ± 4) nm.

Stage III' (SGC): The backbone spacing of the polymer crystals is already optimized. However, the intensity of the GIWAXS scattering peak increases, which shows the ongoing formation of polymer crystals. The solvent atmosphere is supposed to provide enough mobility for the materials inside the film to further rearrange. This is also seen in the increasing GISAXS signal, which indicates the progress in the formation of PCBM aggregates. The PCBM aggregate size, however, does not vary significantly any more. From solvent annealing experiments, the positive effect of the solvent atmosphere on the film

morphology is known to be even more advantageous than thermal annealing of a film without solvent annealing. [226]

Stage IV (DGC and SGC): The final morphology of the active layer is reached after a long-term relaxation process. For the DGC sample, the lower limit of the final P3HT crystal size is (14.7 ± 0.4) nm and the PCBM aggregate size is (5.5 ± 0.3) nm at a distance of (31 ± 6) nm. For the SGC sample, the P3HT crystals with (14.3 ± 0.8) nm are slightly smaller, and the PCBM aggregates with (5.7 ± 0.2) nm are larger, leading to a similar lateral spacing compared to the DGC sample.

Figure 8.15b shows the percentage of time the individual stages hold upon obtaining the final film morphology for the different atmospheric conditions. The evaporation of the initial solvent, until the critical solution concentration for polymer crystallization is reached, needs between 20-30 % of the formation process. The high partial pressure of the solvent in the SGC atmosphere leads to an extended duration of the evaporation. The main structure formation process (stage II and II') happens very quickly. However, for the SGC sample, it differs in the sense that the solvent vapor surrounding the film stimulates further crystallization in stage III'. For the DGC sample, the respective stage III only optimizes the packing of the already formed crystals. This difference also explains the improved phase separation found in different studies. [137, 226]

8.3 Summary

The influence of a solvent enriched atmosphere compared to a dry gas atmosphere on a printed organic film for photovoltaic applications is investigated with *in situ* X-ray scattering. For that purpose, a custom made slot-die coater is equipped with a chamber allowing for the control of the atmosphere during solidification of the printed thin film. The impact of the atmosphere is tested with two environments, a dry gas flow and a chlorobenzene solvent enriched gas flow during printing. The film formation is monitored simultaneously on two length scales, in the GIWAXS regime for crystallization kinetics and in the GISAXS regime for phase separation and PCBM aggregation.

The structure evolution process is divided into four stages. It is found that for the two atmospheric conditions the second and third stage deviate from each other. The first stage is dominated by the evaporation of the excess solvent and characterized by small PCBM aggregates forming mainly towards the end of this stage. Once the critical solution concentration is reached, the polymer starts to crystallize in the next stage. For the film printed under dry gas conditions the crystallization is finished at the end of the second stage with not yet optimized crystal packing. In contrast, for the film printed under solvent enriched gas conditions, the polymer crystals exhibit their optimized packing at the end

of the second stage, while the crystallization process is not yet finished. In both cases, the crystallization of the polymer crystals leads to a repulsion of the PCBM aggregates. During the third stage, the polymer crystals in the film printed in a dry gas atmosphere optimize their packing, while in the film printed under solvent enriched gas conditions, the polymer further crystallizes. The solvent annealing during that stage provides enough mobility to the material within the film to rearrange and optimize its packing before the fourth stage, the final film, is reached.

The presented investigation provides a path to control the solidification process through the choice of atmosphere surrounding the printed sample. The structure formation is modified by the immediate solvent annealing of the printed film.

9 Conclusion and outlook

This work presents investigations of the structure formation and manipulation in printed thin films for applications in organic solar cells. The objective of this thesis is to provide insights into the mechanisms of the morphological evolution in a printing process. Moreover, it introduces potential pathways to influence the structure formation and thereby the performance of the printed solar cells. It contributes to the understanding necessary to upscale the organic solar cell production to large area devices. The investigations focus on the inner morphology by applying grazing incidence wide and small angle X-ray scattering (GIWAXS and GISAXS) as well as X-ray reflectometry. The structure-function relation is verified by electronic characterization of the thin films in terms of solar cell performance and charge carrier mobility measurements.

The basis of all investigations is a slot-die coating setup that meets the requirements to print organic solar cells while performing *in situ* GIWAXS and GISAXS experiments. It was successfully constructed and set up in close collaboration with the Advanced Light Source (ALS) at the Lawrence Berkeley National Laboratory (LBNL) in Berkeley, USA. The modular design of the setup allows to implement further features like electrodes for simultaneous application of an external electric field while printing. An additional modular feature is a chamber that allows the control over the chemical atmosphere during the deposition process. The printer, including this chamber, is of light weight to be implemented into a synchrotron beamline allowing *in situ* GIWAXS and GISAXS and simultaneous optical characterization via reflectometry or absorption spectroscopy. This sophisticated experimental setup enables the tailoring of the nano-structure of freshly printed thin organic films while tracking its formation on a nano-scale. It allows us to influence the self-assembly process in thin films by tuning a handful of macroscopic thermodynamic parameters (temperature, humidity, printing speed, flow rate) which enable the production of functional films with enhanced properties.

The aim to understand the structure formation process in printed organic thin films is addressed by *in situ* GIWAXS and GISAXS investigations at different substrate temperatures and thus different film solidification speeds. As model system, an active layer with poly(3-hexyl-thiophene) (P3HT) and [6,6]-phenyl-C_{61}butyric acid methyl ester (PCBM) is deposited. For data treatment, an algorithm to logarithmically bin the scattering data

is applied. The thereby improved statistics of the scattering data allows to keep a high time resolution of the performed experiment without loss of spatial resolution and hence enables an improved data modeling of the GISAXS data. The experiments yield a general model of the structure formation that is divided into five stages, two of which are dominated by the crystal growth. During the first stage, the solvent evaporates until a critical solution concentration is reached. The crystal growth starts with a modest speed in well aligned edge-on crystals followed by a rapid increase of crystal size and packing. This rapid crystallization leads to a crystallization-driven phase separation. A further optimization of the crystal packing yields the final film structure. The results of solar cell experiments and the structure formation analysis propose a preferential slow growth of the structure in order to improve the solar cell performance. The findings provide an important part to understand the mechanisms taking place during solidification of slot-die coated thin organic films and are an essential contribution towards tailoring the thin film morphology.

The transfer of an industrial printing process using an electric field during ink deposition to the coating process of organic solar cells provides an approach to influence the structure formation. The electrophoresis-assisted printing of active layers forces the P3HT crystals to reorient due to dielectric forces acting on the forming polymer crystals. This reorientation improves the hole mobility in the active layer. The intentional choice of chloroform as solvent for the P3HT and PCBM exhibits an electrophoretic mobility of the macromolecules in solution. This property is used during film deposition to actively move the polymer and fullerene vertically within the still wet film directly after deposition. The vertical film composition is improved, yielding an intrinsic blocking layer as well as improved percolation paths towards the electrodes. At the same time, the lateral structures are conserved. This leads to an improvement of the fill factor and short circuit current by 15% and 10%, respectively. Consequently the overall device performance is improved by 25%. The findings indicate that electrophoresis-assisted printing can be transferred to different material combinations, including small molecules, that exhibit an electrophoretic mobility in the respective solvent.

The application of the atmospheric control chamber during thin film deposition allows the control of the solidification process of the printed P3HT:PCBM active layer. The morphology evolution is investigated for two atmospheric conditions with *in situ* GISAXS and simultaneous GIWAXS of the main crystallographic peak. The two investigated atmospheric cases are a constant stream of dry helium gas above the sample and a stream of chlorobenzene gas-enriched helium above the sample during solidification, thereby enabling a solvent annealing process. The structure formation is divided into four stages. The first and the last stage are the same for both conditions, namely the evaporation of

the excess solution during the first stage and the final film in the last stage. However, the structure evolution is found to differ in the middle stages. During the second stage, consisting of two phases of slow and fast crystal growth, the crystallization is finished with not yet optimally packed P3HT crystals in the case of solidification under a dry gas stream. In contrast, the polymer crystals exhibit an optimized packing at the end of the second stage in the case of a stream of solvent-enriched gas. However, in that case, the crystallization of the film has not yet finished. Consequently, the third stage of structure evolution comprises an optimization of the crystal packing for the dry gas conditions while a further crystallization is observed for the solvent enriched atmosphere. The findings suggest that the solvent annealing implemented in the latter case provides enough mobility to the material in the sample to rearrange. This investigation provides a path to control the solidification process through the choice of solvent atmosphere surrounding the printed sample. The structure formation is modified by the subsequent solvent annealing of the printed film.

The findings presented in this work give an insight into the structure formation and manipulation during printing of organic thin films. For a broader picture the investigations should be expanded with complementary *in situ* techniques, in particular with optical spectroscopy. P3HT:PCBM is a widely studied model system that provides a benchmark in organic solar cell research. However, for more general statements, the presented processes need to be transfered and tested on other material systems. The presented work and the introduced experimental setup allows to continue investigations on the structure formation and deepen the understanding in a broader context of different materials and parameters. A necessary next step for printed solar cells is to move towards flexible substrates in order to follow the route towards large scale organic solar cells. Therefore, the printer should be expanded with the ability to print in a roll to roll coating approach. Further research on the implications of the film deposition on the device morphology is necessary to address some of the five core technologies necessary for device commercialization.

Bibliography

[1] Ren21, *Renewables 2017 Global Status Report*. Paris: REN21 Secretariat, 2017.

[2] SolarServer, "Ecofys: Mehr als 2300 Quadratkilometer Gebäudefläche für Photovoltaik und Solarthermie nutzbar: http://www.solarserver.de/news/news-7381.html," 2007.

[3] M. Kloos, *Solarer Städtebau: Vom Pilotprojekt zum planerischen Leitbild*. Stuttgart: Kohlhammer, 2007.

[4] P. Gagnon, R. Margolis, J. Melius, C. Phillips, and R. Elmore, *Rooftop Solar Photovoltaic Technical Potential in the United States. A Detailed Assessment*. 2016.

[5] oe a, *OE-A Roadmap for Organic and Printed Electronics: White Paper*. 7 ed., 2017.

[6] C. K. Chiang, C. R. Fincher, Y. W. Park, A. J. Heeger, H. Shirakawa, E. J. Louis, S. C. Gau, and A. G. MacDiarmid, "Electrical Conductivity in Doped Polyacetylene," *Physical Review Letters*, vol. 39, no. 17, pp. 1098–1101, 1977.

[7] Nobelprize.org, "The Nobel Prize in Chemistry 2000: https://www.nobelprize.org/nobel_prizes/chemistry/laureates/2000/," 2000.

[8] M. Kaltenbrunner, M. S. White, E. D. Głowacki, T. Sekitani, T. Someya, N. S. Sariciftci, and S. Bauer, "Ultrathin and lightweight organic solar cells with high flexibility," *Nature Communications*, vol. 3, p. 770, 2012.

[9] J. H. Noh, S. H. Im, J. H. Heo, T. N. Mandal, and S. I. Seok, "Chemical management for colorful, efficient, and stable inorganic-organic hybrid nanostructured solar cells," *Nano letters*, vol. 13, no. 4, pp. 1764–1769, 2013.

[10] M. S. S. Rahman and M. K. Alam, "Effect of angle of incidence on the performance of bulk heterojunction organic solar cells: A unified optoelectronic analytical framework," *AIP Advances*, vol. 7, no. 6, p. 065101, 2017.

[11] R. Steim, T. Ameri, P. Schilinsky, C. Waldauf, G. Dennler, M. Scharber, and C. J. Brabec, "Organic photovoltaics for low light applications," *Solar Energy Materials and Solar Cells*, vol. 95, no. 12, pp. 3256–3261, 2011.

[12] G. Chen, H. Sasabe, Z. Wang, X.-F. Wang, Z. Hong, Y. Yang, and J. Kido, "Co-evaporated bulk heterojunction solar cells with 6.0% efficiency," *Advanced Materials*, vol. 24, no. 20, pp. 2768–2773, 2012.

[13] F. C. Krebs, "Fabrication and processing of polymer solar cells: A review of printing and coating techniques," *Solar Energy Materials and Solar Cells*, vol. 93, no. 4, pp. 394–412, 2009.

[14] R. Søndergaard, M. Hösel, D. Angmo, T. T. Larsen-Olsen, and F. C. Krebs, "Roll-to-roll fabrication of polymer solar cells," *Materials Today*, vol. 15, no. 1-2, pp. 36–49, 2012.

[15] F. C. Krebs, N. Espinosa, M. Hösel, R. R. Søndergaard, and M. Jørgensen, "25th Anniversary Article: Rise to Power - OPV-Based Solar Parks," *Advanced Materials*, vol. 26, no. 1, pp. 29–39, 2014.

[16] R. R. Søndergaard, M. Hösel, and F. C. Krebs, "Roll-to-Roll fabrication of large area functional organic materials," *Journal of Polymer Science Part B: Polymer Physics*, vol. 51, no. 1, pp. 16–34, 2013.

[17] H. Kang, G. Kim, J. Kim, S. Kwon, H. Kim, and K. Lee, "Bulk-Heterojunction Organic Solar Cells: Five Core Technologies for Their Commercialization," *Advanced Materials*, vol. 28, no. 36, pp. 7821–7861, 2016.

[18] F. Zhang, O. Inganäs, Y. Zhou, and K. Vandewal, "Development of polymer–fullerene solar cells," *National Science Review*, vol. 3, no. 2, pp. 222–239, 2016.

[19] J. Nelson, "Polymer:fullerene bulk heterojunction solar cells," *Materials Today*, vol. 14, no. 10, pp. 462–470, 2011.

[20] B. C. Thompson and J. M. J. Fréchet, "Polymer–Fullerene Composite Solar Cells," *Angewandte Chemie International Edition*, vol. 47, no. 1, pp. 58–77, 2008.

[21] M. T. Dang, L. Hirsch, and G. Wantz, "P3HT:PCBM, Best Seller in Polymer Photovoltaic Research," *Advanced Materials*, vol. 23, no. 31, pp. 3597–3602, 2011.

[22] M. T. Dang, L. Hirsch, G. Wantz, and J. D. Wuest, "Controlling the morphology and performance of bulk heterojunctions in solar cells. Lessons learned from the benchmark poly(3-hexylthiophene):6,6-phenyl-C61-butyric acid methyl ester system," *Chemical Reviews*, vol. 113, no. 5, pp. 3734–3765, 2013.

[23] G. Li, R. Zhu, and Y. Yang, "Polymer solar cells," *Nature Photonics*, vol. 6, no. 3, pp. 153–161, 2012.

[24] Y. Tamai, H. Ohkita, H. Benten, and S. Ito, "Exciton Diffusion in Conjugated Polymers: From Fundamental Understanding to Improvement in Photovoltaic Conversion Efficiency," *The Journal of Physical Chemistry Letters*, vol. 6, no. 17, pp. 3417–3428, 2015.

[25] H. Hoppe and N. S. Sariciftci, "Organic solar cells: An overview," *Journal of Materials Research*, vol. 19, no. 07, pp. 1924–1945, 2004.

[26] H. Hoppe and N. S. Sariciftci, "Morphology of polymer/fullerene bulk heterojunction solar cells," *Journal of Materials Chemistry*, vol. 16, no. 1, pp. 45–61, 2006.

[27] G. Yu, J. Gao, J. C. Hummelen, F. Wudl, and A. J. Heeger, "Polymer Photovoltaic Cells: Enhanced Efficiencies via a Network of Internal Donor-Acceptor Heterojunctions," *Science*, vol. 270, no. 5243, pp. 1789–1791, 1995.

[28] S. Günes, H. Neugebauer, and N. S. Sariciftci, "Conjugated Polymer-Based Organic Solar Cells," *Chemical Reviews*, vol. 107, no. 4, pp. 1324–1338, 2007.

[29] J. J. M. Halls, C. A. Walsh, N. C. Greenham, E. A. Marseglia, R. H. Friend, S. C. Moratti, and A. B. Holmes, "Efficient photodiodes from interpenetrating polymer networks," *Nature*, vol. 376, no. 6540, pp. 498–500, 1995.

[30] H. Sirringhaus, P. J. Brown, R. H. Friend, M. M. Nielsen, K. Bechgaard, Langeveld-Voss, B. M. W., Spiering, A. J. H., Janssen, R. A. J., E. W. Meijer, P. Herwig, and de Leeuw, D. M., "Two-dimensional charge transport in self-organized, high-mobility conjugated polymers," *Nature*, vol. 401, no. 6754, pp. 685–688, 1999.

[31] F. C. Spano, "The spectral signatures of Frenkel polarons in H- and J-aggregates," *Accounts of Chemical Research*, vol. 43, no. 3, pp. 429–439, 2010.

[32] J. Clark, C. Silva, R. H. Friend, and F. C. Spano, "Role of intermolecular coupling in the photophysics of disordered organic semiconductors: aggregate emission in regioregular polythiophene," *Physical Review Letters*, vol. 98, no. 20, p. 206406, 2007.

[33] P. J. Brown, D. S. Thomas, A. Köhler, J. S. Wilson, J.-S. Kim, C. M. Ramsdale, H. Sirringhaus, and R. H. Friend, "Effect of interchain interactions on the absorption and emission of poly(3-hexylthiophene)," *Physical Review B*, vol. 67, no. 6, 2003.

[34] P. Müller-Buschbaum, "The Active Layer Morphology of Organic Solar Cells Probed with Grazing Incidence Scattering Techniques," *Advanced Materials*, vol. 26, no. 46, pp. 7692–7709, 2014.

[35] T. Martens, J. D'Haen, T. Munters, Z. Beelen, L. Goris, J. Manca, M. D'Olieslaeger, D. Vanderzande, L. de Schepper, and R. Andriessen, "Disclosure of the nanostructure of MDMO-PPV:PCBM bulk hetero-junction organic solar cells by a combination of SPM and TEM," *Synthetic Metals*, vol. 138, no. 1-2, pp. 243–247, 2003.

[36] T. L. Benanti and D. Venkataraman, "Organic solar cells: an overview focusing on active layer morphology," *Photosynthesis Research*, vol. 87, no. 1, pp. 73–81, 2006.

[37] K. W. Chou, B. Yan, R. Li, E. Q. Li, K. Zhao, D. H. Anjum, S. Alvarez, R. Gassaway, A. Biocca, S. T. Thoroddsen, A. Hexemer, and A. Amassian, "Spin-Cast Bulk Heterojunction Solar Cells: A Dynamical Investigation," *Advanced Materials*, vol. 25, no. 13, pp. 1923–1929, 2013.

[38] L. J. Richter, D. M. DeLongchamp, F. A. Bokel, S. Engmann, K. W. Chou, A. Amassian, E. Schaible, and A. Hexemer, "In Situ Morphology Studies of the Mechanism for Solution Additive Effects on the Formation of Bulk Heterojunction Films," *Advanced Energy Materials*, vol. 5, no. 3, p. 1400975, 2015.

[39] M. Sanyal, B. Schmidt-Hansberg, Klein, Michael F. G., A. Colsmann, C. Munuera, A. Vorobiev, U. Lemmer, W. Schabel, H. Dosch, and E. Barrena, "In Situ X-Ray Study of Drying-Temperature Influence on the Structural Evolution of Bulk-Heterojunction Polymer-Fullerene Solar Cells Processed by Doctor-Blading," *Advanced Energy Materials*, vol. 1, no. 3, pp. 363–367, 2011.

[40] T. Wang, Dunbar, Alan D. F., P. A. Staniec, A. J. Pearson, P. E. Hopkinson, J. E. MacDonald, S. Lilliu, C. Pizzey, N. J. Terrill, A. M. Donald, A. J. Ryan, Jones, Richard A. L., and D. G. Lidzey, "The development of nanoscale morphology in polymer:fullerene photovoltaic blends during solvent casting," *Soft Matter*, vol. 6, no. 17, p. 4128, 2010.

[41] G. R. Strobl, *The physics of polymers: Concepts for understanding their structures and behavior*. Berlin and New York: Springer, 3rd ed., 2007.

[42] L. H. Sperling, *Introduction to physical polymer science*. Hoboken, N.J.: Wiley, 4th ed., 2006.

[43] N. W. Ashcroft and N. D. Mermin, *Festkörperphysik*. München: Oldenbourg, 4th ed., 2013.

[44] M. Grundmann, *The Physics of Semiconductors: An Introduction Including Nanophysics and Applications*. Graduate Texts in Physics, Berlin, Heidelberg: Springer-Verlag Berlin Heidelberg, 2nd ed., 2010.

[45] H. Haken, *Atom- und Quantenphysik: Einfuhrung in die experimentellen und theoretischen Grundlagen*. Berlin, Heidelberg, New York: Springer, 8th ed., 2003.

[46] W. Brütting, C. Adachi, and R. J. D. Holmes, *Physics of organic semiconductors*. Weinheim and Chichester: Wiley-VCH, 2012.

[47] M. Pope and C. E. Swenberg, *Electronic processes of organic crystals and polymers*, vol. 56 of *Monographs on the physics and chemistry of materials*. Oxford: Oxford University Press, 2nd ed., 1999.

[48] A. Köhler and H. Bässler, *Electronic processes in organic semiconductors: An introduction*. Weinheim, Germany: Wiley-VCH Verlag GmbH & Co. KGaA, 1st ed., 2015.

[49] S. F. Kistler and P. M. Schweizer, eds., *Liquid Film Coating*. Dordrecht: Springer Netherlands, 1997.

[50] A. A. Tracton, *Coatings technology: Fundamentals, testing, and processing techniques*. Boca Raton: CRC, 2007.

[51] M. Tolan, *X-Ray Scattering from Soft-Matter Thin Films: Materials Science and Basic Research*, vol. 148 of *Springer Tracts in Modern Physics. Ergebnisse der exakten Naturwissenschaften*. Berlin: Springer Berlin, 2013.

[52] O. Glatter, *Small angle X-ray scattering*. London: Academic Press, 2nd printing ed., 1983.

[53] A. D. Jenkins, P. Kratochvíl, R. F. T. Stepto, and U. W. Suter, "Glossary of basic terms in polymer science (IUPAC Recommendations 1996)," *Pure and Applied Chemistry*, vol. 68, no. 12, 1996.

[54] T. Johansson, W. Mammo, M. Svensson, M. R. Andersson, and O. Inganäs, "Electrochemical bandgaps of substituted polythiophenes," *Journal of Materials Chemistry*, vol. 13, no. 6, pp. 1316–1323, 2003.

[55] R. Kroon, M. Lenes, J. C. Hummelen, P. W. M. Blom, and B. de Boer, "Small Bandgap Polymers for Organic Solar Cells (Polymer Material Development in the Last 5 Years)," *Polymer Reviews*, vol. 48, no. 3, pp. 531–582, 2008.

[56] M. Wright and A. Uddin, "Organic—inorganic hybrid solar cells: A comparative review," *Solar Energy Materials and Solar Cells*, vol. 107, pp. 87–111, 2012.

[57] P. Müller-Buschbaum, *Polymer Physics*. Lecture Notes, Technische Universität München, Garching, 2013.

[58] F. Beniere, S. Haridoss, J. P. Louboutin, M. Aldissi, and J. M. Fabre, "Doping of polyacetylene by diffusion of iodine," *Journal of Physics and Chemistry of Solids*, vol. 42, no. 8, pp. 649–654, 1981.

[59] K. Feron, W. J. Belcher, C. J. Fell, and P. C. Dastoor, "Organic solar cells: understanding the role of Förster resonance energy transfer," *International Journal of Molecular Sciences*, vol. 13, no. 12, pp. 17019–17047, 2012.

[60] G. Hadziioannou and G. G. Malliaras, *Semiconducting polymers: Chemistry, physics and engineering*. Weinheim: Wiley-VCH, 2nd ed. ed., 2006.

[61] A. Salleo, T. W. Chen, A. R. Völkel, Y. Wu, P. Liu, B. S. Ong, and R. A. Street, "Intrinsic hole mobility and trapping in a regioregular poly(thiophene)," *Physical Review B*, vol. 70, no. 11, 2004.

[62] G. Strobl, "Colloquium: Laws controlling crystallization and melting in bulk polymers," *Reviews of Modern Physics*, vol. 81, no. 3, pp. 1287–1300, 2009.

[63] R. Becker, "Die Keimbildung bei der Ausscheidung in metallischen Mischkristallen," *Annalen der Physik*, vol. 424, no. 1-2, pp. 128–140, 1938.

[64] M. V. Massa and K. Dalnoki-Veress, "Homogeneous crystallization of poly(ethylene oxide) confined to droplets: the dependence of the crystal nucleation rate on length scale and temperature," *Physical Review Letters*, vol. 92, no. 25 Pt 1, p. 255509, 2004.

[65] G. Reiter and G. R. Strobl, *Progress in Understanding of Polymer Crystallization*, vol. 714 of *Lecture Notes in Physics*. Berlin, Heidelberg: Springer, 2007.

[66] G. Strobl, "Crystallization and melting of bulk polymers: New observations, conclusions and a thermodynamic scheme," *Progress in Polymer Science*, vol. 31, no. 4, pp. 398–442, 2006.

[67] G. Strobl, "From the melt via mesomorphic and granular crystalline layers to lamellar crystallites: A major route followed in polymer crystallization?," *The European Physical Journal E*, vol. 3, no. 2, pp. 165–183, 2000.

[68] N. S. Sariciftci, L. Smilowitz, A. J. Heeger, and F. Wudl, "Photoinduced electron transfer from a conducting polymer to buckminsterfullerene," *Science*, vol. 258, no. 5087, pp. 1474–1476, 1992.

[69] P. J. Flory, "Thermodynamics of High Polymer Solutions," *The Journal of Chemical Physics*, vol. 10, no. 1, pp. 51–61, 1942.

[70] M. L. Huggins, "Theory of Solutions of High Polymers 1," *Journal of the American Chemical Society*, vol. 64, no. 7, pp. 1712–1719, 1942.

[71] Tanaka and Nishi, "New types of phase separation behavior during the crystallization process in polymer blends with phase diagram," *Physical Review Letters*, vol. 55, no. 10, pp. 1102–1105, 1985.

[72] M. A. Ruderer, R. Meier, L. Porcar, R. Cubitt, and P. Müller-Buschbaum, "Phase Separation and Molecular Intermixing in Polymer–Fullerene Bulk Heterojunction Thin Films," *The Journal of Physical Chemistry Letters*, vol. 3, no. 6, pp. 683–688, 2012.

[73] Y. Gao, T. P. Martin, E. T. Niles, A. J. Wise, A. K. Thomas, and J. K. Grey, "Understanding Morphology-Dependent Polymer Aggregation Properties and Photocurrent Generation in Polythiophene/Fullerene Solar Cells of Variable Compositions," *The Journal of Physical Chemistry C*, vol. 114, no. 35, pp. 15121–15128, 2010.

[74] M. A. Niedermeier, *Novel structuring routines of titania films for application in photovoltaics*. Dissertation, Technische Universität München, Garching, 2013.

[75] D. Hertel and H. Bassler, "Photoconduction in amorphous organic solids," *ChemPhysChem*, vol. 9, no. 5, pp. 666–688, 2008.

[76] T. Förster, "Zwischenmolekulare Energiewanderung und Fluoreszenz," *Annalen der Physik*, vol. 437, no. 1-2, pp. 55–75, 1948.

[77] W. J. D. Beenken, "Excitons in conjugated polymers: Do we need a paradigma change?," *Physica Status Solidi A*, vol. 206, no. 12, pp. 2750–2756, 2009.

[78] P. E. Shaw, A. Ruseckas, and I. D. W. Samuel, "Exciton Diffusion Measurements in Poly(3-hexylthiophene)," *Advanced Materials*, vol. 20, no. 18, pp. 3516–3520, 2008.

[79] C. Deibel and V. Dyakonov, "Polymer–fullerene bulk heterojunction solar cells," *Reports on Progress in Physics*, vol. 73, no. 9, p. 096401, 2010.

[80] R. Sokel and R. C. Hughes, "Numerical analysis of transient photoconductivity in insulators," *Journal of Applied Physics*, vol. 53, no. 11, pp. 7414–7424, 1982.

[81] J. Scott and G. G. Malliaras, "Charge injection and recombination at the metal–organic interface," *Chemical Physics Letters*, vol. 299, no. 2, pp. 115–119, 1999.

[82] M. A. Ruderer and P. Müller-Buschbaum, "Morphology of polymer-based bulk heterojunction films for organic photovoltaics," *Soft Matter*, vol. 7, no. 12, p. 5482, 2011.

[83] M. A. Ruderer, S. Guo, R. Meier, H.-Y. Chiang, V. Körstgens, J. Wiedersich, J. Perlich, S. V. Roth, and P. Müller-Buschbaum, "Solvent-Induced Morphology in Polymer-Based Systems for Organic Photovoltaics," *Advanced Functional Materials*, vol. 21, no. 17, pp. 3382–3391, 2011.

[84] H. Hoppe, M. Niggemann, C. Winder, J. Kraut, R. Hiesgen, A. Hinsch, D. Meissner, and N. S. Sariciftci, "Nanoscale Morphology of Conjugated Polymer/Fullerene-Based Bulk- Heterojunction Solar Cells," *Advanced Functional Materials*, vol. 14, no. 10, pp. 1005–1011, 2004.

[85] F. C. Krebs, J. Fyenbo, and M. Jørgensen, "Product integration of compact roll-to-roll processed polymer solar cell modules: methods and manufacture using flexographic printing, slot-die coating and rotary screen printing," *Journal of Materials Chemistry*, vol. 20, no. 41, p. 8994, 2010.

[86] S. M. Günther, *Implementing an OPV slot die coating device and determining the ramifications on morphology and solar cell performance*. Master's Thesis, Technische Universität München, Garching, 2015.

[87] Y. Yoneda, "Anomalous Surface Reflection of X Rays," *Physical Review*, vol. 131, no. 5, pp. 2010–2013, 1963.

[88] A. Nelson, "Co-refinement of multiple-contrast neutron/X-ray reflectivity data using MOTOFIT," *Journal of Applied Crystallography*, vol. 39, no. 2, pp. 273–276, 2006.

[89] L. G. Parratt, "Surface Studies of Solids by Total Reflection of X-Rays," *Physical Review*, vol. 95, no. 2, pp. 359–369, 1954.

[90] O. S. Heavens, *Optical properties of thin solid films*. New York: Dover Publ, 1991.

[91] L. Névot and P. Croce, "Characterization of surfaces by grazing X-ray reflection - application to the study of polishing of some silicate glasses," *Revue de Physique Applique*, vol. 15, no. 3, pp. 761–780, 1980.

[92] M. Schalke and M. Losche, "Structural models of lipid surface monolayers from X-ray and neutron reflectivity measurements," *Advances in colloid and interface science*, vol. 88, no. 1-2, pp. 243–274, 2000.

[93] H. Kiessig, "Interferenz von Röntgenstrahlen an dünnen Schichten," *Annalen der Physik*, vol. 402, no. 7, pp. 769–788, 1931.

[94] Z. Jiang, "GIXSGUI: A MATLAB toolbox for grazing-incidence X-ray scattering data visualization and reduction, and indexing of buried three-dimensional periodic nanostructured films," *Journal of Applied Crystallography*, vol. 48, no. 3, pp. 917–926, 2015.

[95] D. M. DeLongchamp, R. J. Kline, and A. Herzing, "Nanoscale structure measurements for polymer-fullerene photovoltaics," *Energy & Environmental Science*, vol. 5, no. 3, p. 5980, 2012.

[96] J. L. Baker, L. H. Jimison, S. Mannsfeld, S. Volkman, S. Yin, V. Subramanian, A. Salleo, A. P. Alivisatos, and M. F. Toney, "Quantification of thin film crystallographic orientation using X-ray diffraction with an area detector," *Langmuir*, vol. 26, no. 11, pp. 9146–9151, 2010.

[97] D.-M. Smilgies, "Scherrer grain-size analysis adapted to grazing-incidence scattering with area detectors," *Journal of Applied Crystallography*, vol. 42, no. Pt 6, pp. 1030–1034, 2009.

[98] J. Rivnay, Mannsfeld, Stefan C. B., C. E. Miller, A. Salleo, and M. F. Toney, "Quantitative Determination of Organic Semiconductor Microstructure from the Molecular to Device Scale," *Chemical Reviews*, vol. 112, no. 10, pp. 5488–5519, 2012.

[99] J. Balko, R. H. Lohwasser, M. Sommer, M. Thelakkat, and T. Thurn-Albrecht, "Determination of the Crystallinity of Semicrystalline Poly(3-hexylthiophene) by Means of Wide-Angle X-ray Scattering," *Macromolecules*, vol. 46, no. 24, pp. 9642–9651, 2013.

[100] X. Shen, W. Hu, and T. P. Russell, "Measuring the Degree of Crystallinity in Semicrystalline Regioregular Poly(3-hexylthiophene)," *Macromolecules*, vol. 49, no. 12, pp. 4501–4509, 2016.

[101] R. Lazzari, "IsGISAXS: A program for grazing-incidence small-angle X-ray scattering analysis of supported islands," *Journal of Applied Crystallography*, vol. 35, no. 4, pp. 406–421, 2002.

[102] J. Burle, C. Durniak, J. M. Fisher, M. Ganeva, G. Pospelov, W. Van Herck, and J. Wuttke, "BornAgain: Software for simulating and fitting X-ray and neutron small-angle scattering at grazing incidence (http://www.bornagainproject.org)."

[103] S. T. Chourou, A. Sarje, X. S. Li, E. R. Chan, and A. Hexemer, "HipGISAXS: A high-performance computing code for simulating grazing-incidence X-ray scattering data," *Journal of Applied Crystallography*, vol. 46, no. 6, pp. 1781–1795, 2013.

[104] D. Babonneau, "FitGISAXS: Software package for modelling and analysis of GISAXS data using IGOR Pro," *Journal of Applied Crystallography*, vol. 43, no. 4, pp. 929–936, 2010.

[105] P. Müller-Buschbaum, "Influence of surface cleaning on dewetting of thin polystyrene films," *The European Physical Journal E*, vol. 12, no. 3, pp. 443–448, 2003.

[106] P. Müller-Buschbaum, "Structure Determination in Thin Film Geometry Using Grazing Incidence Small-Angle Scattering," in *Stamm (Hg.) 2008 – Polymer Surfaces and Interfaces*, pp. 17–46.

[107] A. Naudon, D. Babonneau, D. Thiaudière, and S. Lequien, "Grazing-incidence small-angle X-ray scattering applied to the characterization of aggregates in surface regions," *Physica B: Condensed Matter*, vol. 283, no. 1-3, pp. 69–74, 2000.

[108] R. Hosemann, W. Vogel, D. Weick, and F. J. Baltá-Calleja, "Novel aspects of the real paracrystal," *Acta Crystallographica Section A*, vol. 37, no. 1, pp. 85–91, 1981.

[109] G. Renaud, R. Lazzari, and F. Leroy, "Probing surface and interface morphology with Grazing Incidence Small Angle X-Ray Scattering," *Surface Science Reports*, vol. 64, no. 8, pp. 255–380, 2009.

[110] J. Tauc, R. Grigorovici, and A. Vancu, "Optical Properties and Electronic Structure of Amorphous Germanium," *physica status solidi (b)*, vol. 15, no. 2, pp. 627–637, 1966.

[111] N. Ghobadi, "Band gap determination using absorption spectrum fitting procedure," *International Nano Letters*, vol. 3, no. 1, p. 2, 2013.

[112] J. W. Swan and E. M. Furst, "A simpler expression for Henry's function describing the electrophoretic mobility of spherical colloids," *Journal of Colloid and Interface Science*, vol. 388, no. 1, pp. 92–94, 2012.

[113] G. Juška, N. Nekrašas, and K. Genevičius, "Investigation of charge carriers transport from extraction current transients of injected charge carriers," *Journal of Non-Crystalline Solids*, vol. 358, no. 4, pp. 748–750, 2012.

[114] A. Armin, G. Juska, M. Ullah, M. Velusamy, P. L. Burn, P. Meredith, and A. Pivrikas, "Balanced Carrier Mobilities: Not a Necessary Condition for High-Efficiency Thin Organic Solar Cells as Determined by MIS-CELIV," *Advanced Energy Materials*, vol. 4, no. 4, p. 1300954, 2014.

[115] S. Mansi, *Optimization of a charge carrier mobility measurement setup for the characterization of semiconducting organic thin films.* Bachelor's Thesis, Technische Universität München, Garching, 2016.

[116] M. D. Abràmoff, P. J. Magalhães, and S. J. Ram, "Image processing with ImageJ," *Biophotonics international*, vol. 11, no. 7, pp. 36–42, 2004.

[117] A. Hexemer, W. Bras, J. Glossinger, E. Schaible, E. Gann, R. Kirian, A. MacDowell, M. Church, B. Rude, and H. Padmore, "A SAXS/WAXS/GISAXS Beamline with Multilayer Monochromator," *Journal of Physics: Conference Series*, vol. 247, p. 12007, 2010.

[118] A. F. Huq, A. Ammar, A. M. Al-Enizi, and A. Karim, "In-situ orientation and crystal growth kinetics of P3HT in drop cast P3HT:PCBM films," *Polymer*, vol. 113, pp. 200–213, 2017.

[119] K. A. Page, A. Kusoglu, C. M. Stafford, S. Kim, R. J. Kline, and A. Z. Weber, "Confinement-driven increase in ionomer thin-film modulus," *Nano Letters*, vol. 14, no. 5, pp. 2299–2304, 2014.

[120] G. Benecke, W. Wagermaier, C. Li, M. Schwartzkopf, G. Flucke, R. Hoerth, I. Zizak, M. Burghammer, E. Metwalli, P. Müller-Buschbaum, M. Trebbin, S. Förster, O. Paris, S. V. Roth, and P. Fratzl, "A customizable software for fast reduction and analysis of large X-ray scattering data sets: applications of the new DPDAK package to small-angle X-ray scattering and grazing-incidence small-angle X-ray scattering," *Journal of Applied Crystallography*, vol. 47, pp. 1797–1803, 2014.

[121] G. K. V. Thalluri, J.-C. Bolsée, A. Gadisa, M. Parchine, T. Boonen, J. D'Haen, A. E. Boyukbayram, J. Vandenbergh, T. J. Cleij, L. Lutsen, D. Vanderzande, and J. Manca, "Opto-electrical and morphological characterization of water soluble conjugated polymers for eco-friendly hybrid solar cells," *Solar Energy Materials and Solar Cells*, vol. 95, no. 12, pp. 3262–3268, 2011.

[122] C. S. Kuo, F. G. Wakim, S. K. Sengupta, and S. K. Tripathy, "Schottky and Metal-Insulator-Semiconductor Diodes Using Poly(3-hexylthiophene)," *Japanese Journal of Applied Physics*, vol. 33, no. Part 1, No. 5A, pp. 2629–2632, 1994.

[123] Y. Sun, Y. Han, and J. Liu, "Controlling PCBM aggregation in P3HT/PCBM film by a selective solvent vapor annealing," *Chinese Science Bulletin*, vol. 58, no. 22, pp. 2767–2774, 2013.

[124] J. W. Kiel, B. J. Kirby, C. F. Majkrzak, B. B. Maranville, and M. E. Mackay, "Nanoparticle concentration profile in polymer-based solar cells," *Soft Matter*, vol. 6, no. 3, pp. 641–646, 2010.

[125] G. Garcia-Belmonte, A. Munar, E. M. Barea, J. Bisquert, I. Ugarte, and R. Pacios, "Charge carrier mobility and lifetime of organic bulk heterojunctions analyzed by impedance spectroscopy," *Organic Electronics*, vol. 9, no. 5, pp. 847–851, 2008.

[126] B. R. Saunders, "Hybrid polymer/nanoparticle solar cells: preparation, principles and challenges," *Journal of Colloid and Interface Science*, vol. 369, no. 1, pp. 1–15, 2012.

[127] D. W. Schubert and T. Dunkel, "Spin coating from a molecular point of view: Its concentration regimes, influence of molar mass and distribution," *Materials Research Innovations*, vol. 7, no. 5, pp. 314–321, 2003.

[128] O. Filonik, *Influence of electric fields on printed conductive thin films for applications in organic photovoltaics*. Master's Thesis, Technische Universität München, Garching, 20.04.2016.

[129] F. Englbrecht, *Influence of drying dynamics on the performance of printed organic solar cells*. Bachelor's Thesis, Technische Universität München, Garching, 18.08.2015.

[130] K. Norrman, A. Ghanbari-Siahkali, and N. B. Larsen, "6 Studies of spin-coated polymer films," *Annual Reports Section C (Physical Chemistry)*, vol. 101, pp. 174–201, 2005.

[131] R. M. Beal, A. Stavrinadis, J. H. Warner, J. M. Smith, H. E. Assender, and A. A. R. Watt, "The Molecular Structure of Polymer−Fullerene Composite Solar Cells and Its Influence on Device Performance," *Macromolecules*, vol. 43, no. 5, pp. 2343–2348, 2010.

[132] W. Wang, S. Pröller, M. A. Niedermeier, V. Körstgens, M. Philipp, B. Su, D. Moseguí González, S. Yu, S. V. Roth, and P. Müller-Buschbaum, "Development of the Morphology during Functional Stack Build-up of P3HT:PCBM Bulk Heterojunction Solar Cells with Inverted Geometry," *ACS Applied Materials & Interfaces*, vol. 7, no. 1, pp. 602–610, 2015.

[133] A. M. Hiszpanski and Y.-L. Loo, "Directing the film structure of organic semiconductors via post-deposition processing for transistor and solar cell applications," *Energy Environ. Sci.*, vol. 7, no. 2, pp. 592–608, 2014.

[134] A. Cristadoro, G. Lieser, H. J. Räder, and K. Müllen, "Field-force alignment of disc-type pi systems," *ChemPhysChem*, vol. 8, no. 4, pp. 586–591, 2007.

[135] G. Schweicher, N. Paquay, C. Amato, R. Resel, M. Koini, S. Talvy, V. Lemaur, J. Cornil, Y. Geerts, and G. Gbabode, "Toward Single Crystal Thin Films of Terthiophene by Directional Crystallization Using a Thermal Gradient," *Crystal Growth & Design*, vol. 11, no. 8, pp. 3663–3672, 2011.

[136] N. K. Zawacka, T. R. Andersen, J. W. Andreasen, L. H. Rossander, H. F. Dam, M. Jørgensen, and F. C. Krebs, "The influence of additives on the morphology and stability of roll-to-roll processed polymer solar cells studied through ex situ and in situ X-ray scattering," *Journal of Materials Chemistry A*, vol. 2, no. 43, pp. 18644–18654, 2014.

[137] G. Li, Y. Yao, H. Yang, V. Shrotriya, G. Yang, and Y. Yang, "Solvent Annealing Effect in Polymer Solar Cells Based on Poly(3-hexylthiophene) and Methanofullerenes," *Advanced Functional Materials*, vol. 17, no. 10, pp. 1636–1644, 2007.

[138] Y. Diao, Y. Zhou, T. Kurosawa, L. Shaw, C. Wang, S. Park, Y. Guo, J. A. Reinspach, K. Gu, X. Gu, B. C. K. Tee, C. Pang, H. Yan, D. Zhao, M. F. Toney, Mannsfeld, Stefan C. B., and Z. Bao, "Flow-enhanced solution printing of all-polymer solar cells," *Nature Communications*, vol. 6, p. 7955, 2015.

[139] A. Hexemer and P. Müller-Buschbaum, "Advanced grazing-incidence techniques for modern soft-matter materials analysis," *IUCrJ*, vol. 2, no. 1, pp. 106–125, 2015.

[140] F. Liu, W. Zhao, J. R. Tumbleston, C. Wang, Y. Gu, D. Wang, A. L. Briseno, H. Ade, and T. P. Russell, "Understanding the Morphology of PTB7:PCBM Blends in Organic Photovoltaics," *Advanced Energy Materials*, vol. 4, no. 5, p. 1301377, 2014.

[141] W. Wang, C. J. Schaffer, L. Song, V. Körstgens, S. Pröller, E. D. Indari, T. Wang, A. Abdelsamie, S. Bernstorff, and P. Müller-Buschbaum, "In operando morphology investigation of inverted bulk heterojunction organic solar cells by GISAXS," *Journal of Materials Chemistry A*, vol. 3, no. 16, pp. 8324–8331, 2015.

[142] S. Pröller, F. Liu, C. Zhu, C. Wang, T. P. Russell, A. Hexemer, P. Müller-Buschbaum, and E. M. Herzig, "Following the Morphology Formation In Situ in Printed Active Layers for Organic Solar Cells," *Advanced Energy Materials*, vol. 6, no. 1, p. 1501580, 2016.

[143] F. Liu, S. Ferdous, E. Schaible, A. Hexemer, M. Church, X. Ding, C. Wang, and T. P. Russell, "Fast Printing and In Situ Morphology Observation of Organic Photovoltaics Using Slot-Die Coating," *Advanced Materials*, vol. 27, no. 5, pp. 886–891, 2015.

[144] S. Pröller, D. Moseguí González, C. Zhu, E. Schaible, C. Wang, P. Müller-Buschbaum, A. Hexemer, and E. M. Herzig, "Note: Setup for chemical atmospheric control during in situ grazing incidence X-ray scattering of printed thin films," *Review of Scientific Instruments*, vol. 88, no. 6, p. 066101, 2017.

[145] C. M. Palumbiny, F. Liu, T. P. Russell, A. Hexemer, C. Wang, and P. Müller-Buschbaum, "The Crystallization of PEDOT:PSS Polymeric Electrodes Probed In Situ during Printing," *Advanced Materials*, vol. 27, no. 22, pp. 3391–3397, 2015.

[146] IFA - Institute for Occupational Safety and Health of the German Social Sccident Insurance, "GESTIS Substance Database: Safety Data Sheet Polytetrafluoroethylene - www.dguv.de/ifa/gestis-database."

[147] J. Blumm, A. Lindemann, M. Meyer, and C. Strasser, "Characterization of PTFE Using Advanced Thermal Analysis Techniques," *International Journal of Thermophysics*, vol. 31, no. 10, pp. 1919–1927, 2010.

[148] J. W. Nicholson, *The chemistry of polymers*. Cambridge: RSC Pub, 4th ed., 2012.

[149] C.-F. Lin, B.-K. Wang, C. Tiu, and T.-J. Liu, "On the Pinning of Downstream Meniscus for Slot Die Coating," *Advances in Polymer Technology*, vol. 32, no. S1, pp. E249–E257, 2013.

[150] Y.-R. Chang, C.-F. Lin, and T.-J. Liu, "Start-up of slot die coating," *Polymer Engineering & Science*, vol. 49, no. 6, pp. 1158–1167, 2009.

[151] A. Buffet, A. Rothkirch, R. Dohrmann, V. Korstgens, M. M. Abul Kashem, J. Perlich, G. Herzog, M. Schwartzkopf, R. Gehrke, P. Muller-Buschbaum, and S. V. Roth, "P03, the microfocus and nanofocus X-ray scattering (MiNaXS) beamline of the PETRA III storage ring: the microfocus endstation," *Journal of Synchrotron Radiation*, vol. 19, pp. 647–653, 2012.

[152] R. Dohrmann, S. Botta, A. Buffet, G. Santoro, K. Schlage, M. Schwartzkopf, S. Bommel, J. F. H. Risch, R. Mannweiler, S. Brunner, E. Metwalli, P. Muller-Buschbaum, and S. V. Roth, "A new highly automated sputter equipment for in situ investigation of deposition processes with synchrotron radiation," *Review of Scientific Instruments*, vol. 84, no. 4, p. 043901, 2013.

[153] Y. Lee and R. S. Porter, "Double-melting behavior of poly(ether ether ketone)," *Macromolecules*, vol. 20, no. 6, pp. 1336–1341, 1987.

[154] A. M. Jonas, T. P. Russell, and D. Y. Yoon, "Synchrotron X-ray Scattering Studies of Crystallization of Poly(ether-ether-ketone) from the Glass and Structural Changes during Subsequent Heating-Cooling Processes," *Macromolecules*, vol. 28, no. 25, pp. 8491–8503, 1995.

[155] R. K. Goyal, A. N. Tiwari, U. P. Mulik, and Y. S. Negi, "Thermal expansion behaviour of high performance PEEK matrix composites," *Journal of Physics D: Applied Physics*, vol. 41, no. 8, p. 085403, 2008.

[156] Y. Huang, E. J. Kramer, A. J. Heeger, and G. C. Bazan, "Bulk heterojunction solar cells: morphology and performance relationships," *Chemical Reviews*, vol. 114, no. 14, pp. 7006–7043, 2014.

[157] E. Verploegen, C. E. Miller, K. Schmidt, Z. Bao, and M. F. Toney, "Manipulating the Morphology of P3HT–PCBM Bulk Heterojunction Blends with Solvent Vapor Annealing," *Chemistry of Materials*, vol. 24, no. 20, pp. 3923–3931, 2012.

[158] E. Verploegen, R. Mondal, C. J. Bettinger, S. Sok, M. F. Toney, and Z. Bao, "Effects of Thermal Annealing Upon the Morphology of Polymer-Fullerene Blends," *Advanced Functional Materials*, vol. 20, no. 20, pp. 3519–3529, 2010.

[159] M. Reyes-Reyes, K. Kim, J. Dewald, R. Lopez-Sandoval, A. Avadhanula, S. Curran, and D. L. Carroll, "Meso-structure formation for enhanced organic photovoltaic cells," *Organic Letters*, vol. 7, no. 26, pp. 5749–5752, 2005.

[160] X. Gu, I. Gunkel, A. Hexemer, W. Gu, and T. P. Russell, "An in situ grazing incidence X-ray scattering study of block copolymer thin films during solvent vapor annealing," *Advanced Materials*, vol. 26, no. 2, pp. 273–281, 2014.

[161] F. Liu, L. Zhang, Y. Zhang, Mannsfeld, Stefan C. B., T. P. Russell, and A. L. Briseno, "Interpenetrating morphology based on highly crystalline small molecule and PCBM blends," *Journal of Materials Chemistry C*, vol. 2, no. 44, pp. 9368–9374, 2014.

[162] S. Guo, E. M. Herzig, A. Naumann, G. Tainter, J. Perlich, and P. Müller-Buschbaum, "Influence of solvent and solvent additive on the morphology of PTB7 films probed via X-ray scattering," *The Journal of Physical Chemistry B*, vol. 118, no. 1, pp. 344–350, 2014.

[163] H.-C. Liao, C.-C. Ho, C.-Y. Chang, M.-H. Jao, S. B. Darling, and W.-F. Su, "Additives for morphology control in high-efficiency organic solar cells," *Materials Today*, vol. 16, no. 9, pp. 326–336, 2013.

[164] F. Gao, S. Himmelberger, M. Andersson, D. Hanifi, Y. Xia, S. Zhang, J. Wang, J. Hou, A. Salleo, and O. Inganäs, "The Effect of Processing Additives on Energetic

Disorder in Highly Efficient Organic Photovoltaics: A Case Study on PBDTTT-C-T:PC71BM," *Advanced Materials*, vol. 27, no. 26, pp. 3868–3873, 2015.

[165] Böttiger, Arvid P. L., M. Jørgensen, A. Menzel, F. C. Krebs, and J. W. Andreasen, "High-throughput roll-to-roll X-ray characterization of polymer solar cell active layers," *Journal of Materials Chemistry*, vol. 22, no. 42, p. 22501, 2012.

[166] K. Sarkar, E. V. Braden, S. Pogorzalek, S. Yu, S. V. Roth, and P. Müller-Buschbaum, "Monitoring Structural Dynamics of In situ Spray-Deposited Zinc Oxide Films for Application in Dye-Sensitized Solar Cells," *ChemSusChem*, vol. 7, no. 8, pp. 2140–2145, 2014.

[167] V. D. Mihailetchi, H. Xie, B. de Boer, L. M. Popescu, J. C. Hummelen, P. W. M. Blom, and L. J. A. Koster, "Origin of the enhanced performance in poly(3-hexylthiophene): [6,6]-phenyl C[sub 61]-butyric acid methyl ester solar cells upon slow drying of the active layer," *Applied Physics Letters*, vol. 89, no. 1, p. 12107, 2006.

[168] F. Liu, Y. Gu, J. W. Jung, W. H. Jo, and T. P. Russell, "On the morphology of polymer-based photovoltaics," *Journal of Polymer Science Part B: Polymer Physics*, vol. 50, no. 15, pp. 1018–1044, 2012.

[169] B. Schmidt-Hansberg, Klein, M. F. G., K. Peters, F. Buss, J. Pfeifer, S. Walheim, A. Colsmann, U. Lemmer, P. Scharfer, and W. Schabel, "In situ monitoring the drying kinetics of knife coated polymer-fullerene films for organic solar cells," *Journal of Applied Physics*, vol. 106, no. 12, p. 124501, 2009.

[170] M. Sanyal, B. Schmidt-Hansberg, M. F. Klein, C. Munuera, A. Vorobiev, A. Colsmann, P. Scharfer, U. Lemmer, W. Schabel, H. Dosch, and E. Barrena, "Effect of Photovoltaic Polymer/Fullerene Blend Composition Ratio on Microstructure Evolution during Film Solidification Investigated in Real Time by X-ray Diffraction," *Macromolecules*, vol. 44, no. 10, pp. 3795–3800, 2011.

[171] L. A. Perez, K. W. Chou, J. A. Love, T. S. van der Poll, D.-M. Smilgies, T.-Q. Nguyen, E. J. Kramer, A. Amassian, and G. C. Bazan, "Solvent additive effects on small molecule crystallization in bulk heterojunction solar cells probed during spin casting," *Advanced Materials*, vol. 25, no. 44, pp. 6380–6384, 2013.

[172] B. Schmidt-Hansberg, M. Sanyal, Klein, Michael F. G., M. Pfaff, N. Schnabel, S. Jaiser, A. Vorobiev, E. Müller, A. Colsmann, P. Scharfer, D. Gerthsen, U. Lemmer, E. Barrena, and W. Schabel, "Moving through the Phase Diagram: Morphology Formation in Solution Cast Polymer–Fullerene Blend Films for Organic Solar Cells," *ACS Nano*, vol. 5, no. 11, pp. 8579–8590, 2011.

[173] L. H. Rossander, N. K. Zawacka, H. F. Dam, F. C. Krebs, and J. W. Andreasen, "In situ monitoring of structure formation in the active layer of polymer solar cells during roll-to-roll coating," *AIP Advances*, vol. 4, no. 8, p. 87105, 2014.

[174] A. J. Parnell, A. J. Cadby, O. O. Mykhaylyk, Dunbar, Alan D. F., P. E. Hopkinson, A. M. Donald, and Jones, Richard A. L., "Nanoscale Phase Separation of P3HT PCBM Thick Films As Measured by Small-Angle X-ray Scattering," *Macromolecules*, vol. 44, no. 16, pp. 6503–6508, 2011.

[175] S. Guo, M. A. Ruderer, M. Rawolle, V. Körstgens, C. Birkenstock, J. Perlich, and P. Müller-Buschbaum, "Evolution of lateral structures during the functional stack build-up of P3HT:PCBM-based bulk heterojunction solar cells," *ACS Applied Materials & Interfaces*, vol. 5, no. 17, pp. 8581–8590, 2013.

[176] M.-Y. Chiu, U.-S. Jeng, C.-H. Su, K. S. Liang, and K.-H. Wei, "Simultaneous Use of Small– and Wide–Angle X–ray Techniques to Analyze Nanometerscale Phase Separation in Polymer Heterojunction Solar Cells," *Advanced Materials*, vol. 20, no. 13, pp. 2573–2578, 2008.

[177] W.-R. Wu, U.-S. Jeng, C.-J. Su, K.-H. Wei, M.-S. Su, M.-Y. Chiu, C.-Y. Chen, W.-B. Su, C.-H. Su, and A.-C. Su, "Competition between fullerene aggregation and poly(3-hexylthiophene) crystallization upon annealing of bulk heterojunction solar cells," *ACS Nano*, vol. 5, no. 8, pp. 6233–6243, 2011.

[178] M.-Y. Chiu, U.-S. Jeng, M.-S. Su, and K.-H. Wei, "Morphologies of Self-Organizing Regioregular Conjugated Polymer/Fullerene Aggregates in Thin Film Solar Cells," *Macromolecules*, vol. 43, no. 1, pp. 428–432, 2010.

[179] M. Schindler, S. Pröller, T. Geue, and P. Müller-Buschbaum, "Near-Interface Composition in Pressure Sensitive Adhesives at the Adhesive-Adherent Interface," *Macromolecular Reaction Engineering*, vol. 7, no. 10, pp. 549–554, 2013.

[180] P. Kohn, Z. Rong, K. H. Scherer, A. Sepe, M. Sommer, P. Müller-Buschbaum, R. H. Friend, U. Steiner, and S. Hüttner, "Crystallization-Induced 10-nm Structure Formation in P3HT/PCBM Blends," *Macromolecules*, vol. 46, no. 10, pp. 4002–4013, 2013.

[181] B. A. Collins, E. Gann, L. Guignard, X. He, C. R. McNeill, and H. Ade, "Molecular Miscibility of Polymer−Fullerene Blends," *The Journal of Physical Chemistry Letters*, vol. 1, no. 21, pp. 3160–3166, 2010.

[182] H. W. Ro, B. Akgun, B. T. O'Connor, M. Hammond, R. J. Kline, C. R. Snyder, S. K. Satija, A. L. Ayzner, M. F. Toney, C. L. Soles, and D. M. DeLongchamp, "Poly(3-hexylthiophene) and [6,6]-Phenyl-C 61 -butyric Acid Methyl Ester Mixing in Organic Solar Cells," *Macromolecules*, vol. 45, no. 16, pp. 6587–6599, 2012.

[183] H.-C. Liao, C.-S. Tsao, T.-H. Lin, C.-M. Chuang, C.-Y. Chen, U.-S. Jeng, C.-H. Su, Y.-F. Chen, and W.-F. Su, "Quantitative Nanoorganized Structural Evolution for a High Efficiency Bulk Heterojunction Polymer Solar Cell," *Journal of the American Chemical Society*, vol. 133, no. 33, pp. 13064–13073, 2011.

[184] S. Vajjala Kesava, R. Dhanker, D. R. Kozub, K. Vakhshouri, U. H. Choi, R. H. Colby, C. Wang, A. Hexemer, N. C. Giebink, and E. D. Gomez, "Mesoscopic Structural Length Scales in P3HT/PCBM Mixtures Remain Invariant for Various Processing Conditions," *Chemistry of Materials*, vol. 25, no. 14, pp. 2812–2818, 2013.

[185] Y. Kim, S. A. Choulis, J. Nelson, Bradley, D. D. C., S. Cook, and J. R. Durrant, "Composition and annealing effects in polythiophene/fullerene solar cells," *Journal of Materials Science*, vol. 40, no. 6, pp. 1371–1376, 2005.

[186] D. Chen, A. Nakahara, D. Wei, D. Nordlund, and T. P. Russell, "P3HT/PCBM bulk heterojunction organic photovoltaics: correlating efficiency and morphology," *Nano letters*, vol. 11, no. 2, pp. 561–567, 2011.

[187] T. Erb, U. Zhokhavets, G. Gobsch, S. Raleva, B. Stühn, P. Schilinsky, C. Waldauf, and C. J. Brabec, "Correlation Between Structural and Optical Properties of Composite Polymer/Fullerene Films for Organic Solar Cells," *Advanced Functional Materials*, vol. 15, no. 7, pp. 1193–1196, 2005.

[188] C. R. Singh, G. Gupta, R. Lohwasser, S. Engmann, J. Balko, M. Thelakkat, T. Thurn-Albrecht, and H. Hoppe, "Correlation of charge transport with structural order in highly ordered melt-crystallized poly(3-hexylthiophene) thin films," *Journal of Polymer Science Part B: Polymer Physics*, vol. 51, no. 12, pp. 943–951, 2013.

[189] G. Li, V. Shrotriya, J. Huang, Y. Yao, T. Moriarty, K. Emery, and Y. Yang, "High-efficiency solution processable polymer photovoltaic cells by self-organization of polymer blends," *Nature Materials*, vol. 4, no. 11, pp. 864–868, 2005.

[190] M. Campoy-Quiles, T. Ferenczi, T. Agostinelli, P. G. Etchegoin, Y. Kim, T. D. Anthopoulos, P. N. Stavrinou, Bradley, Donal D. C., and J. Nelson, "Morphology evolution via self-organization and lateral and vertical diffusion in polymer:fullerene solar cell blends," *Nature Materials*, vol. 7, no. 2, pp. 158–164, 2008.

[191] F. Molina-Lopez, H. Yan, X. Gu, Y. Kim, M. F. Toney, and Z. Bao, "Electric Field Tuning Molecular Packing and Electrical Properties of Solution-Shearing Coated Organic Semiconducting Thin Films," *Advanced Functional Materials*, vol. 27, no. 8, p. 1605503, 2017.

[192] D. M. DeLongchamp, B. M. Vogel, Y. Jung, M. C. Gurau, C. A. Richter, O. A. Kirillov, J. Obrzut, D. A. Fischer, S. Sambasivan, L. J. Richter, and E. K. Lin, "Vari-

ations in Semiconducting Polymer Microstructure and Hole Mobility with Spin-Coating Speed," *Chemistry of Materials*, vol. 17, no. 23, pp. 5610–5612, 2005.

[193] J. J. van Franeker, M. Turbiez, W. Li, M. M. Wienk, and R. A. J. Janssen, "A real-time study of the benefits of co-solvents in polymer solar cell processing," *Nature Communications*, vol. 6, p. 6229, 2015.

[194] F. Padinger, R. S. Rittberger, and N. S. Sariciftci, "Effects of Postproduction Treatment on Plastic Solar Cells," *Advanced Functional Materials*, vol. 13, no. 1, pp. 85–88, 2003.

[195] C.-C. Lin, Y.-Y. Lin, S.-S. Li, C.-C. Yu, C.-L. Huang, S.-H. Lee, C.-H. Du, J.-J. Lee, H.-L. Chen, and C.-W. Chen, "Electric field-assisted self-organization of polymer:fullerene hybrids on the photovoltaic performance," *Energy & Environmental Science*, vol. 4, no. 6, p. 2134, 2011.

[196] A. Solanki, A. Bagui, G. Long, B. Wu, T. Salim, Y. Chen, Y. M. Lam, and T. C. Sum, "Effectiveness of External Electric Field Treatment of Conjugated Polymers in Bulk-Heterojunction Solar Cells," *ACS Applied Materials & Interfaces*, vol. 8, no. 47, pp. 32282–32291, 2016.

[197] M. Elshobaki, R. Gebhardt, J. Carr, W. Lindemann, W. Wang, E. Grieser, S. Venkatesan, E. Ngo, U. Bhattacharjee, J. Strzalka, Z. Jiang, Q. Qiao, J. Petrich, D. Vaknin, and S. Chaudhary, "Tailoring Nanoscale Morphology of Polymer:Fullerene Blends Using Electrostatic Field," *ACS Applied Materials & Interfaces*, vol. 9, no. 3, pp. 2678–2685, 2017.

[198] Y.-M. Shen, C.-S. Chen, P.-C. Yang, S.-Y. Ma, and C.-F. Lin, "Improvement of surface morphology of thin films and performance by applying electric field on P3HT: PCBM based solar cells," *Solar Energy Materials and Solar Cells*, vol. 99, pp. 263–267, 2012.

[199] R. Vijayan, K. Swathi, and K. S. Narayan, "Synergistic Effects of Electric-Field-Assisted Annealing and Thermal Annealing in Bulk-Heterojunction Solar Cells," *ACS Applied Materials & Interfaces*, 2016.

[200] A. Bagui and S. S. K. Iyer, "Increase in hole mobility in poly (3-hexylthiophene-2,5-diyl) films annealed under electric field during the solvent drying step," *Organic Electronics*, vol. 15, no. 7, pp. 1387–1395, 2014.

[201] A. Bagui and S. S. K. Iyer, "Effect of Solvent Annealing in the Presence of Electric Field on P3HT:PCBM Films Used in Organic Solar Cells," *IEEE Transactions on Electron Devices*, vol. 58, no. 11, pp. 4061–4066, 2011.

[202] S.-Y. Ma, Y.-M. Shen, P.-C. Yang, C.-S. Chen, and C.-F. Lin, "Morphological

modification induced by external electric field during solution process of organic solar cells," *Organic Electronics*, vol. 13, no. 2, pp. 297–301, 2012.

[203] E. Schäffer, T. Thurn-Albrecht, T. P. Russell, and U. Steiner, "Electrically induced structure formation and pattern transfer," *Nature*, vol. 403, no. 6772, pp. 874–877, 2000.

[204] M. Mas-Torrent, D. d. Boer, M. Durkut, P. Hadley, and Schenning, A P H J, "Field effect transistors based on poly(3-hexylthiophene) at different length scales," *Nanotechnology*, vol. 15, no. 4, pp. S265–S269, 2004.

[205] C. X. Zhao, X. Wang, W. Zeng, Z. K. Chen, B. S. Ong, K. Wang, L. Deng, and G. Xu, "Organic photovoltaic power conversion efficiency improved by AC electric field alignment during fabrication," *Applied Physics Letters*, vol. 99, no. 5, p. 053305, 2011.

[206] A. Solanki, B. Wu, T. Salim, E. K. L. Yeow, Y. M. Lam, and T. C. Sum, "Performance Improvements in Polymer Nanofiber/Fullerene Solar Cells with External Electric Field Treatment," *The Journal of Physical Chemistry C*, vol. 118, no. 21, pp. 11285–11291, 2014.

[207] M. Fromm, V. Maess, G. Landmesser, and T. Montag, "Transfer station for a liquid toner printing system - US 9405237 B2," 2016.

[208] J. Thanner, M. Viechter, and S. Pröller, "Anordnung zum Wiederaufbereiten und Rückführen von Trägerflüssigkeit in einem Drucker oder Kopierer sowie zugehöriges Verfahren - DE102013103964 A1," 2014.

[209] A. Wagenpfahl, D. Rauh, M. Binder, C. Deibel, and V. Dyakonov, "S-shaped current-voltage characteristics of organic solar devices," *Physical Review B*, vol. 82, no. 11, 2010.

[210] K. Liu, T. T. Larsen-Olsen, Y. Lin, M. Beliatis, E. Bundgaard, M. Jørgensen, F. C. Krebs, and X. Zhan, "Roll-coating fabrication of flexible organic solar cells: Comparison of fullerene and fullerene-free systems," *Journal of Materials Chemistry A*, vol. 4, no. 3, pp. 1044–1051, 2016.

[211] R. J. Kline, M. D. McGehee, and M. F. Toney, "Highly oriented crystals at the buried interface in polythiophene thin-film transistors," *Nature materials*, vol. 5, no. 3, pp. 222–228, 2006.

[212] Y. Kim, S. Cook, S. M. Tuladhar, S. A. Choulis, J. Nelson, J. R. Durrant, Bradley, Donal D. C., M. Giles, I. McCulloch, C.-S. Ha, and M. Ree, "A strong regioregularity effect in self-organizing conjugated polymer films and high-efficiency polythiophene:fullerene solar cells," *Nature Materials*, vol. 5, no. 3, pp. 197–203, 2006.

[213] C. N. Hoth, P. Schilinsky, S. A. Choulis, and C. J. Brabec, "Printing Highly Efficient Organic Solar Cells," *Nano letters*, vol. 8, no. 9, pp. 2806–2813, 2008.

[214] X. Gu, Y. Zhou, K. Gu, T. Kurosawa, Y. Guo, Y. Li, H. Lin, B. C. Schroeder, H. Yan, F. Molina-Lopez, C. J. Tassone, C. Wang, Mannsfeld, Stefan C. B., H. Yan, D. Zhao, M. F. Toney, and Z. Bao, "Roll-to-Roll Printed Large-Area All-Polymer Solar Cells with 5% Efficiency Based on a Low Crystallinity Conjugated Polymer Blend," *Advanced Energy Materials*, vol. 26, p. 1602742, 2017.

[215] N. Gasparini, L. Lucera, M. Salvador, M. Prosa, G. D. Spyropoulos, P. Kubis, H.-J. Egelhaaf, C. J. Brabec, and T. Ameri, "High-performance ternary organic solar cells with thick active layer exceeding 11% efficiency," *Energy & Environmental Science*, vol. 10, no. 4, pp. 885–892, 2017.

[216] M. Li, K. Gao, X. Wan, Q. Zhang, B. Kan, R. Xia, F. Liu, X. Yang, H. Feng, W. Ni, Y. Wang, J. Peng, H. Zhang, Z. Liang, H.-L. Yip, X. Peng, Y. Cao, and Y. Chen, "Solution-processed organic tandem solar cells with power conversion efficiencies >12%," *Nature Photonics*, vol. 11, no. 2, pp. 85–90, 2016.

[217] P. Cheng, M. Zhang, T.-K. Lau, Y. Wu, B. Jia, J. Wang, C. Yan, M. Qin, X. Lu, and X. Zhan, "Realizing Small Energy Loss of 0.55 eV, High Open-Circuit Voltage 1 V and High Efficiency 10% in Fullerene-Free Polymer Solar Cells via Energy Driver," *Advanced Materials*, vol. 29, no. 11, 2017.

[218] X. Gu, H. Yan, T. Kurosawa, B. C. Schroeder, K. L. Gu, Y. Zhou, J. W. F. To, S. D. Oosterhout, V. Savikhin, F. Molina-Lopez, C. J. Tassone, Mannsfeld, Stefan C. B., C. Wang, M. F. Toney, and Z. Bao, "Comparison of the Morphology Development of Polymer-Fullerene and Polymer-Polymer Solar Cells during Solution-Shearing Blade Coating," *Advanced Energy Materials*, vol. 6, no. 22, p. 1601225, 2016.

[219] L. Lu, T. Zheng, Q. Wu, A. M. Schneider, D. Zhao, and L. Yu, "Recent Advances in Bulk Heterojunction Polymer Solar Cells," *Chemical Reviews*, vol. 115, no. 23, pp. 12666–12731, 2015.

[220] Y. Kim, S. A. Choulis, J. Nelson, Bradley, Donal D. C., S. Cook, and J. R. Durrant, "Device annealing effect in organic solar cells with blends of regioregular poly(3-hexylthiophene) and soluble fullerene," *Applied Physics Letters*, vol. 86, no. 6, p. 063502, 2005.

[221] W. Ma, C. Yang, X. Gong, K. Lee, and A. J. Heeger, "Thermally Stable, Efficient Polymer Solar Cells with Nanoscale Control of the Interpenetrating Network Morphology," *Advanced Functional Materials*, vol. 15, no. 10, pp. 1617–1622, 2005.

[222] S. E. Shaheen, C. J. Brabec, N. S. Sariciftci, F. Padinger, T. Fromherz, and J. C.

Hummelen, "2.5% efficient organic plastic solar cells," *Applied Physics Letters*, vol. 78, no. 6, pp. 841–843, 2001.

[223] J. Peet, J. Y. Kim, N. E. Coates, W. L. Ma, D. Moses, A. J. Heeger, and G. C. Bazan, "Efficiency enhancement in low-bandgap polymer solar cells by processing with alkane dithiols," *Nature Materials*, vol. 6, no. 7, pp. 497–500, 2007.

[224] F. Zhang, K. G. Jespersen, C. Björström, M. Svensson, M. R. Andersson, V. Sundström, K. Magnusson, E. Moons, A. Yartsev, and O. Inganäs, "Influence of Solvent Mixing on the Morphology and Performance of Solar Cells Based on Polyfluorene Copolymer/Fullerene Blends," *Advanced Functional Materials*, vol. 16, no. 5, pp. 667–674, 2006.

[225] Z. Li, X. Xu, W. Zhang, X. Meng, W. Ma, A. Yartsev, O. Inganäs, M. R. Andersson, Janssen, René A. J., and E. Wang, "High Performance All-Polymer Solar Cells by Synergistic Effects of Fine-Tuned Crystallinity and Solvent Annealing," *Journal of the American Chemical Society*, vol. 138, no. 34, pp. 10935–10944, 2016.

[226] R. C. Nieuwendaal, H. W. Ro, D. S. Germack, R. J. Kline, M. F. Toney, C. K. Chan, A. Agrawal, D. Gundlach, D. L. VanderHart, and D. M. DeLongchamp, "Measuring Domain Sizes and Compositional Heterogeneities in P3HT-PCBM Bulk Heterojunction Thin Films with 1H Spin Diffusion NMR Spectroscopy," *Advanced Functional Materials*, vol. 22, no. 6, pp. 1255–1266, 2012.

[227] N. S. Güldal, T. Kassar, M. Berlinghof, T. Unruh, and C. J. Brabec, "In situ characterization methods for evaluating microstructure formation and drying kinetics of solution-processed organic bulk-heterojunction films," *Journal of Materials Research*, vol. 32, no. 10, pp. 1855–1879, 2017.

[228] K. Vegso, P. Siffalovic, M. Jergel, P. Nadazdy, V. Nadazdy, and E. Majkova, "Kinetics of Polymer-Fullerene Phase Separation during Solvent Annealing Studied by Table-Top X-ray Scattering," *ACS Applied Materials & Interfaces*, vol. 9, no. 9, pp. 8241–8247, 2017.

[229] S. Engmann, H. W. Ro, A. Herzing, C. R. Snyder, L. J. Richter, P. B. Geraghty, and D. J. Jones, "Film morphology evolution during solvent vapor annealing of highly efficient small molecule donor/acceptor blends," *Journal of Materials Chemistry A*, vol. 4, no. 40, pp. 15511–15521, 2016.

[230] S. Engmann, F. A. Bokel, A. A. Herzing, H. W. Ro, C. Girotto, B. Caputo, C. V. Hoven, E. Schaible, A. Hexemer, D. M. DeLongchamp, and L. J. Richter, "Real-time X-ray scattering studies of film evolution in high performing small-molecule-fullerene organic solar cells," *Journal of Materials Chemistry A*, vol. 3, no. 16, pp. 8764–8771, 2015.

[231] J. Min, X. Jiao, I. Ata, A. Osvet, T. Ameri, P. Bäuerle, H. Ade, and C. J. Brabec, "Time-Dependent Morphology Evolution of Solution-Processed Small Molecule Solar Cells during Solvent Vapor Annealing," *Advanced Energy Materials*, vol. 6, no. 10, p. 1502579, 2016.

[232] N. S. Güldal, T. Kassar, M. Berlinghof, T. Ameri, A. Osvet, R. Pacios, G. Li Destri, T. Unruh, and C. J. Brabec, "Real-time evaluation of thin film drying kinetics using an advanced, multi-probe optical setup," *Journal of Materials Chemistry C*, vol. 4, no. 11, pp. 2178–2186, 2016.

[233] J. A. Reinspach, Y. Diao, G. Giri, T. Sachse, K. England, Y. Zhou, C. Tassone, B. J. Worfolk, M. Presselt, M. F. Toney, S. Mannsfeld, and Z. Bao, "Tuning the Morphology of Solution-Sheared P3HT:PCBM Films," *ACS Applied Materials & Interfaces*, vol. 8, no. 3, pp. 1742–1751, 2016.

[234] J. H. Gibbs and E. A. DiMarzio, "Nature of the Glass Transition and the Glassy State," *The Journal of Chemical Physics*, vol. 28, no. 3, pp. 373–383, 1958.

[235] C. Müller, "On the Glass Transition of Polymer Semiconductors and Its Impact on Polymer Solar Cell Stability," *Chemistry of Materials*, vol. 27, no. 8, pp. 2740–2754, 2015.

[236] G. Reiter, "Some unique features of polymer crystallisation," *Chemical Society Reviews*, vol. 43, no. 7, pp. 2055–2065, 2014.

[237] M. Koppe, M. Scharber, C. Brabec, W. Duffy, M. Heeney, and I. McCulloch, "Polyterthiophenes as Donors for Polymer Solar Cells," *Advanced Functional Materials*, vol. 17, no. 8, pp. 1371–1376, 2007.

[238] B. A. Collins, J. R. Tumbleston, and H. Ade, "Miscibility, Crystallinity, and Phase Development in P3HT/PCBM Solar Cells: Toward an Enlightened Understanding of Device Morphology and Stability," *The Journal of Physical Chemistry Letters*, vol. 2, no. 24, pp. 3135–3145, 2011.

[239] N. D. Treat, M. A. Brady, G. Smith, M. F. Toney, E. J. Kramer, C. J. Hawker, and M. L. Chabinyc, "Interdiffusion of PCBM and P3HT Reveals Miscibility in a Photovoltaically Active Blend," *Advanced Energy Materials*, vol. 1, no. 1, pp. 82–89, 2011.

List of publications

Publications related to the dissertation

- S. Pröller, O. Filonik, S. Mansi, C. Zhu, E. Schaible, A. Hexemer, P. Müller-Buschbaum, E. M. Herzig, "Electrophoresis assisted printing: a method to control the morphology in organic thin films", *submitted*
- S. Pröller, D. Moseguí González, C. Zhu, E. Schaible, C. Wang, P. Müller-Buschbaum, A. Hexemer, E. M. Herzig, "Note: Setup for chemical atmospheric control during in situ grazing incidence X-ray scattering of printed thin films", *Review of Scientific instruments*, 88 (6), 066101, 2017
- S. Pröller, F. Liu, C. Zhu, C. Wang, T. P. Russell, A. Hexemer, P. Müller-Buschbaum, E. M. Herzig, "Following the Morphology Formation In Situ in Printed Active Layers for Organic Solar Cells", *Advanced Energy Materials*, 6 (1), 1501580, 2016

Further publications

- M. Reichenberger, D. Kroh, G. M. M. Matrone, K. Schötz, S. Pröller, O. Filonik, M. E. Thordardottir, Eva M. Herzig, H. Bässler, N. Stingelin, A. Köhler, "Controlling aggregate formation in conjugated polymers by spin-coating below the critical temperature of the disorder–order transition", *Journal of Polymer Science Part B: Polymer Physics*, 56 (6), 532-542, 2018
- L. Song, W. Wang, S. Pröller, D. Moseguí González, J. Schlipf, C. J. Schaffer, K. Peters, E. M. Herzig, S. Bernstorff, T. Bein, D. Fattakhova-Rohlfing, P. Müller-Buschbaum, "In Situ Study of Degradation in P3HT–Titania-Based Solid-State Dye-Sensitized Solar Cells", *ACS Energy Letters*, 2 (5), 991-997, 2017
- D. Moseguí González, C. J. Schaffer, S. Pröller, J. Schlipf, L. Song, S. Bernstorff, E. M. Herzig, P. Müller-Buschbaum, "Codependence between Crystalline and Photovoltage Evolutions in P3HT:PCBM Solar Cells Probed with in-Operando GI-WAXS", *ACS Applied Materials & Interfaces*, 9 (4),3282-3287, 2017

- W. Wang, C. J. Schaffer, L. Song, V. Körstgens, S. Pröller, E. Dwi Indari, T. Wang, A. Abdelsamie, S. Bernstorff, P. Müller-Buschbaum, "In-operando morphology investigation of inverted bulk heterojunction organic solar cells by GISAXS", *Journal of Materials Chemistry A*, 3 (16), 8324-8331, 2015
- V. Körstgens, S. Pröller, T. Buchmann, D. Moseguí González, L. Song, Y. Yao, W. Wang, J. Werhahn, G. Santoro, S. V. Roth, H. Iglev, R. Kienberger, P. Müller-Buschbaum, "Laser-ablated titania nanoparticles for aqueous processed hybrid solar cells", *Nanoscale*, 7 (1), 2900-2904, 2015
- W. Wang, S. Pröller, M. A. Niedermeier, V. Körstgens, M. Philipp, B. Su, D. Moseguí González, S. Yu, S. V. Roth, P. Müller-Buschbaum, "Development of the Morphology during Functional Stack Build-up of P3HT:PCBM Bulk Heterojunction Solar Cells with Inverted Geometry", *ACS Applied Materials & Interfaces*, 7 (1), 602-610, 2015
- M. Schindler, S. Pröller, T. Geue, P. Müller-Buschbaum, "Near-Interface Composition in Pressure Sensitive Adhesives at the Adhesive-Adherent Interface", *Macromolecular Reaction Engineering*, 7 (10), 549-554, 2013

Scientific reports

- S. Pröller, F. Liu, C. Zhu, C. Wang, T. P. Russell, A. Hexemer, P. Müller-Buschbaum, E. M. Herzig, "Following the Morphology Formation In Situ in Printed Active Layers for Organic Solar Cells", *Lehrstuhl für Funktionelle Materialien, Annual Report*, 2015
- S. Pröller, F. Liu, C. Zhu, T. P. Russell, A. Hexemer, P. Müller-Buschbaum, E. M. Herzig, "Following the evolution of nanostructure in active layers of printed solar cells", *Munich School of Engineering, Annual Report*, 2015
- S. Pröller, F. Liu, C. Zhu, T. P. Russell, A. Hexemer, P. Müller-Buschbaum, E. M. Herzig, "In-situ morphology investigations of printed photoactive layers for application in organic solar cells", *Lehrstuhl für Funktionelle Materialien, Annual Report*, 2014

Conference talks

- S. Pröller, D. Moseguí González, F. Liu, C. Zhu, C. Wang, E. Schaible, T. P. Russell, A. Hexemer, P. Müller-Buschbaum, E. M. Herzig, "In situ Characterization of the Structure Formation in Printed Organic Films for Photovoltaic Applications", *AVS 64th International Symposium & Exhibition*, Tampa, Florida, USA, 29.10.-03.11.2017
- S. Pröller, O. Filonik, S. Mansi, C. Zhu, E. Schaible, A. Hexemer, P. Müller-Buschbaum, E. M. Herzig, "Manipulating the morphology in printed organic solar cells", *3rd internal biennial science meeting of the MLZ*, Grainau, Germany, 19.-22.06.2017
- S. Pröller, E. M. Herzig, "Slot die printing of OPV", *canSAS-IX*, Stanford, California, USA, 05.-07.06.2017
- S. Pröller, O. Filonik, S. Mansi, C. Zhu, A. Hexemer, P. Müller-Buschbaum, E. M. Herzig, "Manipulating the morphology in printed organic solar cells", *DPG spring meeting*, Dresden, Germany, 20-26.03.2017
- S. Pröller, J. Lebert, "Polymer Blends", *Summer School - Lehrstuhl für Funktionelle Materialien, TUM*, Obertauern, Austria, 21.-24.06.2016
- S. Pröller, F. Liu, C. Zhu, C. Wang, T. P. Russell, A. Hexemer, P. Müller-Buschbaum, E. M. Herzig, "Structure formation dynamics in printed active layers for organic photovoltaics", *GISAS conference*, Nice, France, 08-11.09.2015
- S. Pröller, F. Liu, C. Zhu, C. Wang, T. P. Russell, A. Hexemer, P. Müller-Buschbaum, E. M. Herzig, "Crystallization kinetics in printed active layers for organic solar cells", *DPG spring meeting*, Berlin, Germany, 15.-20.03.2015
- S. Pröller, E. M. Herzig, "OPV research at the Munich School of Engineering", *oe-a workgroup meeting*, München, Germany, 02.03.2015
- S. Pröller, C. Schaffer, "Polymer Crystallization", *Summer School - Lehrstuhl für Funktionelle Materialien, TUM*, Obertauern, Austria, 24.-27.06.2014

Conference poster presentations

- S. Pröller, D. Moseguí González, F. Liu, C. Zhu, C. Wang, E. Schaible, T. P. Russell, A. Hexemer, P. Müller-Buschbaum, E. M. Herzig, "Following the Morphology Formation In Situ in Printed Active Layers for Organic Solar Cells", *GISAS Summer School 2016*, Garching, Germany, 18.-22.07.2016

- S. Pröller, D. Moseguí González, F. Liu, C. Zhu, C. Wang, E. Schaible, T. P. Russell, A. Hexemer, P. Müller-Buschbaum, E. M. Herzig, "Following the Morphology Formation In Situ in Printed Active Layers for Organic Solar Cells", *6th Colloquium of the Munich School of Engineering*, Garching, Germany, 07.07.2016
- S. Pröller, S. Günther, C. Schaffer, F. Englbrecht, E. Metwalli, P. Müller-Buschbaum, E. M. Herzig, "Autark durch gedruckte Energieversorgung", *Bund der Freunde (BdF) TUM Meeting*, München, Germany, 04.12.2015
- S. Pröller, F. Liu, C. Zhu, C. Wang, T. P. Russell, A. Hexemer, P. Müller-Buschbaum, E. M. Herzig, "Following the evolution of nanostructures in active layers of printed solar cells", *RACIRI Summer School*, Sellin (Rügen), Germany, 22.-25.08.2015
- S. Pröller, F. Liu, C. Zhu, C. Wang, T. P. Russell, A. Hexemer, P. Müller-Buschbaum, E. M. Herzig, "Following the evolution of nanostructures in active layers of printed solar cells", *5th Colloquium of the Munich School of Engineering*, Garching, Germany, 09.07.2015
- S. Pröller, M. Coric, F. Liu, C. Zhu, T. P. Russell, A. Hexemer, P. Müller-Buschbaum, E. M. Herzig, "In-situ GISAXS and GIWAXS studies of printed thin films for the application in organic photovoltaics", *SNI conference*, Bonn, Germany, 21.-23.09.2014
- S. Pröller, F. Liu, C. Zhu, T. P. Russell, A. Hexemer, P. Müller-Buschbaum, E. M. Herzig, "Printing Active Layers for Application in Organic Solar Cells", *4th Colloquium of the Munich School of Engineering*, München, Germany, 03.07.2014
- S. Pröller, V. Körstgens, D. Moseguí González, Y. Yao, S. Yu, S. V. Roth, E. M. Herzig, P. Müller-Buschbaum, "Crystallinity investigations on an aqueous-processable conducting polymer for applications in environmentally friendly organic solar cells", *DPG spring meeting*, Dresden, Germany, 30.03-04.04.2014

Acknowledgments

My first thanks are directed to Prof. Eva M. Herzig for the opportunity to be her first PhD student and her trust in me to jointly set up the group and labs. You gave me the freedom to develop my own scientific ideas and elaborate them. Thank you for the possibility to learn so many things, not only in the field of science, but also in negotiation with suppliers and applications for funding. Setting up our facilities gave me a lot of insights and experience in these fields. I extremely enjoyed working on my topic and having the freedom to try out so many things. Additionally, I greatly appreciated the chance to perform parts of my PhD abroad and to present my scientific results at international conferences. I am very happy that you got your new position in Bayreuth and wish you all the best for this next stage in your career. Keep up your infectious enthusiasm about science!

During my studies and my PhD I learned a lot from Prof. Peter Müller-Buschbaum. I thank you for your ongoing support and the collaboration during my research. The scientific discussions about my experiments and results were extremely beneficial for my work. I especially profited from your advise on data analysis and communicating the scientific results to a broad audience. Thank you for always taking time for me despite your busy schedule.

No work can be performed without being funded. Therefore, I acknowledge the Bavarian State Ministry of Science, Research and the Arts for funding via the project "Energy Valley Bavaria". Moreover, I successfully applied for further funding from the Dr.-Ing. Leonhard-Lorenz-Stiftung and from BaCaTec. This funding allowed me to build the printer and perform experiments in Berkeley, California.

Funding itself is not everything for working abroad. Without Dr. Alexander Hexemer, who hosted me in his group in Berkeley, I would not be able to get the experience of working internationally. Thank you for supporting me and offering an office whenever I visited you. An experimental physicist is nothing without a laboratory. Therefore, I am very thankful to Prof. Thomas P. Russell for offering me the possibility to work in your labs during all my stays in Berkeley. Thank you for your advise and discussions on my scientific results. In Berkeley, I also got the change to work together and learn from Prof. Feng Liu. Thank you for introducing me to printed organic solar cells. I enjoyed

working together with you and I'm very thankful for your input and discussions and the joined beamtimes at the ALS.

The beamtimes, which provided me with the data necessary for this thesis, would not have been that successful without a great team and your support. Therefore I thank Dr. Chenhui Zhu, Dr. Eric Schaible, Dr. Cheng Wang and Daniel Moseguí González.

Scattering experiments need a lot of preparation. Interpreting the data is only possible with additional experiments. And the scientific equipment must be optimized to reliably work during the beamtimes. For supporting me in this endeavor, I thank Salma Mansi and my students Oliver Filonik, Fabian Englbrecht, Tom Wollschläger, Mosleh Uddin, Johannes Wüllenweber and Benedikt Fuchs. I was very lucky to have so many motivated and hard-working students and enjoyed working with you.

For the construction of my experimental setups, I got a lot of support from the workshop at the university, in particular from Marc Schönberger and Erik Faber. Without your support, the experiments would not be possible.

Keeping away administrative work gave me time to focus on my experiments. Therefore, I thank Marion Waletzki, Susanna Fink and Angela Brunnbauer for keeping together the work groups and for having an open ear when needed!

I am extremely lucky being able to work together with my colleagues in our group. Indeed, I couldn't imagine any better. I enjoyed amazing times with you, which were only rarely interrupted by short periods of doom, which you helped to overcome! I thank all of you for making the work an experience, for the great journeys, the celebrations, the talks and of course for keeping me on the floor. Thank you, Mihael Coric, Jenny Lebert, Oliver Filonik, Salma Mansi, Eva Kratzer, Tom Wollschläger, Anna Sanina, Ana Aguilera, Leonhard Hofbauer, Leo Katzenmeier, Margret Thordardottir and Grace Guu. Special thanks to the crazy PhD students Jenny, Mihi and Oli, you made this time unique! Thank you all for being friends and not just colleagues.

Additionally, I was lucky to work together with the Chair of Functional Materials at the physics department. Thank you for providing the good atmosphere and your support and discussions. You made it a great time and I'm happy to have met you and stay in touch with you. For your support and joint work, I especially thank Johannes Schlipf, Lorenz Bießmann, Nuri Hohn, Nitin Saxena, Franziska Löhrer, Dr. Christoph Schaffer, Dr. Claudia Palumbiny, Daniel Moseguí González, Dr. Volker Körstgens, Dr. Lin Song, Dr. Markus Schindler, Dr. Martine Philipp, Dr. Kuhu Sarkar, Christoph Heller, Erik Braden, Christian Burger, David Magerl, Dr. Weijia Wang and Dr. Monika Rawolle. Moreover, I thank Dr. Martin Niedermeier for even taking the risk to be my mentor. He supported me in taking decisions and took the time for discussions when needed or just to jointly enjoy the times. Thank you all for your support!

Since I frequently worked in Berkeley, I also enjoyed being a part of a group there. I namely thank Dr. Gregory Su, Dr. Isvar Cordova, Dr. Mirosław Salamończyk, Dr. Singanallur V. Venkatakrishnan, Dr. Dinesh Kumar, Dr. Ronald Pandolfi, Dr. Chenhui Zhu, Dr. Eric Schaible, Dr. Cheng Wang and Dr. Alexander Hexemer for the nice working atmosphere and their support during all the times I visited.

For proof reading this thesis I'm very grateful to Oliver Filonik, Jenny Lebert, Mihael Coric and Franzika Löhrer.

For support from the Munich School of Engineering (MSE) during my PhD project concerning all kinds of problems I'm thankful to Angela Brunnbauer, Prof. Thomas Hamacher, Dr. Philipp Kuhn, Dr. Cornelia Gotterbarm and Dr. Christiane Hamacher.

Moreover, there were people who accompanied me for the complete time during my studies and my PhD. We suffered and celebrated together, went through all exams and supported each other through the good and bad times of our PhD. I namely thank René Richarz, Dr. Hülya Aldemir, Dr. Francoise Schäfers and Anna Sib from the Gulder Group, Marko Cigler, Susanne Mayer, Marie-Kristin von Wrisberg from the Lang group, Philipp Rheinländer and Timon Geppert from the Gasteiger group and Akhila Jambagi, Michael Kramer, Korbinian Schechner and Christian Dirschl from the first generation of MSE-PhDs. Special thanks go to my friends from university, Stefan Sorg, Constantin Grigo, Maximilian Diefenbach, Linda Brützel, Steffen Säubert, Barbara Cervantes and Djuro Bikaljevic.

I'm immensely grateful to all my friends, who accepted me having limited time and never gave up the contact, and who were always available, when needed. Thank you Tobias Breintner, Marian Gutscher, Bettina Hetke, Charlotte Berger, Angelina Schemm, Nadja Fischer, Stefan Karl, Veronika Schreck, Sephardim Koblenz, Michael Henn, Ulrike Thoma, Lukas Fischer, Markus Reichel, Markus Rathke, Sarah Waltenberger and Sebastian Junker. I am looking forward to increasing the frequency of our meetings again and staying in such close friendship until being gray and old!

Last but not least I thank my family for their unlimited support. I'm very happy that I can always rely on you. Although you might not have understood all my decisions, you accepted them and supported me nevertheless! The biggest thank goes to Franzi for your patience and endorsement during all the time.